

**TPF-5(238)**  
**Design and Fabrication Standards to Eliminate Fracture  
Critical Concerns in Two-Girder Bridge Systems**

Phase 2: Experimental Testing

May 2017

Robert. J. Connor, Ph.D.

*Purdue University; rconnor@purdue.edu*

Ryan J. Sherman, Ph.D.

*University of Nevada, Las Vegas; ryan.sherman@unlv.edu*

William N. Collins, Ph.D.

*University of Kansas; william.collins@ku.edu*

## TABLE OF CONTENTS

	Page
Table of Contents.....	i
List of Tables .....	vi
List of Figures.....	ix
ABSTRACT.....	xiii
CHAPTER 1 Introduction.....	1
1.1 Motivation.....	1
1.2 Research Objective .....	2
1.3 Fracture Control Plan.....	2
1.4 Current Fracture Critical Inspection Requirements and Development.....	3
1.5 Current Fracture Critical Toughness Requirements and Development .....	4
1.6 HPS History .....	6
CHAPTER 2 Prior Research and Background .....	8
2.1 Wright (2003).....	8
2.2 Collins (2014) .....	9
2.3 Gentilcore (1996).....	10
2.4 Altstadt (2008) .....	11
2.5 NASA Round Robin (2012).....	12
CHAPTER 3 Experimental Research Program .....	14
3.1 Material Selection.....	14
3.1.1 Material Criteria.....	14
3.1.2 Percent Shear Measurement Method Evaluation.....	15
3.1.3 Initial Material Testing .....	17
3.2 Material Characterization.....	19
3.2.1 Tensile Testing.....	20

3.2.2 Chemical Analysis .....	20
3.2.3 Charpy V-Notch Impact Testing .....	20
3.2.4 Percent Shear Estimation .....	23
3.2.5 Reference Temperature Determination Testing.....	23
3.2.6 Fracture Toughness Measurement .....	29
3.3 Large-scale Specimen Types .....	30
3.4 Loading Frames .....	32
3.4.1 Bending Test Setup.....	32
3.4.2 Axial Fatigue Test Setup .....	37
3.4.3 Axial Fracture Test Setup .....	40
3.5 Specimen Flaws .....	43
3.5.1 Bending Test Specimen Flaws.....	44
3.5.2 Axial Test Specimen Flaws .....	45
3.6 Instrumentation .....	46
3.6.1 Data Logger .....	46
3.6.2 Strain.....	47
3.6.3 Temperature .....	49
3.6.4 Displacement .....	50
3.6.5 Force .....	50
3.7 Temperature Chamber .....	51
3.7.1 Bending Temperature Chamber.....	51
3.7.2 Axial Temperature Chamber .....	52
3.8 Test Sequence .....	53
3.8.1 Bending Test Sequence.....	53
3.8.2 Axial Test Sequence .....	56
3.9 Test Specimens .....	58
3.9.1 Bending Specimen Test Matrix .....	59
3.9.1.1 50_2-0_B Specimens.....	59
3.9.1.1.1 Specimen 50_2-0_1B .....	60
3.9.1.1.2 Specimen 50_2-0_2B .....	62
3.9.1.2 50_2-5_B Specimens.....	64

3.9.1.2.1 Specimen 50_2-5_1B .....	65
3.9.1.2.2 Specimen 50_2-5_2B .....	67
3.9.1.3 70_1-5_B Specimens.....	69
3.9.1.3.1 Specimen 70_1-5_1B .....	70
3.9.1.3.2 Specimen 70_1-5_2B .....	72
3.9.2 Axial Specimen Test Matrix .....	74
3.9.2.1 50_1-5_A Specimens .....	75
3.9.2.1.1 Specimen 50_1-5_1A.....	75
3.9.2.1.2 Specimen 50_1-5_2A.....	76
3.9.2.2 50_2-5_A Specimen.....	77
3.9.2.2.1 Specimen 50_2-5_1A.....	78
3.9.2.3 70_1-5_A Specimens .....	79
3.9.2.3.1 Specimen 70_1-5_1A.....	79
3.9.2.3.2 Specimen 70_1-5_2A.....	80
3.10 Experimental Results .....	82
3.10.1 Material Test Results .....	82
3.10.1.1 Tensile Test Results .....	82
3.10.1.2 Chemical Analysis Results.....	83
3.10.1.3 Impact Testing Results .....	84
3.10.1.4 Percent Shear Results .....	86
3.10.1.5 Reference Temperature Determination Testing .....	86
3.10.1.6 Fracture Toughness Measurement .....	89
3.10.2 Large-scale Test Results .....	91
3.10.2.1 Bending Test Results.....	91
3.10.2.2 Axial Test Results .....	92
CHAPTER 4 Analytical Research Program .....	94
4.1 Finite Element Benchmarking Studies.....	94
4.1.1 Linear-Elastic Fracture Mechanics .....	95
4.1.2 Elastic-Plastic Fracture Mechanics.....	96
4.1.3 Through-Thickness Mesh Density.....	97
4.2 Large-scale Test Specimen Finite Element Models.....	98

4.2.1 Large-scale Test Specimen Model Development .....	99
4.2.1.1 General Model Development .....	99
4.2.1.2 Bending Test Specimen Model Development.....	99
4.2.1.3 Axial Test Specimen Model Development .....	104
4.2.2 Large-scale Test Specimen Model Validation.....	107
4.2.2.1 Bending Test Specimen Model Validation .....	107
4.2.2.1.1 50_2-0_B Specimen Model Validation.....	108
4.2.2.1.2 50_2-5_B Specimen Model Validation.....	110
4.2.2.1.3 70_1-5_B Specimen Model Validation.....	112
4.2.2.2 Axial Test Specimen Model Validation .....	115
4.2.3 Large-scale Test Specimen Model Results.....	116
4.3 Analytical Parametric Study .....	119
4.3.1 Analytical Parametric Study Parameters .....	119
4.3.2 Analytical Parametric Study Model Development.....	121
4.3.3 Analytical Parametric Study Results .....	125
CHAPTER 5 Integrated Fracture Control Plan .....	128
5.1 Considerations.....	129
5.2 Components of an Integrated Fracture Control Plan .....	130
5.2.1 Design Considerations .....	131
5.2.2 Material Properties.....	131
5.2.3 Fabrication Guidelines.....	132
5.2.4 In-Service Inspections .....	133
5.3 An Integrated Approach.....	134
5.3.1 Material Toughness .....	134
5.3.2 Tolerable Size .....	137
5.3.3 Fatigue Life.....	138
5.3.4 Inspection Interval .....	140
5.4 Current versus Integrated Specification.....	141
5.5 Inspection Interval and Critical Flaw Size Summary .....	143
CHAPTER 6 Conclusions.....	145
6.1 Summary of Primary Findings.....	145

6.2 Recommendations for Future Work.....	148
List of References .....	149
Appendix A Fracture Toughness Specimen Design Drawings.....	152
Appendix B Bending Specimen Design Drawings .....	155
Appendix C Axial Specimen Design Drawings.....	159
Appendix D Strain Gage Drawings.....	163
Appendix E Tabular Data for Plastic Material Definition .....	168
Appendix F CVN Impact Data.....	170
Appendix G Master Curve Data.....	191
Appendix H Fatigue Life Estimates .....	200

DRAFT - For Review

## LIST OF TABLES

Table	Page
Table 1.1: Original impact energy requirements .....	5
Table 1.2: LAST zones .....	5
Table 1.3: Current material toughness specification for FCMs.....	6
Table 2.1: CVN impact requirements for uniform fracture resistance .....	12
Table 3.1: Percent shear measurement comparison .....	16
Table 3.2: Screened large-scale testing material summary.....	18
Table 3.3: Specimen distribution .....	58
Table 3.4: Large-scale tensile test results .....	83
Table 3.5: Chemical analysis results.....	84
Table 3.6: Reference temperature results.....	87
Table 3.7: Fracture toughness results.....	89
Table 3.8: Bending test results.....	92
Table 3.9: Axial test results .....	93
Table 4.1: Linear-elastic benchmarking summary.....	95
Table 4.2: Elastic-plastic benchmarking summary.....	97
Table 4.3: Large-scale test specimen model results.....	118
Table 4.4: Parametric study properties .....	121
Table 4.5: Parametric study results.....	126
Table 5.1: Current HPS material CVN impact requirements .....	135
Table 5.2: High-toughness material CVN impact requirements.....	135
Table 5.3: Zone III fracture toughness.....	137
Table 5.4: Tolerable crack sizes.....	138
Table 5.5: Fatigue life .....	140
Table 5.6: Inspection interval .....	141

Table 5.7: Comparison of current and high-toughness FCP specification .....	142
Table E.1: Plate E Abaqus material input .....	169
Table F.2: Plate A CVN impact data .....	171
Table F.3: Plate B CVN impact data .....	173
Table F.4: Plate C CVN impact data .....	175
Table F.5: Plate D CVN impact data .....	177
Table F.6: Plate E CVN impact data .....	179
Table F.7: Plate F CVN impact data .....	181
Table F.8: Plate G CVN impact data .....	183
Table F.9: Plate H CVN impact data .....	185
Table F.10: Plate I CVN impact data .....	187
Table F.11: Plate J CVN impact data .....	189
Table G.12: Plate E reference temperature specimen and test data .....	192
Table G.13: Plate E reference temperature validity data .....	192
Table G.14: Plate H reference temperature specimen and test data .....	194
Table G.15: Plate H reference temperature validity data .....	194
Table G.16: Plate I reference temperature specimen and test data .....	196
Table G.17: Plate I reference temperature validity data .....	196
Table G.18: Plate J reference temperature specimen and test data .....	198
Table G.19: Plate J reference temperature validity data .....	198
Table H.20: Fatigue life edge crack current specification .....	201
Table H.21: Fatigue life edge crack 100 ft.-lbs. ....	202
Table H.22: Fatigue life edge crack 125 ft.-lbs. ....	203
Table H.23: Fatigue life edge crack 150 ft.-lbs. ....	204
Table H.24: Fatigue life edge crack 175 ft.-lbs. ....	205
Table H.25: Fatigue life edge crack 200 ft.-lbs. ....	206
Table H.26: Fatigue life center crack current specification .....	207
Table H.27: Fatigue life center crack 100 ft.-lbs. ....	208
Table H.28: Fatigue life center crack 125 ft.-lbs. ....	209
Table H.29: Fatigue life center crack 150 ft.-lbs. ....	210
Table H.30: Fatigue life center crack 175 ft.-lbs. ....	211

Table H.31: Fatigue life center crack 200 ft.-lbs. ....212

DRAFT - For Review

## LIST OF FIGURES

Figure	Page
Figure 3.1: Comparison of enhanced visual (top) and digital methods (bottom).....	17
Figure 3.2: Screened large-scale testing material percent shear.....	19
Figure 3.3: Type A, 10 mm Charpy v-notch impact specimen.....	21
Figure 3.4: SATEC Series Impact Testing Machine.....	22
Figure 3.5: FTS Systems temperature bath.....	23
Figure 3.6: Reference temperature determination specimen.....	24
Figure 3.7: MTS Model 318.10 load frame setup.....	25
Figure 3.8: Charpy mod displacement gage.....	26
Figure 3.9: Fracture mechanics testing temperature chamber.....	27
Figure 3.10: Example optical fatigue crack measurement.....	28
Figure 3.11: Fracture toughness specimen.....	29
Figure 3.12: 0.25 in. displacement gage.....	30
Figure 3.13: Representative bending test specimen.....	31
Figure 3.14: Representative axial test specimen.....	31
Figure 3.15: Schematic view of bending load frame.....	33
Figure 3.16: Twin bending test setups.....	34
Figure 3.17: Pin bearing (left); Roller bearing (right).....	35
Figure 3.18: End bracing.....	36
Figure 3.19: Lateral torsional buckling bracing.....	37
Figure 3.20: Schematic view of axial test fatigue load frame.....	38
Figure 3.21: Axial test fatigue setup.....	39
Figure 3.22: Axial fatigue test setup lateral bracing.....	40
Figure 3.23: Schematic view of axial test fracture load frame.....	41
Figure 3.24: Axial test fracture setup.....	42

Figure 3.25: Axial load frame pin connection .....	43
Figure 3.26: Straight notching (left); V-notching (right).....	44
Figure 3.27: Example straight notch (left); Example v-notch (right).....	45
Figure 3.28: Grinder jig attached to axial test specimen .....	46
Figure 3.29: CR9000X data logger.....	47
Figure 3.30: Example bending specimen instrumentation layout.....	48
Figure 3.31: Example axial specimen instrumentation layout.....	49
Figure 3.32: Dual zone temperature controller .....	52
Figure 3.33: Bending temperature chamber.....	52
Figure 3.34: Axial temperature chamber .....	52
Figure 3.35: Representative static test load .....	54
Figure 3.36: Representative static test longitudinal stress .....	54
Figure 3.37: Example fracture loading sequence.....	56
Figure 3.38: Specimen 50_2-0_1B .....	61
Figure 3.39: Specimen 50_2-0_1B fracture surface .....	62
Figure 3.40: Specimen 50_2-0_2B .....	63
Figure 3.41: Specimen 50_2-0_2B fracture surface .....	64
Figure 3.42: Example dog-bone fracture arrest detail .....	65
Figure 3.43: Specimen 50_2-5_1B .....	66
Figure 3.44: Specimen 50_2-5_1B fracture surface .....	67
Figure 3.45: Specimen 50_2-5_2B .....	68
Figure 3.46: Specimen 50_2-5_2B fracture surface .....	69
Figure 3.47: Specimen 70_1-5_1B .....	71
Figure 3.48: Specimen 70_1-5_1B fracture surface .....	72
Figure 3.49: Specimen 70_1-5_2B .....	73
Figure 3.50: Specimen 70_1-5_2B fracture surface .....	74
Figure 3.51: Specimen 50_1-5_1A.....	76
Figure 3.52: Specimen 50_1-5_1A fracture surface.....	76
Figure 3.53: Specimen 50_1-5_2A .....	77
Figure 3.54: Specimen 50_1-5_2A fracture surface.....	77
Figure 3.55: Specimen 50_2-5_1A .....	78

Figure 3.56: Specimen 50_2-5_1A fracture surface .....	79
Figure 3.57: Specimen 70_1-5_1A .....	80
Figure 3.58: Specimen 70_1-5_1A fracture surface .....	80
Figure 3.59: Specimen 70_1-5_2A .....	81
Figure 3.60: Specimen 70_1-5_2A fracture surface .....	81
Figure 3.61: Large-scale tensile stress-strain curve .....	83
Figure 3.62: Representative CVN impact data with sigmoidal fit.....	85
Figure 3.63: Representative master curve.....	88
Figure 3.64: Representative unsensored master curve.....	88
Figure 3.65: Representative resistance curve.....	90
Figure 4.1: Through-thickness mesh density for Plate E (left) and Plate H (right) .....	98
Figure 4.2: Bending test specimen model example boundary conditions and loading.....	100
Figure 4.3: Bending test specimen model example stiffener.....	101
Figure 4.4: Bending test specimen example model mesh.....	102
Figure 4.5: Bending test specimen example submodel mesh .....	103
Figure 4.6: Bending test specimen model example refined (right) and course (left) crack tip mesh.....	104
Figure 4.7: Axial test specimen model boundary conditions and loading.....	105
Figure 4.8: Axial test specimen model mesh .....	106
Figure 4.9: Axial test specimen model crack tip mesh .....	107
Figure 4.10: Specimen 50_2-0_1B longitudinal stress at centerline .....	108
Figure 4.11: Specimen 50_2-0_1B stress profile at midspan .....	109
Figure 4.12: Specimen 50_2-0_1B displacement at centerline .....	110
Figure 4.13: Specimen 50_2-5_2B longitudinal stress at centerline .....	111
Figure 4.14: Specimen 50_2-5_2B stress profile at midspan .....	111
Figure 4.15: Specimen 50_2-5_2B displacement at centerline .....	112
Figure 4.16: Specimen 70_1-5_1B longitudinal stress at centerline .....	113
Figure 4.17: Specimen 70_1-5_1B stress profile at midspan .....	114
Figure 4.18: Specimen 70_1-5_1B displacement at centerline .....	115
Figure 4.19: Specimen 50_1-5_1A longitudinal stress at midpoint .....	116
Figure 4.20: Specimen 50_1-5_1A longitudinal stress at 24 in.....	116

Figure 4.21: Through-thickness j-integral demand.....	119
Figure 4.22: Comparison of simplified modeling techniques.....	122
Figure 4.23: Comparison of bending section length.....	123
Figure 4.24: Evaluation of overstrength factor.....	124
Figure 4.25: Representative parametric study model.....	125
Figure 4.26: Flange stress ratio.....	127
Figure 5.1: Representative flanges with through-thickness edge (left) and center (right) cracks.....	138
Figure F.1: Plate A CVN impact data.....	172
Figure F.2: Plate B CVN impact data.....	174
Figure F.3: Plate C CVN impact data.....	176
Figure F.4: Plate D CVN impact data.....	178
Figure F.5: Plate E CVN impact data.....	180
Figure F.6: Plate F CVN impact data.....	182
Figure F.7: Plate G CVN impact data.....	184
Figure F.8: Plate H CVN impact data.....	186
Figure F.9: Plate I CVN impact data.....	188
Figure F.10: Plate J CVN impact data.....	190
Figure G.11: Plate E master curve.....	193
Figure G.12: Plate E uncensored master curve.....	193
Figure G.13: Plate H master curve.....	195
Figure G.14: Plate H uncensored master curve.....	195
Figure G.15: Plate I master curve.....	197
Figure G.16: Plate I uncensored master curve.....	197
Figure G.17: Plate J master curve.....	199
Figure G.18: Plate J uncensored master curve.....	199

## ABSTRACT

Non-redundant steel bridge systems have been used for major bridges in the United States since the late 1800's. Designers recognized the inherent structural efficiency and economy associated with two-girder and truss systems. Unfortunately, early knowledge was limited regarding fatigue, fracture, and overall system behavior; subsequently, a small number of these structures experienced fatigue and fracture issues leading to the creation of the Fracture Control Plan (FCP). The FCP resulted in more stringent design, material, fabrication, and inspection requirements for non-redundant steel bridges; specifically, a 24-month hands-on inspection criteria for all fracture critical members was established. Significant advances have been made over the past 40 years since the original FCP was introduced. Developments in fracture mechanics, material and structural behavior, fatigue crack initiation and growth, and fabrication and inspection technologies now allow fracture to be addressed in a more integrated manner. Through these advances, it is now possible to create an integrated FCP, combining the intent of the original FCP with modern materials, design, fabrication, and inspection methodologies. The current study is focused on the development of new design standards which founded an integrated approach to prevent fracture in steel bridges through the use of high-toughness steel. The project is comprised of small-scale material testing, full-scale fracture testing of steel bridge axial and bending members, three-dimensional finite element modeling, and an analytical parametric study. Results from this research demonstrate large defects are well-tolerated by high-toughness steel. Further, rational inspection intervals were calculated to demonstrate how an integrated FCP will allow for a better allocation of owner resources while also leading to increased steel bridge safety.

## CHAPTER 1 INTRODUCTION

### 1.1 Motivation

Non-redundant steel bridge systems have been used for both major and short span bridges in the United States (U.S.) since the late 1800's due to their structural efficiency. Common examples of these non-redundant structures include trusses, tied arches, and two-girder bridges. In the U.S., two-girder bridge systems gained popularity during the 1950's with the construction of the Interstate highway system. Designers recognized the structural efficiency and economy associated with the two-girder system; however, due to the limited knowledge at the time regarding fatigue, fracture, and overall system behavior, a small number of these structures experienced fatigue and fracture issues. One of the most notable failures occurred in 1967 when the Silver Bridge in Point Pleasant, West Virginia collapsed, leading to legislation attempting to increase safety in non-redundant steel bridges.

Currently, a non-redundant steel bridge member subjected to tension is referred to as a "fracture critical" member (FCM). The American Association of State Highway Transportation Officials (AASHTO) defines a FCM as a:

"Component in tension whose failure is expected to result in the collapse of the bridge or the inability of the bridge to perform its function" (AASHTO, 2014).

As a result, FCMs are held to additional material, fabrication, and inspection requirements as compared to non-FCMs.

The maximum in-service interval between routine inspections for both FCMs and non-FCMs is mandated as 24 months (FHWA, 2013). Routine inspections may be performed from the ground and do not necessarily require any specific access to the structural steel. Additionally, special provisions exist which permit routine inspections to be performed at intervals up to 48 months. Conversely, FCMs require a 'hands-on' type inspection at the 24-month interval. Hands-on inspections require the inspector to be at a distance no greater than one arm length from any portion of any FCM (AASHTO, 2011). Due to the man hours, traffic control, and equipment

required to perform hands-on inspections, the cost associated with them is much higher than standard bridge inspections. Additionally, there is an increased safety risk for both inspection personnel and the motoring public due to the required time on site, access to perform a high-level inspection, and traffic control (Connor, Dexter, & Mahmoud, 2005).

Significant advancements have been made in the past 40 years since the original steel bridge fracture provisions were introduced. Modern, high-toughness steels, in addition to improved fabrication, shop inspection, design standards, and greater body of knowledge regarding fatigue and fracture, can be leveraged to improve the understanding and requirements for non-redundant steel bridge systems. By applying the advances in each of these areas, bridges can be designed using an integrated fracture control plan (FCP) as well as damage tolerant design (DTD). DTD concepts are currently employed by numerous other industries, using similar philosophies for highway bridges will result in substantial cost savings and ultimately lead to safer structures (API, 2007; BSI, 2013).

## **1.2 Research Objective**

The objective of this research project was to demonstrate how through the use of high-toughness steel, rational inspection intervals can be established with an integrated fracture control plan. This project is comprised of small-scale material testing, full-scale fracture testing of steel bridge axial and bending members, three-dimensional finite element modeling, and an analytical parametric study. Rational inspection intervals were calculated to demonstrate how an integrated FCP will allow for a better allocation of owner resources while also leading to increased steel bridge safety.

## **1.3 Fracture Control Plan**

First released in 1978, the original Fracture Control Plan was a guide specification entitled *1978 AASHTO Guide Specification for Fracture Critical Non-Redundant Steel Bridge Members* (AASHTO, 1978). The intention of the original FCP was to prevent bridge fracture through design review, material toughness, fabrication requirements, welder certification, and inspector qualifications. The specification was updated multiple times through its existence; however, the FCP is no longer in the form of a single document. Currently, the FCP has been split into three different codes to address each of the goals independently: *AASHTO/AWS D1.5M/D1.5 Bridge*

*Welding Code* (Section 12), *AASHTO Manual for Bridge Evaluation*, and *AASHTO LRFD Bridge Design Specifications/ASTM A709-13a* (AASHTO & AWS, 2010; AASHTO, 2011, 2014; ASTM, 2013a). Each document is interrelated to prevent fracture in a similar way as the original FCP; however, no integrated FCP exists. The following two sections discuss the current fracture critical inspection and toughness requirements, as well as how they developed to their current form.

#### **1.4 Current Fracture Critical Inspection Requirements and Development**

On December 15, 1967 the Silver Bridge located in Point Pleasant, West Virginia collapsed due to the brittle fracture of a non-redundant eyebar (NTSB, 1968). The collapse resulted in 46 fatalities and made bridge safety a national priority. The investigation following the collapse revealed few bridge owners were performing bridge inspections and no national bridge standard existed prior to the collapse. As a result, U.S. Congress passed the Federal-Aid Highway Act of 1968 which required the creation of a national bridge inspection standard (*Federal-Aid Highway Act of 1968*, 1968).

The National Bridge Inspection Standards (NBIS) were first released in 1971. Included in the standards was national policy for bridge inspection procedures, frequency, reports, inspector qualifications, and maintenance requirements (FHWA, 1971). Three manuals were created to address the NBIS requirements: Federal Highway Administration (FHWA) *Bridge Inspector's Training Manual 70*, *AASHTO Manual for Maintenance Inspection of Bridges*, and *FHWA Recording and Coding Guide for the Structure Inventory and Appraisal of the Nation's Bridges*. Notably in 1971, NBIS mandated a maximum inspection frequency of two years for all bridge structures.

On June 28, 1983 a non-redundant, suspended pin and hanger span of the Mianus River Bridge in Greenwich, Connecticut collapsed (NTSB, 1984). Three fatalities resulted from the failure and again brought bridge safety back to national attention. In response to the collapse, a standalone supplement to the FHWA *Bridge Inspector's Training Manual 70* was released entitled *Inspection of Fracture Critical Bridge Members* (FHWA, 1986). The document provided information on how to properly plan, inspect, and document FCMs. Following in 1987, legislation was implemented via the *Surface Transportation and Uniform Relocation Assistance Act of 1987* to modify bridge inspection and include special procedures for FCMs. In addition, the 1988 NBIS was then revised to require bridge owners to identify and perform hands-on inspection of all FCMs

(FHWA, 1988). This was the first time the federal government required different inspection requirements for FCMs and non-FCMs.

In 2005, the NBIS was once again modified to require a hands-on inspection be performed at a maximum interval of 24 months for all FCMs (FHWA, 2013). To date, these are the current inspection requirements for FCMs.

### **1.5 Current Fracture Critical Toughness Requirements and Development**

The 1967 Point Pleasant Bridge collapse prompted the development of the original material toughness requirements. Prior to the 1970's, no national material toughness specifications were in existence for steel bridge base metal. The 1969 *AASHTO Standard Specification for Highway Bridges 10<sup>th</sup> Edition* mandated recording impact values; however, no minimum value was specified (AASHTO, 1969). Therefore, in response to the Point Pleasant Bridge collapse fracture toughness research, sponsored by the steel industry, was conducted at the U.S. Steel Research Laboratory (Barsom, 1974). Results from this study were used to form the first steel bridge material toughness requirements.

In 1973, the AASHTO Committee on Bridges and Structures adopted the first Charpy V-Notch (CVN) impact energy requirements for primary steel bridge tension members (Barsom, 1974). The original impact energy requirements are shown in Table 1.1 and did not distinguish between non-FCMs and FCMs. Along with the minimum specified impact energy values, three temperature zones were created based on the Lowest Anticipated Service Temperature (LAST) or minimum operating temperature for a given area. The temperature ranges for each zone can be found in Table 1.2 (Barsom, 1974).

**Table 1.1: Original impact energy requirements**

ASTM Designation	Thickness (in.)	Energy Absorbed (ft.-lb.)		
		Zone I	Zone II	Zone III
A36	N/A	15 @ 70 °F	15 @ 40 °F	15 @ 10 °F
A572*	Up to 4.0 mechanically fastened	“	“	“
	Up to 2.0 welded	“	“	“
A440	N/A	“	“	“
A441	N/A	“	“	“
A242	N/A	“	“	“
A588*	Up to 4.0 mechanically fastened	“	“	“
	Up to 2.0 welded	“	“	“
	Over 2.0 welded	20 @ 70 °F	20 @ 40 °F	20 @ 10 °F
A514	Up to 4.0 mechanically fastened	25 @ 30 °F	25 @ 0 °F	25 @ -30 °F
	Up to 2.5 welded	25 @ 30 °F	25 @ 0 °F	25 @ -30 °F
	Over 2.5" to 4.0 welded	35 @ 30 °F	35 @ 0 °F	35 @ -30 °F

\*If the yield point of the material exceeds 65 ksi, the temperature for the CVN value for acceptability shall be reduced by 15 °F for each increment of 10 ksi above 65 ksi.

**Table 1.2: LAST zones**

Zone	Minimum Service Temperature
I	0 °F and Above
II	-1 to -30 °F
III	-31 to -60 °F

In the early existence of the material toughness specification (circa 1975 to 1979) a debate existed over the adequacy of the required CVN values. The debate stemmed from the identification of pop-in cracks located in structures such as the Bryte Bend Bridge near Sacramento, CA (Hartbower & Sunbury, 1975). Two opposing views approached the problem. One approach sought to establish CVN limits and ductility requirements at the LAST to arrest pop-in cracks (Hartbower, 1979). Conversely, the other approach sought to establish CVN limits based on the temperature shift methodology. The temperature shift methodology set CVN limits so macroscopic fatigue cracks under typical bridge load rates do not result in a plane strain cleavage fracture. In this method, testing was performed above the LAST and a temperature shift was used to convert the dynamic rate of the CVN test to a quasi-static bridge loading rate (Barsom, 1975).

Due to the difficulty achieving the toughness required for the Hartbower methodology, the temperature shift approach was accepted and employed.

As a result from the 1970's debate, two primary changes to the material specification were made: 1.) FCM toughness requirements increased and 2.) CVN samples for FCMs were required from each plate (Frank, George, Schluter, Gealy, & Horos, 1993). Subsequently, several updates were made to the material toughness specification for FCMs since its inception. The current form of the specification, shown in Table 1.3, is found in both the *AASHTO LRFD Bridge Design Specifications* and ASTM A709-13a (AASHTO, 2014; ASTM, 2013a).

**Table 1.3: Current material toughness specification for FCMs**

Grade	Thickness (in.)	Minimum Test Value Energy (ft.-lb.)	Minimum Average Energy (ft.-lb.)		
			Zone I	Zone II	Zone III
36F	$\geq 4.0$	20	25 @ 70 °F	25 @ 40 °F	25 @ 10 °F
50 F	$\geq 2.0$	20	25 @ 70 °F	25 @ 40 °F	25 @ 10 °F
50 SF 50 WF	$2.0 \geq 4.0$	24	30 @ 70 °F	30 @ 40 °F	30 @ 10 °F
HPS 50 WF	$\geq 4.0$	24	30 @ 10 °F	30 @ 10 °F	30 @ 10 °F
HPS 70 WF	$\geq 4.0$	28	35 @ -10 °F	35 @ -10 °F	35 @ -10 °F
HPS 100 WF	$\geq 2.5$	28	35 @ -30 °F	35 @ -30 °F	35 @ -30 °F

### 1.6 HPS History

In 1994, the FHWA, U.S. Navy, and American Iron and Steel Institute (AISI) joined in a cooperative research program to develop high performance steel (HPS) for bridges. Also, a research oversight committee was formed to help direct the research. The committee included experts from the FHWA, U.S. Navy, and AISI as well as steel producers, steel fabricators, and the American Welding Society (AWS) (Hamby, Clinton, Nimis, & Lwin, 2002). The program focused on the development of high-strength steels with improved weldability to facilitate improved fabrication and increased toughness for better fracture resistance. Weathering steel was used to give the material the ability to perform without a coating (Wilson, 2005). The initial research focused on HPS 70W and HPS 100W. Due to the quick success of HPS 70W, bridge engineers requested an HPS 50W be developed as well (Hamby et al., 2002). In 1997, the first HPS 70W highway bridge was constructed and opened to traffic in Nebraska. Since, HPS has been used in a variety of applications including complete girders and hybrid systems (AISI, 2011). Currently,

HPS 70W and HPS 100W are the only available bridge steel in those respective grades; conversely, a conventional Grade 50 as well as an HPS 50W grade are available for bridge construction (ASTM, 2013a).

HPS gained its desirable characteristics through material processing; specifically, chemical composition and heat treatments. Continuous improvements have been made in the production methods and techniques throughout the development of HPS. Advances have resulted in consistent strength, increased toughness, increased weldability, and better corrosion resistance of HPS. Due to the low carbon content, HPS can be welded with minimal preheat. The low carbon content also helps retain ductility and toughness in the fabricated state. Increased strength, toughness, corrosion resistance, hardenability, and reduced embrittlement was achieved through the use of alloying. Alloying elements include manganese, silicon, copper, nickel, chromium, vanadium, and molybdenum, many of which provide multiple benefits (ASTM, 2013a). Both the thermo-mechanical control process (TMCP) and the quench and tempered (Q&T) process are actively used to produce HPS. The exact process type depends on the thickness, desired grade of the material, and the individual steel mill. Further information on the manufacturing process is described in ASTM A709 (ASTM, 2013a).

## CHAPTER 2 PRIOR RESEARCH AND BACKGROUND

A comprehensive review of the vast fracture literature was performed as part of the current research. The following chapter contains a brief description of the five studies thought to be most significant to the current work. When necessary, references have been provided throughout this document to additional work reviewed. The first two studies summarized attempted to characterize the fracture behavior of HPS through small-scale and large-scale experimental testing (William Norfleet Collins et al., 2014; Wright, 2003). The third study examined high-toughness Navy steel both experimentally and analytically (Gentilcore, 1996). The fourth study reviewed the current steel bridge fracture toughness requirements as well as explored damage tolerant design concepts for use in steel bridges (Altstadt, 2008). The fifth study documented analytical practices for elastic-plastic materials (Wells & Allen, 2012). Each of these studies offered great value to the current research.

### **2.1 Wright (2003)**

The improved toughness of HPS was demonstrated by CVN impact testing during the early developmental work. Fracture initiation of HPS 70W and HPS 100W were experimentally tested by Wright in 2003 (Wright, 2003). One heat from each grade was included in the study. The experimental program had three parts: 1.) Characterize HPS in terms of loading rate and temperature; 2.) Characterize toughness as a function of loading rate, temperature, and plate thickness; and 3.) Conduct full-scale fracture testing of HPS I-girders and compare to other full-scale fracture experiments on conventional bridge steels.

Tensile and CVN testing were used to attain a full stress-strain curve and CVN temperature transition curve for each grade of HPS. The tensile testing was used to create an idealized Ramberg-Osgood stress-strain curve for analytical predictions. Fatigue crack growth rate testing was performed on both steels and resulted in similar crack growth rates as conventional Grade 50 steel. Seventy-two compact tension, C(T), specimens were tested to characterize the material toughness.

Fracture toughness testing was performed over a range of test temperatures, loading rates, and plate thicknesses to evaluate a range of bridge conditions. Only 3 of the 72 C(T) specimens yielded valid  $K_{Ic}$  results due to the high toughness of the steel. The remaining specimens were evaluated using elastic-plastic methodologies; specifically, the j-integral was used to evaluate the elastic-plastic behavior. Plastic collapse, or limit load, was evaluated for both grades of HPS. The HPS 70W was found to reach limit load above a temperature of 0 °F; however, below a temperature of 0 °F a thickness dependence was noted and limit load was not attained. The HPS 100W was not capable of reaching limit load at the tested temperatures.

Six full-scale bridge I-girders were tested in four point bending using the same two heats of steel from the fracture mechanics experiments. Eight tests were initially planned, however, plans to invert the girders for reuse had limited success. Two flaw geometries were investigated: center crack and edge crack. Center cracks were created naturally through cyclic fatigue loads applied at a transverse stiffener. Conversely, edge cracks were created by saw-cut notches. All cracks were grown in fatigue to the desired test length. Five specimens were tested at the AASHTO Zone II temperature of -30 °F, while the sixth specimen was tested at the AASHTO Zone I temperature of 0 °F. For the fracture event, an overload of  $0.55F_y$  was suddenly applied followed by 10 secondary cycles from 90% to 100% of the maximum load. If no fracture resulted from the test, the cracks were extended in fatigue and the test process to achieve fracture was reattempted. It should be noted, performing multiple fracture tests on a single beam may have resulted in artificially high crack tolerances due to the compressive residual stresses developed around the crack tip when an experiment did not result in a fracture.

The study concluded HPS 70W was capable of reaching the limit state of yield on the net section. Conversely, the HPS 100W was not able to meet the limit state of yield on the net section. The data indicated using HPS for welded plate girders will result in increased critical crack sizes due to the higher toughness, as compared to conventional bridge steels. Additionally, it was expected the increased critical crack sizes would result in a higher probability of detection for fatigue cracks during routine inspections.

## **2.2 Collins (2014)**

In 2014, further material characterization was performed to fully characterize the fracture behavior of HPS for multiple heats, plates, and grades (William Norfleet Collins et al., 2014). Specifically, experiments were performed to acquire yield and tensile strengths, CVN impact

energy, static and dynamic fracture toughness, and crack arrest toughness. A total of 636 fracture specimens were tested as part of the study: 246 CVN impact, 209 static fracture toughness, 126 dynamic fracture toughness, and 55 crack arrest. These specimens were taken from eight HPS plates of Grade 70W and Grade 100W (five and three, respectively). Additionally, the study evaluated the master curve methodology for bridge steels and used it to characterize all HPS plates tested.

All CVN impact specimens exceeded the AASHTO minimum required material toughness specification. Similarly, all plates surpassed the minimum toughness values at the AASHTO Zone III LAST of -60 °F. Crack arrest tests proved to be difficult and only 10 valid results were obtained; therefore, no substantial findings were concluded. The fracture toughness results indicated the HPS 70W tested could tolerate crack sizes 20 times larger than a material just meeting the current AASHTO material toughness specification. For some crack geometries, adequate toughness was available to have only a 1% probability of cleavage fracture prior to attaining net section yield. The HPS 100W tested was able to tolerate crack sizes three times larger than a material just meeting the current AASHTO material toughness specification. The study recommended changes be adopted in the material specification to take advantage of the superior material toughness.

### **2.3 Gentilcore (1996)**

Ductile fracture models to predict fracture in ship hull components were evaluated during a 1996 study performed by Gentilcore (Gentilcore, 1996). The study had three primary objectives: 1.) Conduct full-scale high-toughness experiments on ship hull components; 2.) Determine limitations of current ductile fracture models from experimental test results; and 3.) Develop improved methods for modeling ductile fracture. Five different modeling approaches were implemented and evaluated. Each modeling approach was classified as either a local approach or a global approach. Local approach methods included crack tip opening displacement/crack tip opening angle and constitutive damage models. The local approaches modeled crack extension using the local stress-strain and deformation fields at the crack tip. Conversely, global approach methods included the J-R curve, crack opening angle, and limit-load. The global approaches modeled crack extension using stress-strain and deformation fields throughout the cracked body.

Fracture experiments were conducted on shipbuilding steels including HSLA-80 which had an impact energy requirement of 59 ft.-lbs. at -112 °F. The flange plate thicknesses of 0.5 in. and 1.0 in. examined during the study were considered full-scale for ship hull components; however,

these thicknesses do not translate to typical thickness of bridge girder components. Additionally, the study was performed at a static loading rate which is not representative of bridge loading conditions. Nevertheless, the study provided useful information in regard to the performance of the five methods presented.

The researchers concluded J-R curve analysis and crack opening angle approaches result in non-conservative estimates of fracture resistance for bending members. Conversely, limit load analysis accurately predicted the correlation between load and crack length. Experimental results indicated the HSLA-80 steel had sufficient toughness to reach limit load on the net section. It was concluded structural steels can exhibit ductile behavior at low temperatures if sufficiently high CVN impact energy requirements are met.

#### **2.4 Altstadt (2008)**

Steel bridge requirements for base metal CVN impact toughness and for inspection were examined by Altstadt in 2008 (Altstadt, 2008). Damage tolerant design methods were also investigated based on existing procedures employed by industries such as oil and gas, nuclear, and aerospace. Two common steel bridge details were used to examine these subjects; specifically, the transverse stiffener detail and the cover plate detail. Damage tolerant design methods for the transverse stiffener detail have been well established by other industries; whereas, the cover plate detail has not been included in any of the established crack assessment procedures. The master curve methodology was also reviewed as part of this research.

The study results indicated the current minimum CVN impact requirements for bridge steels provide a variable level of fracture resistance across the various grades. A revised set of CVN impact requirements were proposed providing a consistent level of fracture resistance based on the brittle fracture resistance for Grade 36. Table 2.1 provides the proposed CVN requirements to result in uniform fracture resistance between grades. The author also proposed a course of action to implement a damage tolerant design philosophy for steel bridges. High importance was emphasized for developing probability of detection (POD) curves for steel bridge details. Prior to the study, only one steel bridge POD study had been performed. Also, investigating the applicability of the master curve to bridge steels was one of the most important parameters required prior to implementing a damage tolerant design methodology for steel bridges. Of note, further work on the applicability of the master curve to bridge steels has since been performed by Collins as reviewed above (William N Collins, Sherman, Connor, & Leon, 2016a, 2016b).

**Table 2.1: CVN impact requirements for uniform fracture resistance**

Yield Strength (ksi)	CVN Requirements (ft.-lbs.)		
	Zone I	Zone II	Zone III
36	25 @ 70 °F	25 @ 40 °F	25 @ 10 °F
50	30 @ 25 °F	30 @ -5 °F	30 @ -30 °F
70	30 @ -20 °F	30 @ -50 °F	30 @ -78 °F
100	30 @ -56 °F	30 @ -85 °F	30 @ -114 °F

### **2.5 NASA Round Robin (2012)**

In an effort to develop a new material test standard for the assessment of surface crack toughness in the linear-elastic and elastic-plastic regime, the ASTM Committee on Fatigue and Fracture Task Group on Fracture Toughness of Surface Cracks conducted a round robin study (Wells & Allen, 2012). Participants were given a problem statement including geometry, elastic properties, and tabular stress-strain data for a surface cracked plate. Based on the problem statement, the organizers of the round robin requested participants evaluate the prescribed geometry using their typical modeling techniques. Data requested from the analysis included force versus crack mouth opening displacement (CMOD), j-integral versus phi, and j-integral versus force at a phi of approximately 17 degrees. Model size, formulation, constitutive model, and other general modeling parameters were queried as a point of comparison between participants.

Results from the round robin study were encouraging because little variation in results was found even though no instruction was given regarding analysis methodology. General modeling choices such as analysis package, mesh density, crack tip meshing, or boundary conditions were found to have little to no impact on the overall results. The constitutive model was determined to contribute most variability. Based on the results, the following are a summary of the recommended practices:

1. Perform the analysis using the finite element method.
2. Use quadratic, three-dimensional elements with reduced integration (full integration may be used at the crack tip).
3. Use the domain integral to calculate the j-integral.
  - a. The domains should be as large as possible.
  - b. Minimize element skew from the crack front.

- c. Check all domains for path dependence and only report the highest fully converged value from the outermost domain.
  - d. Check all domains for oscillatory results.
  - e. Use small strain assumptions.
4. Develop constitutive model with the following:
- a. Use tensile data from ASTM E8.
  - b. Use incremental plasticity (Von Mises).
  - c. Employ stress-strain data through table look-up function.
    - i. Elastic modulus from handbook.
    - ii. Engineering stress-strain values.
    - iii. Separate plastic strain from experimental stress-strain.

DRAFT - For Review

## CHAPTER 3 EXPERIMENTAL RESEARCH PROGRAM

### 3.1 Material Selection

#### 3.1.1 Material Criteria

Early in the research, a material toughness level was targeted to achieve a desired behavior. The criteria used to establish the toughness level included the following considerations:

1. Probability of detection: The material must be able to tolerate a crack with a high POD. Based on limited POD data, a 3.0 in. edge crack was selected (Whitehead, 2015).
2. Stress state: The crack must be tolerable at a high-level of applied stress. The limit was set at  $0.75F_y$  based on the maximum permissible overload in the *Manual for Bridge Evaluation* (AASHTO, 2011).
3. Toughness availability: The toughness dictated by items 1 and 2 would need to be reasonably available, if not, another approach would be needed.

Based on these criteria, a minimum impact energy of 125 ft.-lbs. with a shear fracture area of 100% was selected as the target. The rationale behind the selected toughness value was to achieve a desired crack tolerance, while the intent of the shear fracture area requirement was to provide upper shelf, ductile behavior. Similar two-part requirements have been used in other industries; for example, an 85% shear requirement has been used for steels in the linepipe steel industry (Boreas, 2010).

The 125 ft.-lb. requirement was based on fracture mechanics calculations for a 3.0 in. through-thickness edge crack in a 12 in. wide plate subjected to a stress level of 75% of yield for Grade 50. The *Manual for Bridge Evaluation* allows for an overload to result in a stress state of  $0.75F_y$  (AASHTO, 2011). A load level equal to  $0.75F_y$  was selected because if fracture can be resisted at  $0.75F_y$  then the nominal stress of the net section would be at yield. Linear-elastic fracture mechanics was used to conservatively calculate a fracture toughness of  $172.7 \text{ ksi}\sqrt{\text{in}}$  using

Equation 3.1 (Grandt, 2004). BS7910 contained a conservative upper shelf correlation between fracture toughness and CVN impact energy as shown in Equation 3.2 (BSI, 2013). It should be noted, Equation 3.2 requires metric units; therefore, all reported values have been converted from metric to English units. The correlation applied to upper shelf energy at 100% shear; hence, the 100% shear requirement was initially set for the preliminary material screening. Using Equation 3.2, a CVN value of 120.6 ft.-lbs. was calculated. For the initial material requirement the CVN impact energy was rounded up to 125 ft.-lbs.

$$K = \sigma\sqrt{\pi a} * \beta(a/W)$$

Where:

$$\beta(a/W) = 1.12 - 0.23(a/W) + 10.55(a/W)^2 - 21.73(a/W)^3 + 30.39(a/W)^4$$

**Equation 3.1: Linear-elastic fracture mechanics for an edge crack in a finite width plate**

$$K_{mat0.2} = K_{J0.2} = \sqrt{\frac{E(0.53 * CVN_{US}^{1.28})(0.20.133CVN_{US}^{0.256})}{1000(1 - \nu^2)}}$$

**Equation 3.2: Upper shelf CVN to fracture toughness correlation**

**3.1.2 Percent Shear Measurement Method Evaluation**

CVN impact specimens were collected from the Collins work as well as from other testing performed at Purdue University. Specimens were from three different plates of varying grades and thicknesses. A representative sample of these specimens were selected for a percent shear measurement method evaluation. Typically, percent shear is measured visually; however, some contest visual measurements can lead to gross errors in the actual measurement and argue digital techniques are required (Manahan & Mccowan, 2008).

Percent shear was measured for 19 representative CVN specimens using three methods: visual, enhanced visual, and digital. Four additional samples were measured using the two visual methods but not sent for digital measurement due to their clear cleavage fracture surface. The visual measurements were performed according to ASTM E23-12c and were reported to the nearest 10% (ASTM, 2012b). Enhanced visual measurements utilized a digital camera to magnify the fracture surface. Percent shear was then measured on the enhanced surface by the user identifying the cleavage and shear areas. To obtain the digital results, specimens were sent to MPM Technologies in State College, PA. Percent shear was measured using their automated digital imaging system (Manahan & Mccowan, 2008).

Results from the study are shown in Table 3.1. Similar to the results found during a study performed by MPM Technologies, percent shear measurements were consistent between the three methods at the low and high percent shear values (Manahan & Mccowan, 2008). Scatter between the methods was typically found in the 40% to 60% range.

**Table 3.1: Percent shear measurement comparison**

Specimen Name	User 1		User 2		MPM
	Visual	Enhanced Visual	Visual	Enhanced Visual	
H15	100	91.8	90	97.4	99.9
H4	100	97.4	90	97.3	99.8
H24	100	97.9	100	100.0	95.5
H10	100	98.0	100	100.0	96.8
H11	90	78.8	90	84.7	83.6
H18	90	70.7	80	78.4	78.9
H3	90	85.4	90	85.9	80.1
H2	10	2.3	0	2.5	N/A
H19	10	15.5	40	33.5	40.0
H7	10	1.2	0	0.6	N/A
C17	80	84.4	80	69.3	86.3
C15	80	78.3	80	74.3	88.0
C10	70	53.6	80	68.0	73.7
C9	50	44.5	60	61.3	66.2
C22	20	19.1	30	27.9	29.4
C5	10	6.3	20	19.7	15.2
C3	10	7.8	10	10.2	9.9
C19	10	7.6	10	9.6	N/A
J18	90	80.3	60	44.2	36.2
J13	40	48.1	30	47.7	43.5
J12	30	27.7	30	36.9	28.2
J9	10	15.2	10	26.2	15.8
J5	0	2.8	0	1.0	N/A

As a point of illustration, the enhanced visual method was compared directly to the digital method. Figure 3.1 shows the images for specimen H3. The enhanced visual method for User 1 calculated a percent shear of 85.4% compared to the digital method of 80.1%. Additionally, the user and the digital method agreed not only in the percent shear but the specific area of cleavage as displayed by the photographs.

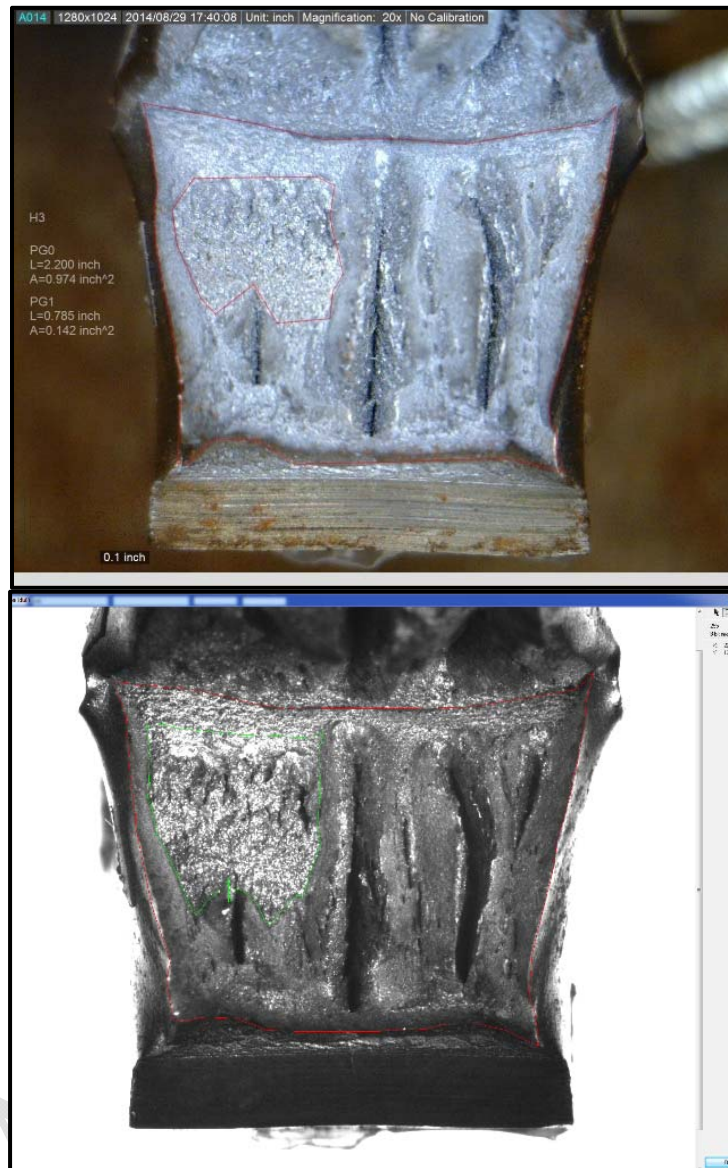


**Figure 3.1: Comparison of enhanced visual (top) and digital methods (bottom)**

### 3.1.3 Initial Material Testing

CVN impact testing was performed to identify materials for large-scale testing satisfying the 125 ft.-lb. and 100% shear requirements. A total of 10 plates were tested during the initial screening process. The plates were identified by letter designations: A through J. Screened materials included ASTM A709 Grades 50 and 70. Material thickness ranged from 1.5 in. to 2.5

in. Table 3.2 presents a summary of the screened plates including letter designation, thickness, grade, and heat number.

**Table 3.2: Screened large-scale testing material summary**

<b>Letter Designation</b>	<b>Grade</b>	<b>Thickness (in.)</b>	<b>Heat Number</b>
A	HPS 70W	1.5	821T02570
B	HPS 70W	1.5	812S35370 - S61761
C	HPS 70W	1.5	812S35370 - S61763
D	HPS 70W	2	A1F064
E	50W	2.5	9104617
F	HPS 70W	1.57	9106460
G	50W	2.25	9106877
H	HPS 70W	1.5	823K71800
I	50W	2	500541
J	50	1.5	3507723

Percent shear was measured for each screened plate. Figure 3.2 plots the percent shear versus CVN impact energy for all CVN test specimens. Based on the percent shear results, no material satisfied the percent shear requirement at 125 ft.-lbs. The lowest impact energy with 100% shear was 158 ft.-lbs. Further, the percent shear values at an impact energy 125 ft.-lbs. were largely in the range of 40% to 60%. As such, when selecting material for the test program, either the toughness requirement needed to be increased or the percent shear requirement needed to be relaxed. It was desired to perform the fracture experiments at as low of an impact energy possible, while still obtaining the desired crack tolerance. Setting any future specification at a lower impact energy than the experiments would be hard to justify. Therefore, due to the variability in percent shear measurement in the 40% to 60% range and the concern of setting too high of an impact energy, the percent shear requirement was not used during the final selection of the large-scale testing material.

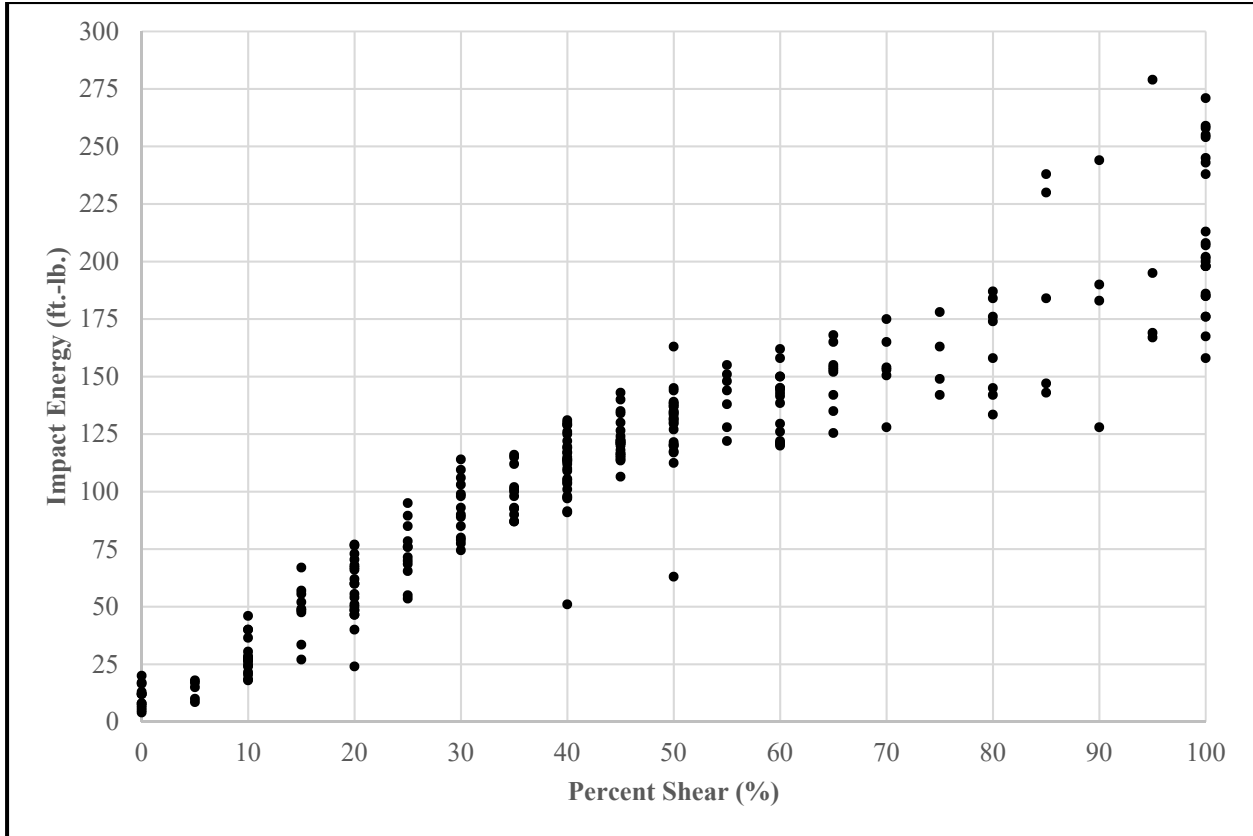


**Figure 3.2: Screened large-scale testing material percent shear**

At the completion of the material screening, Plates E, H, I, and J were selected for large-scale testing. The final plate selections were based on plate availability, plate thickness, and plate grade as well as the ability to satisfy the 125 ft.-lb. requirement at an attainable test temperature. The selected plates are highlighted in Table 3.2.

### **3.2 Material Characterization**

An extensive material testing program was conducted to fully characterize the material behavior of the large-scale test specimens. Material testing included tensile testing, chemistry, CVN impact testing, percent shear measurement, reference temperature determination, and measurement of fracture toughness. Each test was performed to the applicable ASTM specification.

### **3.2.1 Tensile Testing**

Tensile testing was performed in accordance with ASTM E8-15a (ASTM, 2015b). All tensile testing was performed by Westmoreland Mechanical Testing and Research Inc. in Youngstown, PA. Standard 0.5 in. diameter round test specimens were used for all tests. All tensile testing was performed at room temperature. Test data was recorded up to specimen failure. Ultimate tensile strength, yield strength, modulus, percent elongation, percent reduction in area, and ultimate load were reported. Additionally, the raw stress-strain data were provided. Tensile test results can be found in Section 3.10.1.1.

### **3.2.2 Chemical Analysis**

Chemical analysis was performed in accordance with ASTM E1019 and ASTM E415 (ASTM, 2011, 2014). Chicago Spectro Service Laboratory Inc. in Chicago, IL performed the chemical analysis of Plates E, H, and I. Laboratory Testing Inc. in Hatfield, PA performed the chemical analysis of Plate J. For Plates E, H, and I, carbon and sulfur were determined according to ASTM E1019 and all other elements were established according to ASTM E415. ASTM E415 was used to fully characterize Plate J. Results of the chemical analysis can be found in Section 3.10.1.2.

### **3.2.3 Charpy V-Notch Impact Testing**

CVN impact testing was performed in accordance to ASTM E23-12c (ASTM, 2012b). Type A, 10 mm specimens were used for all impact testing, as pictured in Figure 3.3. Specimen machining was performed by Chicago Spectro Service Laboratory Inc. for all material, with the exception of Plate J which was machined by Laboratory Testing Inc. The notch radius were randomly inspected for a number of CVN impact specimens from both machinists. All inspected radii satisfied the ASTM requirements. Most CVN impact testing was performed at Purdue University on a NIST certified Instron SATEC Series Impact Testing Machine with a 300 ft.-lb. capacity, pictured in Figure 3.4. Six specimens from Plate J were tested by Laboratory Testing Inc. due to the low testing temperature required. Initially, 18 CVN specimens were machined and tested for material screening. Plates identified for large-scale experimentation had an additional

18 CVN specimens machined and tested. Subsequently, 12 additional specimens were tested from Plates E and H as part of a plate variability study. CVN test results can be found in Section 3.10.1.3.



**Figure 3.3: Type A, 10 mm Charpy v-notch impact specimen**



**Figure 3.4: SATEC Series Impact Testing Machine**

CVN testing was conducted over a range of temperatures (-120 °F to 205 °F) to develop a full temperature transition curve. Specimen cooling was performed in a FTS Systems Model MC480 Multi-Cool Low Temperature Bath/Circulator. With the use of methanol as a cooling fluid, the temperature bath had the ability to cool specimens to -90 °F. A photograph of the temperature bath is shown in Figure 3.5.



**Figure 3.5: FTS Systems temperature bath**

### **3.2.4 Percent Shear Estimation**

Percent shear estimates were made for all CVN impact specimens based on guidance provided from ASTM E23-12c (ASTM, 2012b). All estimates were performed visually using Figure A4.2.b of Annex A4 for comparison of the fracture appearance. Results of the percent shear estimation can be found in Section 3.10.1.4.

### **3.2.5 Reference Temperature Determination Testing**

Testing for reference temperature determination was performed in accordance to ASTM E1921-13a (ASTM, 2013b). Square, Charpy-sized, single-edge notched bend bars (SE(B)) were used for all reference temperature testing. Notches in the specimens were cut using a wire electrical discharge machine (EDM). After specimen precracking, but prior to reference temperature determination testing, 45 degree angle side grooves were machined into each specimen. Design drawings for the reference temperature determination test specimens can be found in Appendix A. The machining of the specimen blanks and side grooves was performed by Homestead Machining LLC in Eggleston, VA, while the EDM machining completed by Advanced Machining Solution in Roanoke, VA. A photograph of a completed reference temperature determination specimen is shown in Figure 3.6.

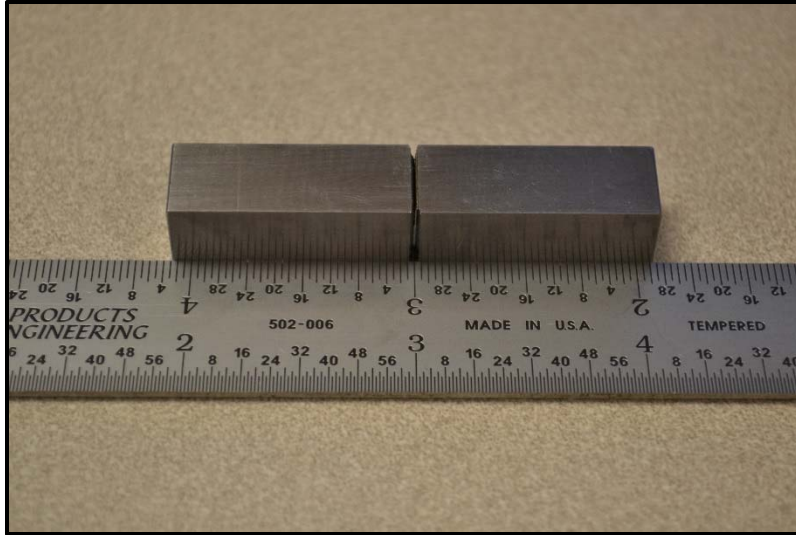


**Figure 3.6: Reference temperature determination specimen**

All reference temperature determination precracking and testing was completed in an MTS Model 318.10 load frame with an 11 kip capacity. The load frame was controlled through a FlexTest 60 controller running both MTS Series 793 and TestSuite MP Elite software. TestSuite contains a specialized software package for precracking and fracture toughness testing. A photograph of the load frame setup and controller is shown in Figure 3.7.

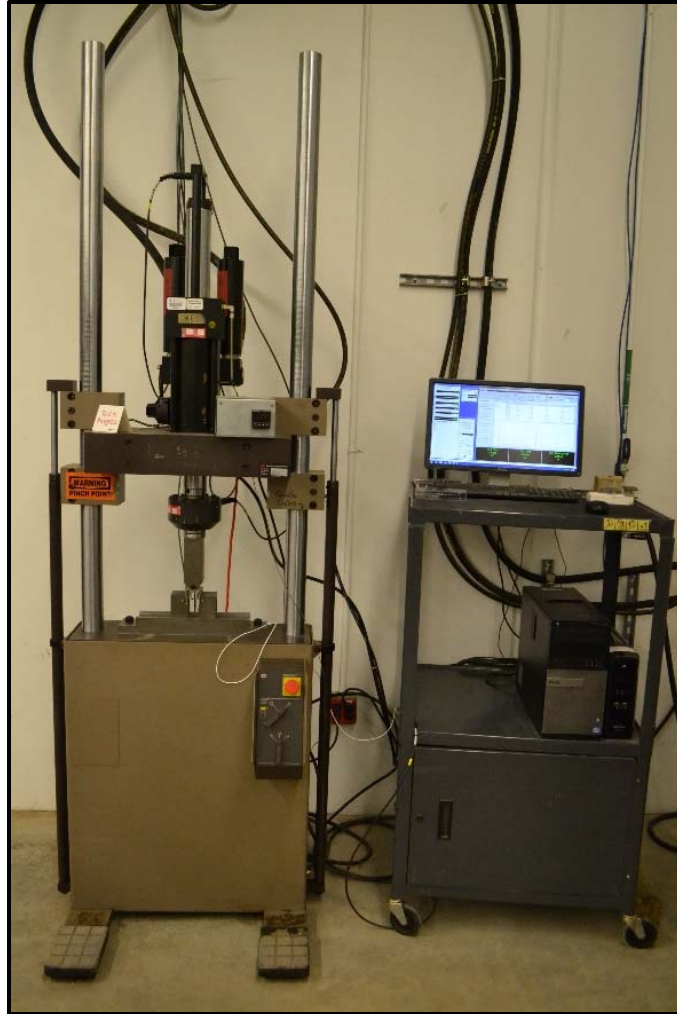


**Figure 3.7: MTS Model 318.10 load frame setup**

Crack size was computed through specimen compliance per ASTM E1820-15a (ASTM, 2015a). Load was measured by the actuator load cell. Crack mouth opening displacement (CMOD) was measured by a Charpy Mod Displacement Gage manufactured by Tension Measurement Inc. in Arvada, CO. The clip gage had a working range of 0.08 in. and is pictured in Figure 3.8. Using load and displacement measurements, TestSuite automatically computed the crack length.

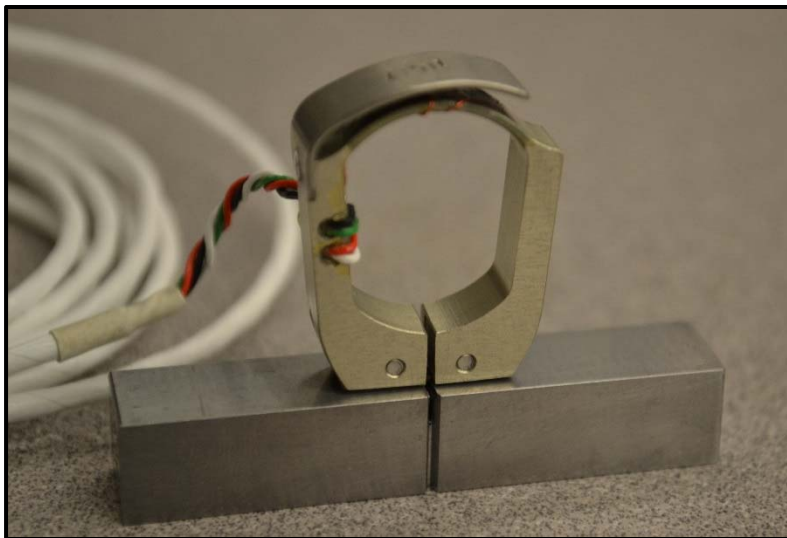


**Figure 3.8: Charpy mod displacement gage**

Precracking for reference temperature determination specimens was performed at a frequency of 25 Hz. A two-step procedure was used for precracking to ensure a straight crack front, as well as to minimize plasticity at the fatigue crack tip. The first step utilized a load shedding feature in TestSuite while the second step was at a constant stress intensity of  $13.1 \text{ ksi}\sqrt{\text{in}}$ . To comply with ASTM E1921-13a, the final crack length was  $0.5W \pm 0.05W$ . Further, a minimum fatigue crack growth beyond the EDM notch of the larger of one half the notch width or 0.05 in. for the Charpy-sized geometry was required (ASTM, 2013b). Equations for force and stress intensity requirements during precracking were also included in the ASTM.

Reference temperature testing requires cleavage-type behavior; therefore, specimens were typically tested at cold temperatures. Specimens were cooled using a temperature chamber and liquid nitrogen. Cooling was controlled through an Asco normally-closed cryogenic solenoid valve, Omega CNi16 series temperature and process controller, and a type T thermocouple placed inside the temperature chamber. ASTM E1820-15a requires specimen temperature to be within  $\pm 5 \text{ }^\circ\text{F}$  for a minimum of 30 minutes for each inch of specimen thickness (ASTM, 2015a). Photographs of the temperature chamber are shown in Figure 3.9. Guidance on selecting an initial test temperature for reference temperature determination testing is described in ASTM E1921-13a (ASTM, 2013b).



**Figure 3.9: Fracture mechanics testing temperature chamber**

Raw data were extracted after testing each specimen to calculate the elastic-plastic stress intensity factor,  $K_{Ic}$ . Optical crack measurements were also required for each specimen. To facilitate optical measurements, each specimen was heat tinted immediately after testing. The initial fatigue crack length was measured as well as any stable tearing. All measurements were made according to the procedure outlined in ASTM E1921-13a (ASTM, 2013b). Nine equally spaced measurements were recorded. The two near-surface measurements were averaged and then averaged with the remaining seven measurements to calculate the final fatigue crack length. An example optical measurement with the measurement locations can be found in Figure 3.10.

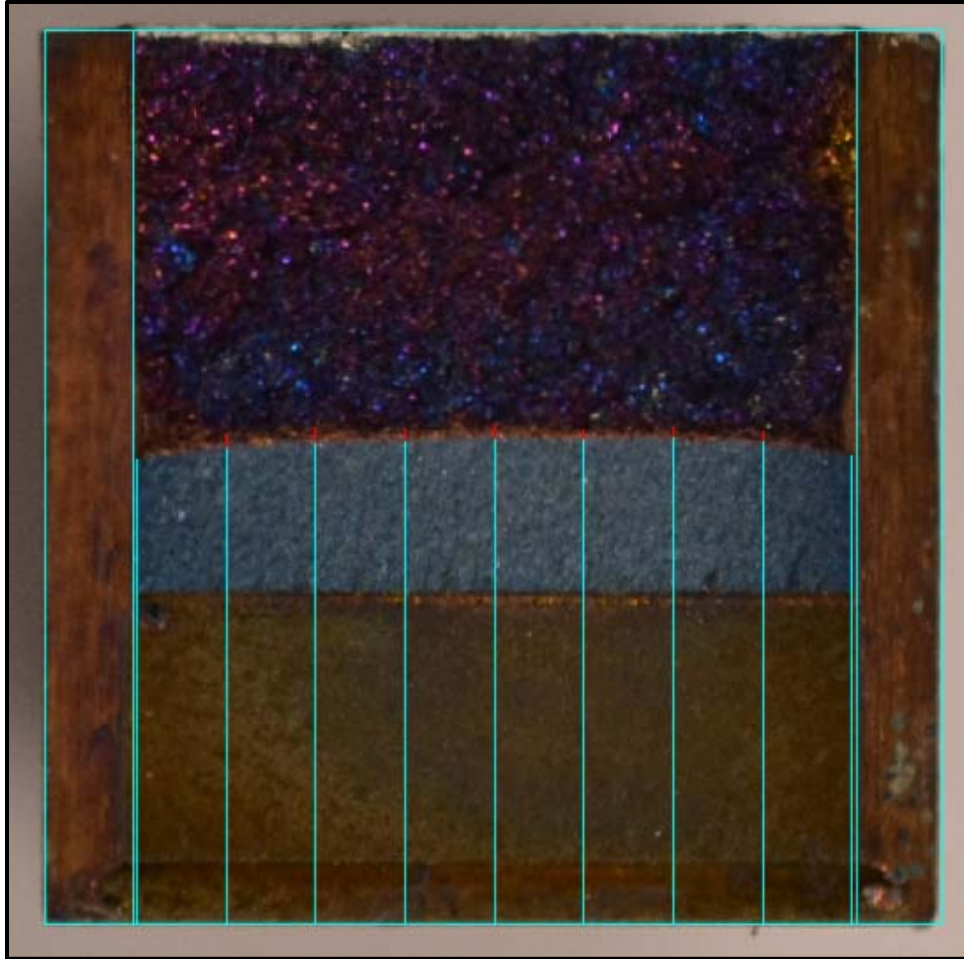


**Figure 3.10: Example optical fatigue crack measurement**

ASTM E1921-13a validity criteria for the maximum allowable elastic-plastic stress intensity as well as for the maximum allowable stable tearing were used to censor the data (ASTM, 2013b). All valid specimens contributed to the weighting factor for the reference temperature determination. The weighting factor for each individual specimen was determined based on the test temperature minus the provisional reference temperature. Each valid specimen contributed either 1/6, 1/7, or 1/8. To be considered a valid reference temperature, the all weighting factor had to sum to greater than 1.0. Results from the reference temperature determination testing can be found in Section 3.10.1.5.

### 3.2.6 Fracture Toughness Measurement

Fracture toughness testing was performed in accordance to ASTM E1820-15a (ASTM, 2015a). Specimens complying with the ASTM recommended single-edge bend specimen geometry were utilized for all testing. Once again, specimen notches were cut using an EDM and 45 degree angle side grooves were cut after precracking. All SE(B) specimen machining was performed by Homestead Machining LLC and Advanced Machining Solutions. General dimensions of the SE(B) specimen were 9.0 in. long by 1.0 in. wide by 2.0 in. tall. Design drawings for the fracture toughness specimen geometry can be found in Appendix A. A photograph of a completed fracture toughness specimen is shown in Figure 3.11.

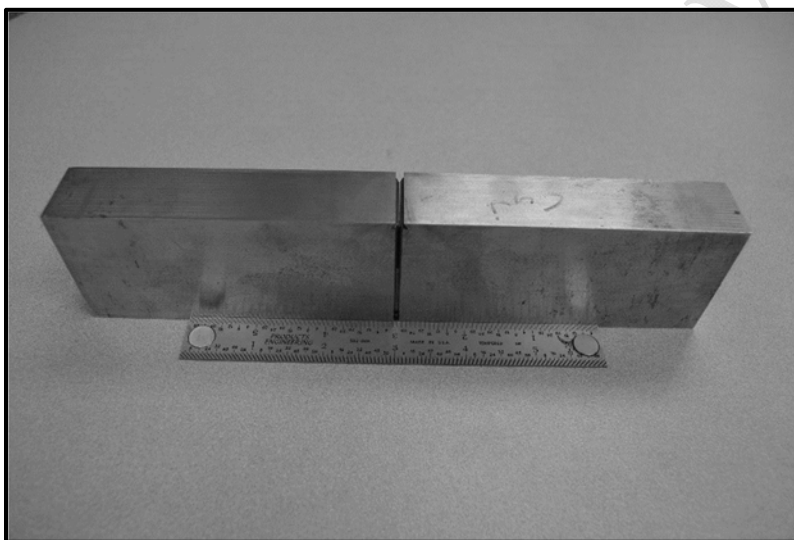


**Figure 3.11: Fracture toughness specimen**

All fracture toughness precracking and testing was performed using the same MTS test frame as the reference temperature determination specimens. Precracking was performed at a frequency of 20 Hz. Once again, compliance was used to measure the fatigue crack length. A Tension Measurement Inc. Displacement Gage with a 0.25 in. range was used to measure CMOD. The displacement clip gage is pictured in Figure 3.12. A two-step precracking procedure was used to ensure a straight crack front. After the first step, the specimen was rotated 180 degrees. Load shedding was used during both precracking steps. In accordance with ASTM E1820-15a, the final crack length was grown to  $0.525W$  and  $0.65W$  for the Grade 50 and Grade 70 specimens, respectively; which is within the required range of  $0.45W$  and  $0.7W$ . The fatigue crack length was longer for the Grade 70 specimens to accommodate the capacity of the test machine. Also, per

ASTM, a required minimum fatigue crack extension of the greater of  $0.025B$  and  $0.05$  in. from the EDM starter notch was achieved (ASTM, 2015a). Equations stipulating the precracking load and stress intensity limits are also found in the ASTM.



**Figure 3.12: 0.25 in. displacement gage**

Fracture toughness testing was performed at cold temperatures; therefore, the temperature chamber described above was used for specimen cooling. All fracture toughness tests were performed at the same temperature as the large-scale experiments. Similarly, raw data were collected and post-processed for each specimen and the specimens were heat tinted. After heat tinting, optical measurements were made of the fatigue crack and any tearing. As described in ASTM E1820-15a the plane-strain fracture toughness was computed for each specimen (ASTM, 2015a). Plane-strain fracture toughness results for each specimen can be found in Section 3.10.1.6.

### **3.3 Large-scale Specimen Types**

Large-scale testing was performed using two specimen types: bending specimens and axial specimens. Bending specimens represented full-scale welded steel bridge plate girders. Axial specimens represented bridge components in pure tension such as a tie girder or tension truss element. Specimens were fabricated from ASTM A709 Grade 50 and 70 material. Flange and plate thickness varied between 1.5 in. and 2.5 in. Representative bending and axial test specimens are pictured in Figure 3.13 and Figure 3.14, respectively. Specimen dimensions will be detailed in the following sections.



**Figure 3.13: Representative bending test specimen**



**Figure 3.14: Representative axial test specimen**

### **3.4 Loading Frames**

Load frames were designed and fabricated for both bending and axial large-scale testing. A pair of identical load frames were fabricated for testing the bending specimens. The entire bending test sequence could be performed in a single test frame. Conversely, the axial test specimens required two load frames for testing. Fatigue crack growth was performed in one frame, while fracture testing was performed in a second test frame. The following sections discuss the details of all large-scale testing load frames.

#### **3.4.1 Bending Test Setup**

To maximize the potential of the bending specimens, new load frames were designed to utilize the largest pair of servo-hydraulic actuators available at the Bowen Laboratory at Purdue University. A schematic of a bending load frame is shown in Figure 3.15. Two 220 kip MTS 244.51 actuators were spaced at 8 ft. on center to create four point bending. Four point bending results in a constant moment region ideal for fracture testing because the uniform stress state allows the flaw to be placed anywhere within the constant moment region. Additionally, spacing the actuators for the four point bending configuration facilitated installation of a temperature chamber required to cool the specimens to the desired test temperature. Each load frame was braced to prevent lateral movement. All braces and load frames were post-tensioned to the laboratory reaction floor. Twin test setups were designed and fabricated as shown in Figure 3.16.

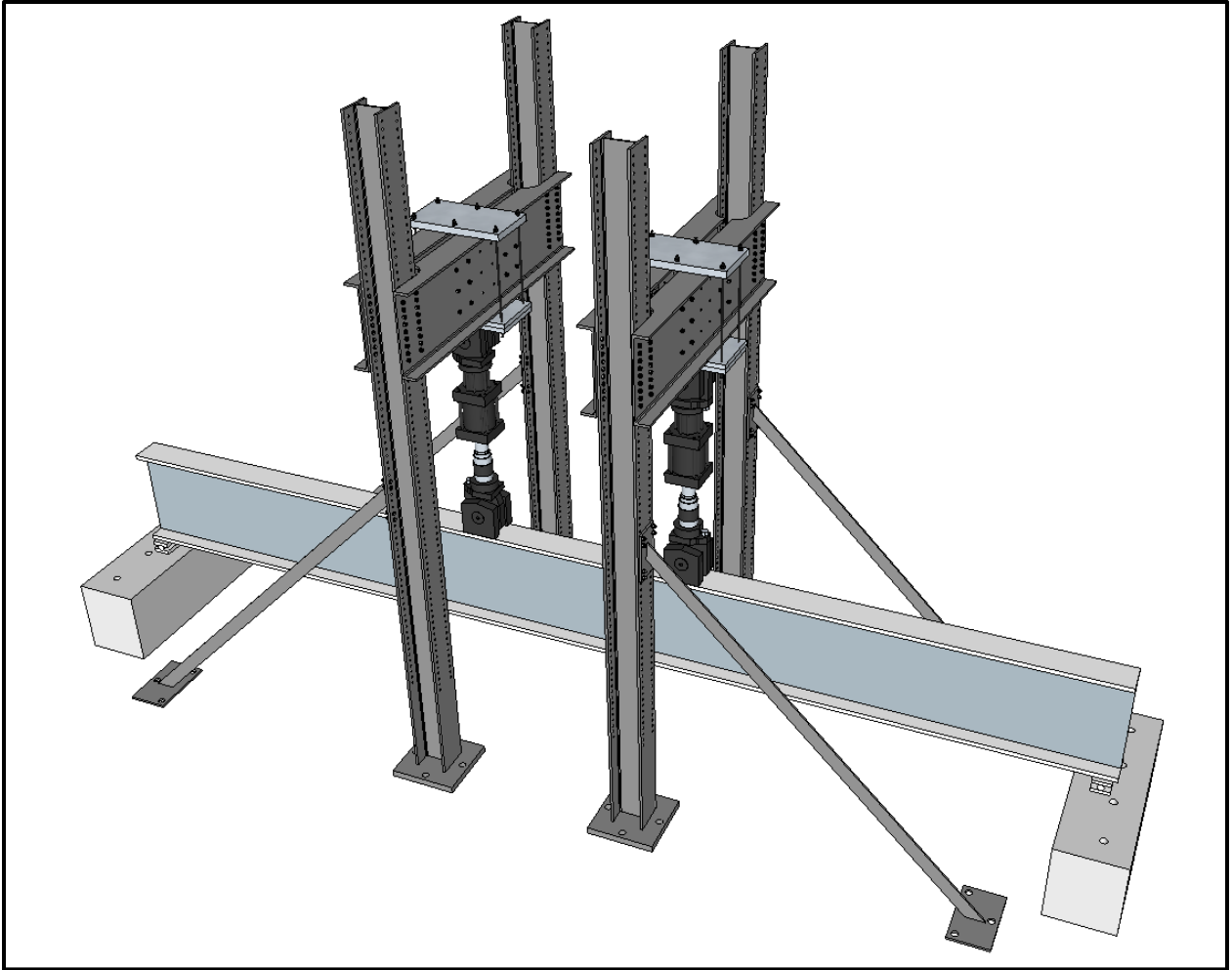


**Figure 3.15: Schematic view of bending load frame**

DRAFT



**Figure 3.16: Twin bending test setups**

Concrete reaction blocks elevated the bending specimens to facilitate visual inspection of the test specimen. Steel bearings rested on the concrete reaction blocks and supported the specimens. A pin and roller bearing configuration was utilized as shown in Figure 3.17. The combination of a pin and roller permitted longitudinal movement during loading. The pin bearing was located on the south end of each specimen and the roller bearing was located on the north end of each specimen.



**Figure 3.17: Pin bearing (left); Roller bearing (right)**

Two types of bracing were used on the bending specimens: end bracing and lateral torsional buckling (LTB) bracing. Both types of bracing were designed to prevent lateral instability. The end bracing was comprised of 4 in. x 4 in. x ½ in. angles with impact resistant slippery UHMW polyethylene bars. The bracing allowed for longitudinal rotation but prevented lateral movement. Concrete expansion anchors were used to secure the bracing to the concrete blocks. A combination of bridge clamps and bolts were used to connect the end bracing components to facilitate different flange widths. Photographs of the end bracing are found in Figure 3.18.



**Figure 3.18: End bracing**

Lateral torsional buckling bracing was located on each side of the top flange at the load points for each bending specimen. The bracing consisted of a 12 in. x 3/16 in. steel plate fastened between the load frame column and the actuator loading plate as shown in Figure 3.19. Lateral forces were resisted through tension in the brace on one side of the specimen, while the brace on the opposite side of the specimen buckled. Due to the plate thickness, the LTB braces provided negligible vertical stiffness and minimally reduced the load from the actuators to the specimen.



**Figure 3.19: Lateral torsional buckling bracing**

The hydraulic system was designed to maximize the loading rate for the fracture experiments. Moog 72-103 servovalves capable of 60 gpm were installed on each actuator. The servovalves were supplied from a dual ported MTS 293.22 hydraulic service manifold with a 100 gpm capacity. Additionally, 1.25 in. hydraulic lines were installed to increase flow capacity and reduce the flow losses. Specialized mounting hardware was used to secure all hydraulic lines to eliminate vibration in the hydraulic supply lines. The actuators were controlled through an MTS FlexTest GT controller with MultiPurpose TestWare software.

### **3.4.2 Axial Fatigue Test Setup**

An existing load frame at the laboratory was modified to perform fatigue cycling of the axial test specimens. A schematic of the axial test fatigue load frame can be found in Figure 3.20. The load frame was outfitted with a 115 kip Shore Western Model 924 servo-hydraulic actuator controlled by an MTS FlexTest GT controller with MultiPurpose TestWare software. Similar to the bending specimen test setup, bracing was provided to prevent lateral movement and buckling

of the plate, and each specimen was supported with pin and roller supports. Figure 3.21 is a photograph of the complete axial fatigue test setup.

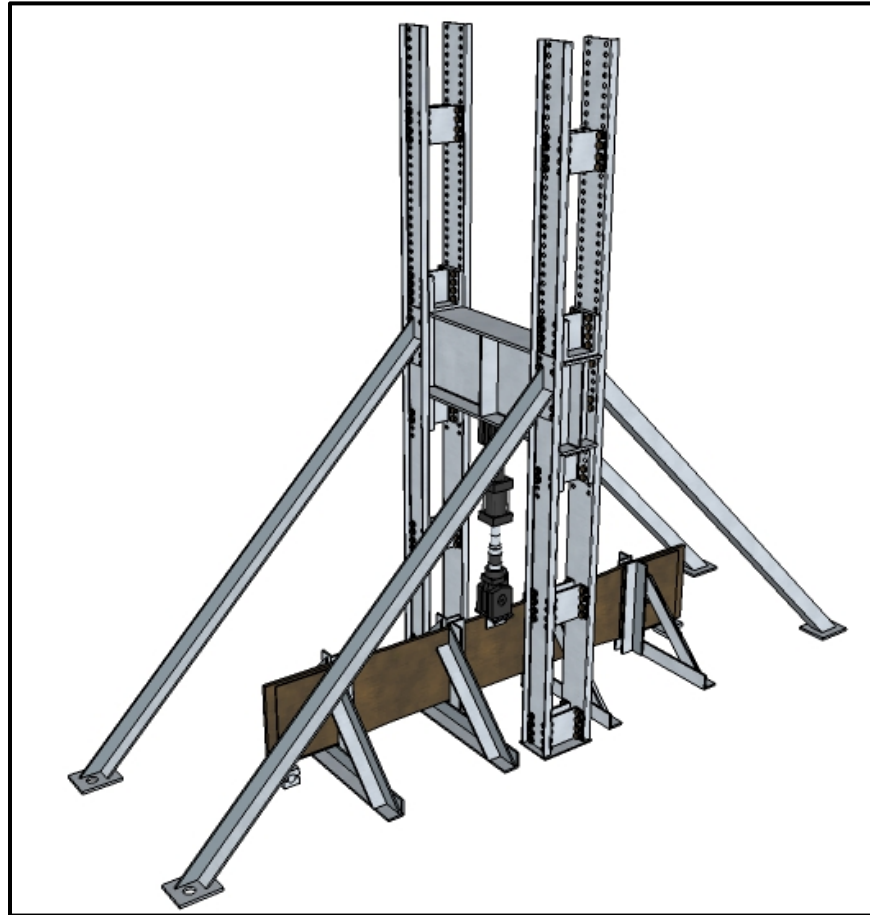


**Figure 3.20: Schematic view of axial test fatigue load frame**



**Figure 3.21: Axial test fatigue setup**

Bracing provided lateral stability during fatigue cycling. Four sets of braces were installed for each axial specimen. A set of braces were placed near each support and two sets of braces were placed near the load point. Braces were constructed from 6 in. x 4 in. x  $\frac{3}{4}$  in. and 6 in. x 6 in. x  $\frac{3}{4}$  in. angles and were connected by high strength bolts and bridge clamps. Using clamps allowed the braces to adapt to a variety of specimen thicknesses. Impact resistant slippery UHMW polyethylene bars were attached to the braces to minimize the load lost to friction. Figure 3.22 is a photograph of a set of lateral bracing.



**Figure 3.22: Axial fatigue test setup lateral bracing**

### **3.4.3 Axial Fracture Test Setup**

A new load frame was designed and fabricated to evaluate the fracture performance of the axial test specimens. Load was applied through six Enerpac RR-1506 double acting cylinders. The combination of cylinders resulted in a total available force of 1871 kips. The frame was self-reacting and oriented in the vertical position to eliminate any bending effects due to gravity. A schematic of the axial load frame can be found in Figure 3.23. A support frame was built around the axial load frame including four columns, stage beams, and bracing. Figure 3.24 is a photograph of the complete axial fracture test setup.

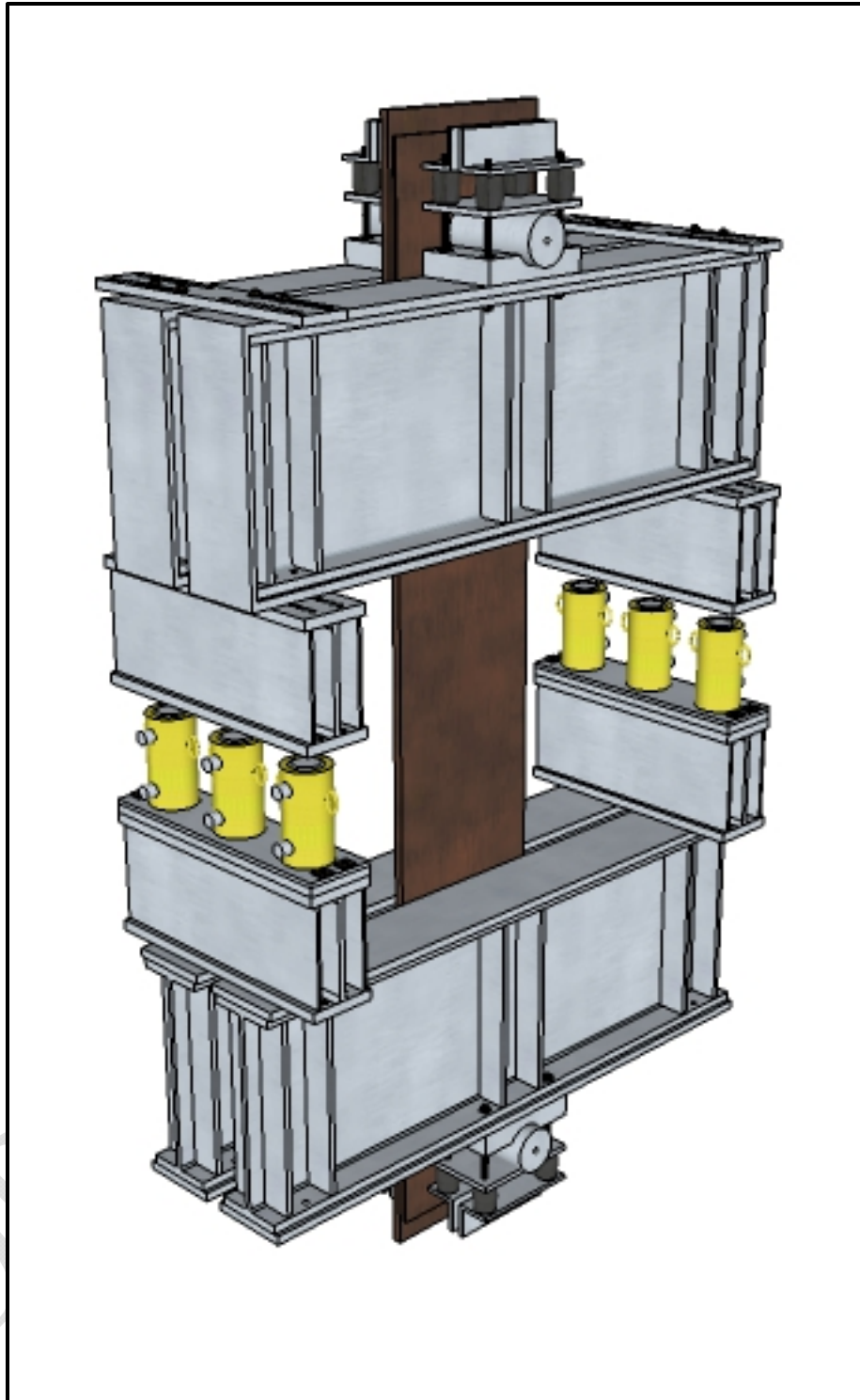


**Figure 3.23: Schematic view of axial test fracture load frame**



**Figure 3.24: Axial test fracture setup**

Axial test specimens were loaded through pin-ended connections to eliminate bending in the test specimens. The pins were 8 in. diameter and rested on machined bearing plates as shown in Figure 3.25. The steel used for all pins and bearing plates was heat-treated A514 100 ksi material. Eight GBA-20 elastomeric bumpers produced by Miner Elastomer Products Corporation

in Geneva, IL were also installed at each bearing location. The bumpers dissipated the energy released at fracture. Two of the bumper are also shown in Figure 3.25.



**Figure 3.25: Axial load frame pin connection**

All six Enerpac cylinders were controlled in unison through a National Instruments data acquisition system running a specialized LabVIEW program. The LabVIEW program was connected to a hydraulic pump and Omega PX302-10KGV General Purpose Pressure Sensor. Load was input to the LabVIEW program causing a voltage signal output to the hydraulic pump. Simultaneously, hydraulic pressure was measured by the pressure transducer. When the supplied pressure corresponded to the input load, the LabVIEW program stopped supplying voltage to the pump. Also, the LabVIEW program had an adjustable voltage output to control the loading speed and included the ability to specify a tolerance for the target load value.

### **3.5 Specimen Flaws**

All large-scale specimens were tested with an edge flaw geometry. From fracture mechanics, an edge flaw is considered the worst-case crack geometry. Therefore, the resulting critical crack sizes were shorter than any other possible crack geometry. As previously introduced, Equation 3.1 presents the calculation of the stress intensity factor of an edge crack in a finite width plate. At the completion of testing, the critical stress intensity was tabulated for each test specimen.

Flaws were introduced to each test specimen using a notch cut by an angle grinder. All test specimens were then cycled in fatigue until a crack initiated at the cut notch. The saw cut notch ensured the fatigue crack was produced at the exact desired location. Further, using the grinder cut notch reduced the time for fatigue crack initiation and growth. Similar notches were cut in both the bending and axial test specimens. The following sections discuss the notches in each specimen type.

### 3.5.1 Bending Test Specimen Flaws

Two types of notches were used for the bending test specimens. The type of notch varied depending on the thickness of the flange and depth of the notch. Four of the specimens had a straight, through-thickness notch. The straight notches were cut freehand with an angle grinder. Flange thicknesses for the straight notches were 1.5 in. and 2.0 in. The two bending specimens with 2.5 in. thick flanges had a v-notch cut with an angle grinder jig. The v-notch was a result of the cutting wheel depth and the thickness of the flange. For the 2.5 in. thick flange, the v-notch had a flat front at the center of the notch and then tapered to the surface resulting in a trapezoidal front. Figure 3.26 are photographs showing the difference between the freehand and jig methods. Also, Figure 3.27 depicts examples of the resulting flat and v-notches.

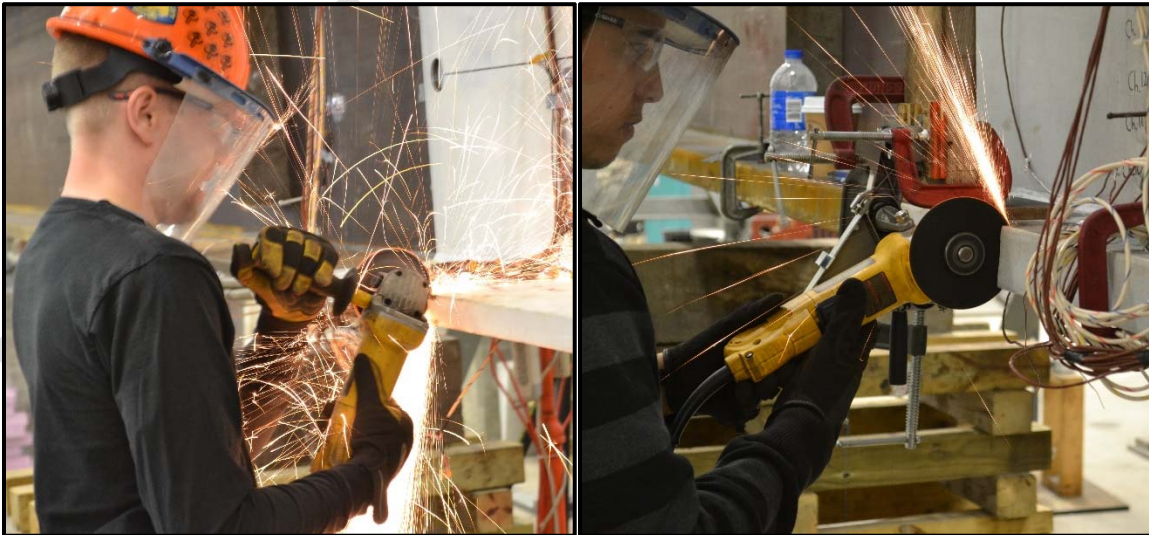


**Figure 3.26: Straight notching (left); V-notching (right)**

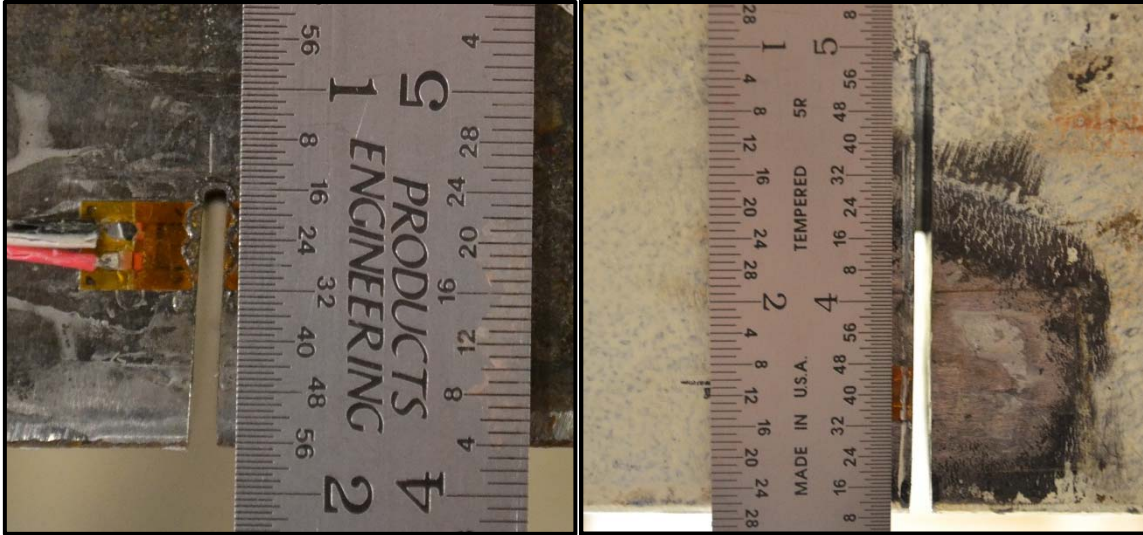


**Figure 3.27: Example straight notch (left); Example v-notch (right)**

### 3.5.2 Axial Test Specimen Flaws

All notches in the axial test specimens were cut using an angle grinder in the grinder jig. Four of the axial specimens had a v-notch coming to a point; whereas, the fifth axial specimen had a front similar to the 2.5 in. bending specimen due to the thickness. Once again, due to the specimen thickness relative to the size of the cutting wheel a trapezoidal front occurred on the 2.5 in. thick axial specimen. Figure 3.28 is a photograph of the grinder jig attached to an axial specimen.

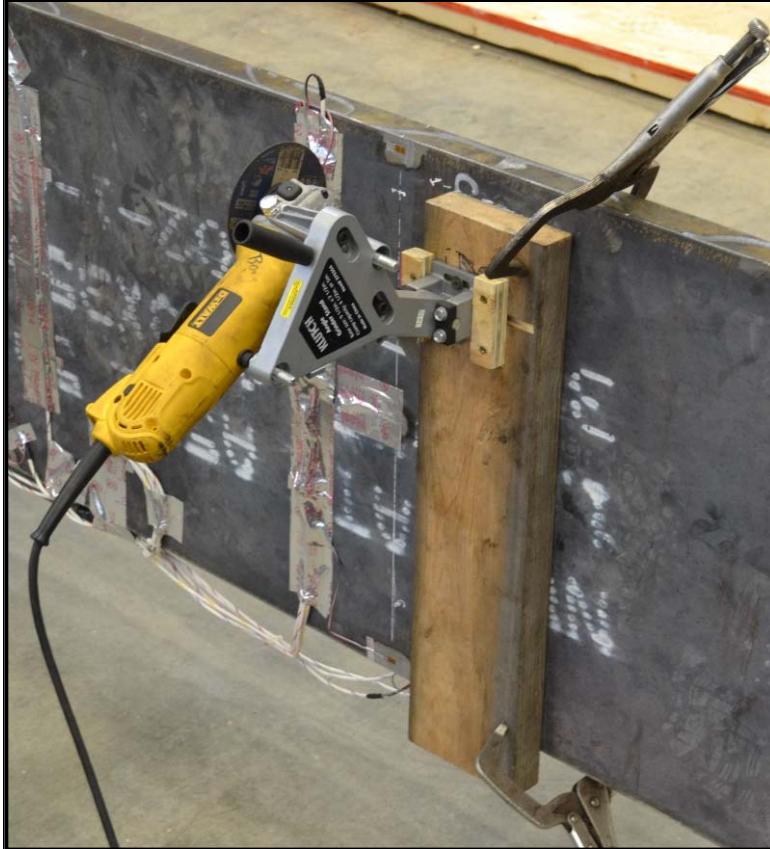


**Figure 3.28: Grinder jig attached to axial test specimen**

### **3.6 Instrumentation**

Instrumentation was used to measure a variety of parameters including strain, temperature, load, and displacement. Each type of instrumentation will be discussed individually in the following sections. Also, any instrumentation differences between the bending and axial specimens will be discussed.

#### **3.6.1 Data Logger**

Large-scale testing required the measurement of strain, temperature, displacement, and load. Data were collected by a Campbell Scientific CR9000X Data Logger Base System running a combination of CR9050 Modules and CR9052 Filtered Analog Input Modules. The CR9000X is a high speed, multi-channel 16-bit data acquisition system which can be easily adapted to a

variety of instrumentation. Figure 3.29 is a photograph of the CR9000X outfitted for a bending experiment.

All bending experiments utilized a single CR9050 module and five CR9052 modules. During a fracture experiment, strain, displacement, and load data were collected at a rate of 10,000 Hz. Conversely, temperature data were collected at a rate of 1 Hz. During static bending tests, data were collected at a rate of 50 Hz.

For the axial experiments, two different data logger card configurations were utilized. When temperature data were collected the data logger was configured with a single CR9050 module and two CR9052 modules. Whereas, if no temperature data were required, only two CR9052 modules were employed. Strain and pressure data were collected at a frequency of 100 Hz for all fracture experiments. When collected, temperature data were measured at a frequency of 1 Hz.



**Figure 3.29: CR9000X data logger**

### **3.6.2 Strain**

All strain gages were Model CEA-06-250UN-350/P2 produced by Vishay Micro Measurements. The strain gages had a gage length of 0.25 in., resistance of 350 ohms, and

operating temperature range of  $-100\text{ }^{\circ}\text{F}$  to  $350\text{ }^{\circ}\text{F}$ . An excitation voltage of 10 volts was supplied by the Campbell Scientific CR9052 modules. Manufacturer installation instructions were followed for all strain gage applications. M-Coat A, a general-purpose laboratory coating produced by Vishay Micro Measurements, was used to protect all strain gages. Any strain gages exposed to cooling were further protected with a waterproof mastic and covered with aluminum foil tape.

A total of 24 strain gages were installed for all bending test specimens. Strain gages were focused at two beam cross-sections. The primary cross-section was located at the notch location and was referred to as the “cracked section”. The cracked section corresponded to the midpoint of the span. Located 36 in. away from the cracked section was the second strain gage cross-section referred to as the “loading section”. A distance of 36 in. was used to ensure a portion of the strain gages were located outside the temperature chamber but still inside the constant moment region. The cracked section accounted for 20 strain gages and the remaining 4 strain gages were located at the loading section. All bending specimen strain gage locations can be found in the instrumentation plans located in Appendix B. An example bending specimen instrumentation layout is presented in Figure 3.30

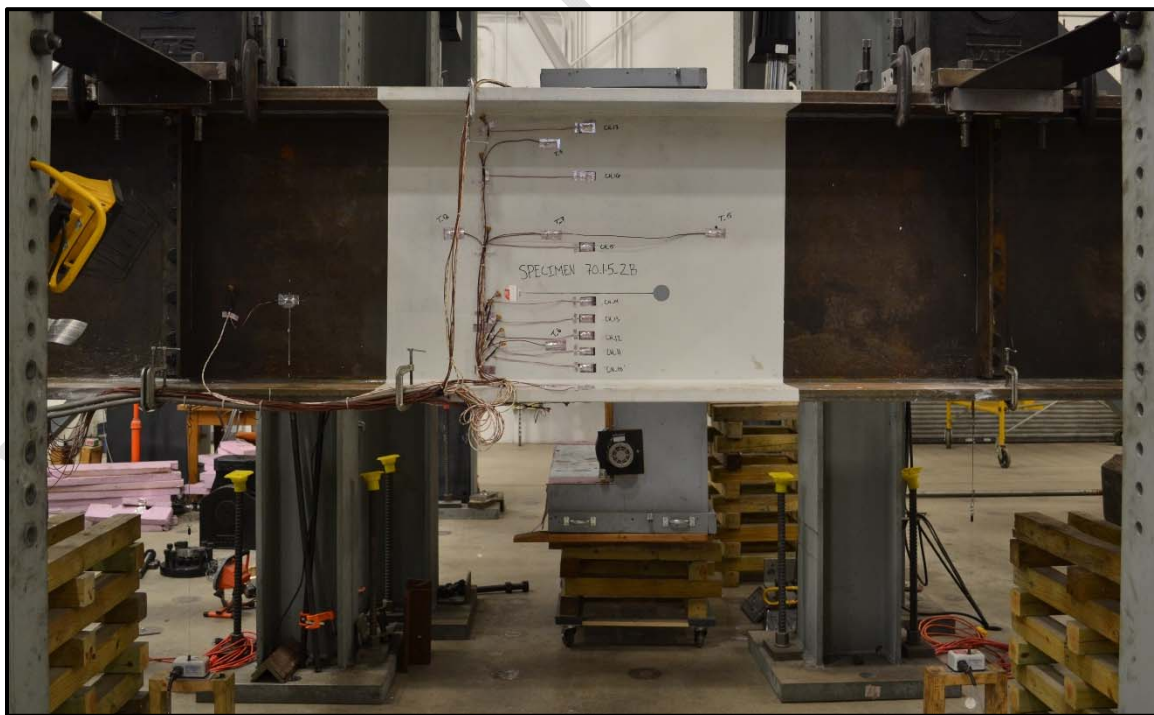


**Figure 3.30: Example bending specimen instrumentation layout**

A total of six strain gages were installed on all axial test specimens. Strain gages were focused at two cross-sections. The first cross-section was located at the notch location. Two strain gages were installed at the notched cross-section at the specimen centerline. A second cross-section with four strain gages was located 24 in. below the notched cross-section. Four strain gages were utilized to account for in-plane and out-of-plane bending of the specimen and were located outside the temperature chamber. All axial specimen strain gage locations can be found in the instrumentation plans located in Appendix D. An example axial specimen instrumentation layout is presented in Figure 3.31.

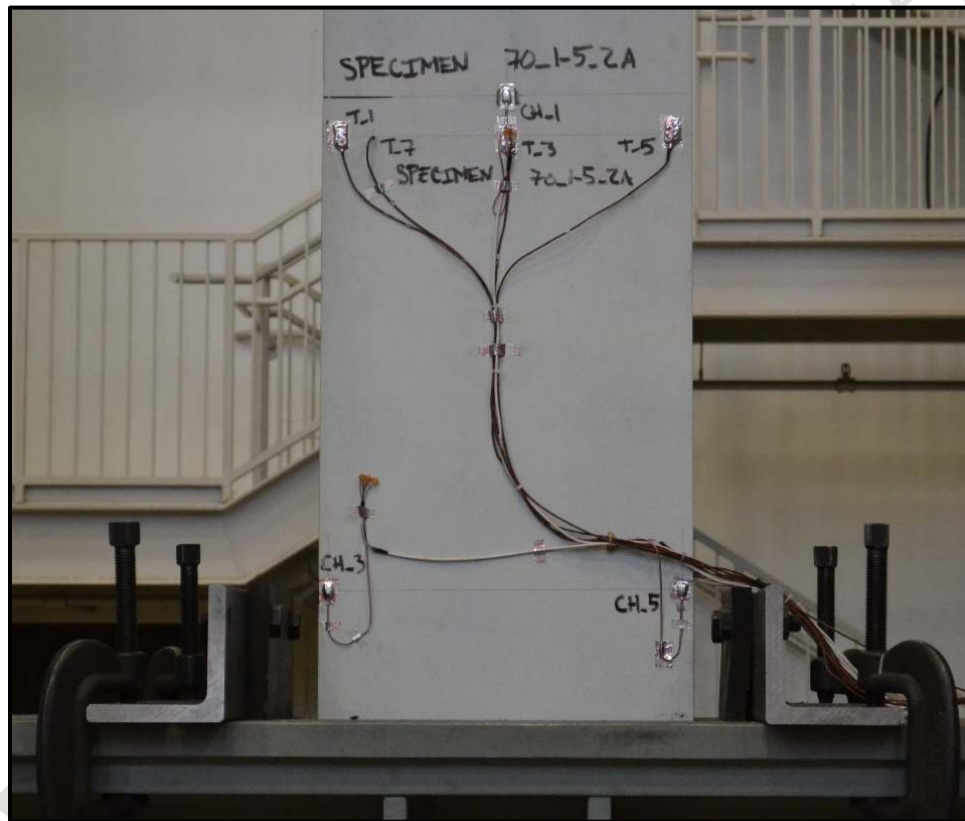


**Figure 3.31: Example axial specimen instrumentation layout**

### 3.6.3 Temperature

Temperature was measured with type J thermocouple wire produced by Omega Engineering. Type J is a general purpose thermocouple wire consisting of iron and constantan. Thermocouples were connected to the data logger to record temperature as well as to a temperature controller used to cool the test specimens. A total of 16 thermocouples were installed on the

bending specimens to ensure a uniform temperature distribution throughout the entire cross-section. The temperature controller required two thermocouples to regulate cooling, while the remaining thermocouples were connected to the data logger. Only seven thermocouples were installed on the axial test specimens. Again, two thermocouples were required for the temperature controller and the remaining five thermocouples were wired to the data logger. Exact thermocouple locations can be found on the instrumentation plans found in Appendix D. Example thermocouple locations can be found in Figure 3.30 and Figure 3.31 for the bending and axial specimens, respectively.

### 3.6.4 Displacement

Displacement was only measured for the bending specimens. Two methods were used to measure displacement: string potentiometers and linear variable displacement transducers (LVDT). The string potentiometers were UniMeasure PA Series. An input voltage of 10 volts was provided by the Campbell Scientific 9052 modules. Using a precision potentiometer, an output voltage was produced directly proportional to the wire rope extension. A pair of string potentiometers were placed at the bottom of each beam, directly below each actuator. The string potentiometer was the primary means of displacement measurement for the bending experiments. Displacement measurements were also obtained from the LVDT located inside each MTS servo-hydraulic actuator.

### 3.6.5 Force

Force was measured through different methods for the axial and bending tests. Analog load cells connected to each actuator, were used to measure force for the bending experiments. On the east bending test setup, both actuators were outfitted with MTS Model 661.31E-01 load cells having a 220 kip capacity. The actuators on the west bending test setup were configured with Honeywell Model 3129-112-300K load cells having a 300 kip capacity.

A Model PX302-10KGV General Purpose Pressure Sensor produced by Omega Engineering was used to measure force for the axial test setup. The pressure transducer was excited with 10 volts by the Campbell Scientific 9052 module. A single pressure transducer connected to the pressure supply line of all six Enerpac cylinders was used to measure the total force.

### **3.7 Temperature Chamber**

Large-scale fracture testing was performed based on a CVN impact energy value of 125 ft.-lbs. Therefore, it was required to cool test specimens to the temperature corresponding to the requisite impact energy. Temperature chambers were constructed from 2 in. rigid insulation for both the bending and axial test setups.

#### **3.7.1 Bending Temperature Chamber**

A removable temperature chamber was designed capable of reaching temperatures well below AASHTO Zone III (-60 °F) LAST for the bending test setup. The chamber was a clamshell design with two halves surrounding the constant moment region of the test specimen. Liquid nitrogen was used to cool the specimens. The liquid nitrogen was supplied in Dewar tanks, plumbed through cryogenic hoses, brass fittings, and copper pipe. Small holes in copper pipes within the temperature chamber diffused the liquid nitrogen as it was released into the chamber. The diffusing pipes were located on both the top and bottom of the chamber. Electronic solenoid valves were used to meter the liquid nitrogen. An Omega Engineering CN79000 1/32 DIN Dual-Zone Controller was used to control the solenoid based on measurements from type J thermocouples located within the chamber. A photograph of the temperature controller is shown in Figure 3.32. Two squirrel cage fans, located on either end of the chamber, circulated the heavy gaseous nitrogen back to the top of the chamber to help maintain a uniform temperature distribution. Photographs of the temperature chamber and liquid nitrogen setup are shown in Figure 3.33.



**Figure 3.32: Dual zone temperature controller**



**Figure 3.33: Bending temperature chamber**

### 3.7.2 Axial Temperature Chamber

Similarly, a removable clamshell design was used for the axial temperature chamber and liquid nitrogen was used to cool the specimens. The same solenoids and temperature controller as the bending test setup were used for the axial cooling configuration. No circulating fans were required for the axial specimens because a much smaller volume was cooled. Photographs of the axial temperature chamber can be seen in Figure 3.34.



**Figure 3.34: Axial temperature chamber**

### **3.8 Test Sequence**

The same general test sequence was used for all large-scale experimentation. First, a notch was cut into the specimen. Next, the specimen was cycled in fatigue to grow a fatigue crack to a desired length. Once the desired crack length was attained, if necessary, the specimen was cooled to attain the target 125 ft.-lb. behavior. After the temperature stabilized, a load equal to 75% of the gross yield strength was applied in an attempt to initiate a fracture. If no fracture occurred, the fatigue crack was extended through further cyclic loading after which the entire fracture process was repeated. The fatigue crack was grown and the fracture process was repeated until fracture initiated.

Early tests focused on growing the fatigue crack in small increments in an attempt to capture the critical flaw size within a fraction of an inch. As testing progressed, finite element models were continuously being updated for increasing crack lengths. For large crack lengths, the models indicated large compressive residual stresses were formed during experiments not resulting in fracture. Therefore, the crack growth approach was modified to testing at crack lengths with a high probability of fracture. The following sections address the specific test sequences for the bending and axial experiments including data collection.

#### **3.8.1 Bending Test Sequence**

The bending load frames allowed for the entire test sequence to be performed in a single test frame. Prior to notching, static load tests were performed on the bending test specimens. Static tests provided baseline data as well as provided an opportunity to ensure the beam and test setup were performing as expected. Load was applied in steps of 25 kips per actuator up to the target fracture load. A minimum of three static tests were performed to confirm data consistency. Typically, data were recorded at a rate of 50 Hz during the static tests. A representative static load sequence can be found in Figure 3.35 with the resulting longitudinal stresses presented in Figure 3.36.

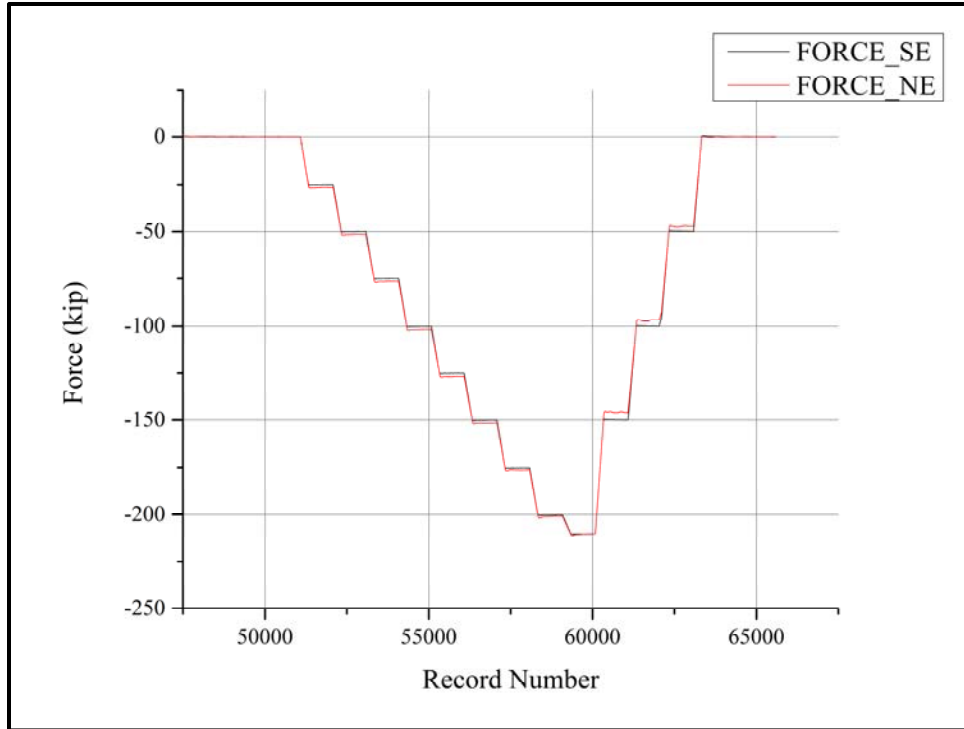


Figure 3.35: Representative static test load

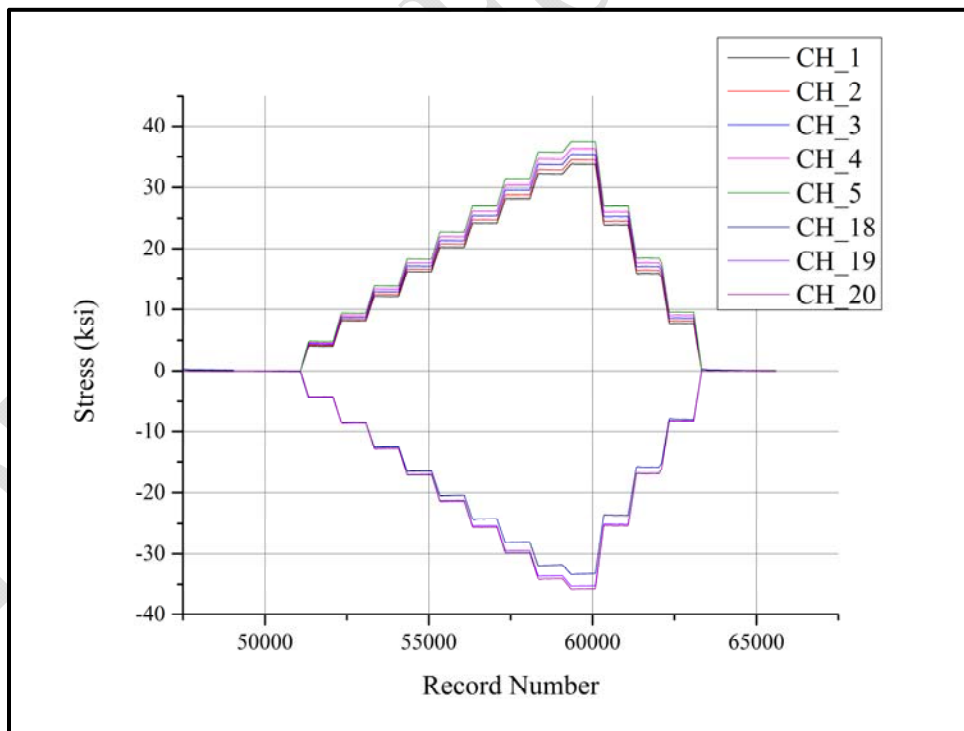


Figure 3.36: Representative static test longitudinal stress

Following the static tests a simulated fracture test was performed on the girder. The simulated fracture was performed to ensure the loading program functioned as intended. In general, once the beam was notched any applied load was kept below the peak fatigue load to minimize any crack tip plasticity.

Once all preliminary static and simulated fracture tests were completed, the beam was notched as previously described in Section 3.5.1. Exact notch lengths will be detailed in the discussion of each specimen. After notching, additional static tests were performed. For consistency, the notched static tests were loaded in 25 kip steps up to the peak fatigue load.

Following the notch static tests, the beam was cycled in fatigue. Fatigue stress ranges were started at approximately 13 ksi to initiate a fatigue crack. As crack growth progressed, the stress range was tapered down to a range corresponding to a stress intensity range of approximately 30 ksi $\sqrt{\text{in.}}$  with a peak stress intensity of approximately 90 ksi $\sqrt{\text{in.}}$ . The peak stress intensity was limited to minimize plasticity at the crack tip and assure the critical stress intensity during the fracture experiment was greater than the peak cyclic stress intensity. Data were recorded at 20 Hz during fatigue cycling in case fracture occurred during the crack growth phase. The cyclic data were not stored for future use.

Crack growth was monitored during cyclic loading through the use of magnetic particle testing and traditional visual inspection using a 10x magnifying glass. Magnetic particle testing was performed with the peak load applied from cyclic loading. At the desired crack length for fracture testing, static tests were once again performed. The static tests were performed in 25 kip steps up to the maximum cyclic load.

After completing all cyclic tests, the temperature chamber was installed and the beam was cooled to the desired test temperature corresponding to the CVN test temperature at which the sigmoidal fit had an impact energy of 125 ft.-lb. Exact test temperatures will be detailed in the discussion of each test specimen. Also, the beams were cooled just below the target test temperature to allow for the removal of the temperature chamber and subsequent warming during the test process. Cooling was performed under no load. Once the target test temperature was reached, the temperature was held for at least 20 minutes to guarantee a uniform temperature distribution through the thickness of the flange. Temperature stabilization allowed the flanges to soak and ensured there was not a temperature variation through the flange thickness. Preliminary testing was performed early in the research to establish the required soak time for large test girders.

The fracture test process began by removing the temperature chamber. High definition and high speed cameras were positioned to record the fracture event. Loading was applied in three phases. The first phase provided a simulated dead load corresponding to the peak cyclic force. Dead load was applied over a period of 5 seconds. A dwell command was used to hold this load for a few seconds. The second phase applied the target load of  $0.75F_y$ . Exact peak loads will be detailed in the discussion of each test specimen. Early experiments applied the fracture load in 0.1 seconds. Later tests applied the fracture load over 5 seconds to ensure a uniform loading from the pair of actuators. If the beam did not fracture initially, the load was then held for 2 seconds followed by 10 cycles between 90% and 100% of the fracture load. Cycling at the fracture load was intended to simulate additional vibrations corresponding to a load crossing a bridge in real-world conditions. At the completion of cycling the load was removed. A similar test process was employed by Wright during his initial large-scale fracture experiments on HPS I-girders (Wright, 2003). Data were recorded at 10,000 Hz during the entire fracture test sequence. Figure 3.37 is an example of the loading sequence during a fracture test.

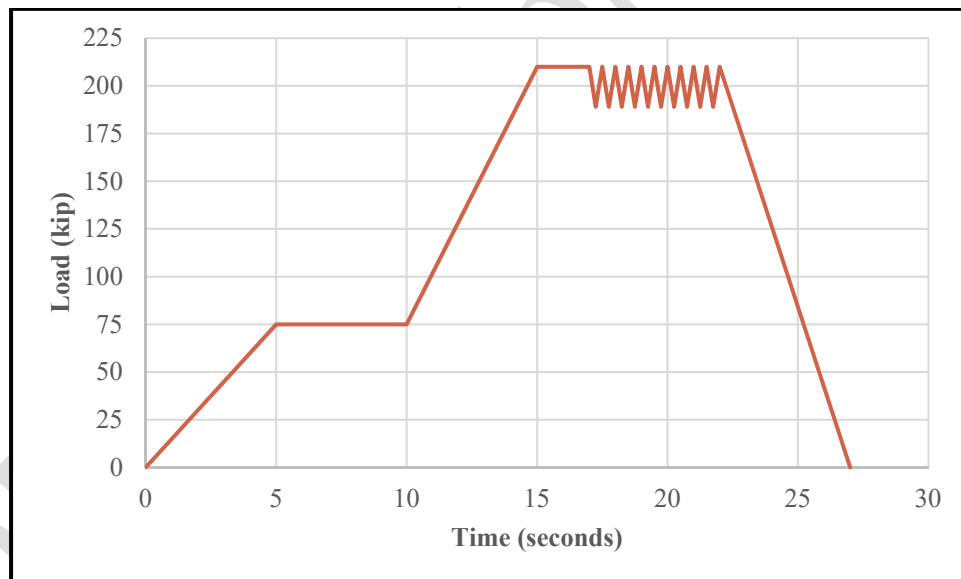


**Figure 3.37: Example fracture loading sequence**

### 3.8.2 Axial Test Sequence

As explained previously, two load frames were required to test the axial specimens, specifically one for fatigue cycling and another for fracture testing. The Enerpac cylinders used for fracture testing could not be efficiently employed for cyclic loading. Additionally, fatigue

cycling the axial specimens in a bending configuration reduced the required load to reach the required cyclic stress range.

Notching was performed prior to installing the axial test specimens into the fatigue frame. Exact notch lengths will be detailed in the discussion of each specimen. After notching, all axial specimens were installed in the fatigue test frame. A cyclic stress range of approximately 15 ksi was applied. The peak stress intensity at the target crack length was limited to 40% of the yield strength. ASTM E1820-15a suggests the 40% limit for precracking during fracture toughness test for SE(B) specimens (ASTM, 2015a). The axial test specimens acted like oversized SE(B) specimens during the fatigue crack growth period; as such, the 40% limit was employed resulting in peak stress intensity values of 20 ksi $\sqrt{\text{in}}$ . and 28 ksi $\sqrt{\text{in}}$ . for the Grade 50 and Grade 70 specimens, respectively. Limiting the stress intensity ensures the stress intensity during precracking is less than the critical stress intensity during the fracture test. Fatigue cracks were measured using magnetic particle inspection. Measurements were taken with the peak cyclic force applied to the specimen. No data were recorded during the fatigue crack growth phase of the axial test specimens.

Once the fatigue cracks reached the desired length, the axial specimens were removed from the fatigue load frame and installed into the fracture load frame. Strain gages and thermocouples, if necessary, were attached to the specimens after installation into the fracture load frame. In contrast to the bending test, only a single static load test was performed for all the axial test specimens. The static load test was performed on an uncracked specimen and was used to establish any bending in the axial fracture test frame and was performed on a specimen without a notch.

For specimens where cooling was required, the temperature chamber was installed after all instrumentation was installed and verified. Cooling was applied under no load and only in the region 12 in. above and below the crack. After the target test temperature was attained, the temperature was held constant for a minimum of 20 minutes. Specimens were cooled beyond the target test temperature to allow for removal of the temperature chamber. Additionally, loading for the axial fracture test was at a slower rate than the bending fracture test. Therefore, the specimens were cooled beyond the target value to allow warming during the experiment.

The fracture test process began by bringing the Enerpac cylinders into contact with the upper crosshead of the test frame, lifting the specimen. To permit installation of the lower pin, the upper crosshead rested on a set of shelves creating a gap between the lower pin and lower bearing plates. As the specimen was lifted, prior to contact with the bearing plate, the instrumentation was

electronically zeroed. Zeroing the instrumentation removed all dead load effects of the specimen. Once in contact with the bearing plate, the lower energy absorption system was secured to the bottom bearing.

An electronic valve was used to control the flow of oil into the Enerpac cylinders. Due to control limitations, the first two electronic pulses to the valve resulted in a load of approximately 100 kips. After the initial two pulses, very fine control of the valve was possible. Therefore, after the first pulse, the energy absorption system was secured. For cooled specimens, the temperature chamber was removed after the second pulse, and then all cameras were positioned and focused. The specimen temperature was monitored and loading commenced when the internal specimen temperature was approximately 5 °F below the target test temperature. Load was applied until fracture occurred or the target load corresponding to  $0.75F_y$  was attained. Data were recorded at 100 Hz for all axial specimen testing.

### 3.9 Test Specimens

Large-scale testing consisted of performing fracture experimentation on 11 test specimens: six full-scale beams and five axial plates. Table 3.3 provides the distribution of specimen types for each plate. Specimen geometry, fabrication information, flaw sizes, and test temperature for each specimen type will be discussed in the following sections.

**Table 3.3: Specimen distribution**

Plate	Specimen Type	
	Bending	Axial
E	2	1
H	2	2
I	2	0
J	0	2

A unique naming convention was used for all specimens which indicated the material grade, flange or plate thickness, and specimen count and type. An underscore was used to separate each parameter. For example, Specimen 50\_2-5\_2B was made from Grade 50 steel, had a 2.5 in. thick flange, and was the second bending specimen from the same heat with the same properties.

### 3.9.1 Bending Specimen Test Matrix

Three specimen groups were tested as part of large-scale bending experimentation. Two specimens were tested for each group, resulting in a total of six bending specimens. Within a given specimen group, the specimens had the same geometry and the bottom flange was made from the same heat of steel. Bottom flange thickness for the bending specimens varied from 1.5 in. to 2.5 in. The width of the bottom flanges tested varied between 14 in. and 18 in. Specimens were tested with both Grade 50 and 70 flanges. The following sections describe the specimen groups and each specimen in detail. Design drawings for all large-scale bending test specimens can be found in Appendix B.

#### 3.9.1.1 50\_2-0\_B Specimens

50\_2-0\_B specimens were made from Plate I and were the only specimens tested not satisfying the 125 ft.-lb. requirement. CVN testing revealed Plate I narrowly satisfied the current Grade 50 AASHTO Zone III fracture critical toughness requirements. Original testing of Plate I did not meet the Zone III requirements; however, after performing a retest in accordance with ASTM A673-07, Plate I met the Zone III requirements (ASTM, 2012a). Therefore, testing of both 50\_2-0\_B specimens was performed at -60 °F. As such, 50\_2-0\_B specimens were used to compare the high-toughness specimens to the current specification. Further, the 50\_2-0\_B specimens provided an example of the typical critical flaw in the existing inventory.

Previous testing at the laboratory on built-up members used the 50\_2-0\_B specimens. A base section consisting of a 0.5 in. x 36 in. web fillet welded to a 2 in. x 14 in. flange was fabricated for reuse for the built-up member testing. Fabrication of the base section was performed by Hirschfeld Industries. For the second flange, the built-up member testing replaced the flange angles and cover plates for different tests. To use the built-up member specimens for the current testing, the girders were flipped and the base section was evaluated. A pair of 6 in. x 6 in. x ¾ in. flange angles and a single ¾ in. x 14 in. cover plate were attached as a compression flange. Each 50\_2-0\_B specimen was 40 ft. long with a total supported length of 39 ft. Bearing stiffeners were bolted to the web at the loading and bearing points.

Different base specimens remained at the completion of the built-up member project. As a result, Specimen 50\_2-0\_1B and Specimen 50\_2-0\_2B had a few minor differences. The

differences included the termination length of the compression flange cover plate, the stitch spacing of the bolts, and the fastener type in the web of the constant moment region. Specimen 50\_2-0\_1B had a cover plate termination length of 66 in. whereas Specimen 50\_2-0\_2B had a termination length of 102 in. Stitch spacing for Specimen 50\_2-0\_1B was 8 in. as compared to 10 in. for Specimen 50\_2-0\_2B. For Specimen 50\_2-0\_1B, rivets were used in the web to flange angle connection in the constant moment; conversely, the entirety of Specimen 50\_2-0\_2B was bolted. The differences between the two specimens had no impact on the performance or results of current tests because the built-up portion of the beam was the compression flange.

#### *3.9.1.1.1 Specimen 50\_2-0\_1B*

Specimen 50\_2-0\_1B was the first large-scale specimen tested. The bottom flange was notched to 0.25 in. with an angle grinder. A fatigue crack was grown to a length of 0.5 in. and a fracture test was performed. The test did not result in a fracture. At a length of 1.0 in. a second fracture test was performed and no fracture resulted. The crack was extended to 1.6875 in. and tested a third time resulting in a fracture of the bottom flange and web. The fracture arrested after severing the web and did not jump into the built-up components of the compression flange. An average actuator load of 149.2 kips was recorded at the time of fracture resulting in a bottom flange longitudinal stress of 26.3 ksi. A general photograph of Specimen 50\_2-0\_1B taken after fracture can be found in Figure 3.38. Figure 3.39 is a photograph of the fracture surface from Specimen 50\_2-0\_1B.

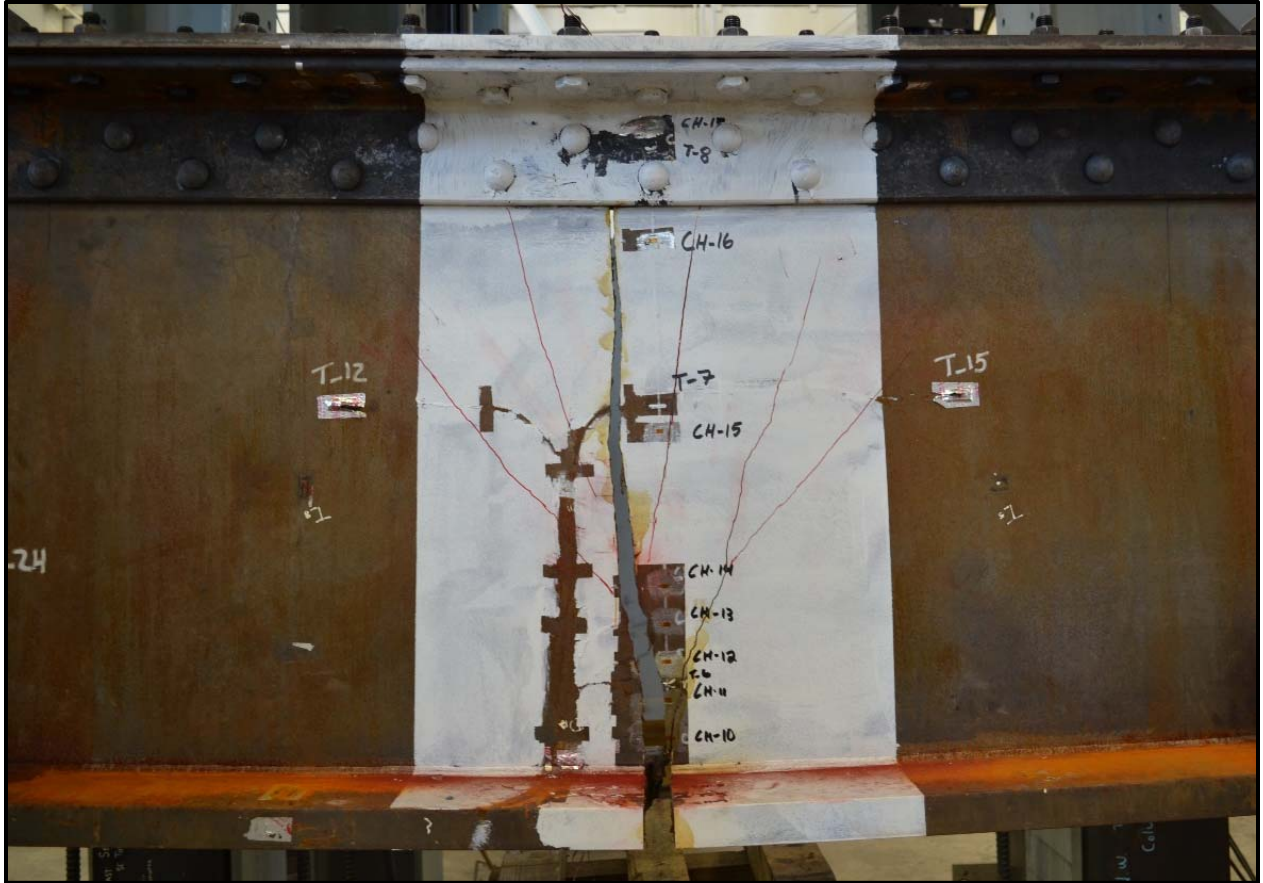


Figure 3.38: Specimen 50\_2-0\_1B



**Figure 3.39: Specimen 50\_2-0\_1B fracture surface**

#### *3.9.1.1.2 Specimen 50\_2-0\_2B*

Specimen 50\_2-0\_2B was initially notched to 0.625 in. with an angle grinder. A fatigue crack was grown to 1.0625 in. and a fracture test was performed. The fracture test resulted in complete fracture of the tension flange as well as the web. The fracture did not jump to any of the built-up components of the compression flange. At fracture, the average actuator load was 128.6 kips. The calculated bottom flange stress was 22.6 ksi. A general photograph of Specimen 50\_2-0\_2B taken after fracture can be found in Figure 3.40. Figure 3.41 is a photograph of the fracture surface from Specimen 50\_2-0\_2B.

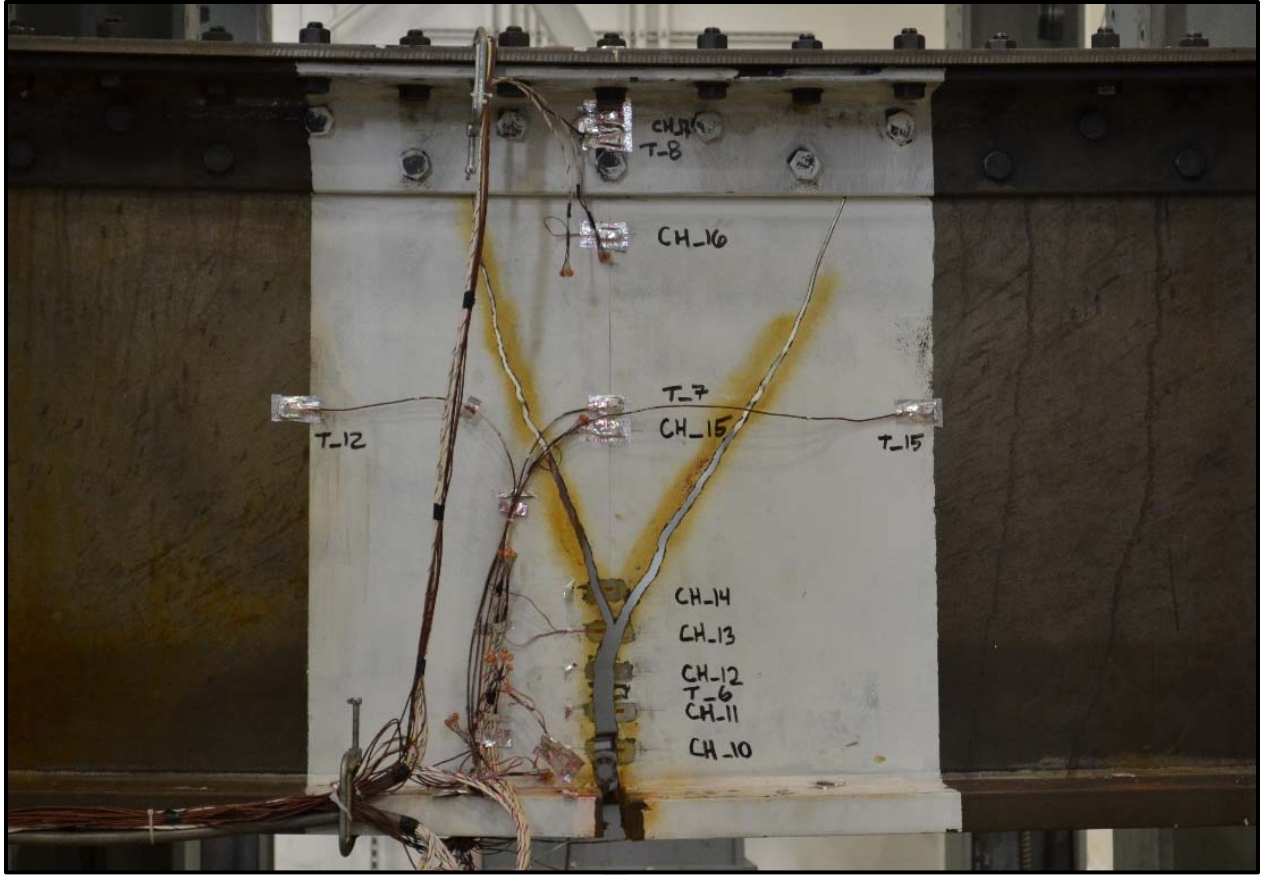


**Figure 3.40: Specimen 50\_2-0\_2B**



**Figure 3.41: Specimen 50\_2-0\_2B fracture surface**

### ***3.9.1.2 50\_2-5\_B Specimens***

50\_2-5\_B Specimens were fabricated from Plate E. Two 50\_2-5\_B bending test specimens were fabricated by Hirschfeld Industries. Each girder was 46 ft. long with a supported length of 45 ft. Plate E was shorter than the required 46 ft. length; therefore, two full-penetration splices were added to the bottom flange of the girders. No splices were required for the web or compression flange. Material used for the compression flange and area outside the test zone of the tension flange was donated by SSAB. Both flanges were 2.5 in. x 14 in. and the web was 0.5 in. x 33 in. Bearing stiffeners were bolted to the web at the loading and bearing points. Fracture testing was performed at -30 °F, as established from CVN impact testing.

To prevent a fracture from completely severing the test specimen into two pieces, fracture arrest details were added to the 50\_2-5\_B specimens. The detail was known as a ‘dog-bone’. A dog-bone detail consisted of a pair of holes connected by a through-thickness cut. The holes in the 50\_2-5\_B specimens were 1.0625 in. in diameter and drilled with a magnetic drill. Center-to-center hole spacing was 18 in. The slot connecting the two holes was cut with an oxy-acetylene track torch resulting in a width of approximately 0.125 in. Figure 3.42 is a photograph of an example dog-bone fracture arrest detail.

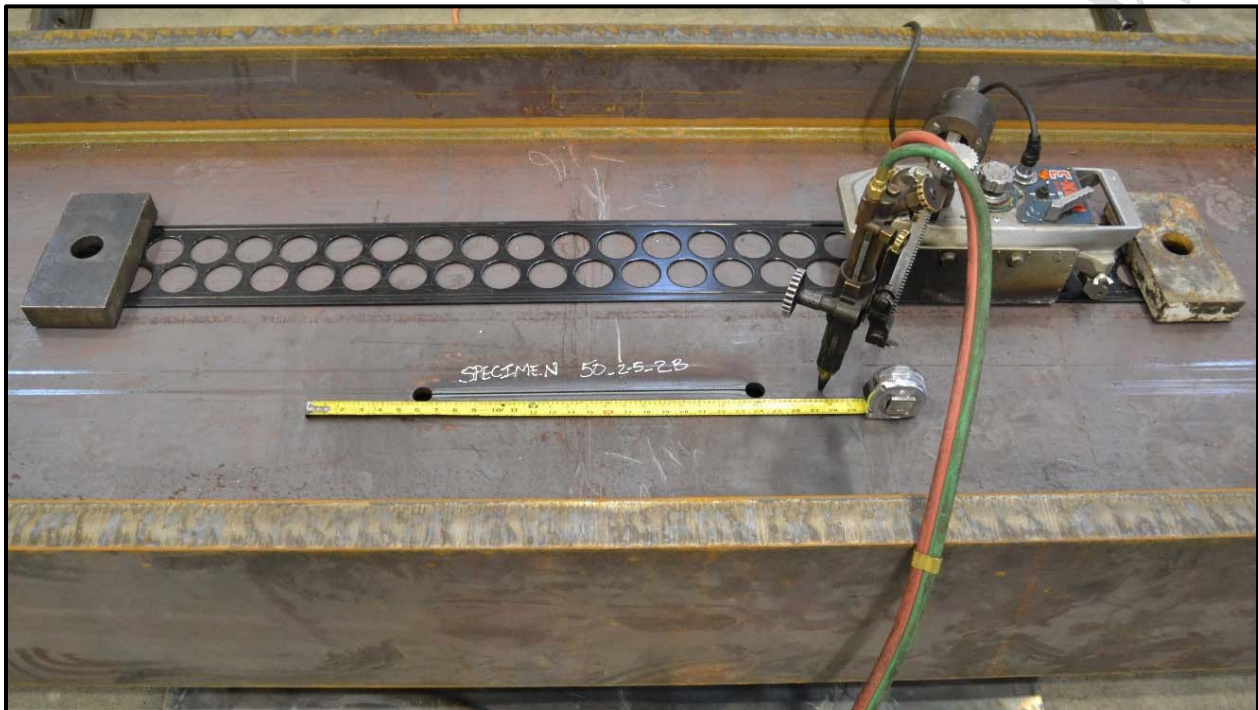


**Figure 3.42: Example dog-bone fracture arrest detail**

#### 3.9.1.2.1 Specimen 50\_2-5\_1B

Specimen 50\_2-5\_1B was originally prepared with a 0.625 in. straight notch. After minimal fatigue cycling the north actuator on the test setup malfunctioned. In the time the load cell was out for repair, the v-notch technique was discovered and the approach was changed to grow the fatigue cracks to a known fracture length. Therefore, Specimen 50\_2-5\_1B was notched a second time with a trapezoidal front. The through-thickness notch was 0.9375 in. long and tapered to surface length of 1.9375 in.

The final fatigue crack of Specimen 50\_2-5\_1B was grown to 5.0 in. Fracture occurred at an average actuator load of 104.6 kips. The resulting bottom flange stress was 18.7 ksi. Complete

specimen fracture was prevented by the dog-bone detail. A general photograph of Specimen 50\_2-5\_1B taken after fracture can be found in Figure 3.43. Figure 3.44 is a photograph of the fracture surface from Specimen 50\_2-5\_1B.

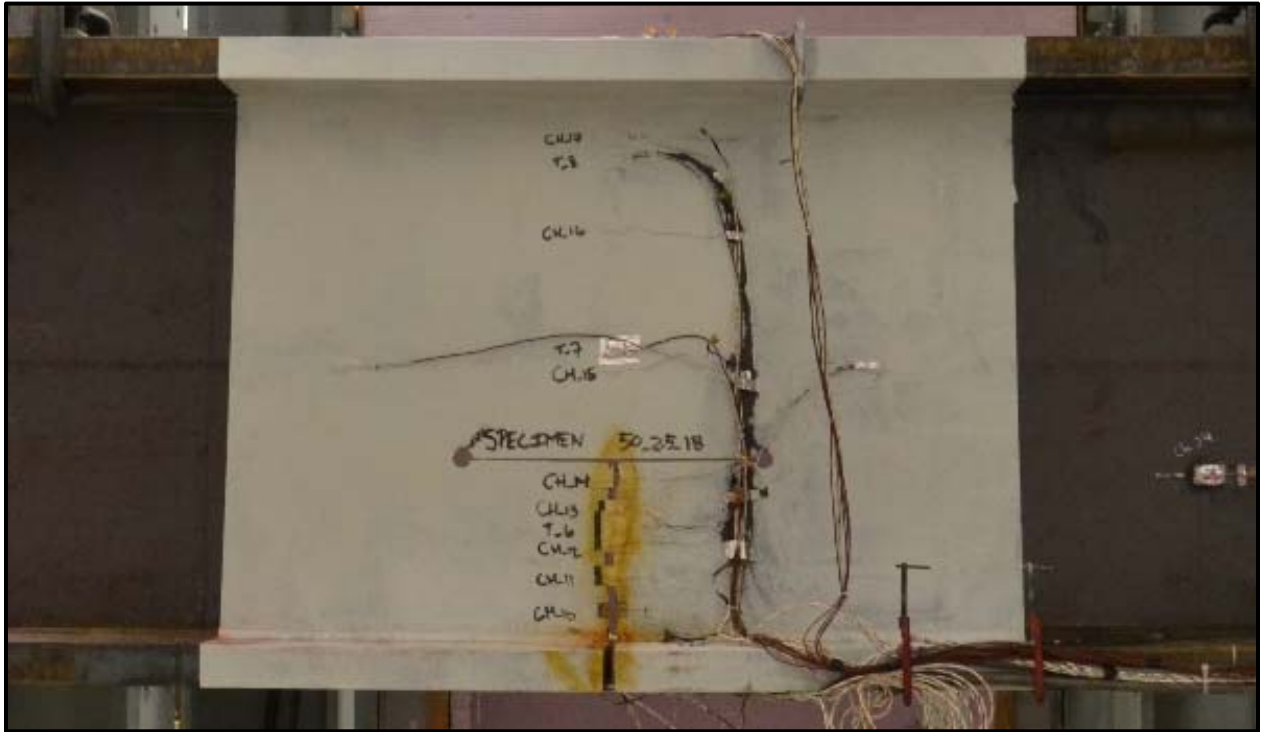


**Figure 3.43: Specimen 50\_2-5\_1B**



**Figure 3.44: Specimen 50\_2-5\_1B fracture surface**

#### *3.9.1.2.2 Specimen 50\_2-5\_2B*

Similarly, Specimen 50\_2-5\_2B was notched with a trapezoidal front. The through-thickness notch was 0.9375 in. long and tapered to a surface length of 2.0 in. A fatigue crack with an average length of 4.375 in. was grown for the fracture experiment. High-strength, 1.0 in. diameter bolts were fully pretensioned in the dog-bone fracture arrest detail. The fracture was

arrested by the detail. At fracture, the average actuator load was 163.3 kips. The resulting bottom flange stress was 29.2 ksi. A general photograph of Specimen 50\_2-5\_2B taken after fracture can be found in Figure 3.45. Figure 3.46 is a photograph of the fracture surface from Specimen 50\_2-5\_2B.

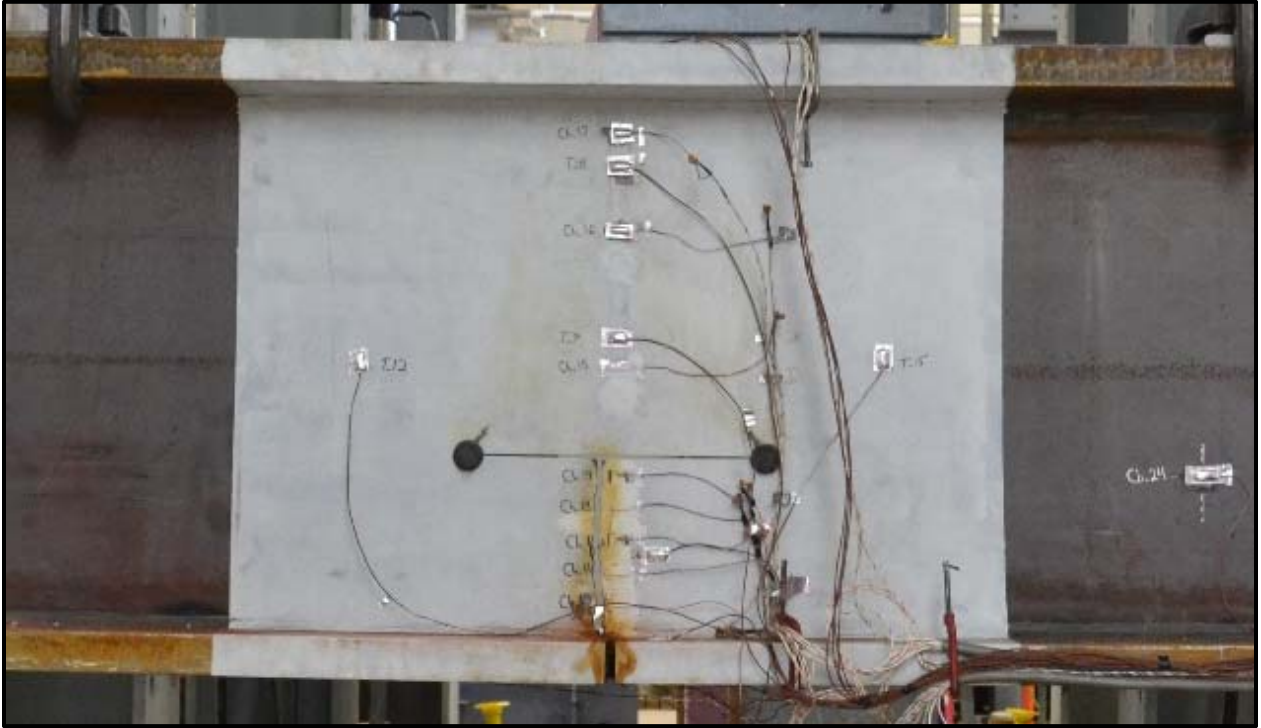


**Figure 3.45: Specimen 50\_2-5\_2B**

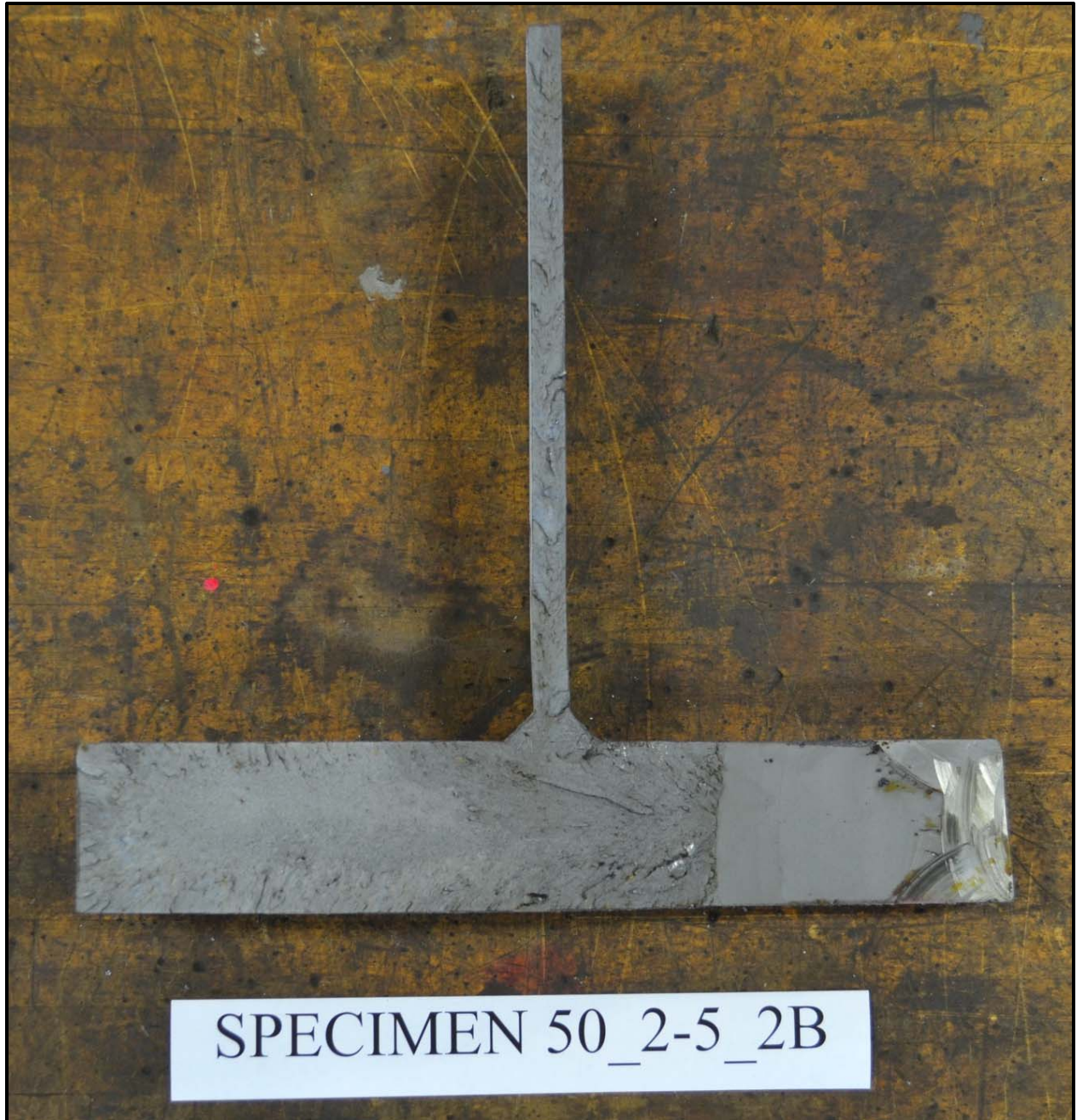


**Figure 3.46: Specimen 50\_2-5\_2B fracture surface**

### ***3.9.1.3 70\_1-5\_B Specimens***

70\_1-5\_B Specimens were fabricated from Plate H by High Steel Structures. High Steel Structures donated the Plate H material. Each girder was 50 ft. long with a supported length of 49 ft. Plate H was shorter than the required 50 ft. length; therefore, two full-penetration splices were

added to the bottom flange of the girders. No splices were required for the web or compression flange. Material used for the web, compression flange, and area outside the test zone of the compression flange was donated by Nucor Corporation. Both flanges were 1.5 in. x 18 in. and the web was 0.5 in. x 33 in. Bearing stiffeners were bolted to the web at the loading and bearing points. Fracture testing was performed at -35 °F, as established by CVN impact testing.

To prevent a fracture from completely severing the test specimen into two pieces fracture arrest details were added to the 70\_1-5\_B specimens. The holes in the 70\_2-5\_B specimens were 2.0 in. in diameter and drilled with a magnetic drill. Center-to-center hole spacing varied between 18 in. and 36 in. The slot connecting the two holes was cut with an oxy-acetylene track torch resulting in a width of approximately 0.125 in.

#### *3.9.1.3.1 Specimen 70\_1-5\_1B*

Specimen 70\_1-5\_1B was notched with a 0.625 in. through-thickness straight notch. The center-to-center hole spacing of the dog-bone detail was 36 in. for Specimen 70\_1-5\_1B. Unsuccessful fracture attempts were made at fatigue crack lengths of 1.0 in., 2.5 in., and 3.625 in. Specimen 70\_1-5\_1B fractured at a fatigue crack length of 5.0625 in. The average actuator load was 160.4 kips at fracture. The resulting bottom flange stress was 40.4 ksi. Complete specimen fracture was prevented by the dog-bone detail. A general photograph of Specimen 70\_1-5\_1B taken after fracture can be found in Figure 3.47. Figure 3.48 is a photograph of the fracture surface from Specimen 70\_1-5\_1B.

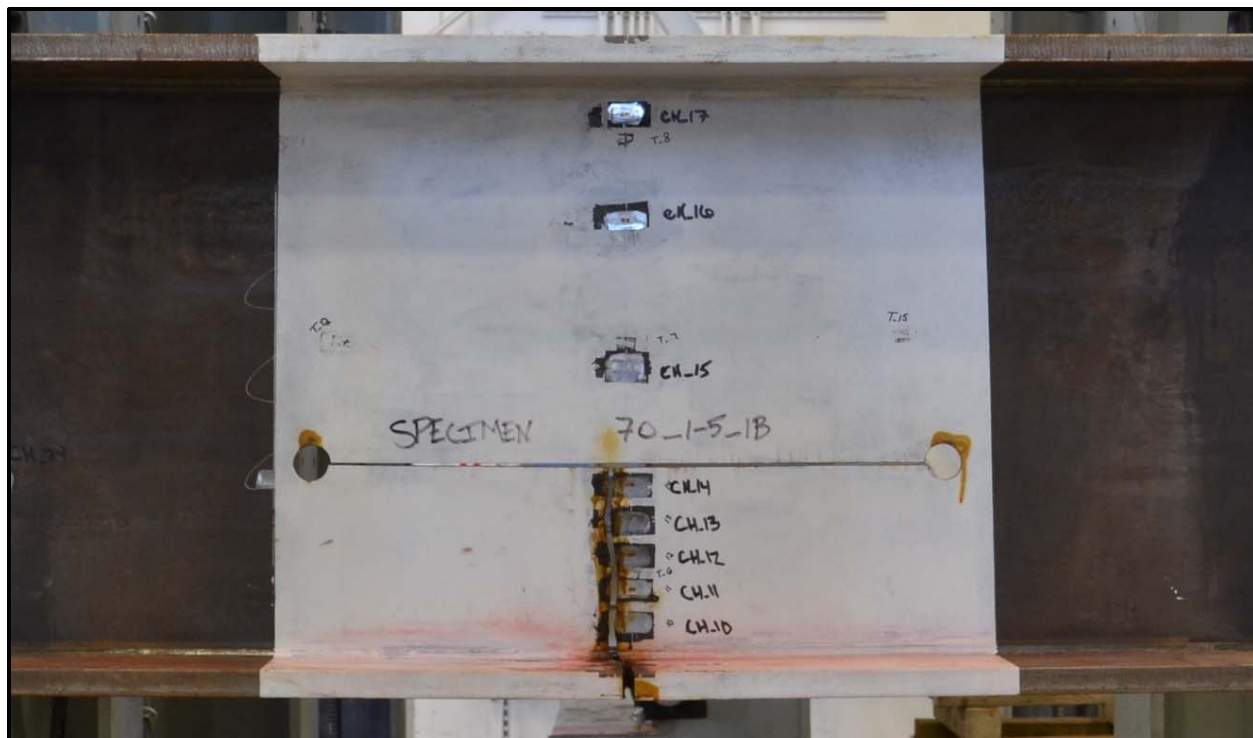


Figure 3.47: Specimen 70\_1-5\_1B



**Figure 3.48: Specimen 70\_1-5\_1B fracture surface**

#### *3.9.1.3.2 Specimen 70\_1-5\_2B*

Specimen 70\_1-5\_2B was notched with a 1.125 in. through-thickness straight notch. The center-to-center hole spacing of the dog-bone detail was 18 in. for Specimen 70\_1-5\_2B. Unsuccessful fracture attempts were made at fatigue crack lengths of 3.625 in., 5.0 in., and 5.75 in. Specimen 70\_1-5\_2B fractured at a fatigue crack length of 7.5 in. The average actuator load was 164.6 kips at fracture. The resulting bottom flange stress was 41.5 ksi. Complete specimen fracture was prevented by the dog-bone detail. A general photograph of Specimen 70\_1-5\_2B taken after fracture can be found in Figure 3.49. Figure 3.50 is a photograph of the fracture surface from Specimen 70\_1-5\_2B.

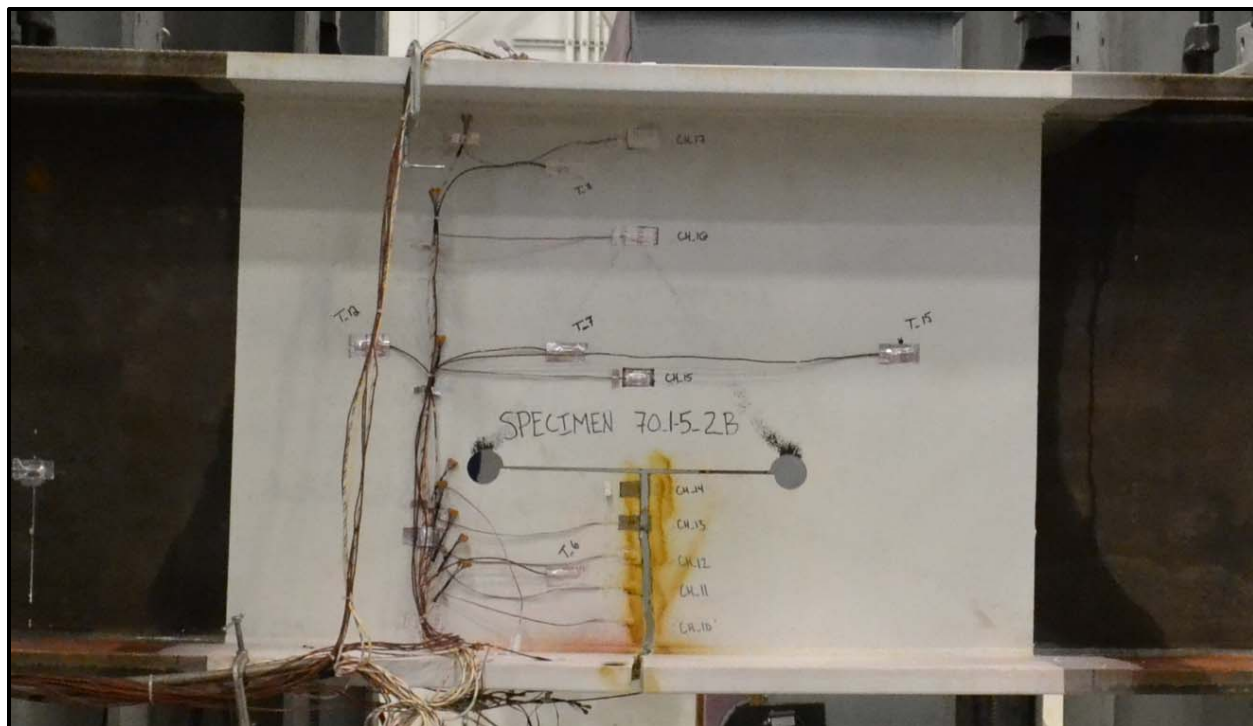


**Figure 3.49: Specimen 70\_1-5\_2B**



**Figure 3.50: Specimen 70\_1-5\_2B fracture surface**

### **3.9.2 Axial Specimen Test Matrix**

Three specimen groups were tested as part of the large-scale axial experimentation. Two of the groups had two specimens tested and one group had a single specimen tested, resulting in a total of five axial specimens. A given specimen group had the same geometry and were fabricated from the same plate of steel. Plate thickness varied from 1.5 in. to 2.5 in. for axial testing. The plate widths varied between 14 in. and 22 in. Specimens were tested from both Grade 50 and Grade 70. The following sections describe the specimen groups and each specimen in detail. Design drawings for all large-scale axial test specimens can be found in Appendix C.

### **3.9.2.1 50\_1-5\_A Specimens**

50\_1-5\_A specimens were fabricated from Plate J. Two 50\_1-5\_A axial test specimens were fabricated by H&R Industrial. Plate J material was donated by Nucor Corporation. All 50\_1-5\_A Specimens were 1.5 in. thick by 22 in. wide. Fracture testing was performed at room temperature, as established by CVN impact testing. Room temperature of the laboratory during the 50\_1-5\_A Specimen test was approximately 60 °F.

#### **3.9.2.1.1 Specimen 50\_1-5\_1A**

Specimen 50\_1-5\_1A was initially loaded with no notch. The test was performed to a load equal to 75% of nominal yield. An initial test with no notch was performed to verify the functionality of the load frame. Further, measurements were taken to establish if any adjustments were required to remove any bending in the specimen. The initial test indicated minimal bending was present; as such, fracture experimentation ensued.

An initial v-notch was cut into Specimen 50\_1-5\_1A. The notch had a through-thickness length of 1.125 in. at which point a v-notch tapered to a final surface length of 2.0 in. An unsuccessful fracture attempt was performed at a fatigue crack length of 2.5 in. After the initial attempt, the fatigue crack was grown to 4.875 in. for a second fracture attempt. Fracture occurred at a load of 859.1 kips. The resulting stress was 26.0 ksi. A general photograph of Specimen 50\_1-5\_1A taken after fracture can be found in Figure 3.51. Figure 3.52 is a photograph of the fracture surface from Specimen 50\_1-5\_1A.

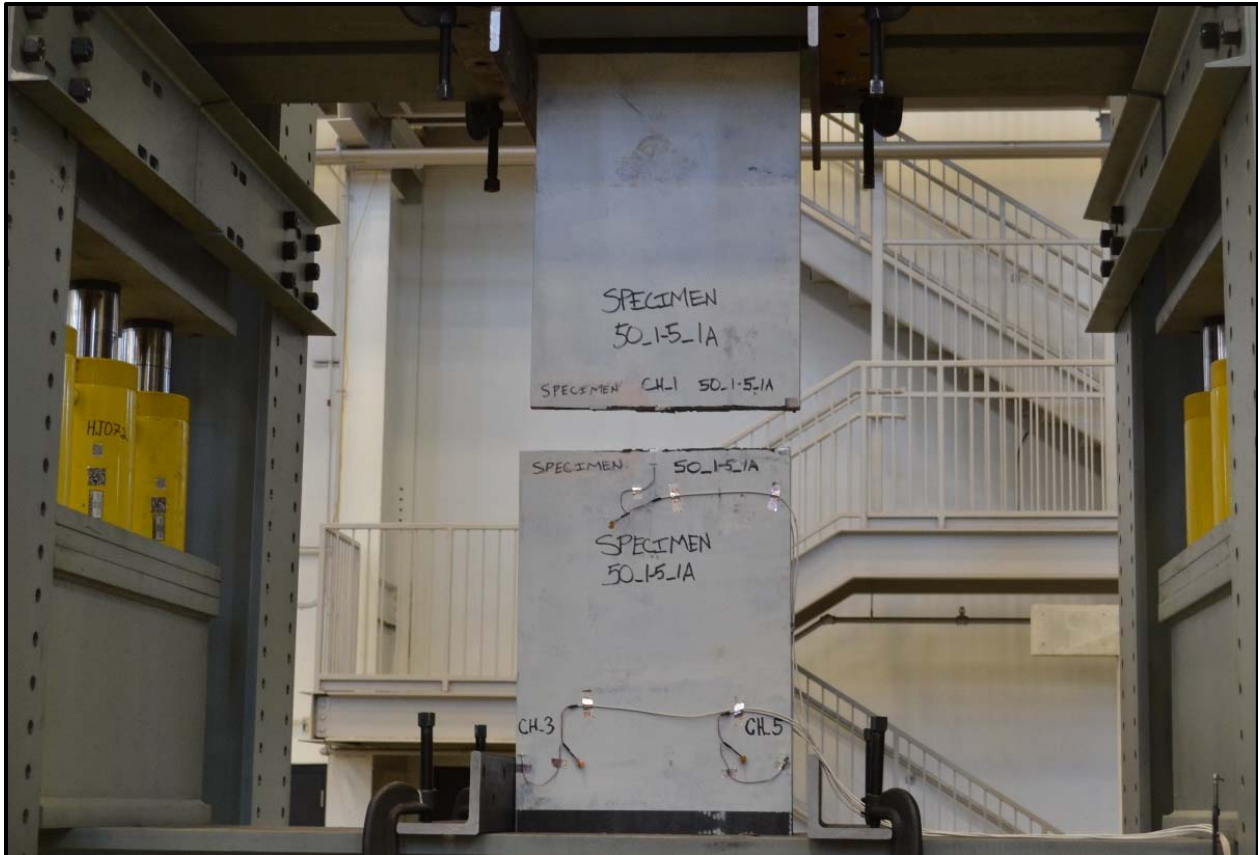


**Figure 3.51: Specimen 50\_1-5\_1A**



**Figure 3.52: Specimen 50\_1-5\_1A fracture surface**

#### 3.9.2.1.2 Specimen 50\_1-5\_2A

Specimen 50\_1-5\_2A was initially notched identical to Specimen 50\_1-5\_1A. The notch had a through-thickness depth of 1.125 in. and a v-notch tapered to a surface length of 2.0 in. At a fatigue crack length of 3.0 in., Specimen 50\_1-5\_2A was loaded resulting in no fracture. The specimen was removed from the fracture frame to grow the crack further. After difficulty growing through the plastic zone created during the initial fracture test, a grinder was used to notch the

specimen. The notch was extended with the grinder to a length of 6.5 in. A fatigue crack was grown to a final length of 6.9375 in. for the second fracture attempt. Fracture occurred at a load of 728.3 kips. The resulting stress was 22.1 ksi. A general photograph of Specimen 50\_1-5\_2A taken after fracture can be found in Figure 3.53. Figure 3.54 is a photograph of the fracture surface from Specimen 50\_1-5\_2A.



**Figure 3.53: Specimen 50\_1-5\_2A**



**Figure 3.54: Specimen 50\_1-5\_2A fracture surface**

### **3.9.2.2 50\_2-5\_A Specimen**

The 50\_2-5\_A specimen was fabricated from Plate E. A single 50\_1-5\_A axial test specimen was fabricated by H&R Industrial. The 50\_2-5\_A Specimen was 2.5 in. thick by 14 in. wide. Fracture testing was performed at -35 °F, as established by CVN impact testing.

### 3.9.2.2.1 Specimen 50\_2-5\_1A

An initial v-notch with a trapezoidal front was cut into Specimen 50\_2-5\_1A. The notch had a through-thickness length of 1.125 in. The trapezoidal front tapered to a final surface length of 3.875 in. The final fatigue crack for Specimen 50\_2-5\_1A was grown to 4.9375 in. and fracture occurred at a load of 581.7 kips. The resulting stress was 16.6 ksi. A general photograph of Specimen 50\_2-5\_1A taken after fracture can be found in Figure 3.55. Figure 3.56 is a photograph of the fracture surface from Specimen 50\_2-5\_1A.



Figure 3.55: Specimen 50\_2-5\_1A



**Figure 3.56: Specimen 50\_2-5\_1A fracture surface**

### **3.9.2.3 70\_1-5\_A Specimens**

70\_1-5\_A Specimens were fabricated from Plate H. Two 70\_1-5\_A axial test specimens were fabricated by H&R Industrial. Plate H material was donated by High Steel Structures. All 70\_1-5\_A Specimens were 1.5 in. thick by 18 in. wide. Fracture testing was performed at -30 °F, as established by CVN impact testing.

#### **3.9.2.3.1 Specimen 70\_1-5\_1A**

An initial v-notch was cut into Specimen 70\_1-5\_1A. The notch had a through-thickness length of 2.5 in. and a v-notch tapered to a surface length of 3.25 in. The fatigue crack for Specimen 70\_1-5\_1A was grown to 6.0 in. Fracture occurred at a load of 424.4 kips. The resulting stress was 15.7 ksi. A general photograph of Specimen 70\_1-5\_1A taken after fracture can be found in Figure 3.57. Figure 3.58 is a photograph of the fracture surface from Specimen 70\_1-5\_1A.



**Figure 3.57: Specimen 70\_1-5\_1A**



**Figure 3.58: Specimen 70\_1-5\_1A fracture surface**

**3.9.2.3.2 Specimen 70\_1-5\_2A**

An initial v-notch was cut into Specimen 70\_1-5\_2A. The notch had a through-thickness length of 2.5 in. and the v-notch tapered to a surface length of 3.5 in. The fatigue crack for

Specimen 70\_1-5\_2A was grown to 4.625 in. Fracture occurred at a load of 871.0 kips with a resulting stress of 32.3 ksi. A general photograph of Specimen 70\_1-5\_2A taken after fracture can be found in Figure 3.59. Figure 3.60 is a photograph of the fracture surface from Specimen 70\_1-5\_2A.



Figure 3.59: Specimen 70\_1-5\_2A



Figure 3.60: Specimen 70\_1-5\_2A fracture surface

### **3.10 Experimental Results**

The experimental test program was comprised of small-scale material testing as well as large-scale fracture testing. Small-scale testing for material characterization included tensile testing, chemical analysis, CVN impact testing, percent shear measurement, reference temperature determination, and measurement of fracture toughness. Each test type was performed in accordance with the applicable ASTM Specification. Large-scale experiments of both bending and axial members was conducted. The following sections contain the results from each test performed as part of the experimental testing program.

#### **3.10.1 Material Test Results**

Material characterization was performed for each heat of steel used for large-scale experimentation. Results for tensile testing, chemical analysis, CVN impact testing, percent shear measurement, reference temperature determination, and measurement of fracture toughness are detailed in the following sections. Preliminary screening results from the additional heats obtained during initial material screening were not included in the following discussion.

##### ***3.10.1.1 Tensile Test Results***

Tensile testing was performed by Westmoreland Mechanical Testing and Research Inc. in accordance to ASTM E8-15a for all large-scale test material. Ultimate tensile strength, yield strength, modulus, percent elongation, percent reduction in area, and ultimate load were reported. All plates satisfied the tensile requirements of ASTM A709. Table 3.4 is a summary of the test results. Figure 3.61 is a plot of the resulting stress-strain curves for each plate. The stress-strain data were used as input for the finite element analysis (FEA) and will be discussed in Chapter 4 during model construction.

Table 3.4: Large-scale tensile test results

Plate	Ultimate Tensile Strength (ksi)	Yield Strength (ksi)	Elongation (%)	Reduction in Area (%)	Modulus (ksi)	Ultimate Load (kip)
E	80.9	57.9	31	77	32,200	15.8
H	92.2	76.8	28	76	31,200	18.1
I	81.3	53.5	30	74	34,000	16.0
J	78.7	50.9	30	71	30,100	15.4

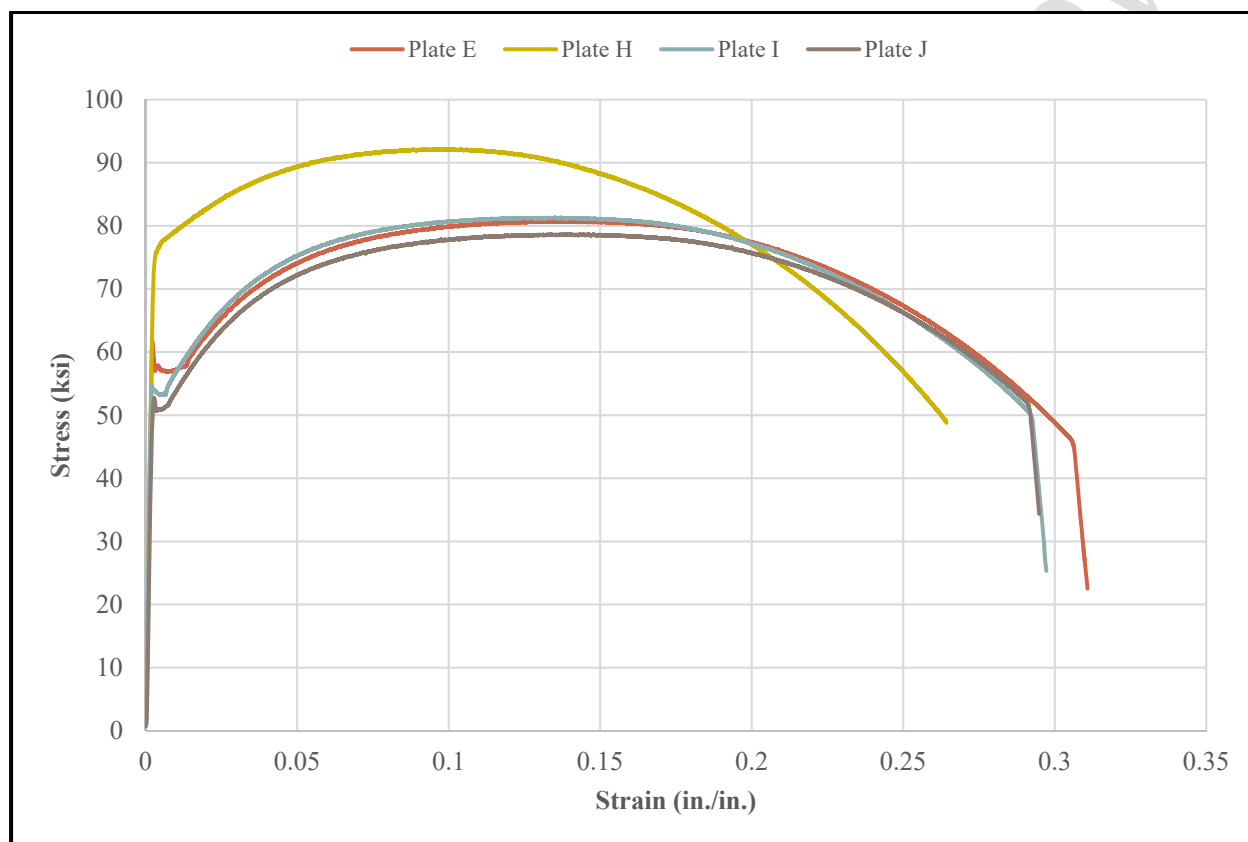


Figure 3.61: Large-scale tensile stress-strain curve

### 3.10.1.2 Chemical Analysis Results

A chemical analysis was performed for all plates used for the large-scale test program. All analyses were performed in accordance with ASTM E1019 or ASTM E415. The chemical analyses of Plates E, H, and I were conducted by Chicago Spectro Service Laboratory Inc. and by Laboratory Testing Inc. for Plate J. Results for the chemical analysis are presented in Table 3.5. A dash (-) was used to indicate any element not reported for a given plate. Interestingly, all plates

satisfied the chemistry requirements of ASTM A709-13a for the Mill Test Reports; however, the independent testing indicated some trace elements did not satisfy the ASTM requirements (ASTM, 2013a).

**Table 3.5: Chemical analysis results**

Element		Plate E (%)	Plate H (%)	Plate I (%)	Plate J (%)
Al	Aluminum	0.02	0.02	0.02	0.029
As	Arsenic	-	-	-	0.005
B	Boron	-	-	0.0005	0.002
C	Carbon	0.13	0.2	0.13	0.15
Co	Cobalt	-	-	-	0.002
Cr	Chromium	0.51	0.41	0.51	0.093
Cu	Copper	0.33	0.24	0.31	0.36
Mn	Manganese	1.34	1.19	1.34	1.15
Mo	Molybdenum	0.02	0.05	0.03	0.067
Nb	Niobium	-	-	0.005	< 0.001
Ni	Nickel	0.24	0.25	0.22	0.082
P	Phosphorous	0.01	0.013	0.013	0.009
S	Sulfur	< 0.005	0.011	< 0.005	0.007
Sb	Antimony	-	-	-	0.003
Si	Silicon	0.31	0.45	0.33	0.21
Sn	Tin	-	-	-	0.007
Ti	Titanium	0.01	< 0.005	< 0.005	0.001
V	Vanadium	0.06	0.04	0.06	0.044

### **3.10.1.3 Impact Testing Results**

Charpy v-notch impact testing was used to initially screen material for the large-scale experimentation program. Additional CVN impact testing was performed on the four plates used for large-scale testing. In total, 276 CVN impact specimens were tested at temperatures ranging from -120 °F to 205 °F. All testing was performed in accordance to ASTM E23-12c (ASTM, 2012b).

A five parameter sigmoidal function was fit to all preliminary data using the software SigmaPlot. The sigmoidal fit was used to identify plates suitable for large-scale testing. Additionally, the sigmoidal fit was used to identify the large-scale test temperature. The fit temperature corresponding to 125 ft.-lbs. was used for the large-scale experiments.

At the completion of large-scale testing, additional CVN impact specimens were prepared from each test plate. The additional specimens were used to evaluate the CVN impact variability throughout the test specimens. All five parameter sigmoidal fits were updated to include all tested CVN impact specimens for a given plate. The CVN impact results for all tested plates, including the raw data as well as the plots and five parameter sigmoidal fits, can be found in Appendix F. Figure 3.62 depicts a representative plot of CVN impact data for Plate J with the five parameter sigmoidal fit.

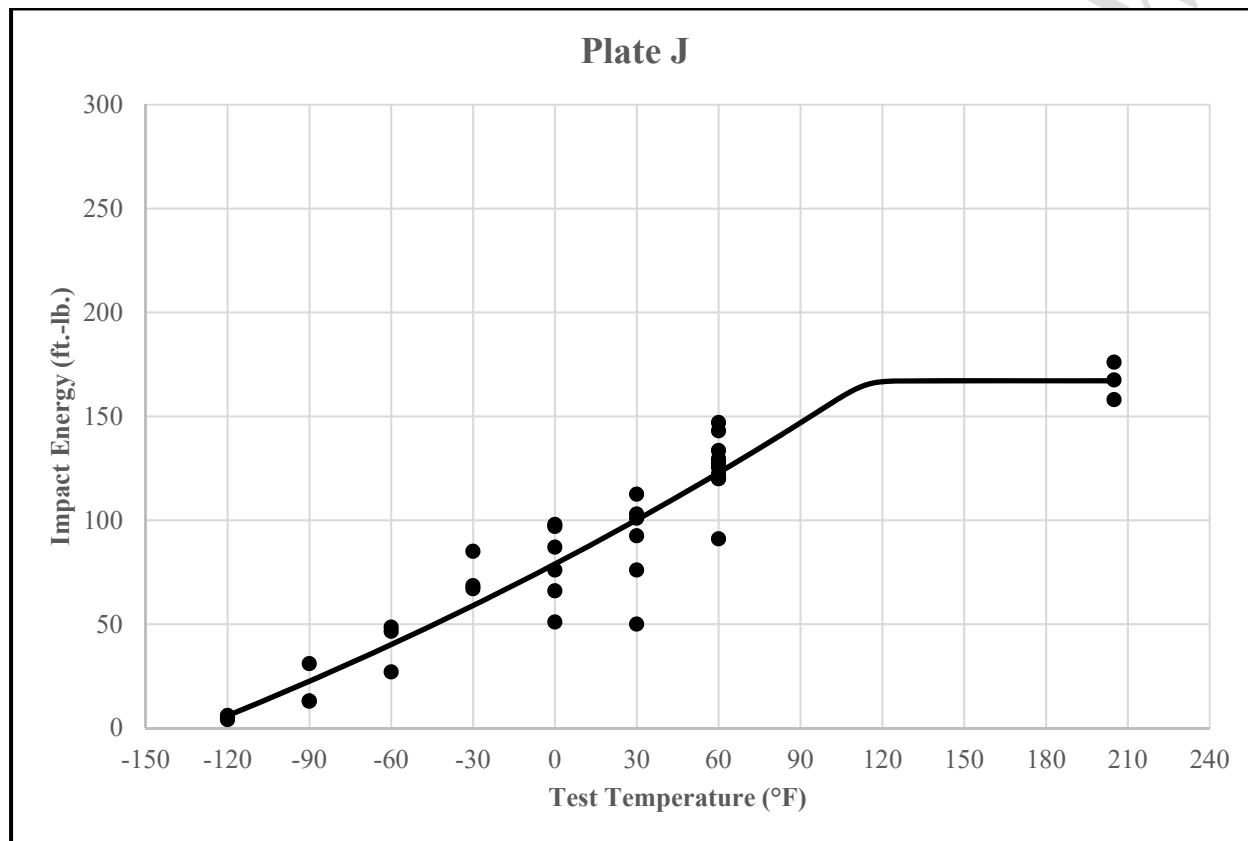


**Figure 3.62: Representative CVN impact data with sigmoidal fit**

CVN variability and scatter were evaluated for Plates E and H. To examine variability within a given plate, six CVN impact specimens were removed from each end of an axial test specimen. All impact specimens for a given plate were tested at the temperature of the large-scale experiment: -30 °F and -35 °F for Plates E and H, respectively. Results for both plates demonstrated minimal variability within the given plate. However, large scatter was observed for Plate E. Impact energies for Plate E ranged from 8.5 ft.-lbs. to 175 ft.-lbs. at a test temperature of -30 °F with an average CVN impact energy of 97.4 ft.-lbs. and a standard deviation of 42.7 ft.-lbs.

Conversely, Plate H CVN impact results ranged from 90 ft.-lbs. to 198 ft.-lbs. with an average impact energy of 121 ft.-lbs. and a standard deviation of 19.6 ft.-lbs. at a test temperature of -35 °F. A possible explanation for the reduced scatter for Plate H was the processing used for the HPS plate; specifically, Plate H was HPS 70W and underwent a quench and tempering process. Plate E was not processed and was provided in the as-rolled. All raw data included in the variability and scatter evaluation can be found in Appendix F along with the rest of the raw CVN impact data.

#### ***3.10.1.4 Percent Shear Results***

Percent shear was visually estimated for all but six CVN impact specimens. The six specimens for which percent shear was not measured were impact tested at a commercial laboratory and not returned after testing. Guidance provided in ASTM E23-12c Annex A4 was used to estimate percent shear values; specifically, specimens were compared to Figure A4.2b of Annex A4 (ASTM, 2012b). Figure 3.2 plots the percent shear value against the impact energy.

Several observations were made during the evaluation of the percent shear versus CVN impact energy data. The minimum CVN impact energy with 100% shear was 158 ft.-lbs. Percent shear values for a CVN impact energy value of 125 ft.-lbs. ranged from 40% to 90%. Overall, the data shows a general correlation between percent shear and impact energy. At any given percent shear, typical variation in impact energy was approximately 50 ft.-lbs. Scatter in the impact energy data increases as percent shear increases. Raw percent shear data can be found in Appendix F along with the raw CVN impact data.

#### ***3.10.1.5 Reference Temperature Determination Testing***

Reference temperature determination testing was performed in accordance to ASTM E1921-13a (ASTM, 2013b). A total of 39 Charpy-sized SE(B) specimens were tested for the four plates used during large-scale experimentation. Test temperatures ranged from -103 °F to -292 °F. Extremely low temperatures were required to ensure brittle, cleavage-type behavior. The calculated reference temperatures are presented in Table 3.6.

**Table 3.6: Reference temperature results**

Plate	Reference Temperature ( $T_0$ )	
	(°C)	(°F)
E	-128.9	-200.0
H	-169.4	-272.9
I	-154.1	-245.4
J	-169.1	-272.4

The reference temperature anchors the exponential master curve and corresponds to the temperature resulting in  $100 \text{ MPa}\sqrt{\text{m}}$ . A minimum of six to eight valid test specimens were required to obtain a valid reference temperature. A weighting factor of  $1/6$ ,  $1/7$ , or  $1/8$  was assigned to each valid test specimen. The exact weighting factor depends on the difference between the specimen test temperature and the provisional reference temperature. To be considered a valid reference temperature, the sum of the weighting factors needed to be greater than 1.0. Data analysis for all specimens from each plate can be found in Appendix G. Representative plots of a master curve and an uncensored master curve for Plate I can be found in Figure 3.63 and Figure 3.64, respectively. The difference between the two plots was the censoring procedure used for data violating one of the validity limits. Both plots also include the 5% and 95% tolerance bounds. Master curve plots for all large-scale test specimen plates can be found in Appendix G with the master curve data analysis.

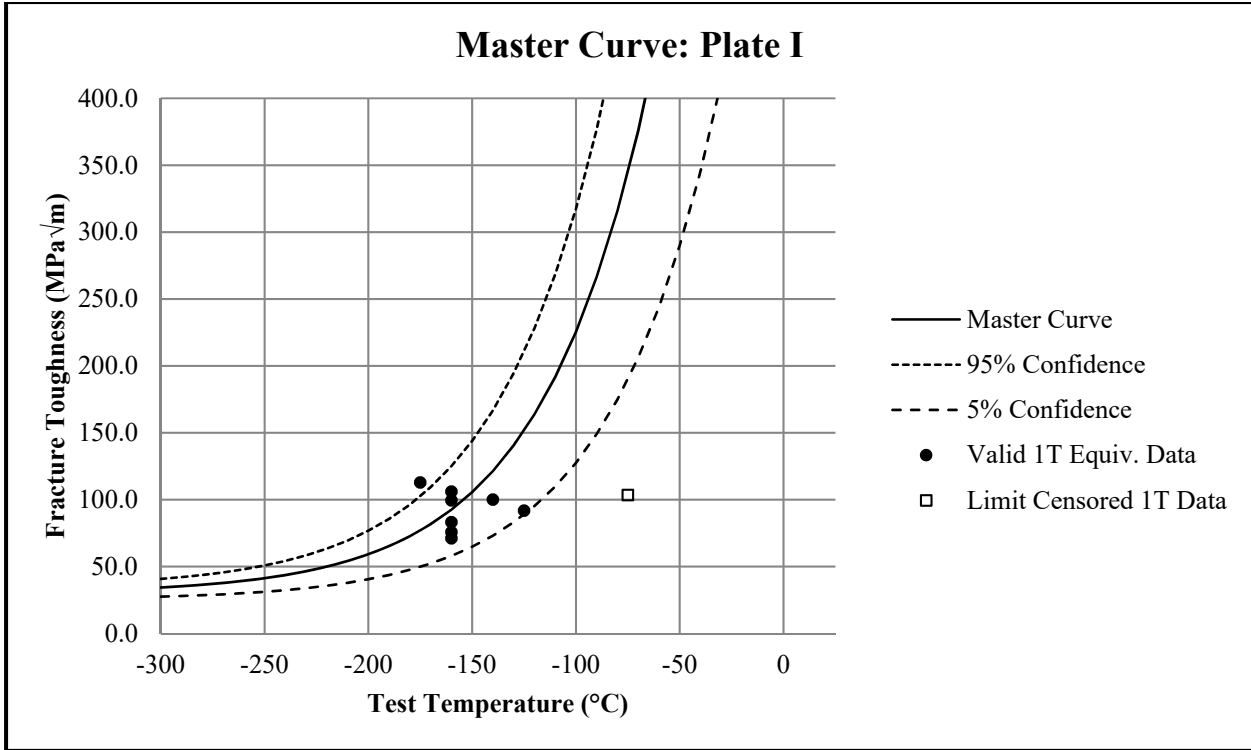


Figure 3.63: Representative master curve

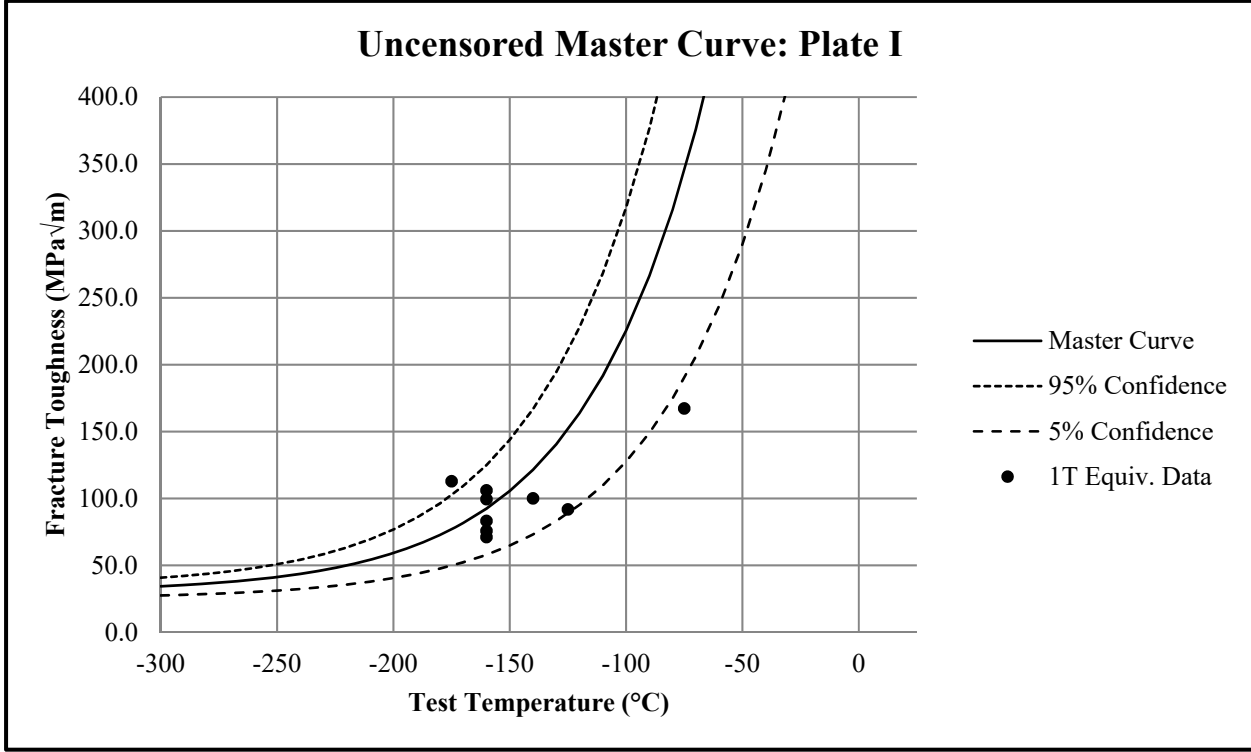


Figure 3.64: Representative uncensored master curve

### 3.10.1.6 Fracture Toughness Measurement

Fracture toughness testing was performed in accordance to ASTM E1820-15a (ASTM, 2015a). Two SE(B) specimens were tested for each of the four plates used during the large-scale experimentation. Fracture toughness testing was performed at the same test temperatures as the large-scale bending and axial experiments. The test temperatures ranged from -60 °F to 60 °F. Fracture toughness results are presented in Table 3.7. No size correction was applied to the SE(B) specimens because their nominal thickness was 1.0 in. or 1T.

**Table 3.7: Fracture toughness results**

Specimen	Temperature	K <sub>Jc</sub>
	(°F)	(ksi√in.)
EJ1	-30	145.8
EJ2	-30	234.9
HJ1	-35	303.8*
HJ2	-35	281.1
IJ1	-60	58.3
IJ2	-60	160.3
JJ1	60	248.3
JJ2	60	297.9

\*Did not satisfy ASTM E1820-15a crack front straightness requirement.

Specimens from Plates E, H, and J satisfied the 125 ft.-lb. requirement; whereas, specimens from Plate I narrowly satisfied the current AASHTO Zone III fracture critical requirements. The average fracture toughness for the 125 ft.-lb. specimens was 252.0 ksi√in. with a standard deviation of 58.7 ksi√in. It should also be noted, fracture toughness specimen HJ1 was marked with an asterisks because it did not satisfy the crack front straightness requirements detailed in ASTM E1820-15a.

The fracture toughness testing procedure was conducted to evaluate the toughness near the onset of stable crack extension ( $J_{Ic}$ ). Periodic unloads were performed during the test process to develop a resistance curve. Compliance was used to measure the crack size while testing and verified optically after the test. ASTM E1820-15a details the requirements to obtain a valid  $J_{Ic}$  from the resistance curve (ASTM, 2015a). A representative resistance curve for Specimen HJ2 is shown in Figure 3.65. The ASTM requirements for the construction of the resistance curve

required the use of metric units; thus the data below are presented in metric units. None of the specimens achieved a valid  $J_{IC}$  value because all tests resulted in brittle fracture as opposed to stable ductile tearing at the temperature of each test; therefore, the remaining resistance curves were not included. Additionally, the plot shown in Figure 3.65 omits several construction limits and a power law regression line because the data did not result in a valid  $J_{IC}$ . An example of a fully constructed plot can be found in ASTM E1820-15a.

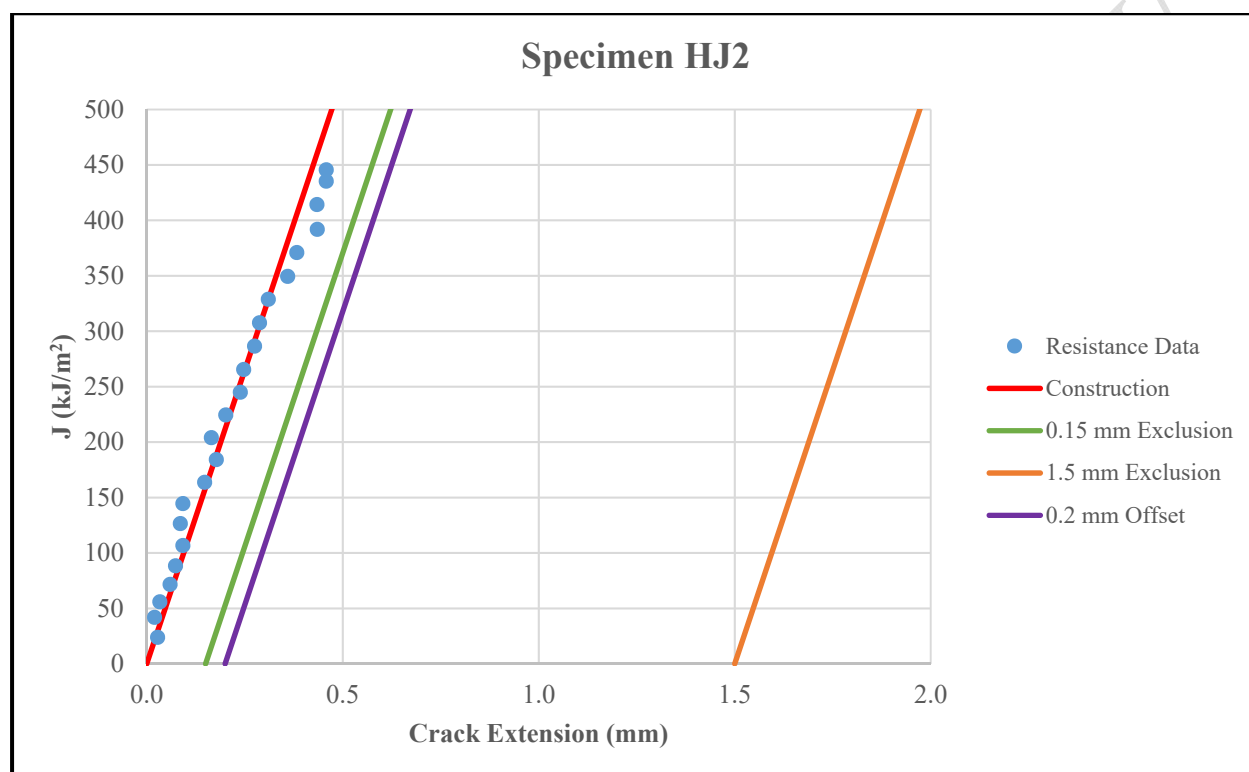


**Figure 3.65: Representative resistance curve**

It should also be noted, the  $K_{Jc}$  results from the full-sized SE(B) specimens were plotted on the master curves developed from the Charpy-sized SE(B) specimens. Results for the full-scale SE(B) specimens generally fell below the 95% tolerance bound of the master curves. It is believed the Charpy-sized SE(B) specimens do not provide enough crack tip constraint for high-toughness steel.

### 3.10.2 Large-scale Test Results

Large-scale fracture testing was performed on bending and axial members. The bending members were welded plate girders and the axial members were plain plates cut in the shape of a typical tensile specimen. All specimens were notched with an angle grinder and cycled in fatigue to initiate a crack from the saw cut as previously discussed. The specimens were cooled to a temperature corresponding to 125 ft.-lbs. A load producing a stress of  $0.75F_y$  on the gross, uncracked section was applied. If no fracture occurred the crack was extended further via fatigue. Once a specimen fractured, the final crack length and peak load were recorded. The crack length and load at failure were used as input for the FEA of the large-scale test specimens. Results for the bending and axial test specimens are discussed in the following sections.

#### 3.10.2.1 Bending Test Results

In total, six large-scale bending experiments were conducted on three heats of steel. Two of the three steel heats, Plates E and H, satisfied the 125 ft.-lb. requirement. The third heat, Plate I, was the closest material tested to the current Zone III fracture critical requirement. Therefore, Plate I served as a model for the current specification and was compared against the specification proposed by the current research for high-toughness steel. However, it should be noted, while some CVN impact specimens from Plate I were close to the current specification others were much greater, potentially resulting in larger crack lengths than a material just meeting the current specification. Testing was performed at temperatures ranging from  $-60\text{ }^{\circ}\text{F}$  to  $-30\text{ }^{\circ}\text{F}$ , as established by the initial CVN testing.

Table 3.8 contains the results for the large-scale bending experiments. Final crack length, fracture load, fracture stress, and deflection are reported. The final crack length was the average fatigue crack length measured after the fracture surface was removed from the specimen. Values are reported to the nearest sixteenth of an inch. The fracture load was the average load at fracture from the two actuators. Based on the measured fracture load, a fracture stress was tabulated using fundamental equations from mechanics of materials. The fracture stress was defined as the gross section stress due to the applied fracture load. Stress from the strain gage data were not reported in Table 3.8 because of the impacts of the crack tip and out-of-plane bending. The deflection was defined as the average measurement from the string potentiometers located on the bottom on the

beam directly below each actuator at the instant prior to fracture. All measured values were taken from the last measurement just before fracture was recorded.

**Table 3.8: Bending test results**

Plate	Specimen	Final Crack	Fracture Load	Fracture Stress	Deflection
		(in.)	(kip)	(ksi)	(in.)
E	50_2-5_1B	5.0	104.6	18.7	0.96
	50_2-5_2B	4.375	163.3	29.2	1.52
H	70_1-5_1B	5.0625	160.4	40.4	2.52
	70_1-5_2B	7.5	164.6	41.5	2.66
I	50_2-0_1B	1.6875	149.2	26.3	1.09
	50_2-0_2B	1.0625	128.6	22.6	0.94

Results for each plate cannot be directly compared because the testing protocol changed. During the experimental test phase, the fracture test process was changed from incrementally growing the fatigue crack and attempting multiple fracture attempts to growing directly to a length with a high probability of fracture. As such, some of the specimens presented in Table 3.8 would be expected to tolerate shorter crack lengths at a stress state of  $0.75F_y$ . Therefore, the data presented in Table 3.8 was used as input for FEA. The fracture toughness demand for a given crack length and fracture load was extracted from the FEA and used to compare specimen performance. Results from finite element modeling is discussed in Chapter 4.

### 3.10.2.2 Axial Test Results

In total, five large-scale axial experiments were conducted on three heats of steel, including Plates E, H, and J. Each heat satisfied the 125 ft.-lb. requirement. Testing was performed at temperatures ranging from  $-35\text{ }^{\circ}\text{F}$  to  $60\text{ }^{\circ}\text{F}$ , as established by the initial CVN testing.

Results from the large-scale axial experiments are presented in Table 3.9. Final crack length, fracture load, and fracture stress were presented. Deflection was not measured for the large-scale axial experiments. The final crack length was defined as the average fatigue crack length measured after the fracture surface was removed from the specimen. Values in the table are reported to the nearest sixteenth of an inch. The fracture load was defined as the total load from all six Enerpac cylinders taken from the final complete measurement before fracture.

Typically, fracture could be identified by the loss of center two strain gages. Based on the measured fracture load, a fracture stress was tabulated using fundamental mechanics of materials. The fracture stress was defined as the nominal gross section stress at the time of fracture.

**Table 3.9: Axial test results**

Plate	Specimen	Final Crack	Fracture Load	Fracture Stress
		(in.)	(kip)	(ksi)
E	50_2-5_1A	4.9375	581.7	16.6
H	70_1-5_1A	6.0	424.4	15.7
	70_1-5_2A	4.625	871.0	32.3
J	50_1-5_1A	4.875	859.1	26.0
	50_1-5_2A	6.9375	728.3	22.1

Results presented in Table 3.9 cannot be directly compared due to the change in test procedure. Rather, the final crack length and fracture stress were used as input for the FEA. The fracture toughness demands as calculated using FEA are presented in the discussion of the large-scale specimen FEA. Found in Chapter 4, the fracture toughness demands can be used to compare the performance of the specimens.

## CHAPTER 4 ANALYTICAL RESEARCH PROGRAM

Finite element analysis was performed to calculate the fracture toughness demand of various cracked geometries. Benchmarking of the FEA was initially performed on geometries with linear-elastic fracture mechanics handbook solutions. After achieving excellent agreement between the closed-form LEFM solutions and the FEA, elastic-plastic FEA analysis was performed. A NASA round robin study was used to benchmark the elastic-plastic analyses (Wells & Allen, 2012). Recommendations for performing elastic-plastic fracture mechanics from the NASA round robin were also used to model the large-scale test specimens. Finite element models of the test specimens were further validated using the experimental test data. The elastic-plastic fracture toughness demand was extracted from the large-scale models. Once a reliable approach to the modeling was established, it was used to perform a parametric study to extrapolate the test specimen behavior to an array of girder geometries. All analytical work was performed using Abaqus CAE version 6.13-1 produced by Dassault Systemes. This chapter describes the benchmarking studies, large-scale specimen FEA, and the parametric study.

### **4.1 Finite Element Benchmarking Studies**

Benchmarking studies were performed to ensure the analytical studies accurately calculated and represented the fracture parameters of the experiments. Linear-elastic benchmark studies were initially performed to compare FEA techniques to closed-form handbook solutions for an array of typical geometries. Elastic-plastic benchmarking studies were performed to compare FEA techniques to a NASA round robin study. Initial studies were also performed to ensure the methods used to model the full-scale bending specimens resulted in accurate results for the constant moment region created by the four-point bending.

### 4.1.1 Linear-Elastic Fracture Mechanics

Benchmarking of the FEA LEM models consisted of creating finite element models of common crack geometries and comparing the results to closed-form stress intensity handbook solutions. The geometries included a center crack, single-edge crack, double-edge crack, single-cracked hole, and double-cracked hole. In each case, the stress intensity factor was extracted from the simulation output file.

All models created for the linear-elastic benchmarking studies were three dimensional solids. No degeneracy was used at the crack tip and all elements were fully integrated (C3D20). Load was applied through a pressure on one end of the model, while an encastre boundary condition was on the opposite end of the model.

A comparison of the FEA output to the handbook solutions can be found in Table 4.1. The FEA output provided a stress intensity value for every node across the crack front; therefore, the average, maximum, and minimum values were extracted. Conversely, a single handbook value was reported because the solutions were formulated from curve-fit solutions. All handbook formulas were taken from *Fundamentals of Structural Integrity* (Grandt, 2004).

**Table 4.1: Linear-elastic benchmarking summary**

<b>Solution</b>	<b>Center Crack (ksi√in.)</b>	<b>Single-Edge Crack (ksi√in.)</b>	<b>Double-Edge Crack (ksi√in.)</b>	<b>Single-Cracked Hole (ksi√in.)</b>	<b>Double-Cracked Hole (ksi√in.)</b>
FEA (maximum)	26.4	30.9	30.7	22.3	30.0
FEA (average)	25.3	29.7	29.5	21.8	27.4
FEA (minimum)	21.8	25.7	25.6	21.4	25.4
Handbook Solution	25.2	29.7	28.1	20.4	25.0

Initial linear-elastic benchmarking studies indicated the finite element modeling practices provided reasonable results. The average stress intensity for the center crack, single-edge crack, and double-edge crack geometries were within 5% of the handbook solutions. Results for the single-cracked and double-cracked hole geometries were within 10% of the handbook solutions; however, the closed-form handbook solutions for the cracked hole geometries were based on an

infinitely wide body. While excellent results were obtained during the initial linear-elastic benchmarking study, later work revealed better modeling practices. Specifically, the NASA round robin study, previously described, was employed for elastic-plastic fracture mechanics.

#### 4.1.2 Elastic-Plastic Fracture Mechanics

The stress intensity factor is an important parameter for linear-elastic fracture mechanics; however, the high-toughness steels used for the current research were highly ductile. As such, elastic-plastic fracture parameters, such as the  $j$ -integral, were required to appropriately describe the material behavior. Handbook solutions were sparse for elastic-plastic benchmarking studies. Further, the limited solutions available were typically for either pure plane stress or pure plane strain. General Electric released an approach utilizing graphical methods in the early 1980's (Kumar, German, & Shih, 1981). Solutions were based on FEA, which is the current standard for elastic-plastic fracture mechanics.

As noted during the literature review, a round robin study was performed by NASA for ASTM E2899: Standard Test Method for Measurement of Initiation Toughness in Surface Cracks under Tension and Bending. The NASA round robin study was used for the elastic-plastic benchmarking efforts (Wells & Allen, 2012). To validate the modeling techniques used to capture the  $j$ -integral, an analysis was performed for the round robin geometry and material input. The problem statement included the geometry of the surface-cracked plate as well as the elastic material properties and stress-strain data for the ductile aluminum alloy. The  $j$ -integral was evaluated at the prescribed critical angle from the problem statement of 17 degrees for three different load levels as well as for a CMOD of 0.15 mm. Results from the round robin final report were compared to the results attained from the FEA. As shown in Table 4.2, agreement was found with the current industry standard.

All models were created using a quarter symmetry scheme, which was implemented through the use of boundary conditions. Material stress-strain data were provided in the problem statement. For the elastic properties, the problem statement required the use a modulus of elasticity of 10,800 ksi and a Poisson's ratio of 0.33. Using the provided stress-strain data, the plastic material properties were implemented using table look-up. At the crack tip, the elements were collapsed with duplicate nodes and a 0.5 mid-side node parameter. Eight contours were used for

the j-integral calculation with the outermost contour used as the value reported in Table 4.2. All plates were modeled as solid, continuum elements (C3D20R). Quadratic elements were used to capture the crack tip singularity. Reduced integration was used to minimize shear locking, as well as to ensure the stiffness was not over predicted. The domain integral method was used to calculate the j-integral.

**Table 4.2: Elastic-plastic benchmarking summary**

Assessment Condition	J-Integral at $\phi = 17^\circ$ (kJ/m <sup>2</sup> )			CMOD
	200 kN	252 kN	289 kN	0.15 mm
Round Robin (maximum)	10.1	18.4	34.6	32.5
Round Robin (average)	9.6	17.0	29.7	30.3
Round Robin (minimum)	8.7	14.9	24.7	26.2
Benchmarking Results	9.9	17.8	32.7	30.3

#### 4.1.3 Through-Thickness Mesh Density

A through-thickness mesh density study was conducted for the thinnest and thickest specimens used in the current study. The study established the largest size element resulting in an accurate calculation of the j-integral demand to maximize computational efficiency. Finite element models were created for Plates E and H. The Plate E model was 2.5 in. thick by 14 in. wide while, the Plate H model was 1.5 in. thick by 18 in. wide. The models utilized symmetry about the crack plane enforced using boundary conditions. Each model had a length equal to twice the plate width. A crack length to plate width ratio of approximately 20% was used for both models. Resulting edge crack lengths were 2.75 in. and 3.5 in. for Plate E and H, respectively. Full stress-strain curves obtained from testing were used for both material models. Elastic-plastic models utilized quadratic continuum three dimensional elements with reduced integration; specifically, C3D20R elements. Load was applied through a surface traction on the face opposite of the crack.

The through-thickness element size varied from 0.03125 in. to 0.125 in. J-integral demand was calculated at 10 load increments for eight contours around the crack tip. The results for both plates at the final load increment for the eighth contour are plotted in Figure 4.1. A negligible

difference in peak j-integral demand was found by increasing the through-thickness mesh density. Therefore, all models were created having 0.125 in. elements through the thickness.

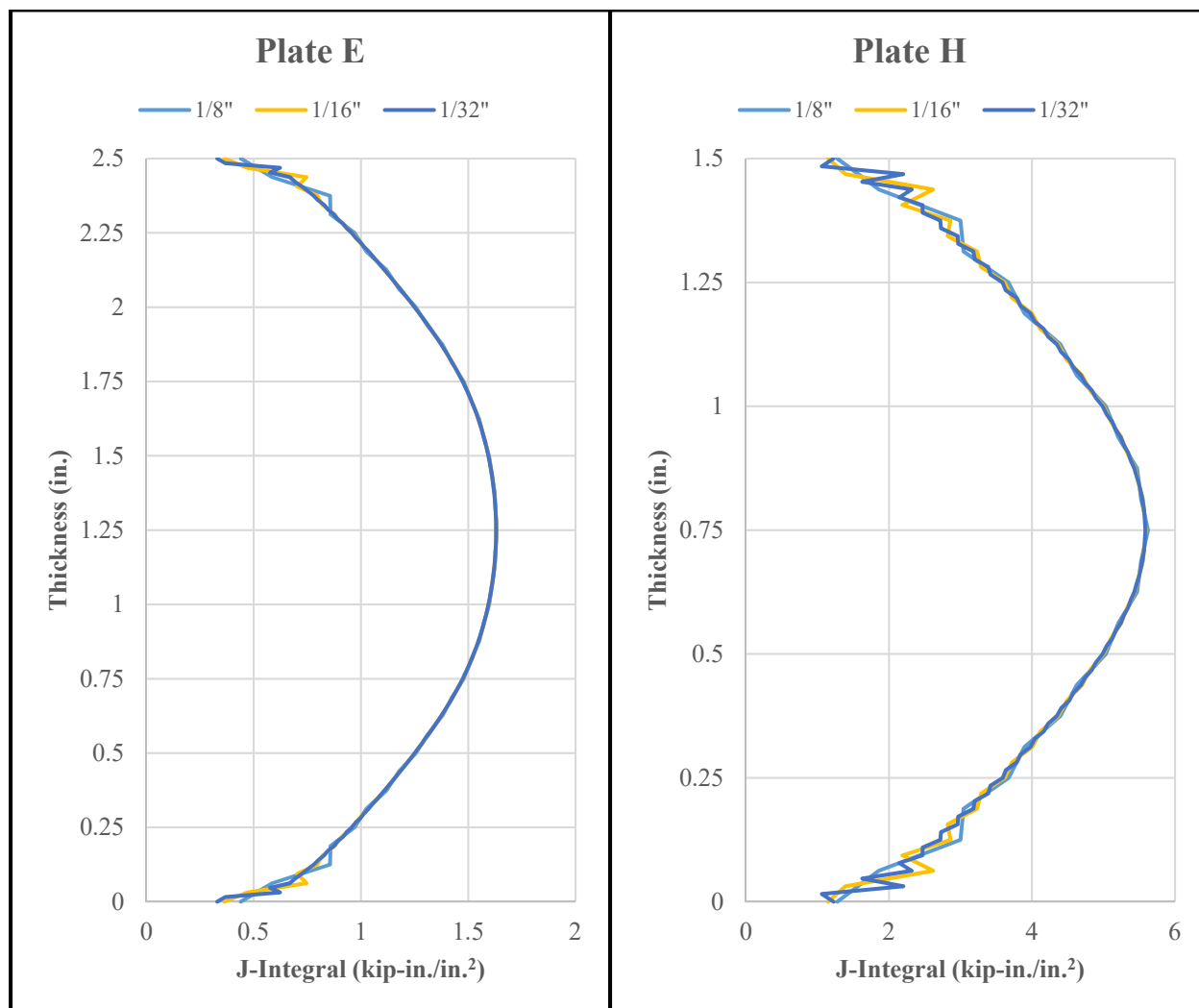


**Figure 4.1: Through-thickness mesh density for Plate E (left) and Plate H (right)**

## **4.2 Large-scale Test Specimen Finite Element Models**

Finite element models were created for each of the 11 large-scale test specimens. The models were used to compute the j-integral demand at failure. The following sections summarize the model development, validation, and results. Using the FEA results, a comparison was made between the performance of the high-toughness specimens and the current specification specimens.

## 4.2.1 Large-scale Test Specimen Model Development

Abaqus/Standard CAE was used to model the large-scale test specimens. The finite element models were used to establish the j-integral demand at the time of fracture. As such, the fatigue crack length and load at fracture were used as input for the models. All models were constructed using the suggested practices from the NASA round robin study (Wells & Allen, 2012). General model development shared between all large-scale models will be summarized in the following section, while specifics to the bending and axial specimens will be described in individual sections.

### 4.2.1.1 General Model Development

Each specimen consisted of three dimensional deformable solid elements. Material properties for each plate were obtained from tensile test results. Identical elastic material properties were used for all specimens: modulus of elasticity of 29,000 ksi and Poisson's ratio of 0.29. Plastic material properties were input through table look-up. The plastic material input for each plate can be found in Appendix E.

A ramp loading with a minimum of 20 increments was used for each analysis. Depending on the analysis type, either the j-integral or stress intensity factor could be extracted at each increment. Two analyses were performed for each specimen: linear-elastic and elastic-plastic. The linear-elastic analyses provided the crack demand in terms of stress intensity while an elastic-plastic analysis provided the crack demand in terms of j-integral.

The singularity at the crack tip was modeled using collapsed elements. Duplicate nodes were used at the crack tip for all analyses. Additionally, the mid-side node for each parameter was left at the mid-point. The creation of the crack as well as the exact crack tip geometry will be discussed under each specimen type.

### 4.2.1.2 Bending Test Specimen Model Development

Six large-scale bending test specimens from three heats of steel were modeled using FEA. Each beam was modeled as tested at the time of fracture, including boundary conditions, fracture load, and final fatigue crack length. To mimic the experimental test setup, boundary conditions

included the pin and roller bearings as well as the LTB bracing. Both bearings were located 6 in. from each end of the beam. The pin bearing was modeled as a boundary condition preventing vertical, lateral, and longitudinal movement; while, the roller bearing was modeled as a boundary condition preventing vertical and lateral movement. Preventing lateral movement at the bearings simulated the lateral angle braces near each support. Plates simulating the LTB bracing were modeled for each beam. The plates were extruded from the top flange of each beam and pinned at the column location. Modeling the actual LTB bracing captured the reduction in flange stress due to the load carried by the LTB braces.

Results from large-scale testing, including the fracture load and final fatigue crack length, can be found in Table 3.8. The fracture load was applied as a point load in the model to the centerline node at each actuator location. Figure 4.2 is an example of the load and boundary conditions as modeled for the large-scale bending specimens.

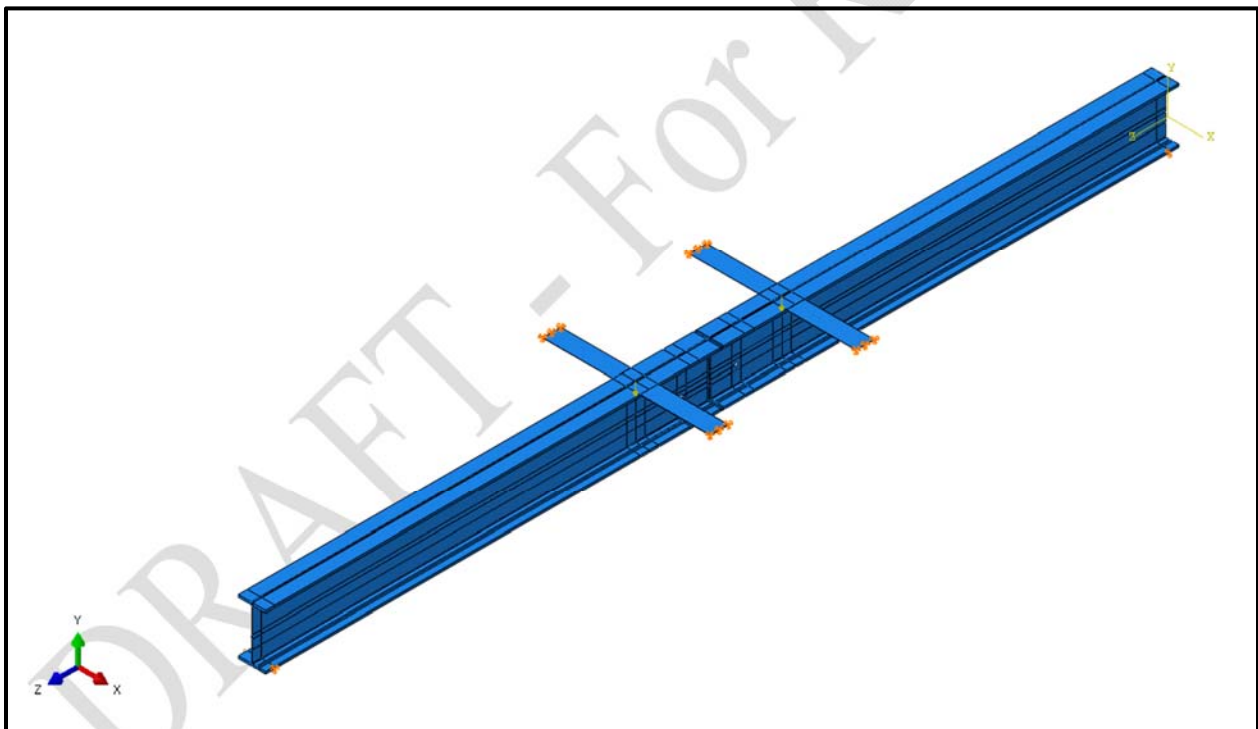


**Figure 4.2: Bending test specimen model example boundary conditions and loading**

Rigid kinematic coupling was used to model the bearing stiffeners. The mid-height node of the web was assigned as the master node. Slave nodes included the remaining web nodes and nodes on the top and bottom flange. Constraint was provided in the U1, U2, and U3 degrees of freedom. Figure 4.3 displays a bending specimen model example stiffener.

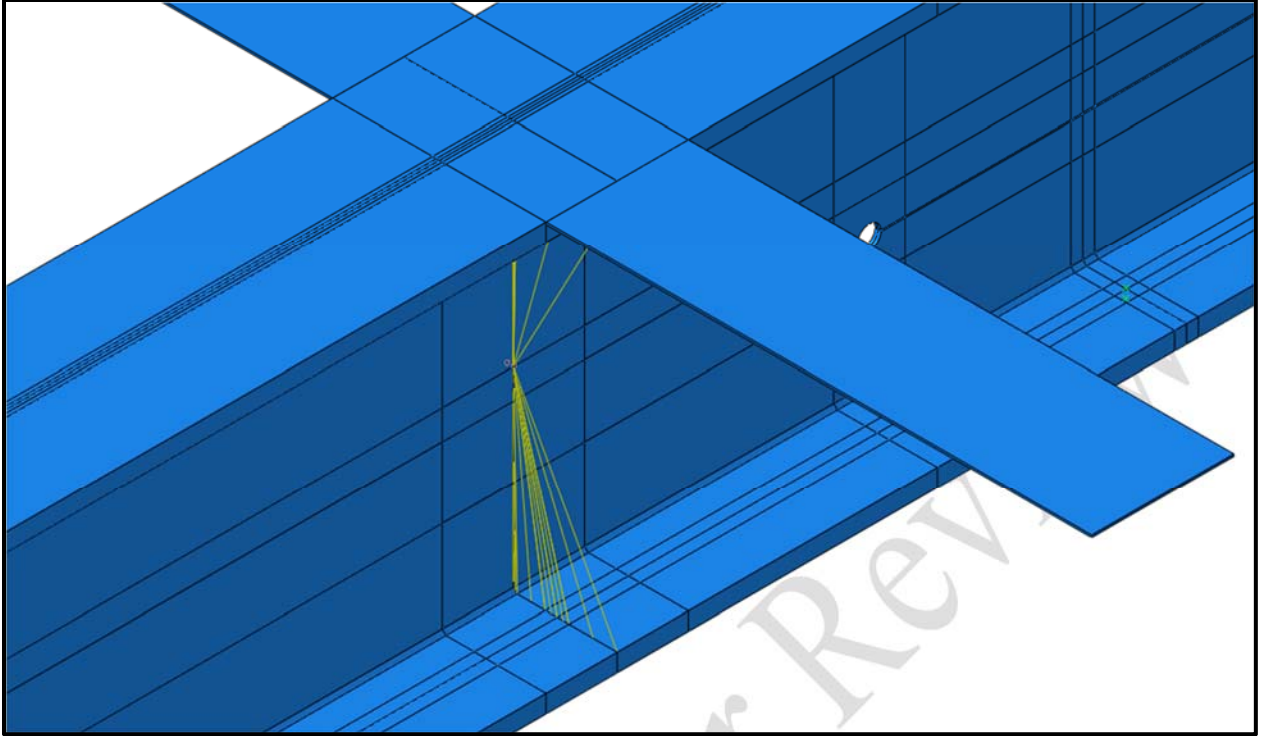


**Figure 4.3: Bending test specimen model example stiffener**

FEA was used to attain the maximum stress intensity and maximum j-integral demand at fracture. As such, both a linear-elastic and elastic-plastic model was created for each specimen. The linear-elastic model was used to obtain the maximum stress intensity demand. Linear-elastic models utilized linear continuum three dimensional hexahedral elements with reduced integration elements (C3D8R). Figure 4.4 is an example of the typical global mesh for the linear-elastic models.

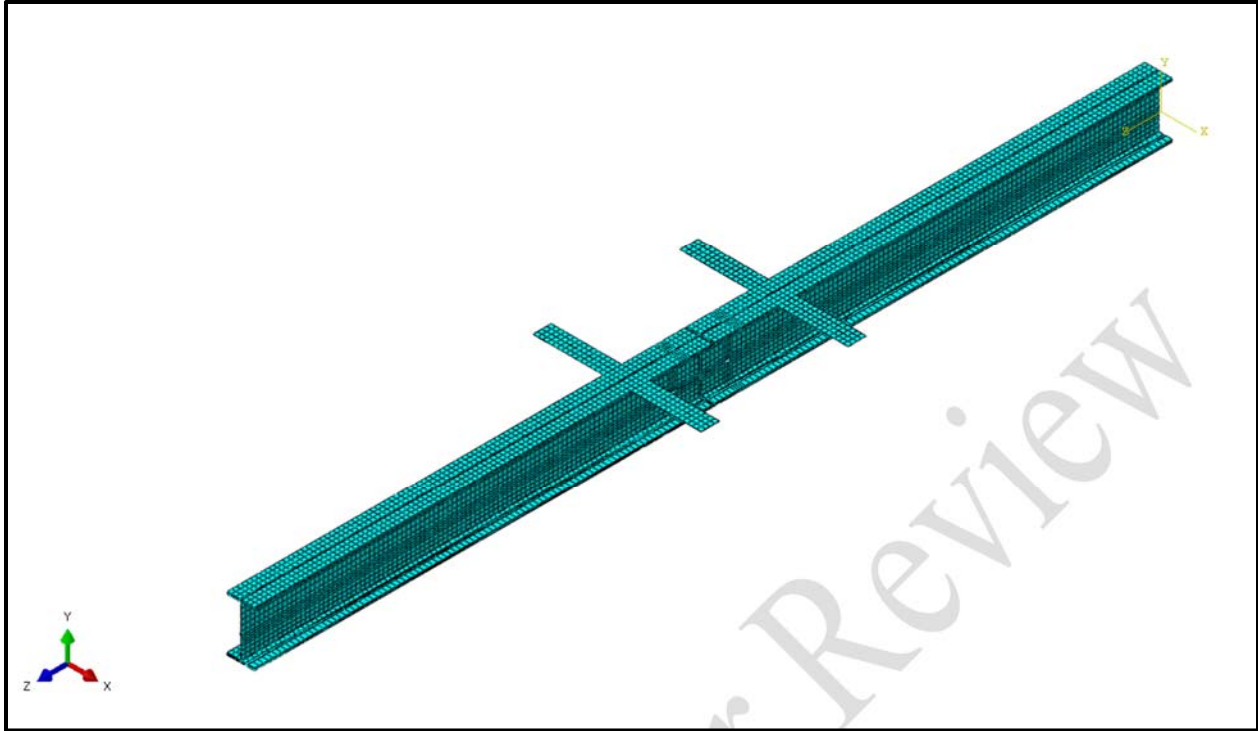


**Figure 4.4: Bending test specimen example model mesh**

The elastic-plastic models were used to obtain the maximum  $j$ -integral demand. Elastic-plastic models utilized quadratic continuum three dimensional elements with reduced integration elements (C3D20R). To improve computational efficiency of the elastic-plastic models, submodeling was employed. A coarse mesh of C3D8R elements were applied to the global model. The global model mesh was similar, but not identical, to Figure 4.4. As discussed in detail later, slight differences were used in at the crack tip location between the linear-elastic model and the global elastic-plastic model. Results from the elastic-plastic global model were applied as boundary conditions to the elastic-plastic submodel. The mesh of the elastic-plastic submodel was refined, using C3D20R elements. An example of a meshed elastic-plastic submodel is shown in Figure 4.5.

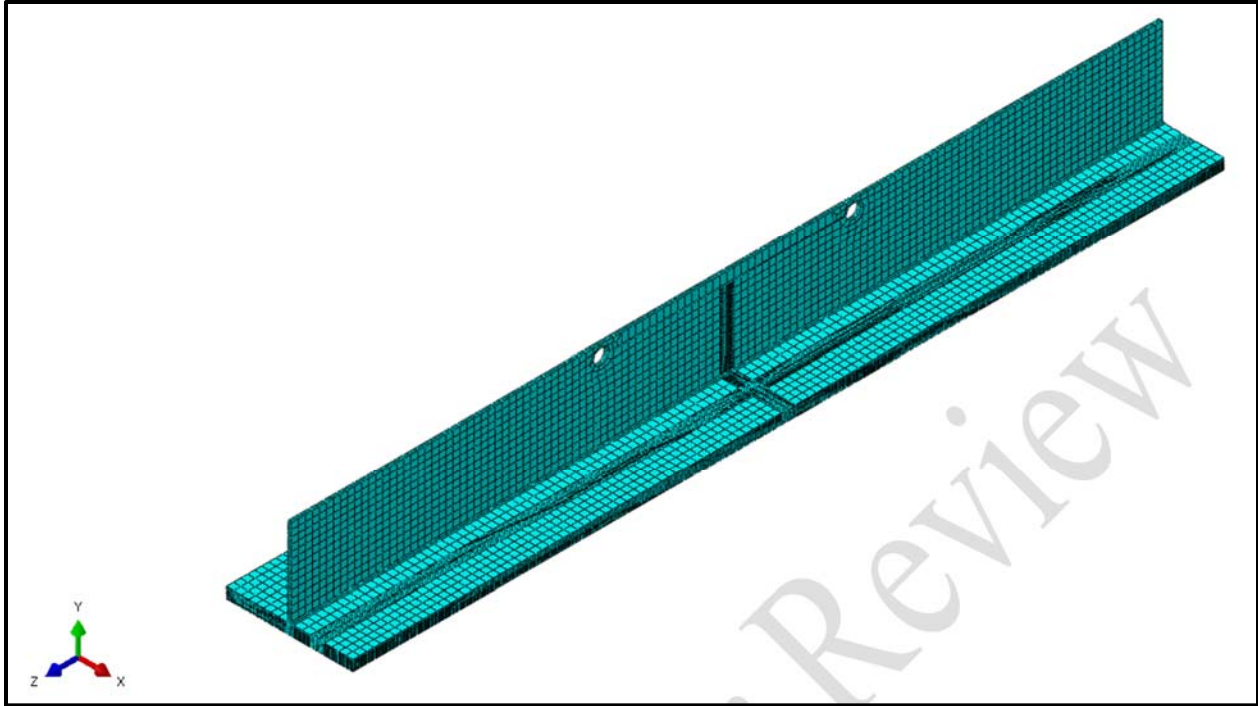


**Figure 4.5: Bending test specimen example submodel mesh**

The fatigue crack was modeled using a seam for all bending test specimens. A straight, through-thickness crack was defined for each test specimen based on the average measured fatigue crack length. Crack extension was defined as a vector normal to the crack plane. The same singularity definition was used for both the linear-elastic and elastic-plastic models. Crack tip elements were collapsed with multiple nodes. Additionally, the midside node parameter was left at the midpoint. The maximum stress intensity and maximum j-integral demands were calculated at each load increment. A total of eight contours were calculated for both parameters.

The mesh was refined in the area around the crack tip the mesh to accurately calculate the maximum stress intensity demand and maximum j-integral demand. Two circular partitions were used around the crack tip. The circle nearest to the crack tip had a radius of 0.01 in., while the larger circle had a radius of 0.11 in. Both the linear-elastic models and the elastic plastic submodels used the same mesh. The area between the two circles was seeded with ten elements. A 2 in. box surrounded the crack tip circles. The box was seeded to result in 0.125 in. elements around the crack tip perimeter. Through the specimen thickness seeding was performed to result in 0.125 in. elements. Conversely, the global elastic-plastic model was seeded to have no additional elements between the crack tip circles. Additionally, all areas were seeded with 0.125

in. elements for the refined models; whereas, the remaining areas in the global model were seeded with 0.25 in. elements. Figure 4.6 depicts the difference between the refined models, left, and the global models, right.

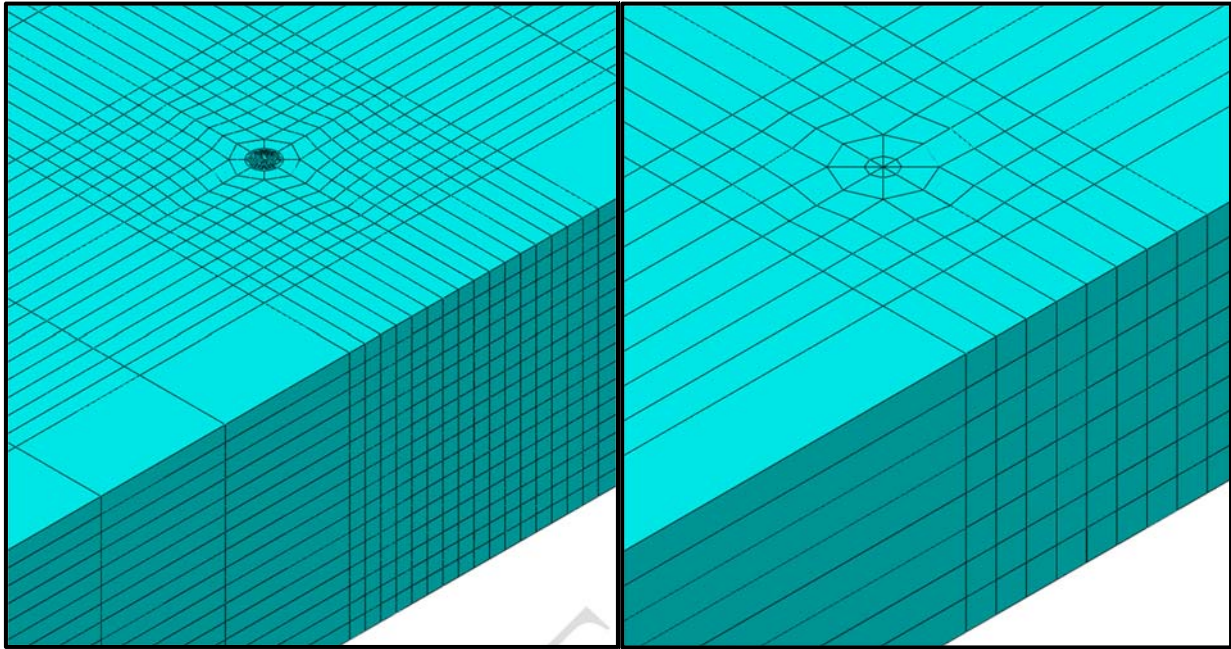


**Figure 4.6: Bending test specimen model example refined (right) and course (left) crack tip mesh**

#### *4.2.1.3 Axial Test Specimen Model Development*

Five large-scale axial test specimens from three heats of steel were modeled using FEA. Each plate was modeled using the stress and fatigue crack length at the time of fracture. Displacement in the U3 direction was fixed at the crack location for the uncracked portion of the plate. Fixing the displacement in the U3 direction creates the symmetry condition, to increase computational efficiency. Figure 4.7 depicts how symmetry boundary condition was imposed.

To simplify the analyses, the pin connection was not explicitly modeled; rather, a surface traction was used to represent the loading condition. Table 3.9 contains the fracture stress results for the axial specimens. The surface traction was applied to the original, undeformed cross-section. To represent the pin bearing condition through applied boundary conditions, loading was not allowed to rotate with the specimen. A length of 60 in. was modeled to ensure the stress was uniformly redistributed between the crack location and loading. The surface traction loading can be seen in Figure 4.7.

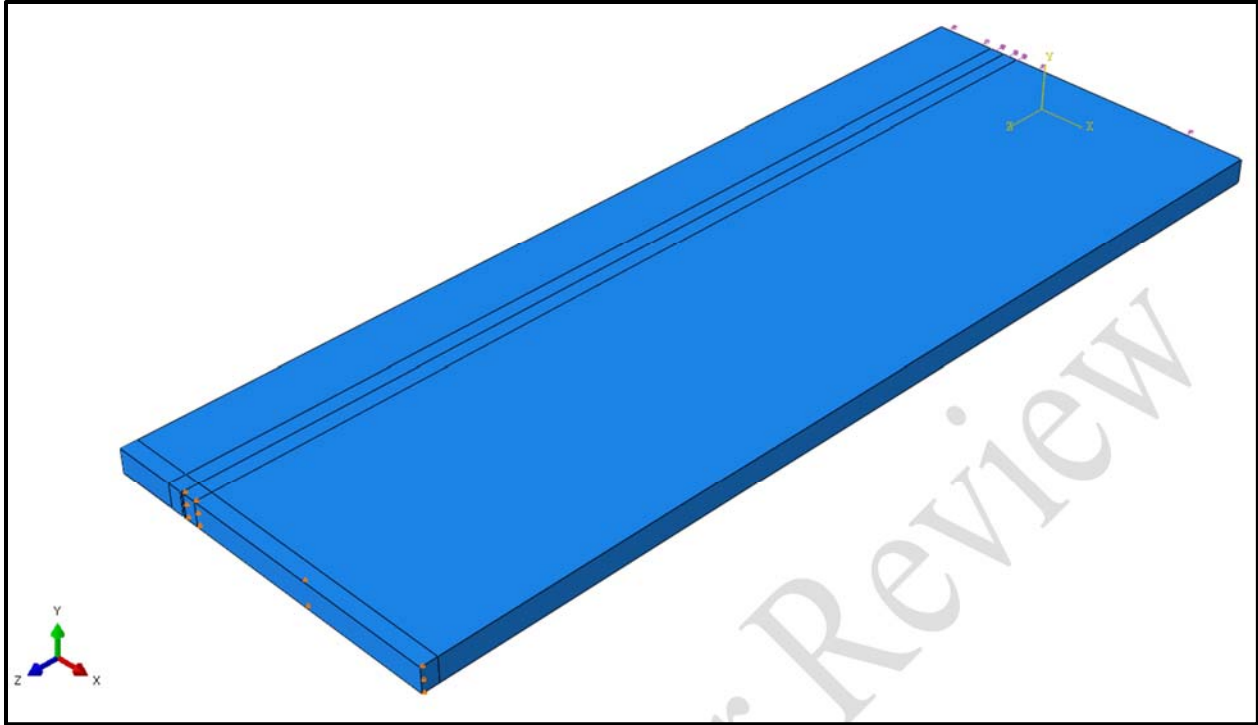


**Figure 4.7: Axial test specimen model boundary conditions and loading**

Both linear-elastic and elastic-plastic axial specimen models were created to capture the maximum stress intensity demand and maximum  $J$ -integral demand, respectively. Like the bending specimen FEA, linear-elastic analyses utilized C3D8R elements, while elastic-plastic analyses used C3D20R elements. Submodeling was not required for the elastic-plastic analyses because of the computational efficiency gained by the use of symmetry. As such, the mesh was identical for both analyses types. Figure 4.8 depicts an example axial test specimen model mesh.

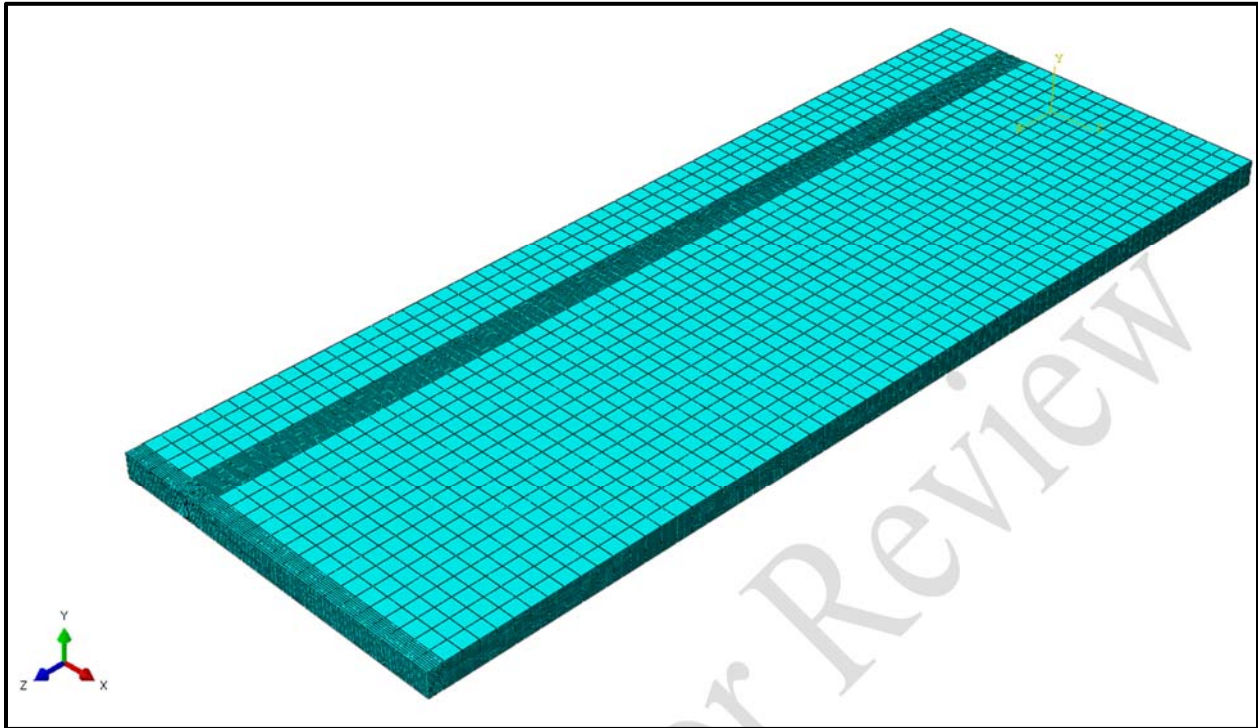


**Figure 4.8: Axial test specimen model mesh**

No seam was required because the fatigue crack was located on the symmetry plane. Crack extension was defined using a normal vector. Collapsed nodes with a 0.5 midside node were used at the crack tip to model the singularity. The maximum stress intensity demand and maximum  $J$ -integral demand were calculated at eight contours for each load increment.

The crack tip mesh for the axial specimens was similar to the refined mesh used for the bending test specimens. Due to the crack being located at the edge of the specimen, semi-circles were used as opposed to full circles. Two semi-circles were drawn at the crack tip with radii of 0.01 in. and 0.11 in, respectively. Seeding was performed to result in 10 elements between the semi-circles. A 1 in. by 2 in. rectangle encased the two semi-circles. Seeding was performed and resulted in 0.125 in. elements at the perimeter of the rectangle. Through the thickness of the axial specimens, seeding was performed and resulted in 0.125 in. elements. Figure 4.9 depicts the axial test specimen model crack tip mesh used for both the linear-elastic and elastic plastic analyses.

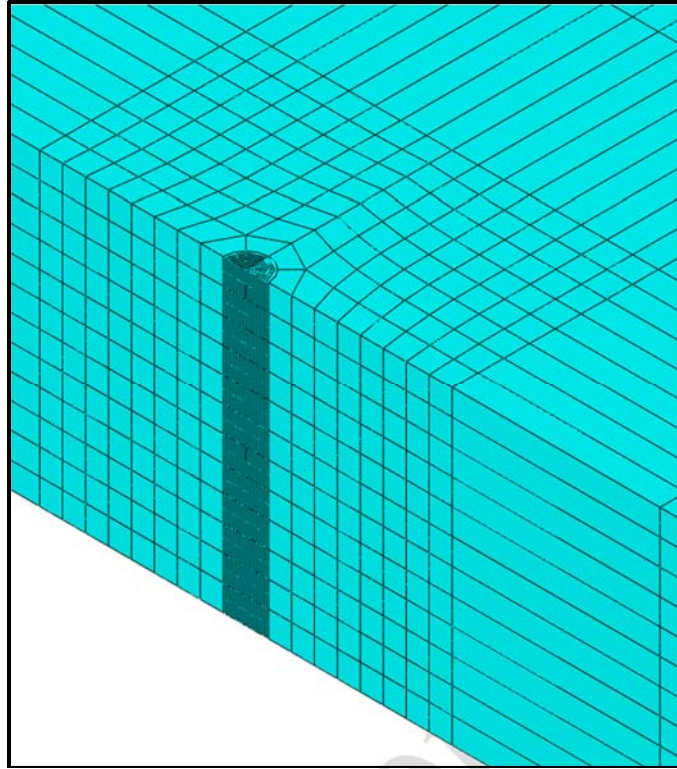


**Figure 4.9: Axial test specimen model crack tip mesh**

#### **4.2.2 Large-scale Test Specimen Model Validation**

Validation of the large-scale test specimen FEA was performed by comparing model results to measurements recorded during static testing. Finite element models were created without cracks for the validation. A static test was performed on each beam specimen prior to notching. Conversely, only a single unflawed axial test was performed. Good agreement was found between all analytical results and static test data. The following sections discuss the bending and axial specimen validation.

##### ***4.2.2.1 Bending Test Specimen Model Validation***

Static test data from all six bending test specimens was used to validate the FEA. A comparison between the data and models was made at an actuator load of 200 kips. All test data was measured prior to specimen notching; as such, no cracks were present in the finite element models. Each specimen was validated individually; however, due to the similarity between

identical specimen pairs only a representative specimen from each of the three pairs will be discussed further.

#### 4.2.2.1.1 50\_2-0\_B Specimen Model Validation

To validate the 50\_2-0\_B Specimen finite element models, a comparison was made between an unflawed Specimen 50\_2-0\_1B model and measured static test data. Strain gage measurements were averaged at three locations for the comparison: the bottom flange midspan, the top flange midspan, and the bottom flange loading section. The average longitudinal stress strain gage measurement at each location was within 1% of the FEA results. Figure 4.10 plots the Specimen 50\_2-0\_1B bottom flange longitudinal stress from the FEA, as well as the average strain gage measurements for the bottom flange midspan and loading sections.

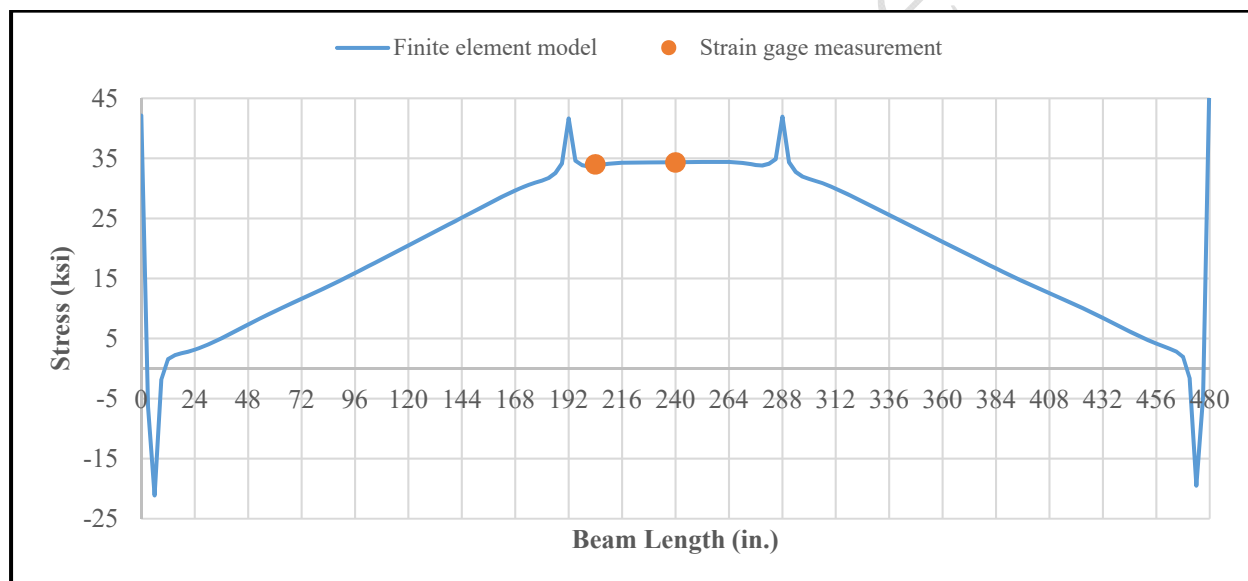


**Figure 4.10: Specimen 50\_2-0\_1B longitudinal stress at centerline**

Strain gages were installed on the top and bottom of the tension flange, the top of the compression flange, and throughout the height of the web. Combining the average strain gage measurements from the flanges with the web strain gage measurements, a stress profile was created. Figure 4.11 plots the stress profile for Specimen 50\_2-0\_1B. The FEA results were combined with the average flange strain gage measurements and the web strain gage measurements. Good agreement was found between the FEA results and the measured stress data.

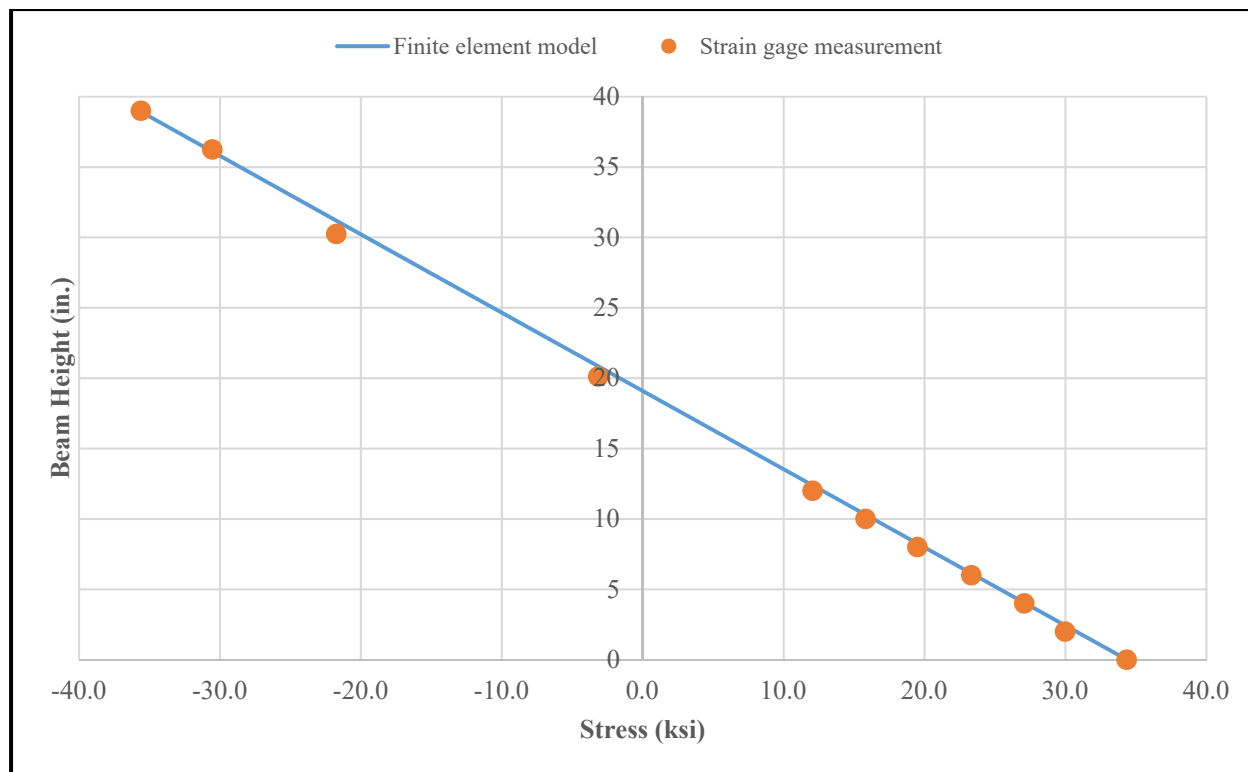


**Figure 4.11: Specimen 50\_2-0\_1B stress profile at midspan**

Deflections computed from the FEA were compared to measurements recorded from the string potentiometers. Measured results were within 1% of the model results. Figure 4.12 plots the bottom flange deflection at centerline as well as the measurement from the string potentiometers for Specimen 50\_2-0\_1B. Good agreement was found between the FEA results and the measured deflection data.

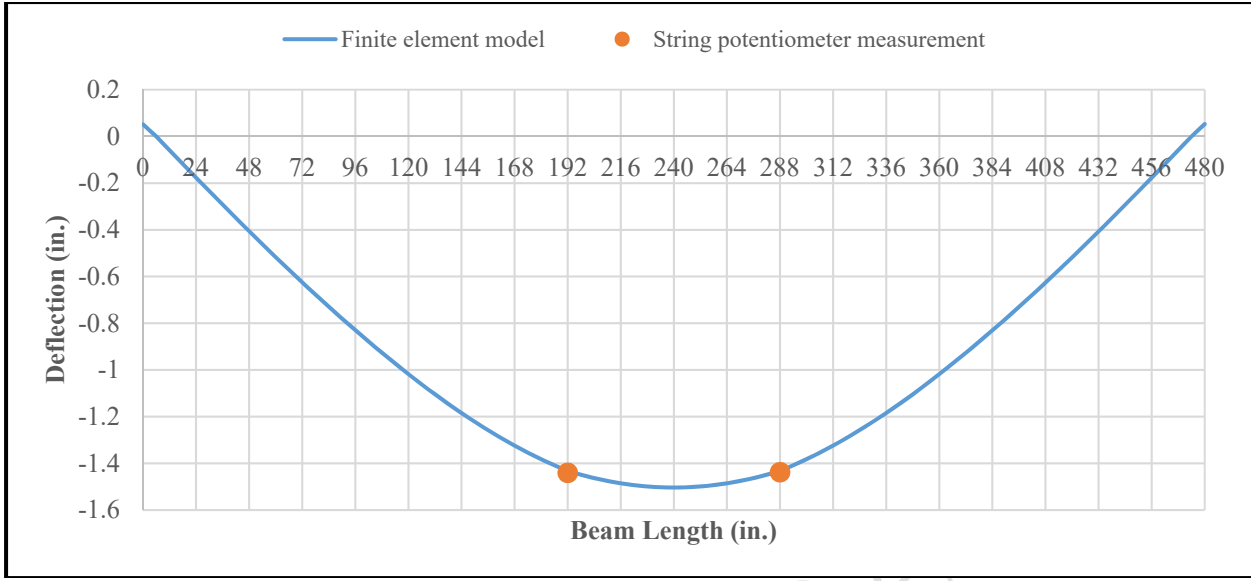


**Figure 4.12: Specimen 50\_2-0\_1B displacement at centerline**

*4.2.2.1.250\_2-5\_B Specimen Model Validation*

To validate the 50\_2-5\_B Specimen finite element models, a comparison was made between an unflawed Specimen 50\_2-5\_2B model and measured static test data. Strain gage measurements were averaged at three locations for the comparison: the bottom flange midspan, the top flange midspan, and the bottom flange loading section. The average longitudinal stress strain gage measurement at each location was within 7% of the FEA results. Figure 4.13 plots the bottom flange longitudinal stress from the FEA as well as the average strain gage measurements for the bottom flange midspan and loading sections for Specimen 50\_2-5\_2B.

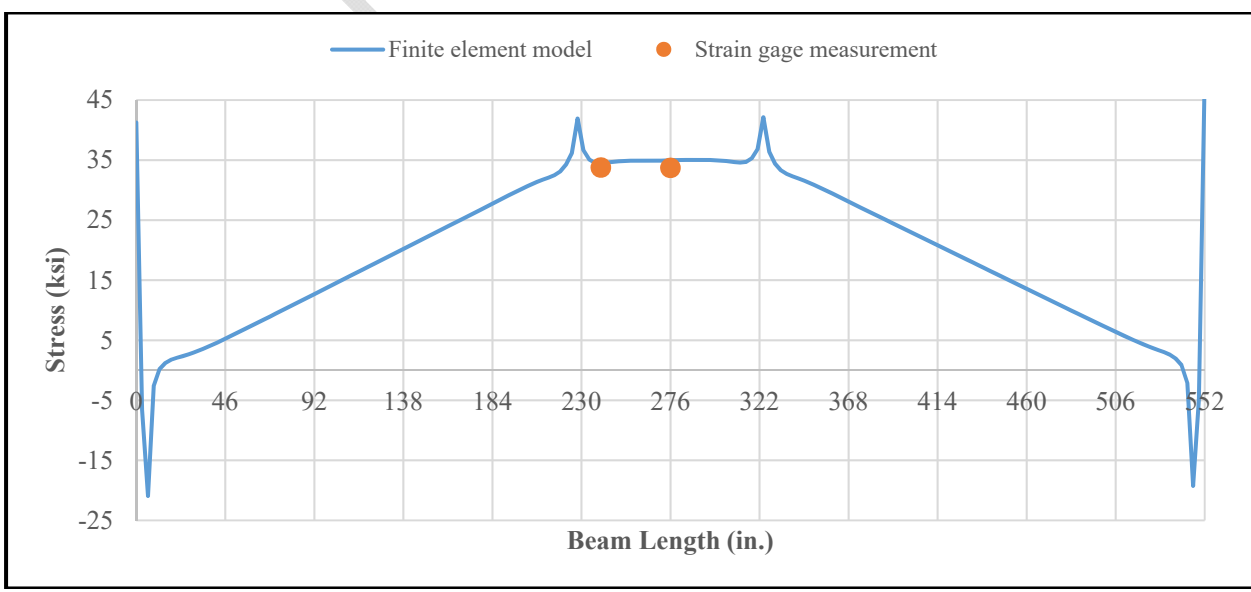


**Figure 4.13: Specimen 50\_2-5\_2B longitudinal stress at centerline**

Strain gages were installed on the top and bottom of the tension flange, the top of the compression flange, and throughout the height of the web. Combining the average strain gage measurements from the flanges with the web strain gage measurements, a stress profile was created. Figure 4.14 plots the stress profile for Specimen 50\_2-5\_2B. The FEA results were combined with the average flange strain gage measurements and the web strain gage measurements. Good agreement was found between the FEA results and the measured stress data.

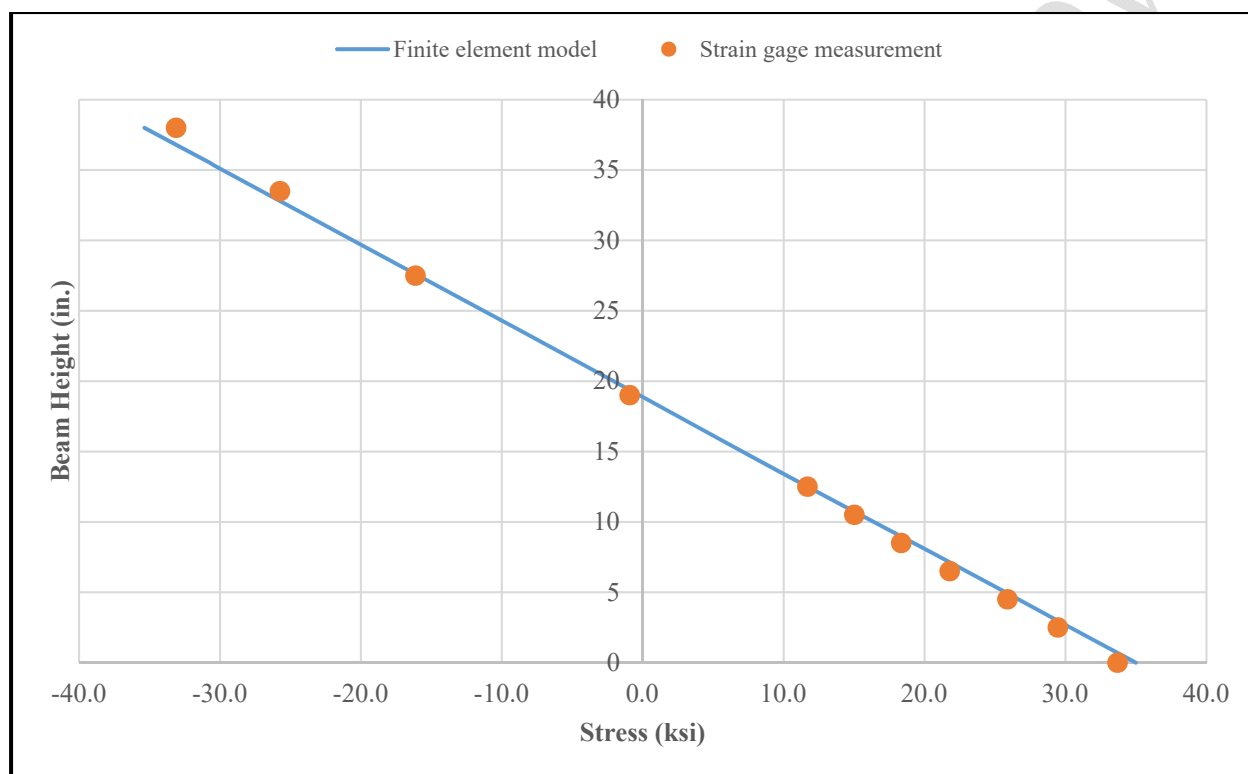


**Figure 4.14: Specimen 50\_2-5\_2B stress profile at midspan**

Deflections computed from the FEA were compared to measurements recorded from the string potentiometers. Measured results were within 6% of the model results. Figure 4.15 plots the bottom flange deflection at centerline as well as the measurement from the string potentiometers for Specimen 50\_2-5\_2B. Good agreement was found between the FEA results and the measured deflection data.

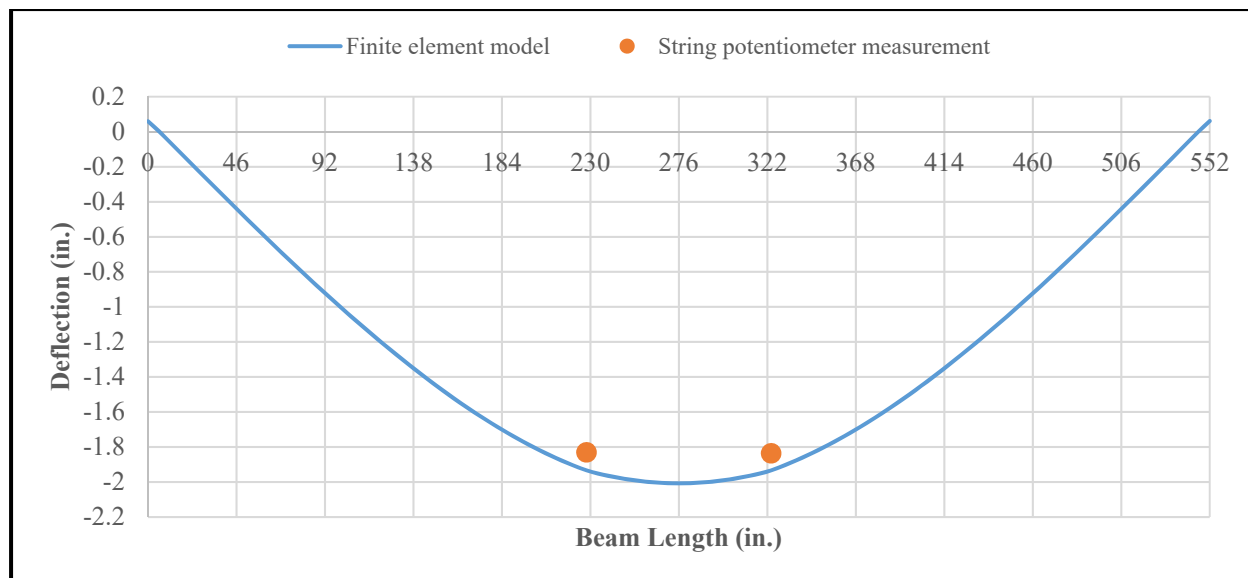


**Figure 4.15: Specimen 50\_2-5\_2B displacement at centerline**

#### 4.2.2.1.3 70\_1-5\_B Specimen Model Validation

To validate the 70\_1-5\_B Specimen finite element models, a comparison was made between an unflawed Specimen 70\_1-5\_1B model and measured static test data. Specimen 70\_1-5\_1B was loaded with 150 kips and 200 kips on the north and south actuators, respectively. Due to an error in the load multiplier for the north actuator, less load was applied than intended. The multiplier error impacted the fracture testing of Specimen 50\_2-0\_1B as well as the entirety of testing for Specimen 50\_2-0\_2B and Specimen 70\_1-5\_1B. All load results for the north actuator were adjusted to the correct value for the FEA.

To demonstrate FEA agreement with the measured data for the corrected load, Specimen 70\_1-5\_1B was evaluated. Strain gage measurements were averaged at three locations for the comparison: the bottom flange midspan, the top flange midspan, and the bottom flange loading section. The average longitudinal stress strain gage measurement at each location was within 4% of the FEA results. Figure 4.16 plots the bottom flange longitudinal stress from the FEA as well as the average strain gage measurements for the bottom flange midspan and loading sections for Specimen 70\_1-5\_1B.

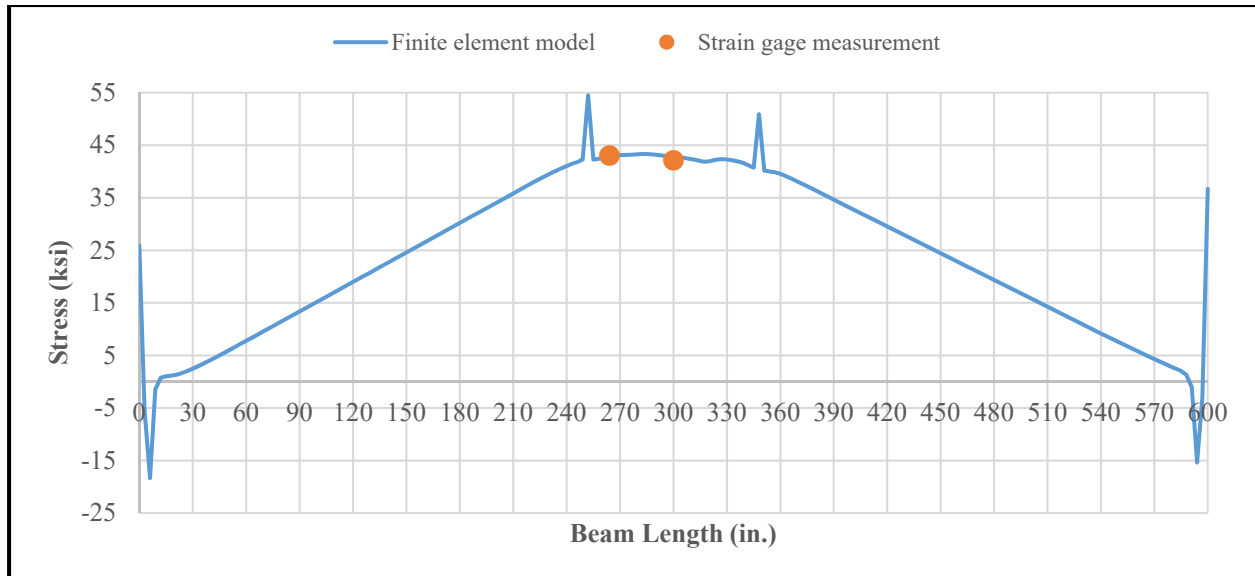


**Figure 4.16: Specimen 70\_1-5\_1B longitudinal stress at centerline**

Strain gages were installed on the top and bottom of the tension flange, the top of the compression flange, and throughout the height of the web. Combining the average strain gage measurements from the flanges with the web strain gage measurements, a stress profile was created. Figure 4.17 plots the stress profile for Specimen 70\_1-5\_1B. The FEA results were combined with the average flange strain gage measurements and the web strain gage measurements. Good agreement was found between the FEA results and the measured stress data.

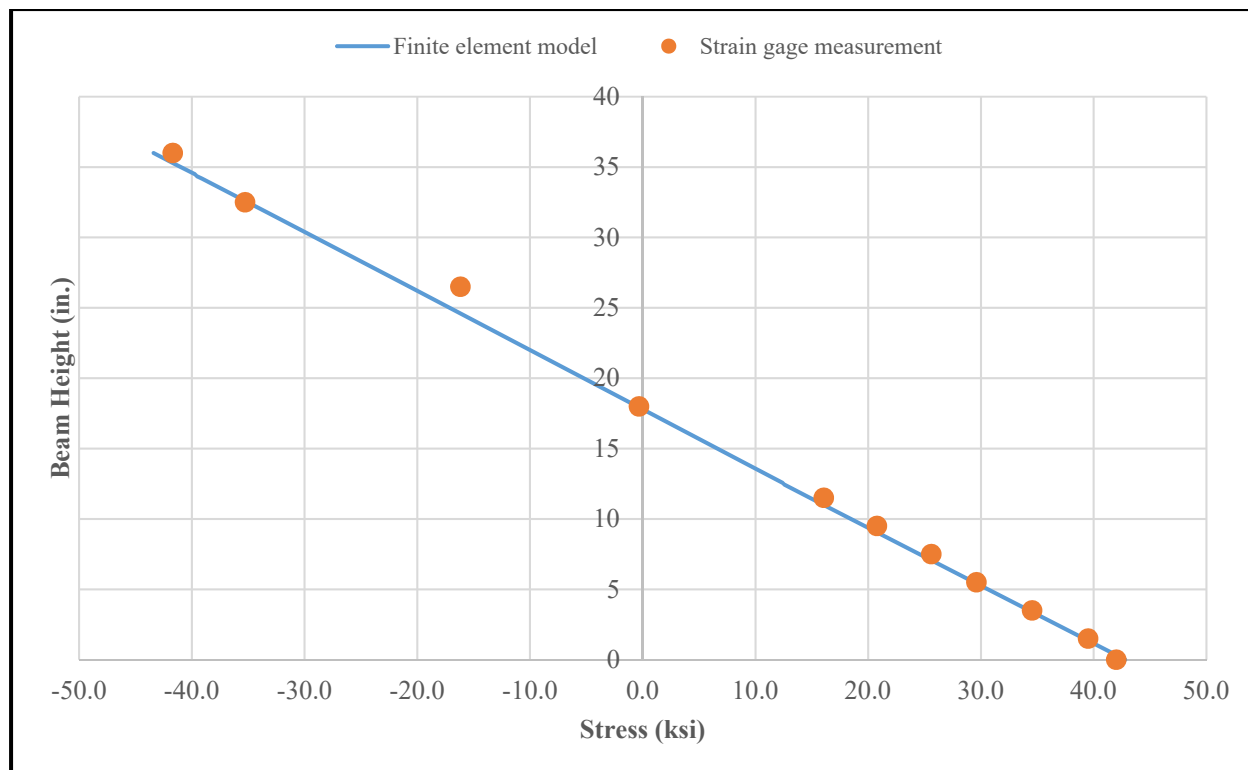


**Figure 4.17: Specimen 70\_1-5\_1B stress profile at midspan**

Deflections computed from the FEA were compared to measurements recorded from the string potentiometers. Measured results were within 5% of the model results. Figure 4.18 plots the bottom flange deflection at centerline as well as the measurement from the string potentiometers for Specimen 70\_1-5\_1B. Good agreement was found between the FEA results and the measured deflection data.

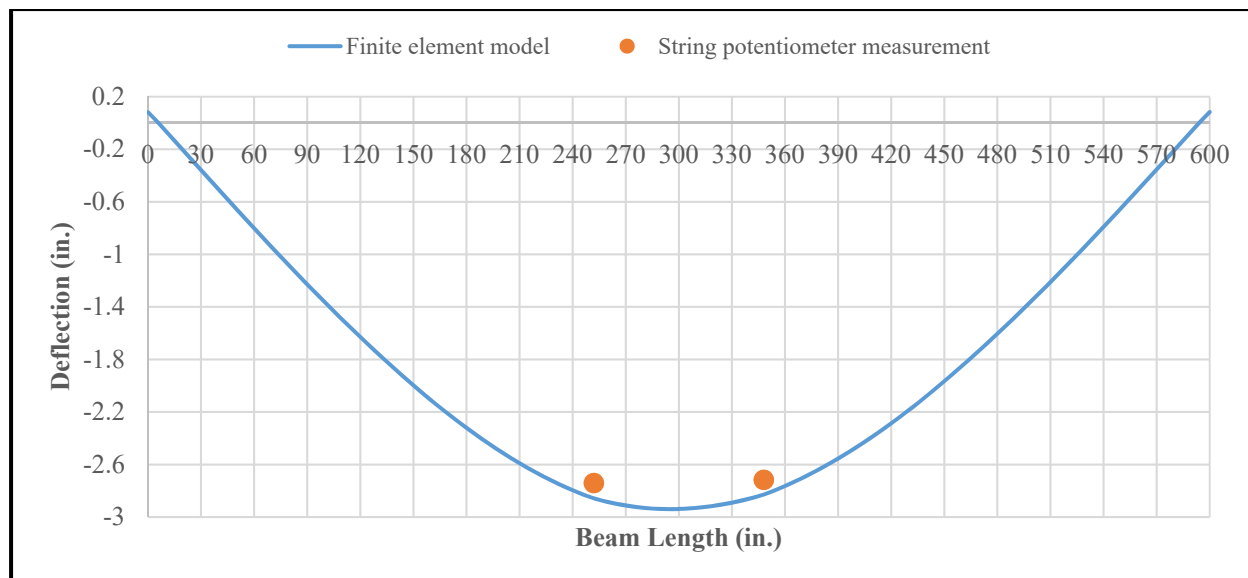


**Figure 4.18: Specimen 70\_1-5\_1B displacement at centerline**

#### 4.2.2.2 Axial Test Specimen Model Validation

Unflawed static testing was performed only on the axial test Specimen 50\_1-5\_1A. A single static test was performed because of the simplicity of the load frame. Results from the static test were used to determine if the axial specimens were experiencing any in-plane or out-of-plane bending. Analysis of the results indicated the in-plane and out-of-plane bending were minimal; therefore, no further unflawed static axial experiments were conducted.

Results from the single unflawed static axial test were used to validate the axial specimen finite element modeling techniques. Good agreement was found between the FEA results and measured data. Figure 4.19 plots the longitudinal stress at the middle of the specimen. The average strain gage measurement was within 3% of the FEA. Figure 4.20 plots the longitudinal stress 24 in. from the middle of Specimen 50\_1-5\_1A. The average strain gage measurements was within 1% of the FEA. Additionally, the plots show the specimen experienced minimal in-plane and out-of-plane bending.

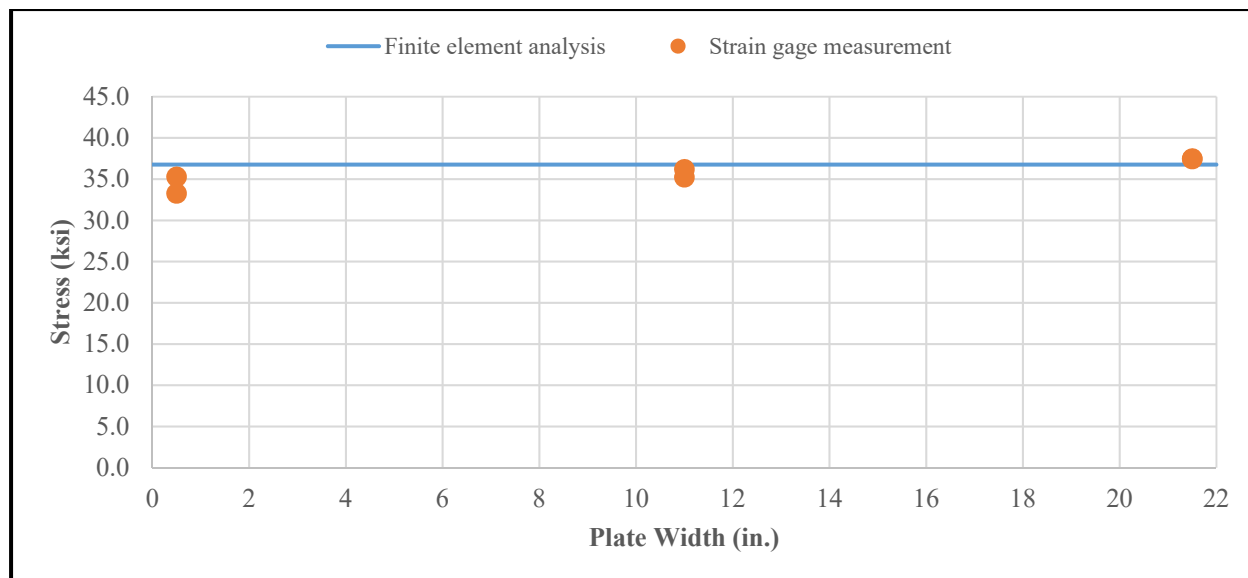


**Figure 4.19: Specimen 50\_1-5\_1A longitudinal stress at midpoint**



**Figure 4.20: Specimen 50\_1-5\_1A longitudinal stress at 24 in.**

### 4.2.3 Large-scale Test Specimen Model Results

Finite element models of the large-scale test specimens were used to calculate fracture parameters at the time of failure. The loading and crack geometry at failure were used as input parameters for model creation. Both linear-elastic and elastic-plastic fracture mechanics parameters were calculated for each test specimen. For linear-elastic analyses, the stress intensity

demand was tabulated; while, for the elastic-plastic analyses, the j-integral demand was computed. Additionally, the large-scale FEA results were used to compare the performance of the specimen representative of the current specification (Plate) and those satisfying the 125 ft.-lb. requirement (Plates E, H, and J).

Table 4.3 presents the large-scale specimen FEA results. The peak stress intensity demand and j-integral demand results from the eighth contour were reported for each specimen. Using the maximum j-integral demand, an elastic-plastic equivalent stress intensity factor demand was computed. A comparison can be made between the linear-elastic stress intensity factor,  $K$ , and the elastic-plastic equivalent stress intensity factor,  $K_J$ , to evaluate the plastic contribution. Additionally, the 1T master curve size correction was applied to all the elastic-plastic equivalent stress intensity factor data. The size-corrected data are presented in Table 4.3.

Specimens marked with an asterisks in Table 4.3 were tested using the incremental growth procedure. As previously discussed, the original test procedure called for incremental fatigue crack growth followed by fracture attempts. The procedure was modified to growing the fatigue crack to a length with a high probability of fracture. Preliminary FEA indicated the experimental test attempts which did not result in fracture using the incremental fatigue crack growth procedure, were attributed to compressive residual stresses at the crack tip. Therefore, the fracture results for these specimens, indicated with an asterisks, are suspected be artificially high; however, it is not apparent to what extent. To ensure potentially unconservative data do not impact the analysis, results from any specimen indicated by an asterisks were censored from the evaluation. It should also be noted, 50\_1-5\_A specimens were initially tested under the incremental growth procedure; however, substantial fatigue crack growth past the compressive residual stresses was performed.

**Table 4.3: Large-scale test specimen model results**

Plate	Specimen	FEA Model K	FEA Model J	FEA Model K <sub>J</sub>	FEA K <sub>J(1T)</sub>
		(ksi√in.)	(kip-in./in. <sup>2</sup> )	(ksi√in.)	(ksi√in.)
E	50_2-5_1B	125.0	0.52	128.3	156.6
	50_2-5_2B	170.9	1.28	200.1	246.9
	50_2-5_1A	137.0	0.64	142.7	174.8
H	70_1-5_1B	236.8*	2.76*	295.8*	325.4*
	70_1-5_2B	355.6*	6.63*	458.2*	505.1*
	70_1-5_1A	136.7	0.58	135.5	148.0
	70_1-5_2A	209.1	1.88	244.0	268.1
I	50_2-0_1B	75.4*	0.17*	74.2*	84.8*
	50_2-0_2B	49.7	0.08	49.0	54.8
J	50_1-5_1A	161.6	1.27	200.2	219.6
	50_1-5_2A	198.4	2.29	269.4	296.2

The fracture data from the large-scale specimen experimental testing demonstrated an increase in fracture resistance for the high-toughness steel. Comparing the worst performing current specification specimen to the worst performing high-toughness specification specimen, the equivalent elastic-plastic stress intensity increased by over 270%. The average high-toughness elastic-plastic stress intensity for all uncensored specimens was 215.7 ksi√in. with a standard deviation of 57.7 ksi√in.

Figure 4.21 demonstrates the through-thickness variation in the j-integral demand of the bending and axial test specimens. The plot excludes specimens marked with an asterisks from Table 4.3. Flange thicknesses were normalized for the plot. Similar through-thickness j-integral variation was observed for all plate thicknesses. J-integral variation was primarily influenced by the maximum j-integral value. Also, Figure 4.21 visually represents the increase in fracture resistance for the high-toughness specimens as compared to the current specification specimens.

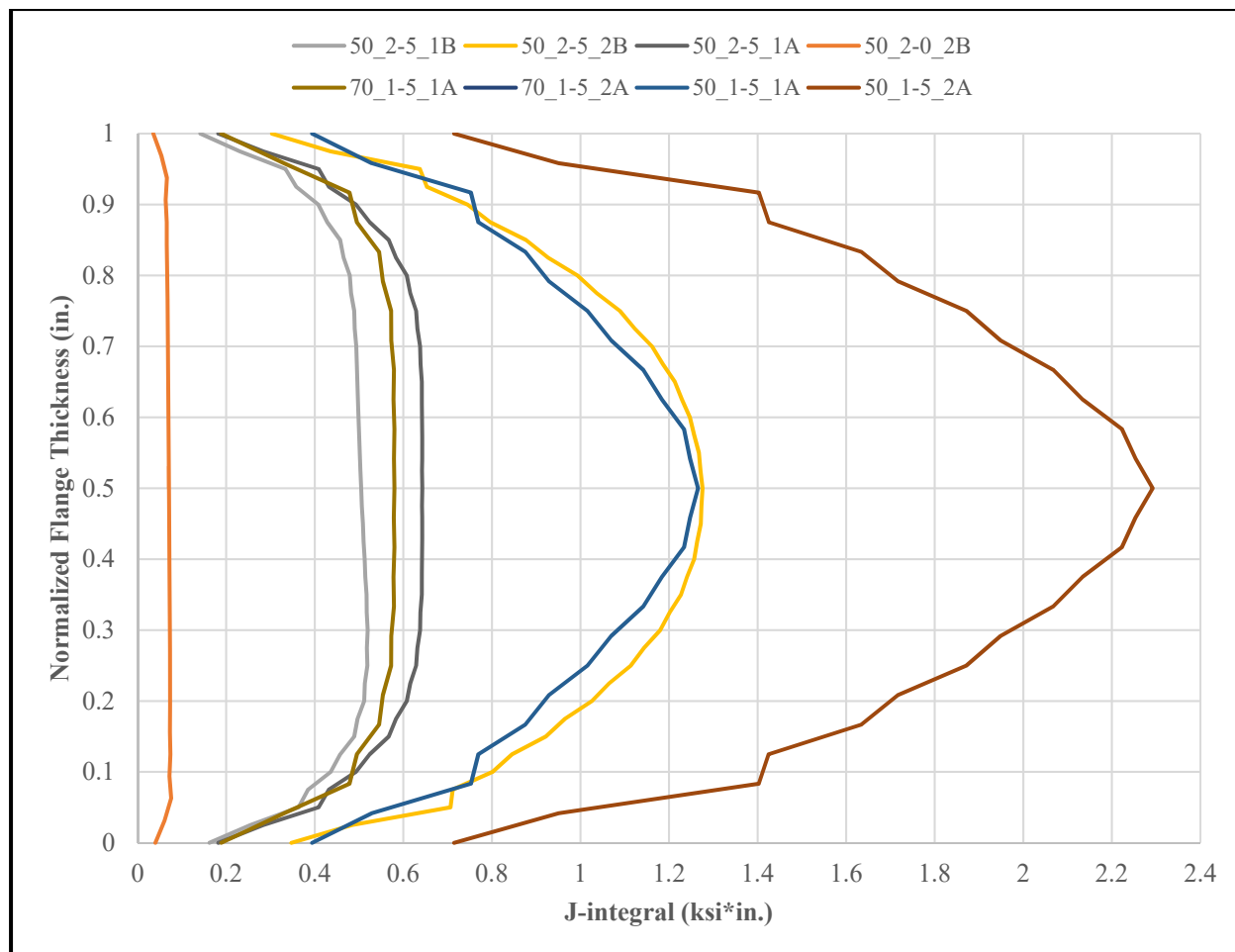


**Figure 4.21: Through-thickness j-integral demand**

### **4.3 Analytical Parametric Study**

An analytical parametric study was conducted in Abaqus CAE to determine the toughness required to resist a 3.0 in. edge crack in an I-girder geometry under a loading of  $0.75F_y$ . Geometric and material properties were varied to bound typical girder geometries for non-redundant bridges. The following sections discuss the parameters investigated, model development, and results of the study.

#### **4.3.1 Analytical Parametric Study Parameters**

The analytical parametric study evaluated the impact of a variety of parameters on the toughness required to resist a 3.0 in. edge crack in an I-girder with a stress state equal to  $0.75F_y$ .

Study parameters included yield strength, flange thickness, flange width, and web height. The maximum stress state for all analyses was  $0.75F_y$  based on the maximum allowable overload in the *Manual for Bridge Evaluation* (AASHTO, 2011). Only edge cracks were examined as part of the parametric study. Using linear-elastic fracture mechanics, an edge crack results in the highest stress intensity for a given crack length (Grandt, 2004).

As suggested by previous work, the crack length was held constant to achieve a constant level of fracture resistance between grades (Altstadt, 2008). A crack length of 3.0 in. was selected based on probability of detection (POD) work performed at Purdue University. The study was focused on visual inspection of out-of-plane cracks, cover plate weld toe cracks, and rivet hole cracks. Results of the POD study revealed the crack lengths with a 50% and 90% rate of detection were 1.25 in. and 8.0 in., respectively (Whitehead, 2015). Based on the POD study, a 3.0 in. crack would have a detection rate of approximately 65%. The POD data was based on all the cracks evaluated during the study, which did not include a through-thickness edge crack. The closest crack type evaluated during the POD study to a through-thickness edge crack was a rivet hole crack. The rivet hole crack resulted in 50% and 90% detection rates for crack lengths of 0.5 in. and 3.5625 in., respectively (Whitehead, 2015). As such, a 3.0 in. edge crack was thought to be reasonable for the parametric study because it was representative of a similar crack geometry having a high POD.

Geometric and material properties bounding typical plate girder design were utilized for the parametric study. Yield strengths of 50 ksi and 70 ksi were examined. The flange width was varied between 12 in. and 48 in. Flange thicknesses of 1.5 in. and 3.0 in. were included. The web height was varied between 36 in. and 144 in. Table 4.4 summarizes the geometric properties examined during the parametric study. Additionally, Table 4.4 presents the ratios for the crack length to flange width, crack length to flange thickness, web height to flange width, and flange width to flange thickness.

**Table 4.4: Parametric study properties**

<b>Web Height</b>	<b>Flange Width</b>	<b>Flange Thickness</b>	<b>Crack Length</b>	<b>a/b<sub>f</sub></b>	<b>a/t<sub>f</sub></b>	<b>h<sub>w</sub>/b<sub>f</sub></b>	<b>b<sub>f</sub>/t<sub>f</sub></b>
<b>(in.)</b>	<b>(in.)</b>	<b>(in.)</b>	<b>(in.)</b>				
36	12	1.5	3.0	0.25	2.0	3.0	8
		3.0	3.0		1.0		4
	18	1.5	3.0	0.17	2.0	2.0	12
		3.0	3.0		1.0		6
72	18	1.5	3.0	0.17	2.0	4.0	12
		3.0	3.0		1.0		6
	24	1.5	3.0	0.13	2.0	3.0	16
		3.0	3.0		1.0		8
	36	1.5	3.0	0.08	2.0	2.0	24
		3.0	3.0		1.0		12
144	24	1.5	3.0	0.13	2.0	6.0	16
		3.0	3.0		1.0		8
	36	1.5	3.0	0.08	2.0	4.0	24
		3.0	3.0		1.0		12
	48	1.5	3.0	0.06	2.0	3.0	32
		3.0	3.0		1.0		16

### 4.3.2 Analytical Parametric Study Model Development

Model refinement was performed to increase the computational efficiency of the parametric study. Previous FEA on bending geometries required the use of submodeling to obtain precise results. A study was conducted to evaluate if any modeling simplifications could be employed to result in conservative yet reasonable results. The study evaluated a plate in tension representing a tension flange without a web as well as an I-girder with a bending stress distribution resulting in compression on the top flange and tension on the bottom flange. To further increase the computation efficiency, both of the simplified geometries employed symmetry.

The simplified geometry results were compared against the previously described submodeling technique for an I-girder section having 2.5 in. thick by 14 in. wide flanges and a 0.5 in. thick by 33 in. tall web. A 3.0 in. crack was used for the evaluation to mimic the parametric study. Figure 4.22 plots the j-integral through the flange thickness for each FEA. Both simplified

procedures resulted in conservative j-integral values. The plate in tension proved to be overly conservative resulting in a maximum j-integral approximately 2.8 times greater than the submodel. Conversely, the bending section proved to be conservative yet reasonable, resulting in a maximum j-integral approximately 1.2 times greater than the submodel. Therefore, the bending section was utilized for the parametric study.

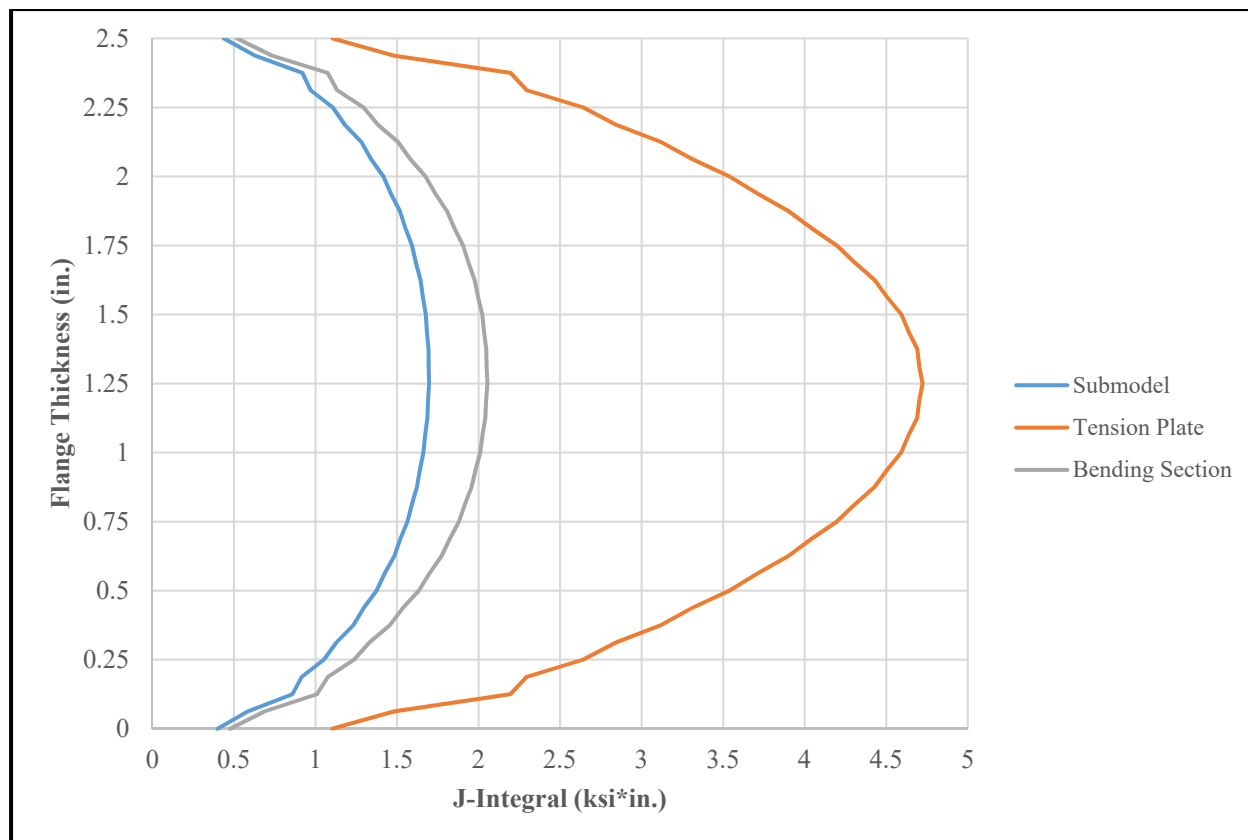


**Figure 4.22: Comparison of simplified modeling techniques**

The length of the bending section was examined to determine the minimum length section required. For the geometry simplification study, the length of the bending section was equal to the web height of 33 in. FEA was performed for bending section lengths equal to 12 in., 24 in., 48 in., and 96 in. Figure 4.23 plots the beam length normalized to the web height versus the maximum j-integral. Minimal variation in the maximum j-integral was found after a length equal to the web height. Therefore, to improve computational efficiency the length of all bending sections in the parametric study was equal to the web height.

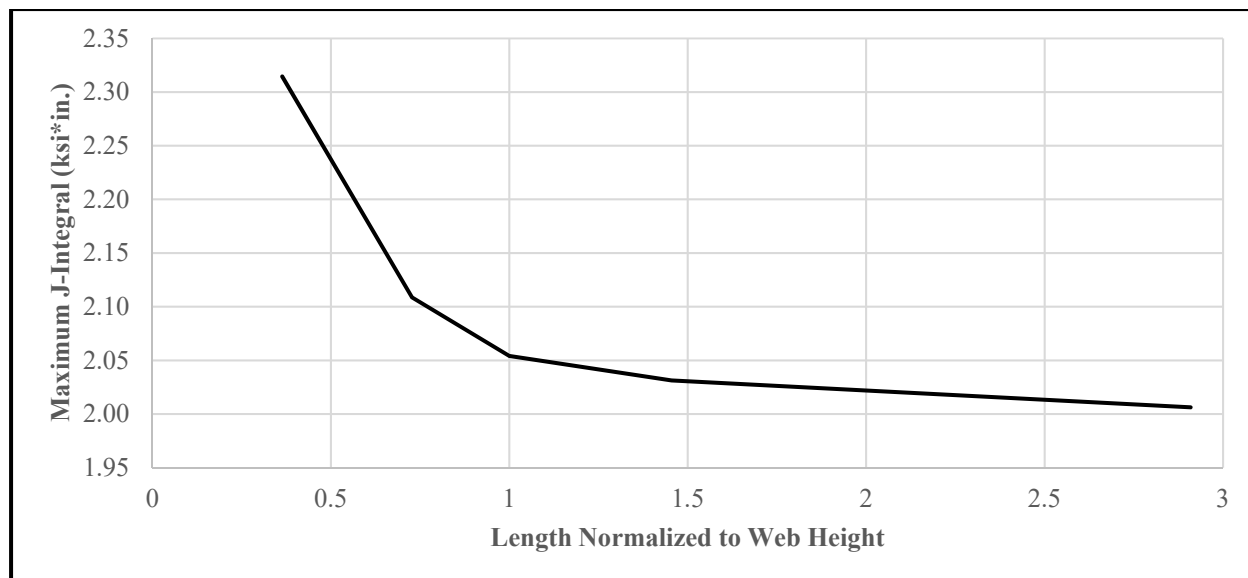


**Figure 4.23: Comparison of bending section length**

The parametric study utilized modified material properties of Plates E and H from the experimental testing program for Grade 50 and Grade 70, respectively. Material properties were modified to ensure yielding occurred at the nominal yield for each grade. To provide lower-bound results, no overstrength factor was applied to the yield strength. Figure 4.24 demonstrates how the application of a 10% overstrength factor resulted in a lower maximum j-integral value.

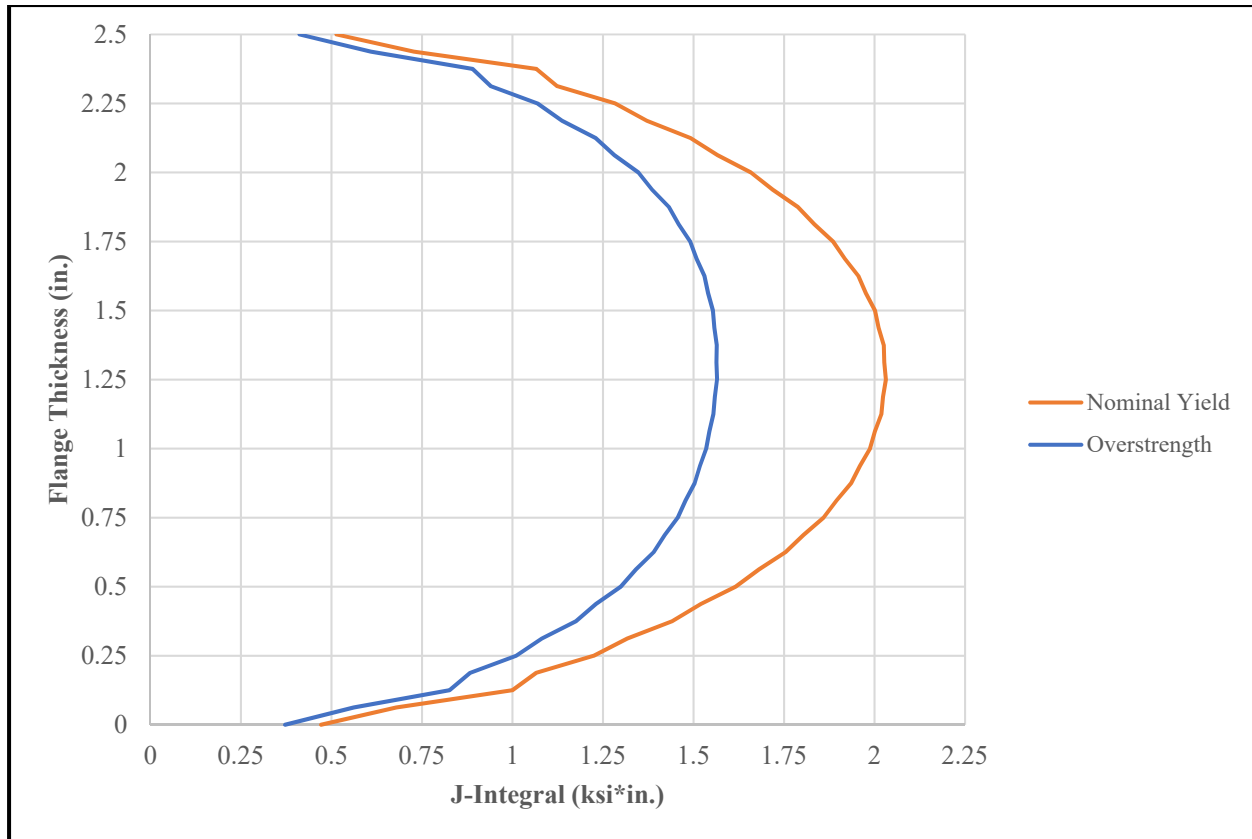


**Figure 4.24: Evaluation of overstrength factor**

All models in the parametric study utilized quadratic continuum three dimensional elements with reduced integration elements (C3D20R). Like the axial models, no seam was required because the fatigue crack was located on the symmetry plane. Crack extension was defined using a normal vector. Collapsed nodes with a 0.5 midside node were used at the crack tip to model the singularity. The maximum j-integral demand was calculated at eight contours for each load increment.

Seeding was similar to the refined submodels created for the large-scale experimental specimens with the exception of the global seeding which was increased to 2.0 in. Global seeding started 6.0 in away from the crack tip. In the first 6.0 in. from the crack tip a general mesh size of 1.0 in. was utilized. The crack tip mesh imitated the axial specimen models and used two semi-circles to encase the crack tip with radii of 0.01 in. and 0.11 in, respectively. Seeding was performed to result in 10 elements between the semi-circles. A 1 in. by 2 in. rectangle encased the two semi-circles. Seeding was performed and resulted in 0.125 in. elements at the perimeter of

the rectangle. Through the thickness, seeding was performed and resulted in 0.125 in. elements. Figure 4.25 depicts a representative parametric study model.

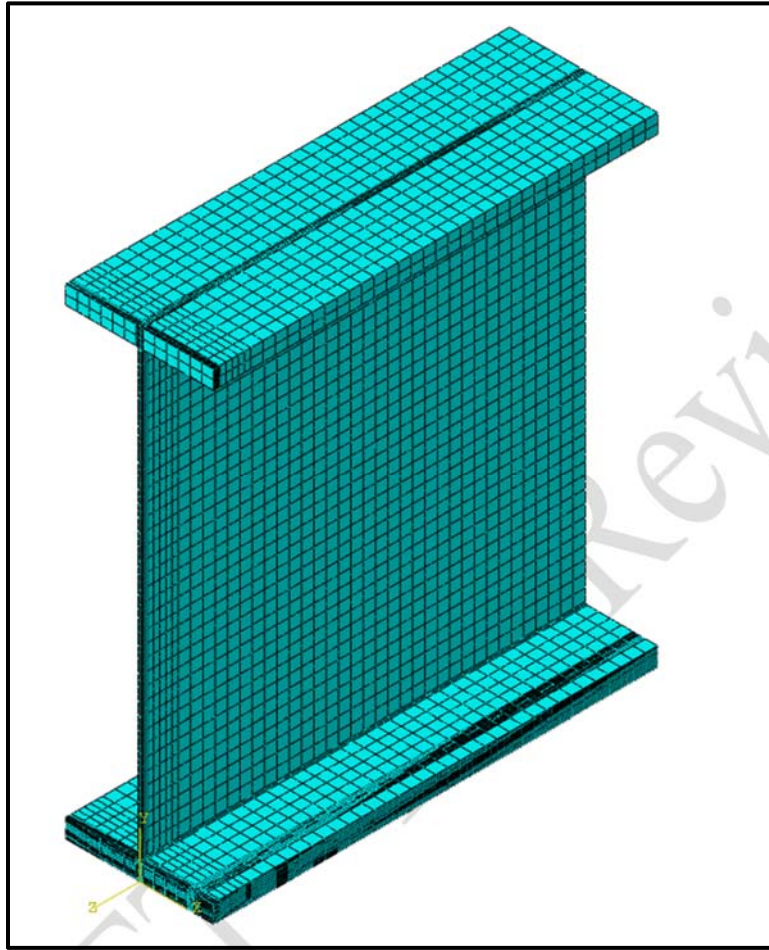


**Figure 4.25: Representative parametric study model**

### **4.3.3 Analytical Parametric Study Results**

A parametric study was conducted to establish the fracture toughness required to resist a 3.0 in. flaw in an I-shaped girder experiencing a stress state equal to  $0.75F_y$ . The parameters of the parametric study included yield strength, flange thickness, flange width, and web height. In total, 32 FEA models were created for the parametric study. The maximum j-integral value in the eighth contour was recorded as the critical value. The critical j-integral value was then converted to an equivalent elastic-plastic stress intensity factor. Table 4.5 presents the results of the parametric study in terms of the maximum equivalent elastic-plastic stress intensity factor.

Table 4.5: Parametric study results

Web Height	Flange Width	Flange Thickness	Crack Length	Grade 50 K <sub>Jc</sub>	Grade 70 K <sub>Jc</sub>	Grade 70/ Grade50 Ratio
(in.)	(in.)	(in.)	(in.)	(ksi√in.)	(ksi√in.)	
36	12	1.5	3.0	282.7	355.4	1.26
		3.0	3.0	276.1	322.2	1.17
	18	1.5	3.0	216.4	273.4	1.26
		3.0	3.0	186.2	238.3	1.28
72	18	1.5	3.0	221.9	280.4	1.26
		3.0	3.0	199.4	251.1	1.26
	24	1.5	3.0	194.8	250.7	1.29
		3.0	3.0	172.4	224.8	1.30
	36	1.5	3.0	176.5	230.3	1.30
		3.0	3.0	156.7	208.1	1.33
144	24	1.5	3.0	197.4	254.0	1.29
		3.0	3.0	178.2	230.8	1.30
	36	1.5	3.0	178.9	233.4	1.30
		3.0	3.0	161.0	212.8	1.32
	48	1.5	3.0	172.8	226.2	1.31
		3.0	3.0	155.6	206.8	1.33

As expected, the Grade 70 material has a higher fracture toughness demand than the Grade 50 material. The increased demand was a result of the higher stress state for the Grade 70 FEA. While the stress demand increased by 40% from 37.5 ksi for Grade 50 to 52.5 ksi for Grade 70, the average increase in fracture toughness was 28.5%. The 16 comparisons resulted in minimum and maximum increases of 16.7% and 32.9%, respectively. Table 4.5 includes the ratio between the Grade 50 and Grade 70 fracture toughness for each model.

For a given web height and flange width, the 1.5 in. thick flange had a larger stress intensity demand than the 3.0 in. thick flange. While the flange thickness doubled, the stress intensity demand for the 3.0 in. flange was on average 90.1% of the 1.5 in. flange. The 16 comparisons had minimum and maximum differences of 97.7% and 86.0%, respectively. For a given web height and flange thickness, an increase in flange width resulted in a decrease in fracture toughness demand. The decrease in demand was the result of a drop in the reference stress with increase plate width.

Increasing the web height for a given flange width resulted in an increase in the fracture toughness demand. A larger increase was noted between the 36 in. and 72 in. deep webs as compared to the increase between the 72 in. and 144 in. deep webs. The reduced change in fracture toughness demand with increasing web height was a result of the through-thickness difference in stress between the top and bottom of the flange. Figure 4.26 displays the flange stress ratio between the two faces of a given flange for a symmetric girder. In Figure 4.26, a web height of 0.0 in. would indicate the neutral axis is between two plates directly on top of each other. For web heights of 30 in. and 54 in. there was less than a ten percent difference in stress between the top and bottom flange faces for a 1.5 in. and 3.0 in. thick flanges, respectively.

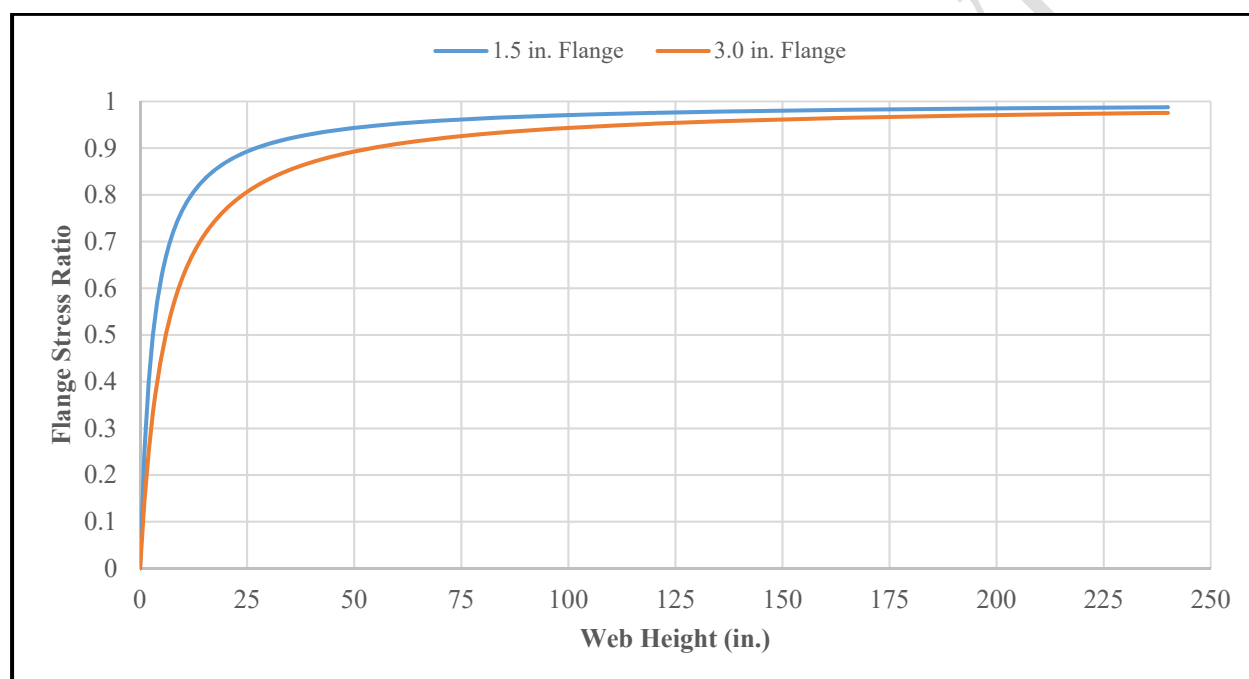


**Figure 4.26: Flange stress ratio**

## CHAPTER 5 INTEGRATED FRACTURE CONTROL PLAN

First released in 1978, the original AASHTO FCP was entitled *1978 AASHTO Guide Specification for Fracture Critical Non-Redundant Steel Bridge Members* (AASHTO, 1978). The intention of the 1978 FCP was to reduce the likelihood of brittle fracture through a process which included design review, material toughness specifications, fabrication requirements, welder certification, and weld inspector qualifications. However, as implemented, the components of the FCP were divided into separate and somewhat isolated or independent specifications designed to address material toughness, design, fabrication, and inspection independently. Design and material requirements are contained in the *AASHTO LRFD Bridge Design Specification* and ASTM A709-13a (AASHTO, 2014; ASTM, 2013a). Fabrication and shop inspection requirements are included housed in Clause 12 of the *AASHTO/AWS D1.5M/D1.5 Bridge Welding Code* (AASHTO & AWS, 2010). In-service inspection requirements are located in the *AASHTO Manual for Bridge Evaluation* (AASHTO, 2011). As such, currently no single, integrated plan addressing steel bridge fracture exists.

Nevertheless, the excellent service record of bridges fabricated to the FCP suggests the current approach has been successful in preventing failure due to brittle fracture. However, the FCP was not developed to ensure any specific performance level, crack tolerance versus inspection capability, or overall reliability. Advances in the understanding of fracture mechanics, material and structural behavior, fatigue crack initiation, fatigue crack growth, fabrication technology, and inspection technology have allowed other industries to address fracture in a more integrated manner. Through these advances, it is now possible to economically create an integrated FCP, combining the original intent of the 1978 FCP, with modern materials, design, fabrication, and inspection methodologies. Further, an integrated FCP will provide an economic benefit to owners by allowing for a better allocation of resources through the use of rational inspection intervals. In summary, an integrated FCP encompassing material, design, fabrication, and inspection can make

fracture no more likely than any other limit state; ultimately, allowing for a better allocation of owner resources and increased steel bridge safety.

### **5.1 Considerations**

To create an integrated FCP, consideration must be given to several factors. These factors include recognizing defects exist, bridge loading is variable, materials are variable, and both shop and in-service inspection methods have limitations and variability. While each of these realities can be concerning, each can be mitigated through a well-designed, integrated plan. Before discussing the components of an integrated FCP, it is important to understand each consideration and how it will impact the approach.

Flaws exist in all structures no matter the age, location, loading, structure type, etc. Such flaws can be introduced during fabrication or erection. Material defects, fatigue crack growth from live load stress, or damage due to an extreme event such as a vehicular impact are also sources. The most important consideration for any flaw is the criticality. It must be established if, under the assumed loading conditions and given material properties, the flaw will cause fracture at some point during the life of the structure. If the flaw is not determined to be critical, the second most important consideration is how much fatigue life exists before the flaw reaches its critical size. Both of these considerations will be evaluated in detail when discussing the components of an integrated FCP.

Bridges experience a variable loading spectrum ranging from passenger cars to super-heavy loads. As such, it is impossible to predict the exact load a given structure will experience at any moment in time. However, loading can be simplified when considering an integrated FCP. First, cracks grow in fatigue due to live load stress range. Therefore, live load stress range controls crack growth. Second, overloads typically control fracture. The exception to overloads controlling fracture is the case of constraint induced fracture (CIF), which is eliminated through proper design and detailing. Simplifying the variable loading spectrum to these two considerations allows it to be incorporated into an integrated FCP.

The fracture toughness data of any steel is highly variable; therefore, material variability must be considered when planning an integrated FCP. Fortunately, work has been performed in other industries to show it is possible to statistically characterize material variability through a

concept known as the master curve (McCabe, Merkle, & Wallin, 2005). Further, recent work has been performed on current ASTM A709 HPS as well as historical bridge steels to demonstrate the master curve concept can be applied to the steels commonly used in the bridge industry (William N Collins et al., 2016a). Statistical characterization of material toughness is an essential part of an integrated FCP because it allows for a reliability-based analysis. Through a reliability analysis the fracture limit state can be treated in design similar to any other reliability-based limit state.

Performing in-depth inspections on highly complex structures comes with a variety of limitations. Examples of such limitations include inspection technique, rigor of inspection method, or limited access, among many others. Regardless of the reason, inspection limitations must be considered when planning an integrated FCP. Recent work has been performed in the areas of setting rational inspection intervals as well as POD (Washer et al., 2014; Whitehead, 2015). Such studies have not only provided much needed insight into inspection limitations but have created tools to deal with these limitations. Further, understanding inspection from a statistical standpoint allows for in-service inspection to be incorporated into the reliability of an integrated FCP.

Fortunately, each consideration can be managed through a well-designed, integrated FCP. For example, material is available with high-toughness, capable of tolerating large cracks. Tolerable crack sizes can be calculated using modern fracture mechanics. Statistical methods are available to quantify material variability. Fatigue crack growth calculations are capable of computing fatigue life based on initial crack sizes. POD studies have begun to quantify detectable crack sizes. Rational inspection intervals can be established based on a safe fatigue crack growth life. Leveraging and integrating the results of such research will allow for fracture to be treated as any other reliability-based limit state.

## **5.2 Components of an Integrated Fracture Control Plan**

The essence of an integrated FCP is to prevent fracture through a series of checks and balances utilizing interrelated components, with redundancy built into the methodology. The idea of the methodology is if a shortcoming exists in one component it is safely compensated by another. Such a process starts with design and continues through the entire life of a structure. For new steel bridges the required components of an integrated FCP include design considerations, material properties, fabrication guidelines, and in-service inspection. Each component will be discussed in

detail in the following subsections. The components will be discussed chronologically of a typical bridge life cycle; however, it is important to remember each component is interrelated and tied to one another. The relationships between the components will also be discussed in the following sections

### **5.2.1 Design Considerations**

An integrated FCP approach needs to be developed and adopted at the outset of design. Early considerations regarding design details and live load stress range can directly impact the success of an integrated FCP. For example, designing a structure to have a low live load stress range and selecting highly fatigue resistant details could effectively eliminate the likelihood of fatigue crack growth during the life of the bridge or at least result in the probability of cracking being so low, it is acceptable to assume fatigue cracking is not a plausible limit state.

Selecting details with superior fatigue performance is only one aspect of detail selection for an integrated FCP. Equally important is selecting details which simplify fabrication. Complex details increase the probably of fabrication errors which can lead to in-service problems. Lastly, utilizing details which can be easily inspected is also imperative.

Design is the foundation for the integrated FCP. Decisions made during design can directly influence the overall performance of the integrated FCP over the lifespan of a structure.

### **5.2.2 Material Properties**

A subset of design considerations is material selection. The properties of the design material are also an important component of the integrated FCP. As such, material properties are treated independent of design considerations.

Material properties directly influences the tolerable crack size of a member. Critical flaw size is a byproduct of the fracture toughness of a given material. A material with a low fracture toughness can only tolerate small flaws before fracture. Conversely, a material with a high fracture toughness will be able to tolerate larger flaws before fracture. Tolerable flaw size is directly related to in-service inspection quality; the larger the flaw, the more likely it is to be detected during a routine inspection. However, if the inspection technique is not capable of detecting flaws that are critical, the material toughness and loading much be adjusted to ensure a defect of a detectible size

can be tolerated or it must be ensured cracks do not exist with a high degree of certainty. As such, when specifying material properties for a structure the designer is actually setting the critical flaw size required to be detected during an in-service inspection. Tying material properties to in-service inspection is fundamentally how the integrated FCP protects against fracture.

Material selection also impacts fabrication as different materials require specific fabrication processes. For example, specifying HPS over conventional A709 steel improves weldability by reducing the amount of preheat and post-weld treatment required. Improved weldability reduces the likelihood of defects in the weld metal or heat affected zone, thus improving the overall structure.

Identifying favorable material properties is a key component to the integrated FCP. Most important is selecting a material with adequate fracture toughness. For example, a damage tolerant material would be able to perform its intended function in the presence of a flaw. Additionally, material with “good” fabrication qualities will also help strengthen the integrated FCP.

### 5.2.3 Fabrication Guidelines

The current FCP is almost entirely focused on the fabrication of welded steel bridges. In fact, much of the FCP resides in Clause 12 of the *AASHTO/AWS D1.5M/D1.5 Bridge Welding Code* (AASHTO & AWS, 2010). Covering everything from weld processes to weld inspection to weld repair, the current FCP provides a necessary foundation for the integrated FCP for welded structures. Through decades of research and experience the current FCP has developed into a refined document. Historically, the current FCP has done a superb job of controlling fracture in steel bridges.

Much of the current FCP can be incorporated into an integrated approach by building upon the strengths of the current plan. For example, the current FCP includes inspection requirements and acceptance criteria for various welds produced during fabrication. At present, the acceptance and rejection criteria are solely based on workmanship with no tie to fatigue crack growth or fracture. An integrated FCP would tie the acceptance and rejection criteria to initial flaw sizes, crack growth rates, and variability in detection of certain inspection technique. In such an approach, the timing of in-service inspection cycles can be rationally established.

### 5.2.4 In-Service Inspections

Once a bridge has passed through the stages of design, fabrication, and erection, and has been put into service, an integrated FCP continues through in-service inspections. While design considerations, material properties, and fabrication guidelines all try to prevent fracture, in-service inspections can be used when it is not possible to exploit another component of an integrated FCP. For example, if it is not economically feasible to lower the design stress range and finite life must be used in design, the in-service inspection strategy can be tailored to adjust the reliability of the overall approach.

The inspection process can be defined by method, rigor, and interval. Method refers to the type of inspection being performed. Different methods might include visual, dye penetrant, magnetic particle, ultrasonic, or radiography. Rigor refers to the rate at which the method is applied. For example, a welded joint might be inspected 100% visually as well as 20% using magnetic particle inspection. Interval refers to the period of time between inspections. Currently, fracture critical members require a more in-depth inspection, commonly referred to as a hands-on inspection at an interval not to exceed 24 months (AASHTO, 2011; FHWA, 2013). The rigor of the inspection is highly variable from state to state, inspector to inspector, and bridge to bridge. For example, some states perform routine inspections from the ground, while others claim they always use snooper access. Clearly, the method, rigor, and interval associated with current bridge inspections are arbitrary and based on engineering judgement rather than an objective rationale.

An integrated FCP would establish the method, rigor, and interval of an inspection rationally. Using knowledge of the design, loading, environment, detection capabilities, and other characteristics would tie into the type and frequency of the inspection performed. With an integrated approach, the finite resources for inspection, maintenance, and repair are most efficiently appropriated. For example, it seems reasonable to suggest that the initial inspection frequency of a brand new bridge designed to the current design codes should not be the same frequency as a structure built before the modern fatigue provisions (Washer et al., 2014).

Further, an integrated FCP would use POD data to establish the reliability of a given inspection as well as to establish detectable flaw sizes. Quantifying inspection reliability is a key to the overall reliability analysis which will ensure fracture is no more likely than any other limit state. Establishing detectable flaw sizes is necessary to tie flaw acceptance criteria to inspection cycles through fatigue crack growth calculations.

### **5.3 An Integrated Approach**

To illustrate how an integrated FCP can be employed, an example of an integrated approach will be presented. A comparison is made between the current material specification and a damage tolerant material specification. The damage tolerant approach inherently accepts defects, assumed to be cracks, exist in all structures. Through the use of an integrated FCP these defects can be controlled ensuring fracture is no more likely than another reliability-based limit state. Using an initial assumed defect size, in-service live load stress range, and crack growth rate, an appropriate inspection interval will be calculated in the example. Further, consideration was given to POD. Following the illustration, a brief discussion compares the results of the two specifications. It must be emphasized that the tolerable sizes, inspections intervals etc. for steels meeting the current specification should only be used as a point of comparison. They are not intended to state that current provisions are unsafe or inadequate in the current non-integrated FCP. However, to make any quantitative comparison between current CVN requirements and those which can be achieved with an integrated approach using tougher steels, a uniform set of reasonable initial parameters must be established.

#### **5.3.1 Material Toughness**

ASTM A709 is the current material specification for structural steels used in bridges (AASHTO, 2014). The fracture critical CVN impact provisions are found in Table 9 of the ASTM Specification. Per ASTM A709, minimum required impact values must be satisfied at a given test temperature. The test temperature varies depending on the temperature zone in which the bridge is located. Each zone is based on the LAST at the location of the bridge: 0 °F for Zone I, -30 °F for Zone II, and -60 °F for Zone III. Specimens are tested at temperatures warmer than the LAST because of the dynamic nature of the CVN impact test versus the quasi-static loading rate of bridge structures, commonly referred to as the temperature shift. The toughness requirements of the Specification are intended to prevent cracks from initiating brittle fractures. To satisfy the requirements of the specification, the average CVN impact energy of three specimens must exceed the specified value. Additionally, the Specification requires all three CVN impact specimens exceed a prescribed minimum value for fracture critical components.

For purposes of simplification, only the HPS grades will be considered for the example. The current fracture critical CVN impact requirements for ASTM A709 HPS steels are presented in Table 5.1. Table 5.2 contains potential CVN impact energy values for a high-toughness, damage tolerant steel grade. To demonstrate the increase in tolerable crack size by increasing the CVN impact energy requirements, the 125 ft.-lbs. value targeted during the large-scale experimentation was applied for all temperature zones at the LAST for this illustration.

**Table 5.1: Current HPS material CVN impact requirements**

Grade	Thickness (in.)	Minimum Test Value Energy (ft.-lb.)	Minimum Average Energy (ft.-lb.)		
			Zone I	Zone II	Zone III
HPS 50W	≥ 4.0	24	30 @ 10 °F	30 @ 10 °F	30 @ 10 °F
HPS 70W	≥ 4.0	28	35 @ -10 °F	35 @ -10 °F	35 @ -10 °F
HPS 100W	≥ 2.5	28	35 @ -30 °F	35 @ -40 °F	35 @ -40 °F

**Table 5.2: High-toughness material CVN impact requirements**

Grade	Thickness (in.)	Minimum Test Value Energy (ft.-lb.)	Minimum Average Energy (ft.-lb.)		
			Zone I	Zone II	Zone III
Damage Tolerant	TBD	TBD	125 @ 0 °F	125 @ -30 °F	125 @ -60 °F

Numerous conversions exist to relate CVN impact energy to fracture toughness (William N Collins et al., 2016b). For this work, the methods presented in *BS7910:2013 Guide to Assessing the Acceptability of Flaws in Metallic Structures* were used to estimate fracture toughness (BSI, 2013). It should be noted, all equations included in BS7910 for the CVN impact energy to fracture toughness conversions use metric units and are presented as published in BS7910.

For the current specification, the master curve procedure was utilized to convert the CVN impact requirements to fracture toughness values. To employ the master curve, reference temperature values ( $T_0$ ) were estimated using BS7910 Equations J.2 and J.3, shown in Equation 5.1 and Equation 5.2, respectively (BSI, 2013). A straight-line fit was assumed between the equations and for any extrapolation.

$$T_0 = T_{27J} - 18 \text{ } ^\circ\text{C}$$

**Equation 5.1: BS7910 Equation J.2 for  $T_0$  estimation**

$$T_0 = T_{40J} - 24 \text{ } ^\circ\text{C}$$

**Equation 5.2: BS7910 Equation J.3 for  $T_0$  estimation**

The master curve procedure includes a size correction for material thickness as well as a 5% statistical tolerance bound on the fracture toughness, meaning there is a 95% probability the toughness will be greater than provided by the estimate. Further, the master curve procedure allows for fracture toughness to be calculated at any temperature once  $T_0$  is obtained. Equation J.4 from BS7910 for the master curve is presented in Equation 5.3 (BSI, 2013).

$$K_{mat} = 20 + \{11 + 77e^{[0.019(T-T_0-T_K)]}\} \left(\frac{25}{B}\right)^{\frac{1}{4}} \left[ \ln\left(\frac{1}{1-P_f}\right) \right]^{\frac{1}{4}}$$

**Equation 5.3: BS7910 Equation J.4 for master curve**

The example integrated FCP specification calls for CVN impact testing to be performed at the LAST, a major contrast to the provisions of the current specification which employ the temperature shift concept. Testing at the LAST permits the use of BS7910 Equation J.1 for the CVN impact energy to fracture toughness conversion, as presented in Equation 5.4, because no temperature conversion is required (BSI, 2013). In other words, the correlation used herein directly estimates static fracture toughness from CVN energy. Equation 5.4 is a lower bound equation for the lower shelf and transitional behavior and includes a size correction.

$$K_{mat} = \left[ (12\sqrt{C_v} - 20) \left(\frac{25}{B}\right)^{0.25} \right] + 20$$

**Equation 5.4: BS7910 Equation J.1 for lower shelf and transitional behavior**

Table 5.3 presents the resulting Zone III fracture toughness value for each steel grade for a 2 in. thick plate. The fracture toughness for the current specification is referred to as  $K_{Spec}$ ; while, the fracture toughness of the integrated FCP specification is referred to as  $K_{DT}$  ('DT' refers to Damage Tolerant). It should be noted for the damage tolerant grade, to ensure a uniform level of fracture resistance, different toughness values would need to be specified for different yield stresses and thicknesses. However, for illustration purposes, a single damage tolerant toughness is discussed and assumed to apply to all grades.

**Table 5.3: Zone III fracture toughness**

<b>CURRENT MATERIAL SPECIFICATION</b>	
<b>Grade</b>	<b><math>K_{Spec}</math> (ksi<math>\sqrt{in.}</math>)</b>
HPS 50W	35
HPS 70W	39
HPS 100W	46
<b>INTEGRATED FCP SPECIFICATION</b>	
<b>Grade</b>	<b><math>K_{DT}</math> (ksi<math>\sqrt{in.}</math>)</b>
Damage Tolerant	122

### 5.3.2 Tolerable Size

Fracture mechanics allows for the calculation of tolerable crack size based on material toughness. Calculations for the example were performed using an Option 1 Failure Assessment Diagram (FAD) as discussed in BS7910 (BSI, 2013). The Option 1 FAD is a conservative procedure used for fracture assessment. Additionally, the FAD considers both pure brittle fracture and pure ductile tearing as well as an interaction between both behaviors. The analysis was performed using an FAD because only using traditional LEFM has the potential to be unconservative due to the ratio of the reference stress to the yield stress.

Two of the most common geometries will be explored for this demonstration: a through-thickness edge crack and a through-thickness center crack. The geometries are presented in Figure 5.1. It should be noted, standard convention defines an edge crack with length  $a$ , and a center crack with length  $2a$ . This designation is followed in the figures, tables, and text of this example; therefore, crack sizes are always presented in terms of total measurable crack length.

Commercial software automating the BS7910 analyses called Signal Fitness-For-Service (FFS) was used for all fracture and crack growth assessments. Several parameters were held constant for all calculations. The width and thickness used in the computations were 18 in. and 2 in., respectively. For non-redundant steel bridges, the selected plate size represents a lower bound flange width and average flange thickness. The applied primary stress for the tolerable crack size calculation was set to 75% of material yield, as it reasonably corresponds to the maximum allowable overload (AASHTO, 2011). All geometries were modeled in Signal FFS as flat plates with cracks perpendicular to stress. Welds were not considered for the analysis and the flaw

location was in parent metal remote from any welds. The selected material was steel in air with a modulus of elasticity of 29,000 ksi. Tensile properties for each grade were defined as 50 ksi, 70 ksi, and 100 ksi for yield strength, while 65 ksi, 85 ksi, and 115 ksi were used for ultimate strength. Tolerable crack size results are presented in Table 5.4.

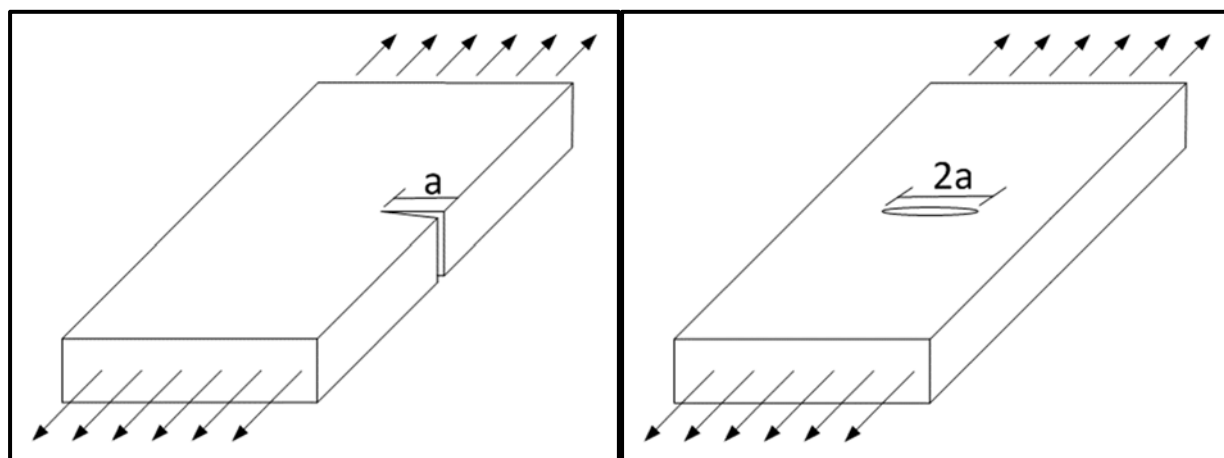


**Figure 5.1: Representative flanges with through-thickness edge (left) and center (right) cracks**

**Table 5.4: Tolerable crack sizes**

$F_y$ (ksi)	Applied Stress ( $0.75F_y$ ) (ksi)	CURRENT MATERIAL SPECIFICATION			INTEGRATED FCP SPECIFICATION		
		$K_{Spec}$ (ksi $\sqrt{in.}$ )	Edge	Center	$K_{DT}$ (ksi $\sqrt{in.}$ )	Edge	Center
			$a$ (in.)	$2a$ (in.)		$a$ (in.)	$2a$ (in.)
50	37.5	35	0.15	0.37	122	1.30	3.06
70	52.5	39	0.10	0.25	122	0.83	2.04
100	75.0	46	0.07	0.17	122	0.46	1.15

### 5.3.3 Fatigue Life

Fatigue life calculations were performed to determine the number of cycles to reach a given crack length. All analyses were performed utilizing the same parameters. A uniform constant amplitude stress range of 3 ksi was used for every analysis. Based on field monitoring performed on several in-service structures 3 ksi was deemed to be realistic and reasonable (Fasl, Helwig, Wood, & Frank, 2012; O'Connell, Dexter, & Bergson, 2001; Sherman, Mueller, Connor, & Bowman, 2011). The ratio of the minimum to maximum stress intensity is known as the R-ratio.

To allow for the influence of residual stresses the R-ratio was assumed to be greater than 0.5, as suggested by BS7910. The BS7910 fatigue coefficients at a temperature of 70 °F were used in conjunction with a piece-wise power law crack growth model (BSI, 2013). The threshold stress intensity value of 1.813 ksi $\sqrt{\text{in.}}$ , as specified in BS7910, was utilized. None of the other the coefficients related to fatigue crack growth were altered from those in BS7910 including  $\Delta K_1$  and  $\Delta K_2$  equal to 9.065 ksi $\sqrt{\text{in.}}$ , C1 equal to 6.452E-15, m1 equal to 8.160, and m2 and m3 equal to 2.880. The coefficients C2 and C3 were automatically calculated by Signal FFS.

Three initial flaw sizes were selected for each geometry. The same set of initial crack sizes values were used for both the geometries: 0.0625 in., 0.125 in., and 0.25 in. As presented in Figure 5.1, holding the initial crack size constant resulted in twice the measureable crack length for the center crack as compared to the edge crack. Shorter initial flaw lengths were selected for the edge crack because it is a more severe geometry from a fracture mechanics perspective. The selected initial flaw sizes were conservatively assumed to be large compared to what would be expected from a fabrication shop. However, a fracture mechanics-based assessment requires an initial flaw, and the selected sizes are thought to be realistic considering potential defects caused during erection or an extreme event such as an impact. All analyses were performed until the critical flaw length, presented in Table 5.4 was achieved. As stated, the overload stress was assumed to be 75% of the material yield strength. Results from the analysis, presented in terms of millions of cycles, can be found in Table 5.5.

The analyses resulting in no fatigue growth are designated by  $<\Delta K_{th}$ , indicating the stress intensity demand was below the threshold stress intensity and cracking was not expected. Conversely, the analyses which resulted in immediate failure because the initial flaw size was greater than critical flaw size were designated by *FAIL*.

Table 5.5: Fatigue life

$F_y$ (ksi)	CURRENT MATERIAL SPECIFICATION				INTEGRATED FCP SPECIFICATION			
	Edge		Center		Edge		Center	
	Initial a (in.)	Cycles (M)	Initial 2a (in.)	Cycles (M)	Initial a (in.)	Cycles (M)	Initial 2a (in.)	Cycles (M)
50	0.0625	$<\Delta K_{th}$	0.125	$<\Delta K_{th}$	0.0625	$<\Delta K_{th}$	0.125	$<\Delta K_{th}$
70		$<\Delta K_{th}$		$<\Delta K_{th}$		$<\Delta K_{th}$		$<\Delta K_{th}$
100		$<\Delta K_{th}$		$<\Delta K_{th}$		$<\Delta K_{th}$		$<\Delta K_{th}$
50	0.125	7.1	0.25	25.0	0.125	30.6	0.25	54.6
70		FAIL		FAIL		28.9		52.5
100		FAIL		FAIL		26.0		48.8
50	0.25	FAIL	0.5	FAIL	0.25	10.9	0.5	19.1
70		FAIL		FAIL		9.2		17.0
100		FAIL		FAIL		6.3		13.4

### 5.3.4 Inspection Interval

Using the calculated fatigue life, an inspection interval was tabulated. A few assumptions were required to convert the millions of cycles calculated from the fatigue life to an interval in years. The previously made assumptions about applied overload, stress range, detectable flaw size, and crack growth properties all still remain. In addition, it was assumed the ADTT for the given structure was 1000. As a point of reference, an ADTT of 1000 represented over 75% of all bridges in Indiana (INDOT, 2014). The objective of the example is to show how to set a rational inspection interval; therefore, any ADTT value can be substituted.

For the demonstration, the calculated inspection interval was tabulated directly from the total fatigue life. However, when setting an actual inspection interval using the integrated FCP, a reduced interval could be considered for added conservatism. Table 5.6 presents the number of years for both geometries at each initial flaw size. Analyses in which no crack growth was tabulated because the threshold stress intensity was not exceeded were designated by *Infinite*. Once again, the analyses resulting in immediate failure were designated by *FAIL*.

Table 5.6: Inspection interval

F <sub>y</sub> (ksi)	CURRENT MATERIAL SPECIFICATION				INTEGRATED FCP SPECIFICATION			
	Edge		Center		Edge		Center	
	Initial a (in.)	Interval (yr.)	Initial 2a (in.)	Interval (yr.)	Initial a (in.)	Interval (yr.)	Initial 2a (in.)	Interval (yr.)
50	0.0625	Infinite	0.125	Infinite	0.0625	Infinite	0.125	Infinite
70		Infinite		Infinite		Infinite		Infinite
100		Infinite		Infinite		Infinite		Infinite
50	0.125	19.6	0.25	68.6	0.125	83.9	0.25	149.5
70		FAIL		FAIL		79.2		143.9
100		FAIL		FAIL		71.2		133.7
50	0.25	FAIL	0.5	FAIL	0.25	29.9	0.5	52.2
70		FAIL		FAIL		25.3		46.6
100		FAIL		FAIL		17.3		36.6

#### 5.4 Current versus Integrated Specification

The above example compares the current fracture critical material specification to a damage tolerant specification, analyzed using an integrated FCP approach. To summarize the results, Table 5.7 combines the calculated inspection interval and final crack length for each geometry and each specification. Not all initial crack lengths are included in Table 5.7. Any initial flaw size resulting in an infinite interval for all grades was omitted from the comparison table: 0.625 in. initial crack length for the edge crack geometry and 0.125 in. initial crack length for the center crack geometry. When the initial crack length would result in immediate failure was designated by  $a_i > a_c$  in Table 5.7.

Table 5.7: Comparison of current and high-toughness FCP specification

Edge Crack					
F <sub>y</sub> (ksi)	Initial a	CURRENT MATERIAL SPECIFICATION		INTEGRATED FCP SPECIFICATION	
		Interval (yr.)	Final Crack Length (in.)	Interval (yr.)	Final Crack Length (in.)
50	0.125	19.6	0.15	83.9	1.30
70		FAIL	$a_i > a_c$	79.2	0.83
100		FAIL	$a_i > a_c$	71.2	0.46
50	0.25	FAIL	$a_i > a_c$	29.9	1.30
70		FAIL	$a_i > a_c$	25.3	0.83
100		FAIL	$a_i > a_c$	17.3	0.46
Center Crack					
F <sub>y</sub> (ksi)	Initial 2a (in.)	CURRENT MATERIAL SPECIFICATION		INTEGRATED FCP SPECIFICATION	
		Interval (yr.)	Final Crack Length (in.)	Interval (yr.)	Final Crack Length (in.)
50	0.25	68.6	0.37	149.5	3.06
70		FAIL	$a_i > a_c$	143.9	2.04
100		FAIL	$a_i > a_c$	133.7	1.15
50	0.5	FAIL	$a_i > a_c$	52.2	3.06
70		FAIL	$a_i > a_c$	46.6	2.04
100		FAIL	$a_i > a_c$	36.6	0.46

Ten out of 18 analyses resulted in immediate failure under the current specification. Aside from the analyses removed because infinite life was achieved for all analyses, the current specification Grade 70 and Grade 100 did not have a single successful analysis resulting in a calculated inspection interval. Further, none of the current specification analyses were able to tolerate an initial edge crack of 0.25 in. or an initial center crack of 0.5 in. Conversely, the integrated FCP specification never resulted in immediate failure. Additionally, the final crack lengths of the integrated FCP specification were on average over 7.5 times larger than the current specification resulting in an increase POD.

### **5.5 Inspection Interval and Critical Flaw Size Summary**

Additional inspection interval and critical flaw size calculations were performed for different CVN impact energies, plate thicknesses, and plate widths. Computations were performed for the current specification toughness values as well as for five high-toughness CVN impact energy values: 100 ft.-lbs., 125 ft.-lbs., 150 ft.-lbs., 175 ft.-lbs., and 200 ft.-lbs. at the Zone III LAST. For each toughness, the inspection interval and critical flaw size was tabulated for 1 in., 2 in., and 3 in. thick plates with an 18 in. width. The thicknesses selected represent common steel bridge components, while the 18 in. flange width represents a lower-bound flange width for a non-redundant steel bridge structures. Additionally, a 24 in. plate width was evaluated for the 2 in. thickness to determine the increase in life for increasing flange width. The same fracture and crack growth properties previously discussed were used for all calculations. Appendix H contains tables with all resulting fatigue life data for both the edge crack and center crack geometries at each fracture toughness. The tables include the initial flaw length, fracture toughness, plate width, yield strength, tensile strength, primary stress, plate thickness, critical flaw size, cycles to failure, and life in years.

A CVN impact energy of 125 ft.-lbs. results in over a 75-year inspection interval for all Grade 50 and 70 analyses with an initial edge flaw of 0.125 in. In addition to the inspection interval, the size of the critical defect as related to POD must be considered. For an initial edge flaw of 0.125 in. and a CVN impact energy of 125 ft.-lbs., it was found all analyses resulting in greater than a 75-year interval had critical flaw lengths greater than 0.7 in. Grade 100 did not result in fatigue growth lives longer than 75 years for 2 in. and 3 in. thicknesses. Additionally, the critical flaw sizes for those Grade 100 analyses not exceeding the 75-year design life were less than 0.5 in.

As stated, the results from the current specification should only be used as a point of comparison. None of the Grade 70 or Grade 100 analyses could tolerate a through-thickness edge crack of 0.125 in. Further, while it was possible to calculate fatigue crack growth lives for the current specification Grade 50, the longest life was only 35.5 years and had a critical flaw length less than 0.2 in.

A review of the inspection interval and critical flaw size results presented in Appendix H for the proposed CVN level of 125 ft.-lbs. demonstrates it is possible to set a fracture toughness specification to eliminate fracture critical hands-on inspections or significantly extend such

inspections using rational criteria. In many cases, the calculated interval is longer than the 75-year bridge service life, indicating no special fracture critical inspection is required. While the critical crack size may be a challenge to identify with traditional visual techniques, the time required to reach the critical crack size exceeds the design life in most cases. Therefore, if a bridge is designed to be in service for 75 years, the toughness and live load stress range levels can be set to ensure the fracture limit state is not plausible during the life of the structure. Alternatively, a highly detailed inspection corresponding to when a crack becomes critical could be performed at an interval less than the life. Such an inspection would utilize non-destructive evaluation to ensure a high POD. Using an integrated approach, as described, traditional routine bridge inspections would only be required to identify other damage such as corrosion, impact, or scour at the traditionally accepted 24-month interval

## CHAPTER 6 CONCLUSIONS

Significant advances have been made over the past 40 years since the introduction of the original FCP. Developments in fracture mechanics, material and structural behavior, fatigue crack initiation and growth, and fabrication and inspection technologies allow fracture to be addressed in a more integrated manner. Through these advances, it is now possible to create an integrated FCP, combining the intent of the original FCP with modern materials, design, fabrication, and inspection methodologies. The purpose of this research was to develop new design standards which were founded using an integrated approach to prevent fracture in steel bridges through the use of high-toughness steel. The project was comprised of small-scale material testing, full-scale fracture testing of steel bridge axial and bending members, three-dimensional FEA, and an analytical parametric study. Results from this research as well as recommendations for future work are summarized below.

### **6.1 Summary of Primary Findings**

1. CVN impact data were used to screen materials for large-scale experimentation. A five-parameter sigmoidal function was fit to the CVN impact data and used to determine the temperature corresponding to 125 ft.-lbs. Up to 30 CVN specimens were tested at a single test temperature for a given plate. Large CVN variability was observed for high-toughness steel. The largest CVN range documented for a given plate at a single test temperature was 166.5 ft.-lbs. for Plate E, a non-HPS grade plate.
2. Percent shear was estimated for all CVN impact specimens. Large percent shear variability was found for a CVN impact energy of 125 ft.-lbs. Percent shear values for 125 ft.-lbs. ranged from 40% to 90%. Additionally, the CVN impact energy ranged approximately 50 ft.-lbs. at any given percent shear.
3. The reference temperature anchors the exponential master curve. Charpy-sized SE(B) specimens were used to determine the reference temperature for the test material from the

large-scale experiments. All four plates demonstrated a reference temperature of  $-200.0^{\circ}\text{F}$  or lower.

4. Full-sized SE(B) specimens were tested in an attempt to determine the onset of stable crack extension ( $J_{Ic}$ ) for the four large-scale test specimen plates. The same test temperature as the large-scale experiments, corresponding to a CVN impact energy of 125 ft.-lbs., were used for the  $J_{Ic}$  tests. None of the test specimens experienced stable tearing; therefore, no valid  $J_{Ic}$  were obtained.
5. The  $K_{Jc}$  results from the full-sized SE(B) specimens were plotted on the master curves developed from the Charpy-sized SE(B) specimens. Results for the full-scale SE(B) specimens generally fell below the 95% tolerance bound of the master curves. It is believed the Charpy-sized SE(B) specimens do not provide enough crack tip constraint for high-toughness steel.
6. The initial large-scale fracture test procedure grew the fatigue crack in small increments in attempt to capture the critical flaw size within a fraction of an inch. FEA indicated large compressive residual stresses were developed at the crack tip when the experiment did not result in a fracture. The compressive stresses lead to large crack lengths. As such, a large load not resulting in a fracture within a cracked structure will increase the fracture resistance.
7. The dog bone fracture arrest detail was capable of arresting a running fracture in an I-girder web during the four high-toughness large-scale bending experiments.
8. The fracture toughness demands calculated using FEA for all plates were comparable for both the bending and axial large-scale experiments.
9. The fracture toughness demands calculated based on the results of the large-scale specimens generally fell below the 95% tolerance bound of the master curves developed from the Charpy-sized SE(B) specimens.
10. The fracture toughness demands calculated using FEA for all large-scale specimens were comparable to the large SE(B) specimens. Hence, for a known fracture toughness, FEA can be reliably employed to determine the critical flaw size for a given geometry.
11. Critical flaw sizes were calculated for the current material specification and for high-toughness steel using linear-elastic fracture mechanics. BS7910 was used to correlate the specified CVN impact energies to a lower-bound fracture toughness for each grade of HPS.

The current AASHTO material toughness requirements can result in small, undetectable critical flaw sizes; conversely, high-toughness steel can result in detectable critical flaw sizes. Therefore, it is possible to set a fracture toughness specification to result in detectable critical flaw sizes.

12. The current AASHTO fracture control plan is fragmented. Design, material, fabrication, and inspection are addressed independently with no tie between each of the components. An integrated FCP has the potential to prevent fracture through a series of checks and balances utilizing interrelated components, with redundancy built into the methodology.
13. Through the use of an integrated FCP, rational inspection intervals can be established. Using rational inspection intervals will lead to safer structures and provide a better allocation of owner resources. No longer does a fracture critical hands-on inspection need to be performed at an arbitrary interval; rather, the remaining fatigue life can be calculated and a rational interval can be set to ensure multiple opportunities to detect a defect before it becomes critical. Finally, it is clear the arbitrary 24-month FC inspection interval provides no specific level of reliability against fracture.
14. It is recommended a CVN impact energy of 125 ft.-lbs. at the LAST be set for non-redundant steel bridges made from Grade 50 and Grade 70. For an initial 0.125 in. through-thickness edge crack, the fatigue crack growth for Grade 50 and Grade 70 is longer than the 75-year bridge service life, indicating no special hands-on fracture critical inspection is required during the bridge service life. As such, routine bridge inspections only need to be performed to identify other forms of damage such as corrosion, impact, or scour.
15. It is recommended a CVN impact energy of 125 ft.-lbs. at the LAST be set for non-redundant steel bridges made from Grade 100. Grade 100 structures should be inspected at an interval of 20 years using non-destructive evaluation. A 20-year interval allows for three inspections prior to cracks becoming critical. Additionally, non-destructive evaluation should be employed because the current POD data suggests visual inspection is not capable of detecting the critical flaw lengths.

## **6.2 Recommendations for Future Work**

1. Large variability in CVN impact energy was measured for the high-toughness steel plates. Prior to setting a CVN impact energy specification for high-toughness steel, the variability within a high-toughness steel plate needs to be quantified.
2. The variability in CVN impact energy for high-toughness steels produced using TMCP versus Q&T plates should be established.
3. Through the current research as well as previous studies, the fracture performance of high-toughness ASTM A709 50, 50W, HPS 70, and HPS 100W has been well established. Limited data exists on the fracture performance of HPS 50W; therefore, future work should focus on quantifying the fracture performance of HPS 50W.
4. The dog bone fracture arrest detail consistently arrested a running fracture in an I-girder web. The fracture performance of a dog bone fracture arrest detail should be tested in the flange for a beam.
5. Fracture toughness data for the large-scale test specimens and full-sized SE(B) specimens typically fell below the 95% confidence interval of the master curves produced using Charpy-sized SE(B) specimens. An evaluation comparing the reference temperature determined by full-sized SE(B) specimens versus Charpy-sized SE(B) specimens for high-toughness steel should be conducted.
6. The CVN impact test is an indirect measure of fracture toughness. While the test is attractive because of its inherent efficiency and low cost, the results are widely variable and do not represent a true fracture toughness. Therefore, further research is needed to identify an accurate, cost effective alternative to CVN impact testing.
7. Setting rational inspection intervals through fatigue crack growth calculations requires an initial flaw size assumption. To accurately compute the fatigue crack life, initial flaw sizes for steel bridge members must be established.
8. The integrated FCP has the capability to assess fracture statistically and make fracture no more likely than any other reliability based limit state. However, a reliability analysis for non-redundant steel bridge members is required to establish appropriate beta values.
9. During material screening, steel plate was identified capable of stopping a 300 ft.-lb. CVN impact hammer. A large-scale fracture experiment, with associated small-scale material testing, should be conducted.

## LIST OF REFERENCES

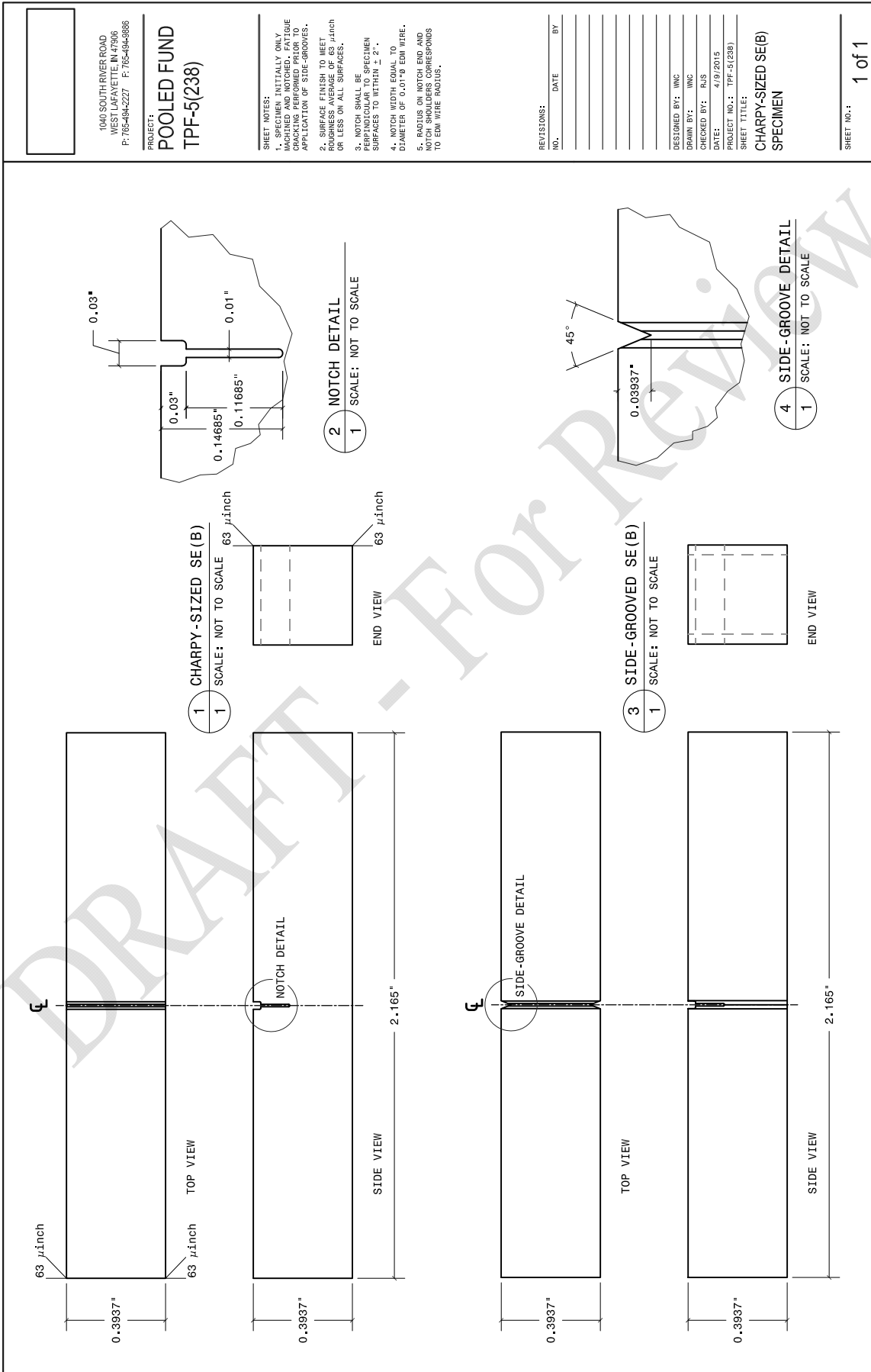
- AASHTO. (1969). *AASHTO Standard Specification for Highway Bridges* (10th ed.). Washington, DC: American Association of State Highway and Transportation Officials.
- AASHTO. (1978). *Guide Specifications for Fracture Critical Steel Bridge Members*. Washington, DC: American Association of State Highway and Transportation Officials.
- AASHTO. (2011). *The Manual For Bridge Evaluation* (2nd ed.). Washington, DC: American Association of State Highway and Transportation Officials.
- AASHTO. (2014). *AASHTO LRFD Bridge Design Specifications* (7th ed.). Washington, DC: American Association of State Highway and Transportation Officials.
- AASHTO, & AWS. (2010). *AASHTO/AWS D1.5 Bridge Welding Code* (6th ed.). American Welding Society.
- AISI. (2011). *Guide Specification for Highway Bridge Fabrication with High Performance Steel* (3rd ed.). Washington, DC: Steel Market Development Institute.
- Altstadt, S. (2008). *A Deterministic Damage Tolerant Design Procedure for Fracture Critical Members in Steel Bridges*. Purdue University.
- API. (2007). *API 579-1 Fitness-For-Service* (2nd ed., Vol. 2007). Washington, DC: American Petroleum Institute.
- ASTM. (2011). ASTM E1019-11: Standard Test Methods for Determination of Carbon, Sulfur, Nitrogen, and Oxygen in Steel and in Steel, Iron, Nickel, and Cobalt Alloys by Various Combustion and Fusion Techniques. West Conshohocken, PA: ASTM International. doi:10.1520/E1019-11.Copyright
- ASTM. (2012a). ASTM A673-07: Sampling Procedure for Sampling for Impact Testing of Structural Steel. West Conshohocken, PA: ASTM International. doi:10.1520/A0673
- ASTM. (2012b). ASTM E23-12c: Standard Test Methods for Notched Bar Impact Testing of Metallic Materials 1. West Conshohocken, PA: ASTM International. doi:10.1520/E0023-12C.2
- ASTM. (2013a). ASTM A709-13a: Standard Specification for Structural Steel for Bridges. West Conshohocken, PA: ASTM International. doi:10.1520/A0709
- ASTM. (2013b). ASTM E1921-13a: Standard Test Method for Determination of Reference Temperature,  $T_o$ , for Ferritic Steels in the Transition Range. West Conshohocken, PA: ASTM International. doi:10.1520/E1921-13A.2
- ASTM. (2014). ASTM E415-14: Standard Test Method for Analysis of Carbon and Low-Alloy Steel by Spark Atomic Emission Spectrometry. West Conshohocken, PA: ASTM International. doi:10.1520/E0415-08.2

- ASTM. (2015a). ASTM E1820-15a Standard Test Method for Measurement of Fracture Toughness. West Conshohocken, PA: ASTM International. doi:10.1520/E1820-15
- ASTM. (2015b). ASTM E8/E8M: Standard Test Methods for Tension Testing of Metallic Materials. West Conshohocken, PA: ASTM International. doi:10.1520/E0008
- Barsom, J. M. (1974). *The Development of AASHTO Fracture-Toughness Requirements for Bridge Steels*. Monroeville, PA.
- Barsom, J. M. (1975). Development of the AASHTO Fracture Toughness Requirements for Bridge Steels. *Engineering Fracture Mechanics*, 7, 605–618.
- Boreas, A. (2010). Don't Drop the Drop-Weight Tear Test. *Journal of Pipeline Engineering*, 9(2).
- BSI. (2013). *BS7910:2013 - Guide to Methods for Assessing the Acceptability of Flaws in Metallic Structures* (3rd ed.). British Standards Institution.
- Collins, W. N., Sherman, R. J., Connor, R. J., & Leon, R. T. (2016a). State-of-the-Art Fracture Characterization. I: Master Curve Analysis of Legacy Bridge Steels. *Journal of Bridge Engineering*.
- Collins, W. N., Sherman, R. J., Connor, R. J., & Leon, R. T. (2016b). State-of-the-Art Fracture Characterization. II: Examination of Correlations between Charpy V-Notch and the Master Curve Reference Temperature, To. *Journal of Bridge Engineering*.
- Collins, W. N., Wright, W. J., Leon, R. T., Cousins, T. E., Dowling, N. E., & Weyers, R. E. (2014). *Fracture Behavior Characterization of Conventional and High Performance Steel for Bridge Applications*. Virginia Polytechnic Institute.
- Connor, R. J., Dexter, R. J., & Mahmoud, H. N. (2005). *NCHRP Synthesis 354: Inspection and Management of Bridges with Fracture-Critical Details*. Washing: Transportation Research Board.
- Fasl, J., Helwig, T., Wood, S. L., & Frank, K. (2012). Use of Strain Data to Estimate Remaining Fatigue Life of a Fracture-Critical Bridge. *Transportation Research Record: Journal of the Transportation Research Board*, 2313(-1), 63–71. doi:10.3141/2313-07
- Federal-Aid Highway Act of 1968, Pub. L. No. 82 Statute 815 (1968).
- FHWA. (1971). National Bridge Inspection Standards. *Federal Register*, 36(81), 26–27.
- FHWA. (1986). *Inspection of Fracture Critical Bridge Members*. McLean, VA: Federal Highway Administration.
- FHWA. (1988). National Bridge Inspection Standards. *Federal Register*, 53, 32611.
- FHWA. 23 CFR §650.311 (2013).
- Frank, K. H., George, D. A., Schluter, C. A., Gealy, S., & Horos, D. R. (1993). *NCHRP Report 355: Notch Toughness Variability in Bridge Steel Plates*. Washington, DC.
- Gentilcore, M. L. (1996). *Ductile tearing of high-toughness steel members*. Lehigh University.
- Grandt, A. F. J. (2004). *Fundamentals of Structural Integrity*. Hoboken, NJ: John Wiley & Sons.
- Hamby, G., Clinton, G., Nimis, R., & Lwin, M. M. (2002). *High Performance Steel Designer's Guide* (2nd ed.). San Francisco, CA.

- Hartbower, C. E. (1979). *Reliability of the AASHTO Temperature Shift in Material Toughness Testing*. Washington, DC.
- Hartbower, C. E., & Sunbury, R. D. (1975). *Variability of Fracture Toughness in A514/517 Plate*. Washington, DC.
- INDOT. (2014). Indiana Department of Transportation Bridge Inventory Database. Indianapolis, IN.
- Kumar, V., German, M. D., & Shih, C. F. (1981). *An Engineering Approach for Elastic-Plastic Fracture Analysis*. Schenectady, NY.
- Manahan, M. P., & Mccowan, C. N. (2008). Percent Shear Area Determination in Charpy Impact Testing Original Charpy Test Development Historical Perspective on the Use of Percent Shear. *Journal of ASTM International*, 1–28.
- McCabe, D. E., Merkle, J. G., & Wallin, K. (2005). *An Introduction to the Development and Use of the Master Curve Method*. West Conshohocken, PA: ASTM International.
- NTSB. (1968). *Collapse of US 35 Highway Bridge Point Pleasant, West Virginia December 15, 1967*. Washington, DC.
- NTSB. (1984). *Collapse of a Suspended Span of Interstate Route 95 Highway Bridge Over the Mianus River Greenwich, Connecticut June 28, 1963*. Washington, DC: National Transportation Safety Board.
- O’Connell, H., Dexter, R., & Bergson, P. (2001). Fatigue evaluation of the deck truss of bridge 9340. *Civil Engineering*. Retrieved from <http://trid.trb.org/view.aspx?id=730436>
- Sherman, R. J., Mueller, J. M., Connor, R. J., & Bowman, M. D. (2011). *Evaluation of Effects of Super-Heavy Loading on the US-41 Bridge over the White River*. West Lafayette, IN.
- Washer, G., Connor, R. J., Ciolko, A., Kogler, R., Fish, P., & Forsyth, D. (2014). *NCHRP Report 782: Proposed Guideline for Reliability-Based Bridge Inspection Practices*. Washington, DC: Transportation Research Board.
- Wells, D. N., & Allen, P. A. (2012). *Analytical Round Robin for Elastic-Plastic Analysis of Surface Cracked Plates : Phase I Results*. Huntsville, AL.
- Whitehead, J. (2015). *Probability of Detection Study for Visual Inspection of Steel*. West Lafayette, IN: Purdue University.
- Wilson, A. (2005). *Improvements to High Performance Steels by* (Vol. 110).
- Wright, W. J. (2003). *Fracture Initiation Resistance of I-girders Fabricated from High-Performance Steels*. Lehigh University.

**Appendix A Fracture Toughness Specimen Design Drawings**

DRAFT - For Review



1040 SOUTH RIVER ROAD  
WEST LAFAYETTE, IN 47906  
P: 765-494-2227 F: 765-494-9886

PROJECT:  
**POOLED FUND**  
**TPF-5(238)**

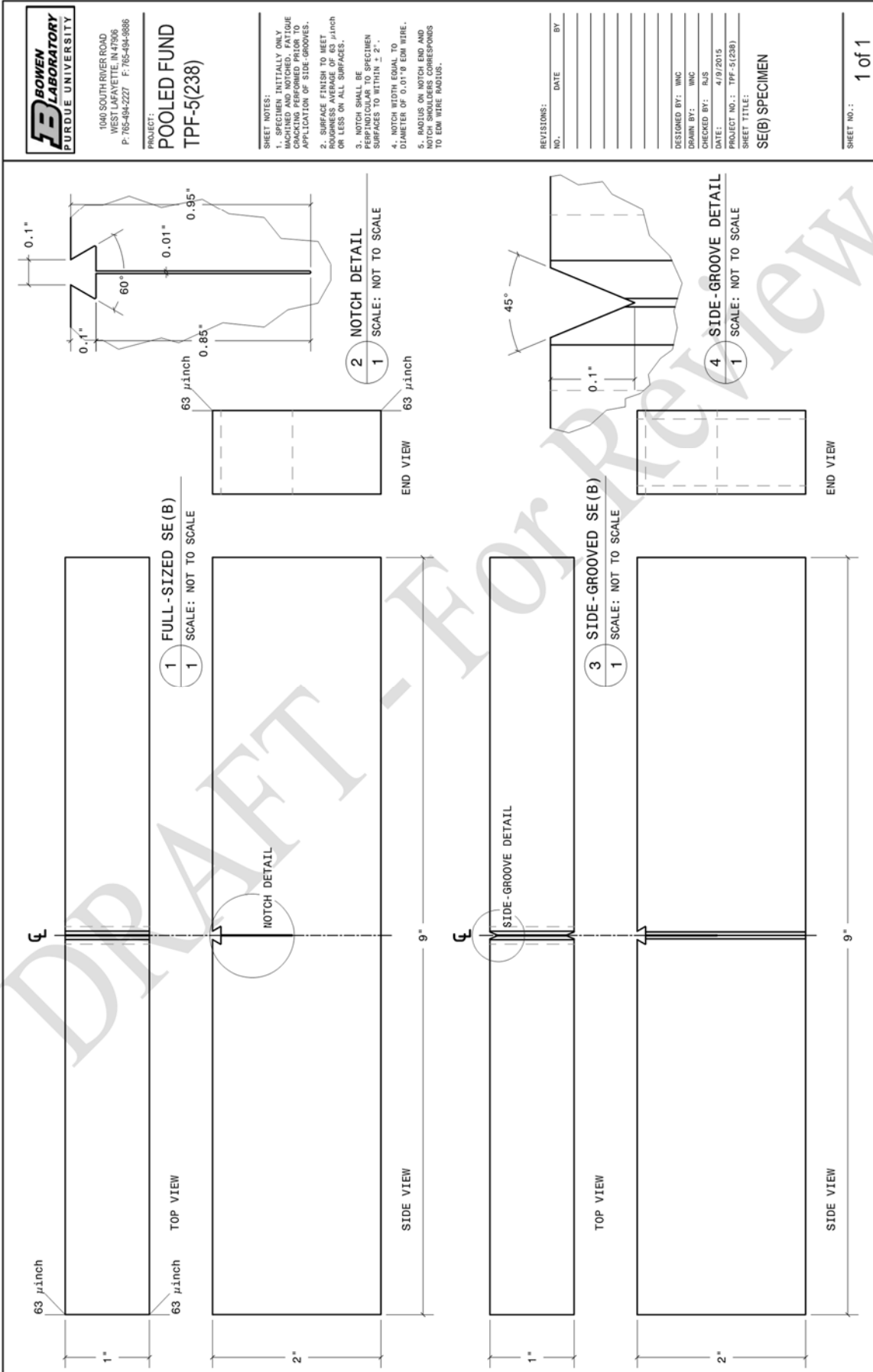
- SHEET NOTES:
1. SPECIMEN INITIALLY ONLY MACHINED AND NOTCHED. FATIGUE SURFACES TO BE FINISHED BY APPLICATION OF SIDE-GROOVES.
  2. SURFACE FINISH TO MEET REQUIREMENTS OF SPECIFICATION OR LESS ON ALL SURFACES.
  3. NOTCH SHALL BE PERPENDICULAR TO SPECIMEN SURFACES TO WITHIN ± 2°.
  4. NOTCH WIDTH EQUAL TO DIAMETER OF 0.01" EDM WIRE.
  5. RADIUS ON NOTCH END AND SIDE-GROOVE END SHALL RESPOND TO EDM WIRE RADIUS.

REVISIONS:

NO.	DATE	BY

DESIGNED BY: WNC  
DRAWN BY: WNC  
CHECKED BY: RJS  
DATE: 4/9/2015  
PROJECT NO.: TPF-5(238)  
SHEET TITLE:

**CHARPY-SIZED SE(B)**  
**SPECIMEN**



**Appendix B Bending Specimen Design Drawings**

DRAFT - For Review



1040 SOUTH RIVER ROAD  
WEST LAFAYETTE, IN 47906  
P: 765-494-2227 F: 765-494-8886

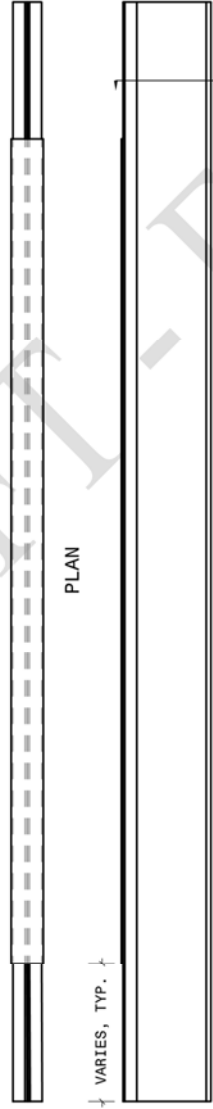
PROJECT:  
**POOLED FUND**  
**TPF-5(238)**

- SHEET NOTES:
- (2) SPECIMENS REQUIRED FOR EACH SPECIMEN SIZE
  - SPICES IN TEST ZONE REGION SHALL BE FROM HEAT 9104617
  - SPICES IN TEST ZONE REGION BOTTOM FLANGE SHALL NOT BE FROM HEAT 9104617
  - ALL TOP FLANGE MATERIAL SHALL NOT BE FROM HEAT 9104617
  - ANY MATERIAL SPliced ON TO THE BOTTOM FLANGE SHALL NOT BE FROM HEAT 9104617
  - FROM HEAT 9104617 SHALL BE SAVED FOR FUTURE SPECIMEN FABRICATION
  - ZONE REGION ON OTHER

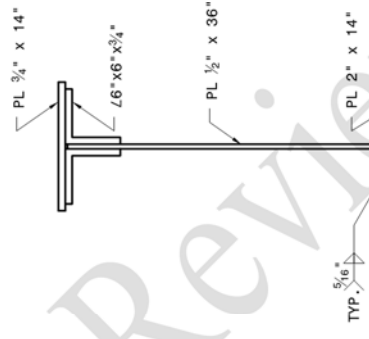
REVISIONS:  
NO. DATE BY

DESIGNED BY: RJS  
DRAWN BY: RJS  
CHECKED BY: RJC  
DATE: 8/27/2015  
PROJECT NO.: TPF-5(238)  
SHEET TITLE:  
SPECIMEN 50\_2-0\_B

SHEET NO.: 1 of 1



1 SPECIMEN 50\_2-0\_B  
SCALE: NOT TO SCALE



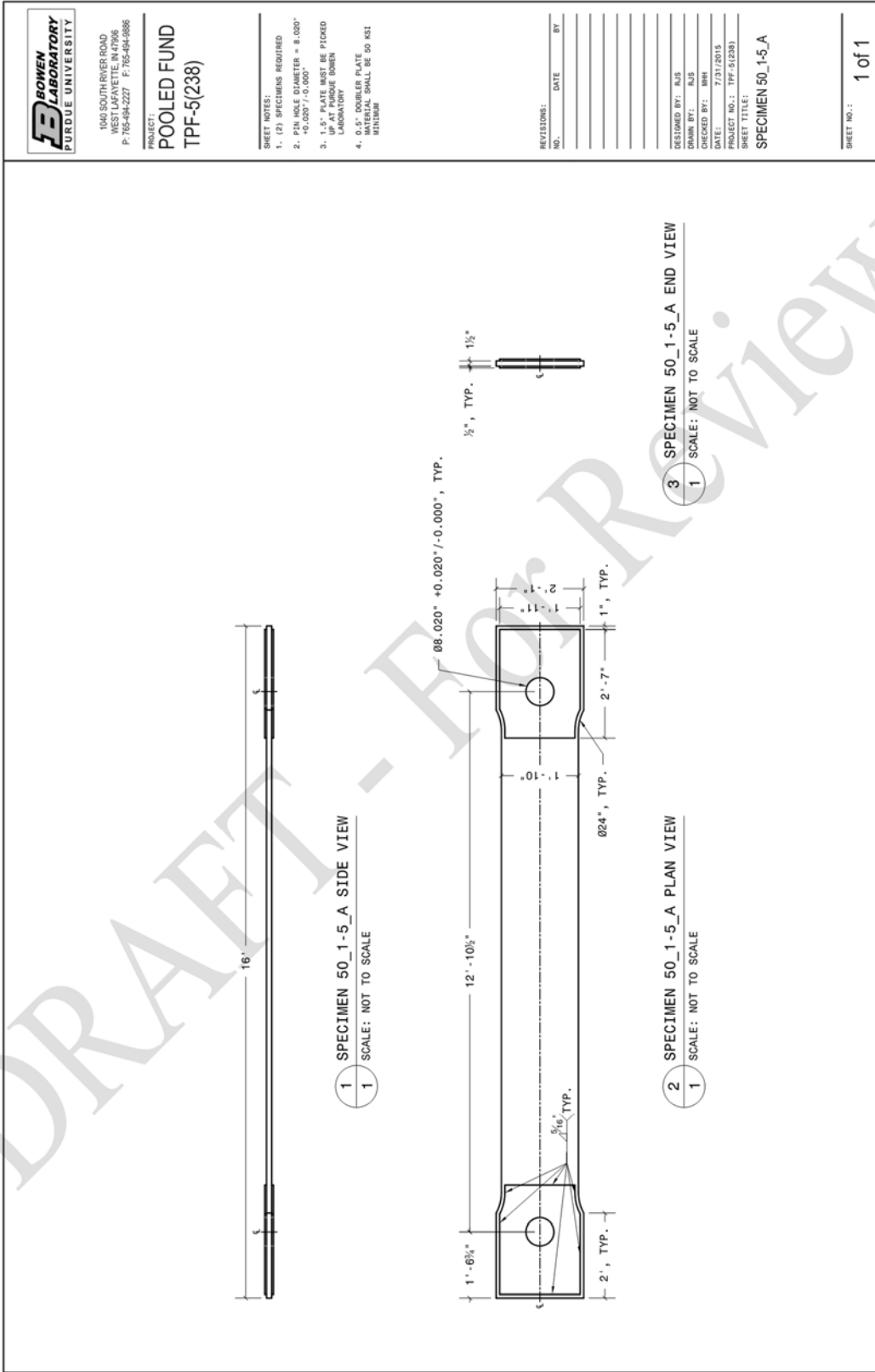
2 SPECIMEN 50\_2-0\_B X-SECTION  
SCALE: NOT TO SCALE





**Appendix C Axial Specimen Design Drawings**

DRAFT - For Review



1645 SOUTHURVERS ROAD  
WEST LAFAYETTE IN 47906  
P: 765-494-2227 F: 765-494-3886

PROJECT:  
**POOLED FUND**  
**TPF-5(238)**

- SHEET NOTES:
- (2) SPECIMENS REQUIRED
  - FIN HOLE DIAMETER = 8.020" ±0.002 / -0.000
  - 1.5" PLATE MUST BE PICKED UP AT BOWEN LABORATORY
  - 0.5" DOUBLER PLATE MATERIAL SHALL BE 50 KSI MINIMUM

REVISIONS:

NO.	DATE	BY

DESIGNED BY: RJS  
DRAWN BY: RJS  
CHECKED BY: MBH  
DATE: 7/31/2015  
PROJECT NO.: TPF-5(238)  
SHEET TITLE:  
**SPECIMEN 50\_1-5\_A**

SHEET NO.: **1 of 1**





**Appendix D Strain Gage Drawings**

DRAFT - For Review



1040 SOUTH RIVER ROAD  
WEST LAFAYETTE, IN 47906  
P: 765-494-2227 F: 765-494-8886

PROJECT:  
**POOLED FUND  
TPF-5(238)**

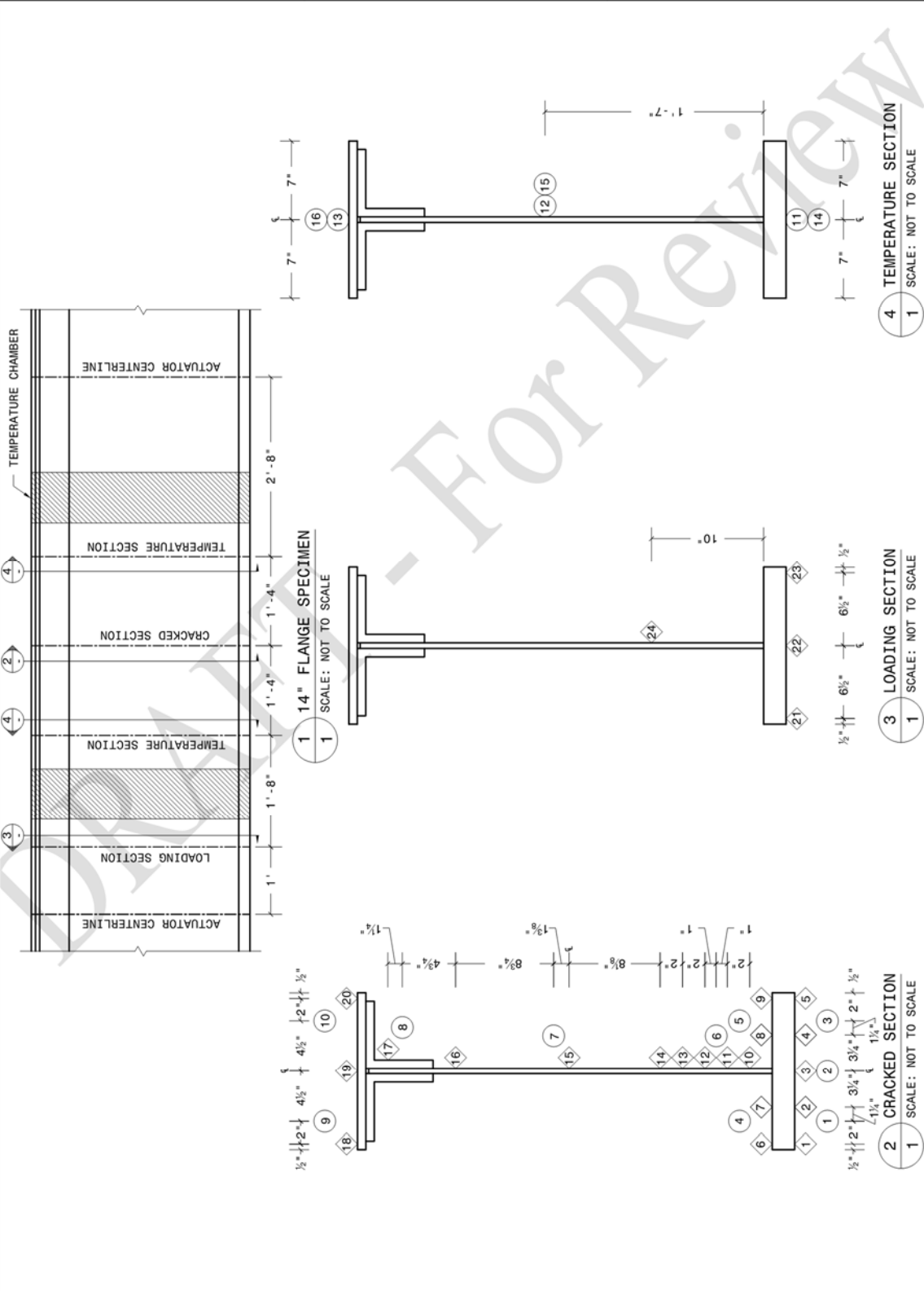
- SHEET NOTES:  
1. DIAMONDS REPRESENT STRAIN GAGES  
2. CIRCLES REPRESENT THERMOCOUPLES  
3. THERMOCOUPLES 1 AND 10 WIRE INTO TEMPERATURE CONTROLLER

REVISIONS:  
NO. \_\_\_\_\_ DATE \_\_\_\_\_ BY \_\_\_\_\_

DESIGNED BY: NJS  
DRAWN BY: NJS  
CHECKED BY: MBH  
DATE: 11/7/2015  
PROJECT NO.: TPF-5(238)  
SHEET TITLE:

**SPECIMEN 50\_2-0-B  
INSTRUMENTATION  
PLAN**

SHEET NO.: **1 of 1**







1040 SOUTH RIVER ROAD  
WEST LAFAYETTE, IN 47906  
P: 765-494-2227 F: 765-494-8886

PROJECT:  
**POOLED FUND  
TPF-5(238)**

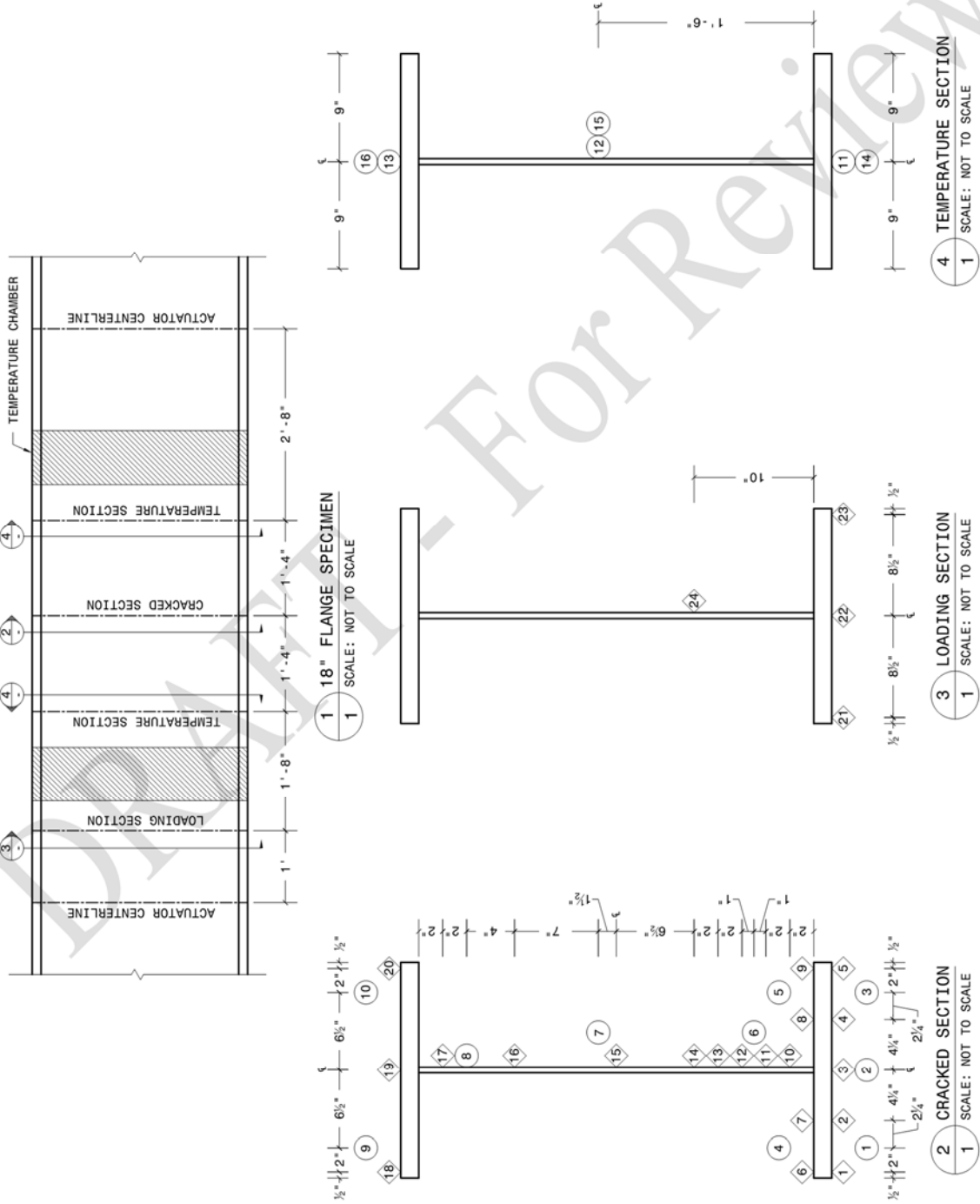
- SHEET NOTES:
- DIAMONDS REPRESENT STRAIN GAGES
  - CIRCLES REPRESENT THERMOCOUPLES
  - THERMOCOUPLES 1 AND 10 WIRE INTO TEMPERATURE CONTROLLER

REVISIONS:  
NO. DATE BY

DESIGNED BY: NJS  
DRAWN BY: NJS  
CHECKED BY: MBH  
DATE: 1/6/2016  
PROJECT NO.: TPF-5(238)  
SHEET TITLE:

**SPECIMEN 70\_1-5-B  
INSTRUMENTATION  
PLAN**

SHEET NO.: **1 of 1**





1040 SOUTH RIVER ROAD  
WEST LAFAYETTE, IN 47906  
P: 765-494-2227 F: 765-494-8886

PROJECT:  
**POOLED FUND  
TPF-5(238)**

- SHEET NOTES:
- DIAMONDS REPRESENT STRAIN GAGES
  - CIRCLES REPRESENT THERMOCOUPLES
  - THERMOCOUPLES 3 AND 4 WIRE INTO TEMPERATURE CONTROLLER
  - THERMOCOUPLE 7 INSTALLED AT MID-PLATE THICKNESS

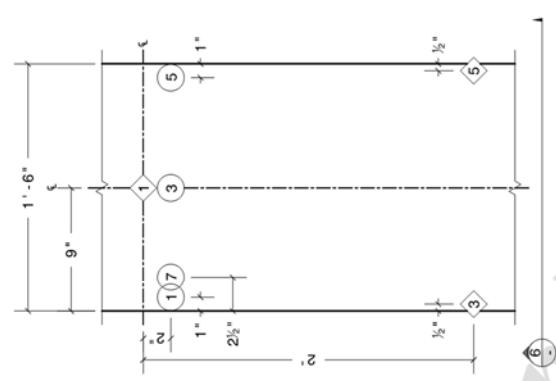
REVISIONS:

NO.	DATE	BY

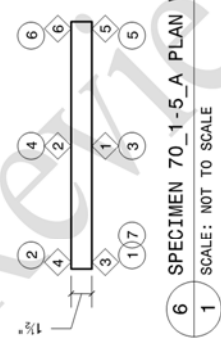
DESIGNED BY: RJS  
DRAWN BY: RJS  
CHECKED BY: MBH  
DATE: 1/20/2016  
PROJECT NO.: TPF-5(238)  
SHEET TITLE:

AXIAL SPECIMENS  
INSTRUMENTATION

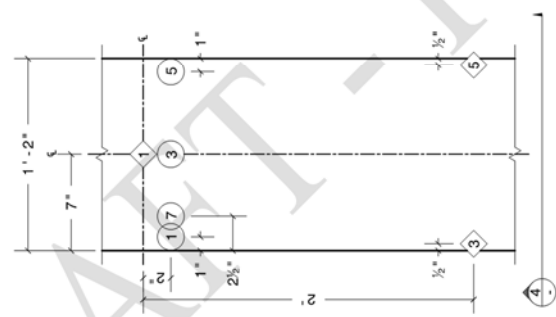
SHEET NO.: **1 of 1**



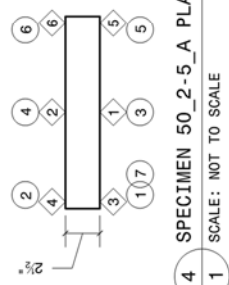
**5** SPECIMEN 70\_1-5\_A  
**1** SCALE: NOT TO SCALE



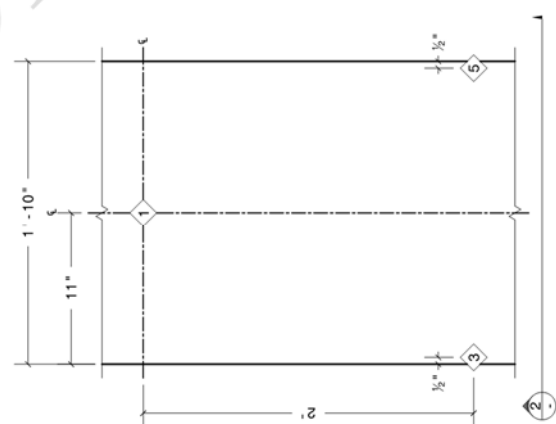
**6** SPECIMEN 70\_1-5\_A PLAN VIEW  
**1** SCALE: NOT TO SCALE



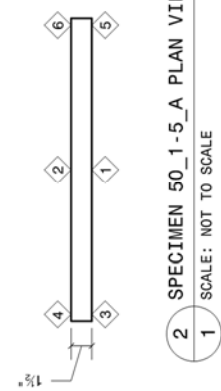
**3** SPECIMEN 50\_2-5\_A  
**1** SCALE: NOT TO SCALE



**4** SPECIMEN 50\_2-5\_A PLAN VIEW  
**1** SCALE: NOT TO SCALE



**1** SPECIMEN 50\_1-5\_A  
**1** SCALE: NOT TO SCALE



**2** SPECIMEN 50\_1-5\_A PLAN VIEW  
**1** SCALE: NOT TO SCALE

**Appendix E Tabular Data for Plastic Material Definition**

DRAFT - For Review

**Table E.1: Plate E Abaqus material input**

Plate E		Plate H		Plate I		Plate J	
Stress	Plastic Strain						
(ksi)	(in./in.)	(ksi)	(in./in.)	(ksi)	(in./in.)	(ksi)	(in./in.)
55.05	0.00000	66.63	0.00000	46.10	0.00000	41.68	0.00000
56.91	0.00017	73.02	0.00034	50.66	0.00017	48.51	0.00024
57.02	0.00134	74.17	0.00046	53.14	0.00024	50.82	0.00033
57.04	0.00702	75.04	0.00061	53.22	0.00358	50.93	0.00311
57.23	0.00826	75.64	0.00084	53.50	0.00458	51.34	0.00450
57.68	0.01029	75.91	0.00100	54.43	0.00560	51.71	0.00541
59.07	0.01238	76.48	0.00159	58.93	0.01100	54.73	0.00897
63.37	0.01893	77.50	0.00285	62.96	0.01672	58.88	0.01456
66.99	0.02582	79.03	0.00673	66.34	0.02244	62.35	0.02014
68.53	0.02921	80.78	0.01168	69.18	0.02824	65.27	0.02576
70.61	0.03461	82.77	0.01736	71.52	0.03394	67.71	0.03133
72.40	0.04009	84.63	0.02320	73.38	0.03954	69.76	0.03693
73.85	0.04546	86.12	0.02896	74.93	0.04504	71.34	0.04257
75.11	0.05075	87.40	0.03456	76.20	0.05069	72.77	0.04810
76.16	0.05609	88.45	0.04016	77.24	0.05631	73.87	0.05358
76.99	0.06140	89.35	0.04563	78.13	0.06184	74.75	0.05902
77.74	0.06667	90.06	0.05108	78.80	0.06727	75.52	0.06435
78.35	0.07195	90.63	0.05661	79.38	0.07269	76.12	0.06966
78.81	0.07719	91.09	0.06195	79.82	0.07803	76.68	0.07498
79.23	0.08237	91.47	0.06727	80.16	0.08331	77.11	0.08021
79.61	0.08749	91.76	0.07255	80.48	0.08860	77.80	0.09083
79.88	0.09265	91.93	0.07787	80.91	0.09895	78.20	0.10160
80.11	0.09773	92.02	0.08327	81.05	0.10405	78.47	0.11231
80.40	0.10623	92.13	0.08864	81.23	0.11423	78.57	0.12277
80.89	0.13021	92.17	0.09031	81.29	0.12564	78.66	0.12624

**Appendix F CVN Impact Data**

DRAFT - For Review

**Table F.2: Plate A CVN impact data**

<b>Plate A</b>			
<b>Thickness: 1.5 in.</b>	<b>Heat: 821T02570</b>		<b>Grade: HPS 70W</b>
<b>Specimen</b>	<b>Energy (ft.-lb.)</b>	<b>Temperature (°F)</b>	<b>% Shear</b>
A1	138.5	-60	50
A2	187	-60	80
A3	135	-60	50
A4	158	-30	60
A5	150	-30	60
A6	178	-30	75
A7	184	0	80
A8	153	0	70
A9	151	0	55
A10	230	30	85
A11	163	30	75
A12	238	30	85
A13	244	60	90
A14	279	60	95
A15	254	60	100
A16	125	-90	40
A17	121	-90	45
A18	109	-90	40

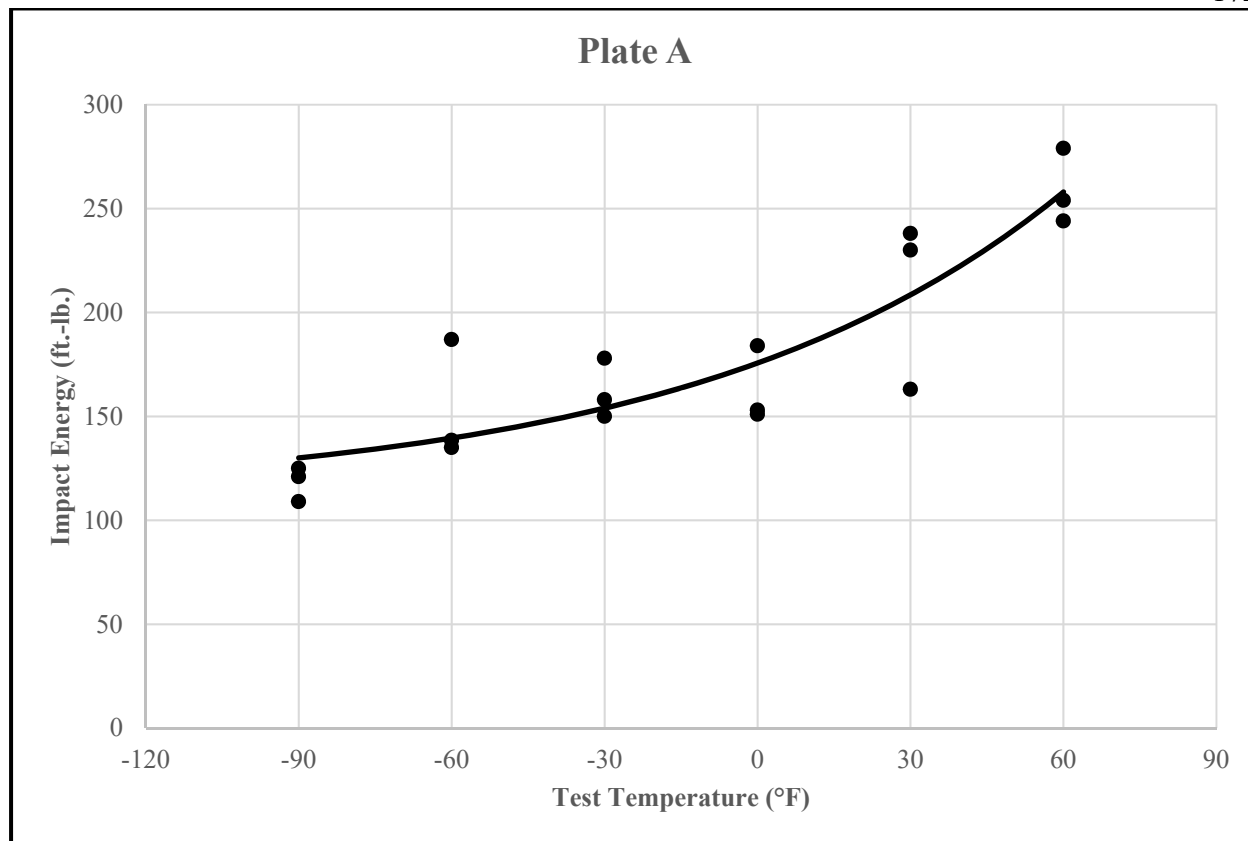


**Figure F.1: Plate A CVN impact data**

DRAFT

**Table F.3: Plate B CVN impact data**

<b>Plate B</b>			
<b>Thickness: 1.5 in.</b>	<b>Heat: 812S35370 S61761</b>		<b>Grade: HPS 70W</b>
<b>Specimen</b>	<b>Energy (ft.-lb.)</b>	<b>Temperature (°F)</b>	<b>% Shear</b>
B1	121	-60	45
B2	168	-60	65
B3	150	-60	60
B4	155	-30	55
B5	144	-30	55
B6	137	-30	50
B7	154	0	65
B8	145	0	60
B9	152	0	65
B10	185	30	100
B11	185	30	100
B12	174	30	80
B13	198	60	100
B14	213	60	100
B15	200	60	100
B16	99	-90	30
B17	70	-90	25
B18	109.5	-90	30

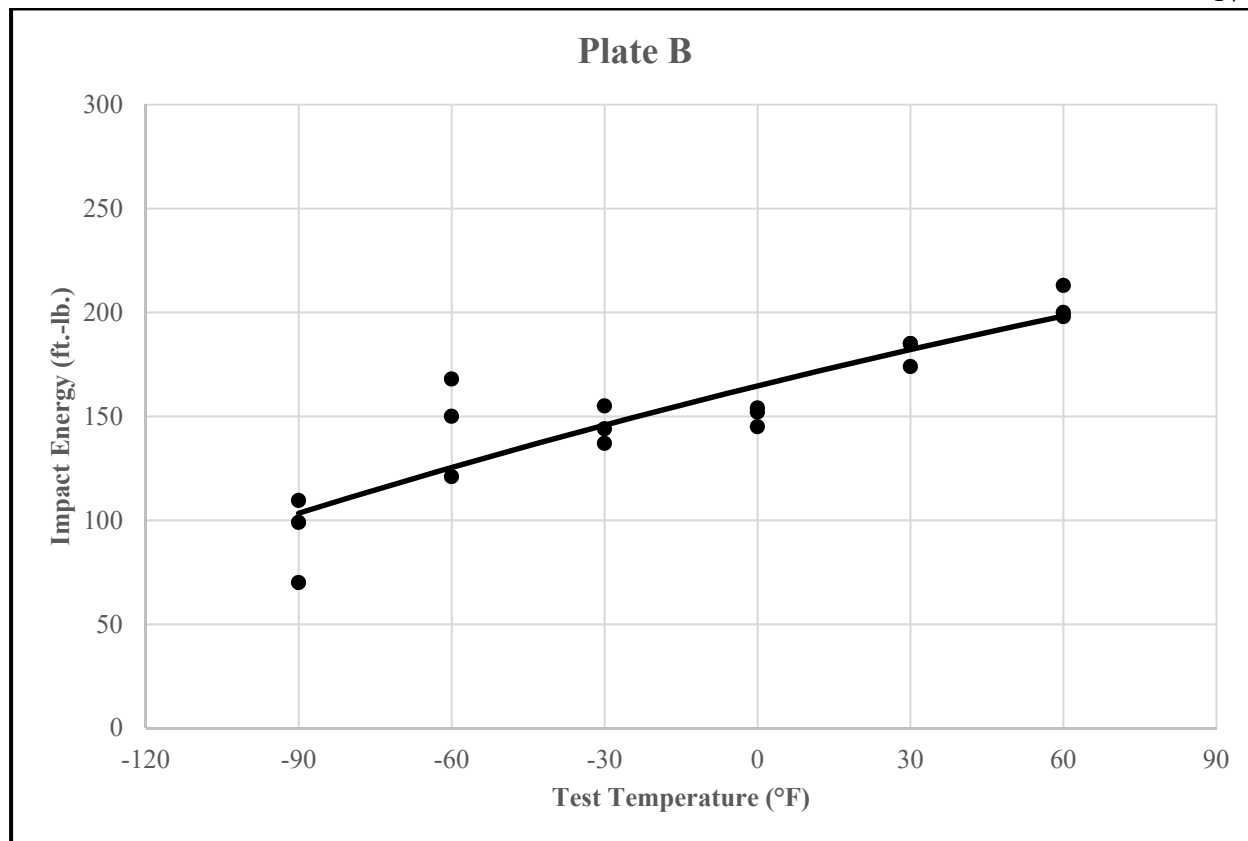


**Figure F.2: Plate B CVN impact data**

**Table F.4: Plate C CVN impact data**

<b>Plate C</b>			
<b>Thickness: 1.5 in.</b>	<b>Heat: 812S35370 S61763</b>		<b>Grade: HPS 70W</b>
<b>Specimen</b>	<b>Energy (ft.-lb.)</b>	<b>Temperature (°F)</b>	<b>% Shear</b>
C1	112	-60	40
C2	130	-60	50
C3	100	-60	35
C4	130	-30	45
C5	134	-30	45
C6	134	-30	50
C7	137	0	50
C8	145	0	60
C9	138	0	55
C10	154	30	70
C11	190	30	90
C12	184	30	85
C13	176	60	80
C14	149	60	75
C15	158	60	80
C16	27	-90	10
C17	70.5	-90	20
C18	67	-90	15

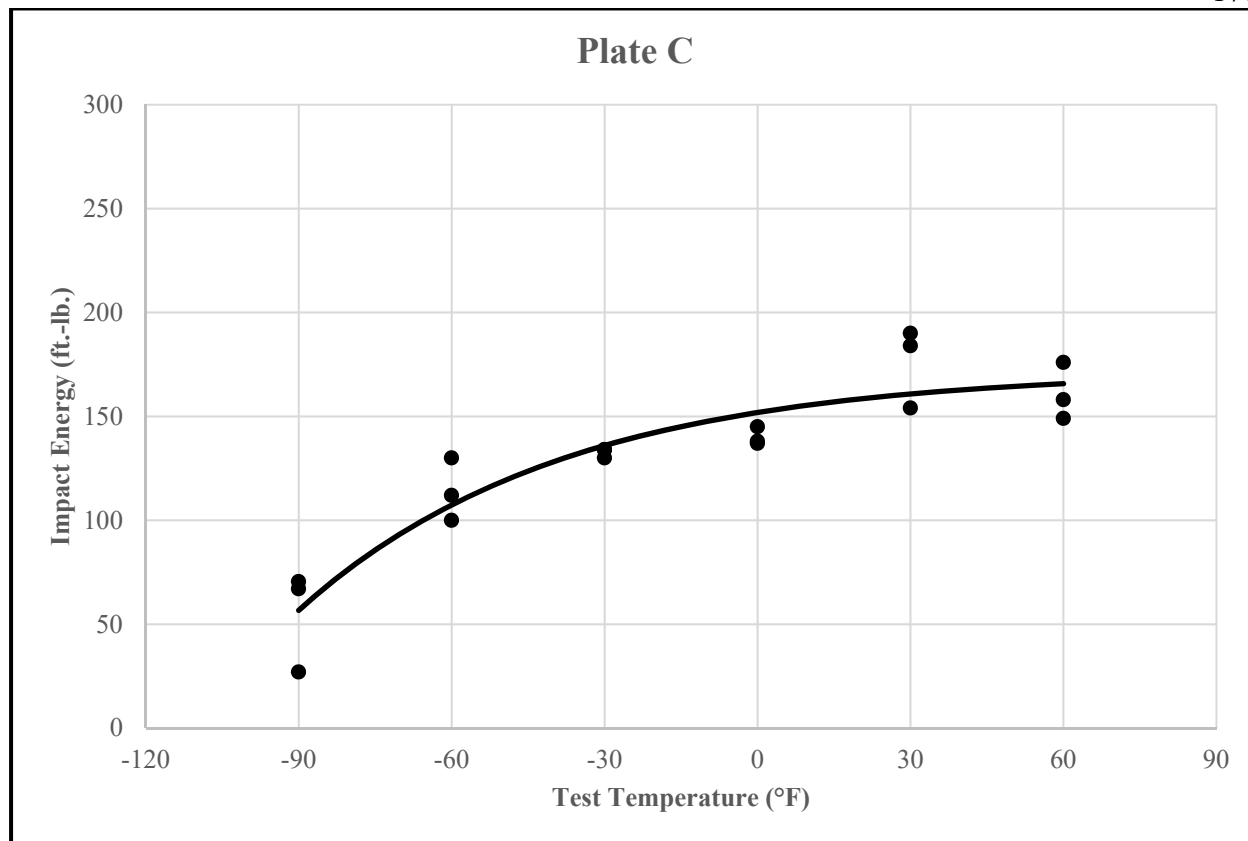


**Figure F.3: Plate C CVN impact data**

DRAFT

**Table F.5: Plate D CVN impact data**

<b>Plate D</b>			
<b>Thickness: 2.0 in.</b>	<b>Heat: A1F064</b>		<b>Grade: HPS 70W</b>
<b>Specimen</b>	<b>Energy (ft.-lb.)</b>	<b>Temperature (°F)</b>	<b>% Shear</b>
D1	8	-60	0
D2	40	-60	10
D3	57	-60	15
D4	130	-30	40
D5	116	-30	35
D6	79	-30	30
D7	163	0	50
D8	129	0	40
D9	115	0	35
D10	258	30	100
D11	140	30	45
D12	112	30	35
D13	155	60	65
D14	142	60	65
D15	143	60	60

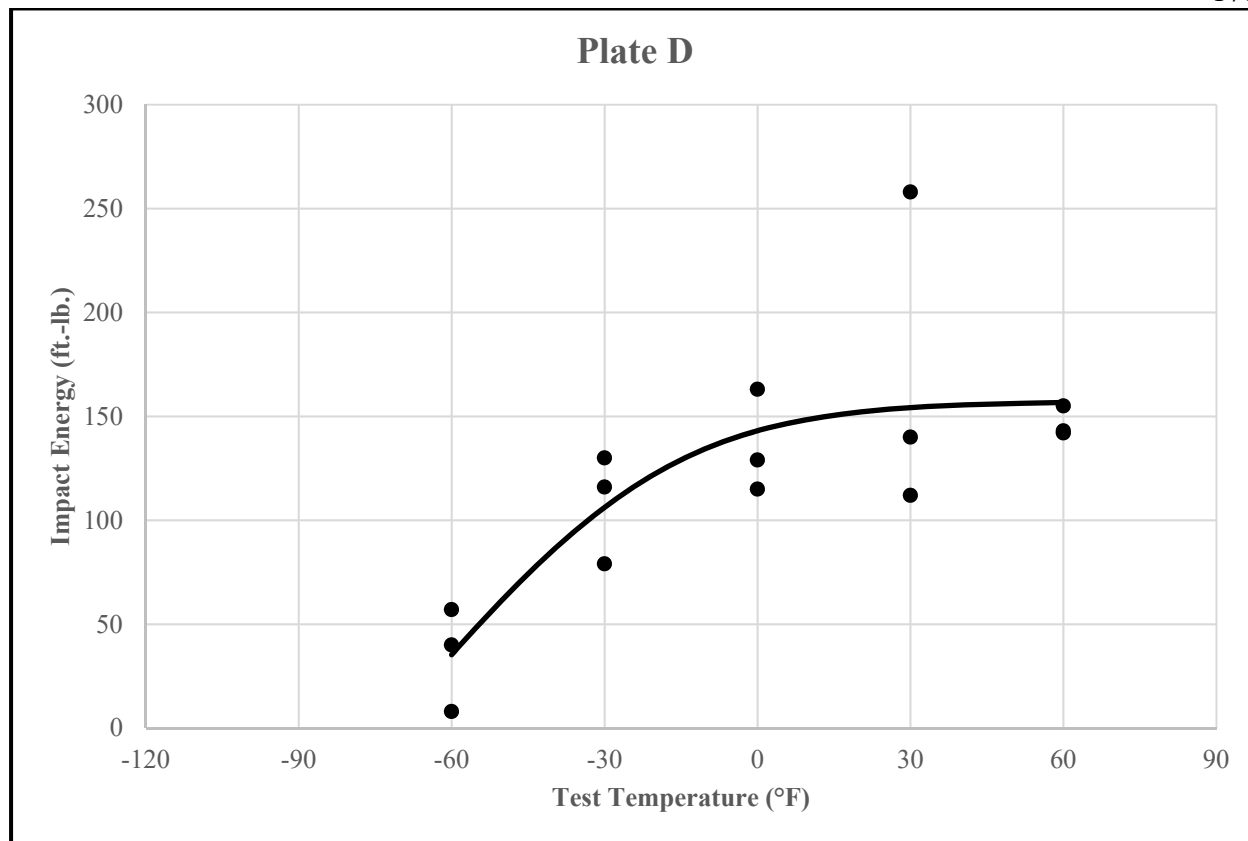


**Figure F.4: Plate D CVN impact data**

DRAFT

**Table F.6: Plate E CVN impact data**

<b>Plate E</b>			
<b>Thickness: 2.5 in.</b>	<b>Heat: 9104617</b>		<b>Grade: 50W</b>
<b>Specimen</b>	<b>Energy (ft.-lb.)</b>	<b>Temperature (°F)</b>	<b>% Shear</b>
E1	145	-60	50
E2	93	-60	35
E3	98	-60	35
E4	129	-30	40
E5	126	-30	40
E6	119	-30	40
E7	165	0	65
E8	208	0	100
E9	245	0	100
E10	271	30	100
E11	243	30	100
E12	238	30	100
E13	113	-30	40
E14	124	-30	45
E15	120	-30	45
E16	36.5	-90	10
E17	46	-90	10
E18	52	-90	15
E19	114	-30	45
E20	103.5	-30	40
E21	144	-30	50
E22	122	-30	45
E23	65.5	-30	25
E24	175	-30	70
E25	138	-30	50
E26	117	-30	40
E27	134.5	-30	50
E28	62	-60	20
E29	48.5	-60	20
E30	98	-60	30
E31	162	0	60
E32	165	0	70
E33	255	0	100
E34	60	-60	20

E35	60	-60	20
E36	85	-60	25
ET1	33.5	-30	15
ET2	104	-30	40
ET3	15	-30	5
ET4	114	-30	40
ET5	28	-30	10
ET6	102	-30	35
EB1	8.5	-30	5
EB2	24.5	-30	10
EB3	89.5	-30	25
EB4	77	-30	20
EB5	110	-30	40
EB6	80	-30	30

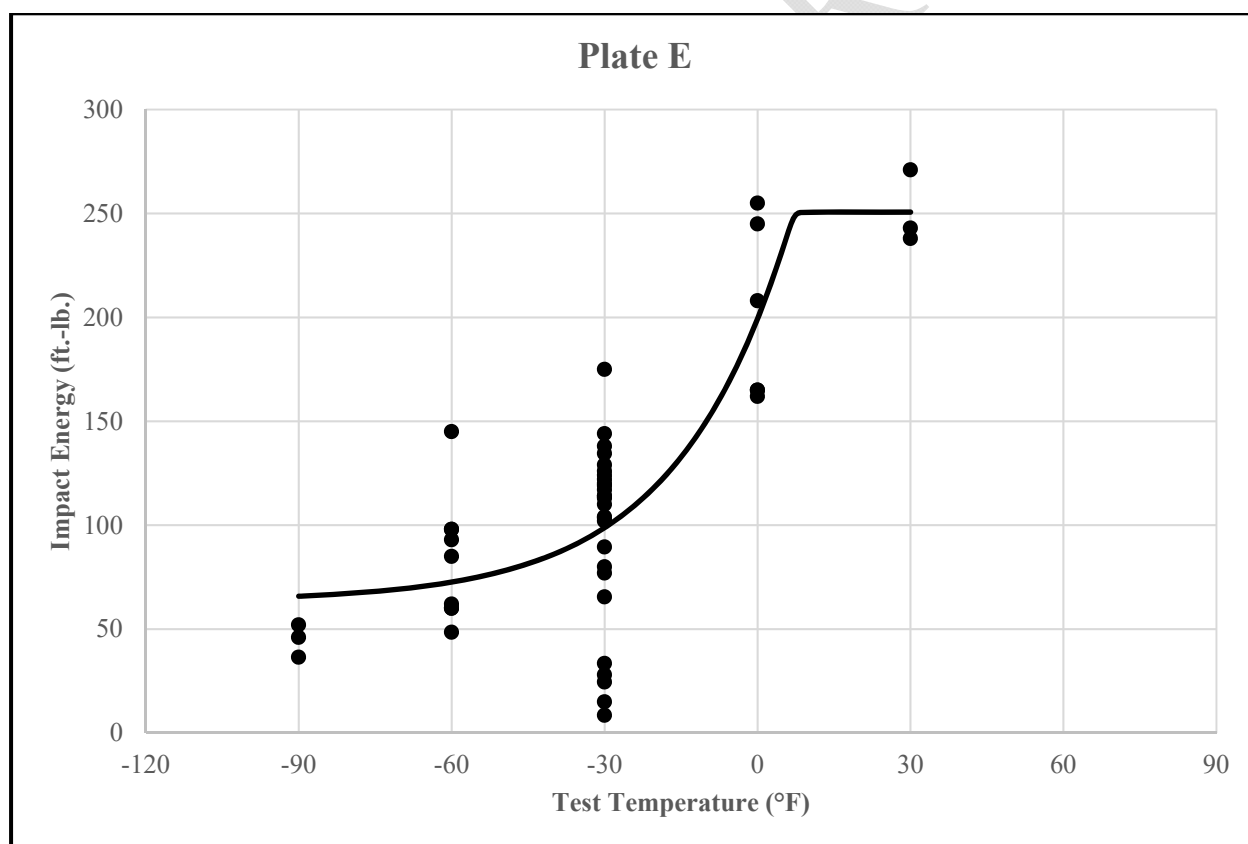


**Figure F.5: Plate E CVN impact data**

**Table F.7: Plate F CVN impact data**

<b>Plate F</b>			
<b>Thickness: 1.57 in. (40 mm)</b>	<b>Heat: 9106460</b>		<b>Grade: HPS 70W</b>
<b>Specimen</b>	<b>Energy (ft.-lb.)</b>	<b>Temperature (°F)</b>	<b>% Shear</b>
F1	63	-60	50
F2	51	-60	40
F3	24	-60	10
F4	128	-30	90
F5	24	-30	20
F6	54	-30	20
F7	73	0	20
F8	101	0	40
F9	183	0	90
F10	198	30	100
F11	167	30	95
F12	169	30	95
F13	186	60	100
F14	195	60	95
F15	202	60	100

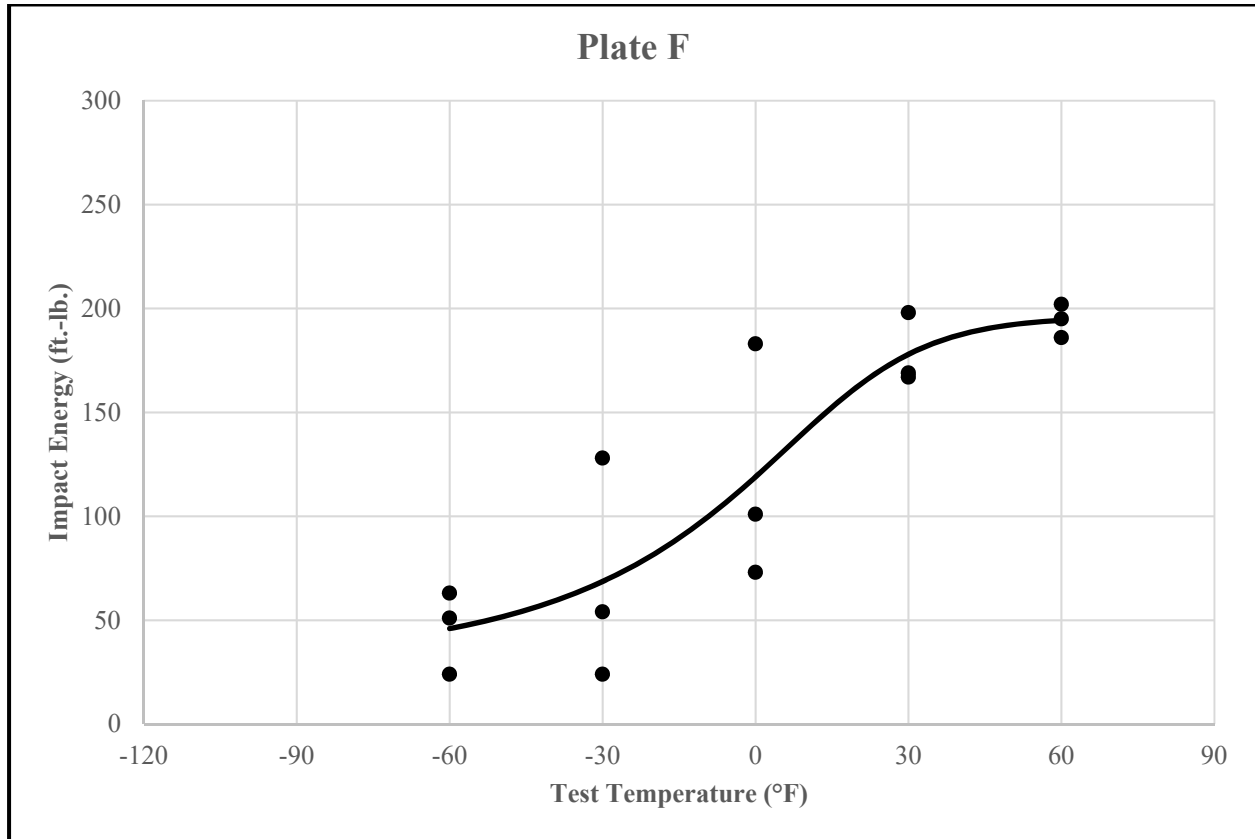


**Figure F.6: Plate F CVN impact data**

DRAFT

**Table F.8: Plate G CVN impact data**

<b>Plate G</b>			
<b>Thickness: 2.25 in.</b>	<b>Heat: 9106877</b>		<b>Grade: 50W</b>
<b>Specimen</b>	<b>Energy (ft.-lb.)</b>	<b>Temperature (°F)</b>	<b>% Shear</b>
G1	20	-60	0
G2	12	-60	0
G3	7	-60	0
G4	90	-30	30
G5	106	-30	30
G6	68	-30	20
G7	148	0	55
G8	114	0	30
G9	95	0	25
G10	122	30	40
G11	135	30	45
G12	143	30	45
G13	259	60	100
G14	131	60	40
G15	153	60	65

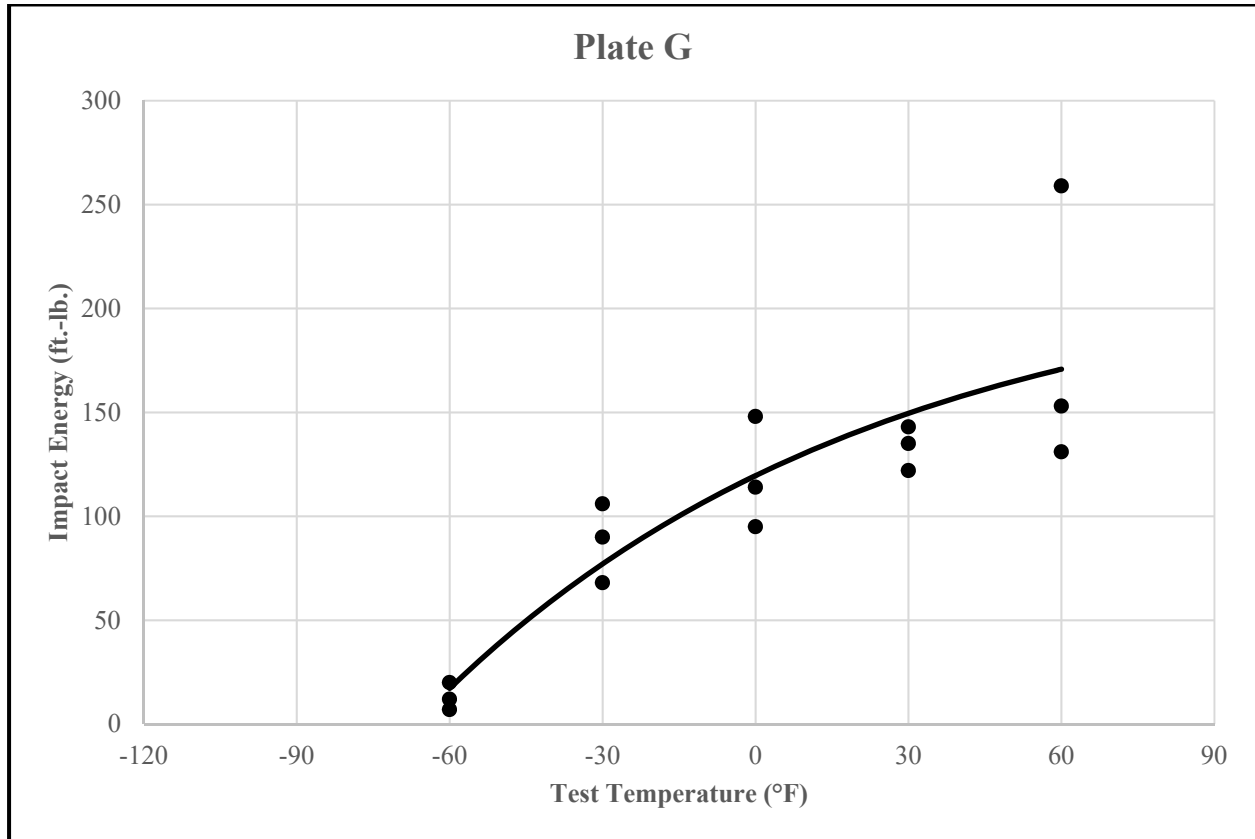


**Figure F.7: Plate G CVN impact data**

DRAFT

**Table F.9: Plate H CVN impact data**

<b>Plate H</b>			
<b>Thickness: 1.5 in.</b>	<b>Heat: 823K71800</b>		<b>Grade: HPS 70W</b>
<b>Specimen</b>	<b>Energy (ft.-lb.)</b>	<b>Temperature (°F)</b>	<b>% Shear</b>
A	113.5	-60	45
B	122	-60	45
C	117.5	-60	50
D	131	-30	50
E	133.5	-30	50
F	121.5	-30	50
G	127	0	50
H	138.5	0	60
I	150.5	0	70
J	142	30	80
K	145	30	80
L	142	30	75
M	201.5	60	100
N	176	60	100
O	207	60	100
P	55.5	-90	20
Q	18	-90	10
R	47.5	-90	15
H19	90	-35	35
H20	105	-35	40
H21	121	-35	45
H22	116.5	-35	45
H23	106.5	-35	45
H24	105.5	-35	40
H25	97.5	-35	40
H26	120	-35	50
H27	91.5	-35	40
H28	122.5	-35	45
H29	115.5	-35	45
H30	117	-35	50
H31	126.5	-35	45
H32	114	-35	40
H33	118	-35	45
H34	117	-35	40

H35	115	-35	40
H36	116.5	-35	45
HT1	129.5	-35	50
HT2	141.5	-35	60
HT3	131.5	-35	50
HT4	120.5	-35	50
HT5	139	-35	50
HT6	198	-35	100
HB1	135	-35	65
HB2	115	-35	45
HB3	119.5	-35	40
HB4	113.5	-35	40
HB5	132	-35	50
HB6	144.5	-35	60

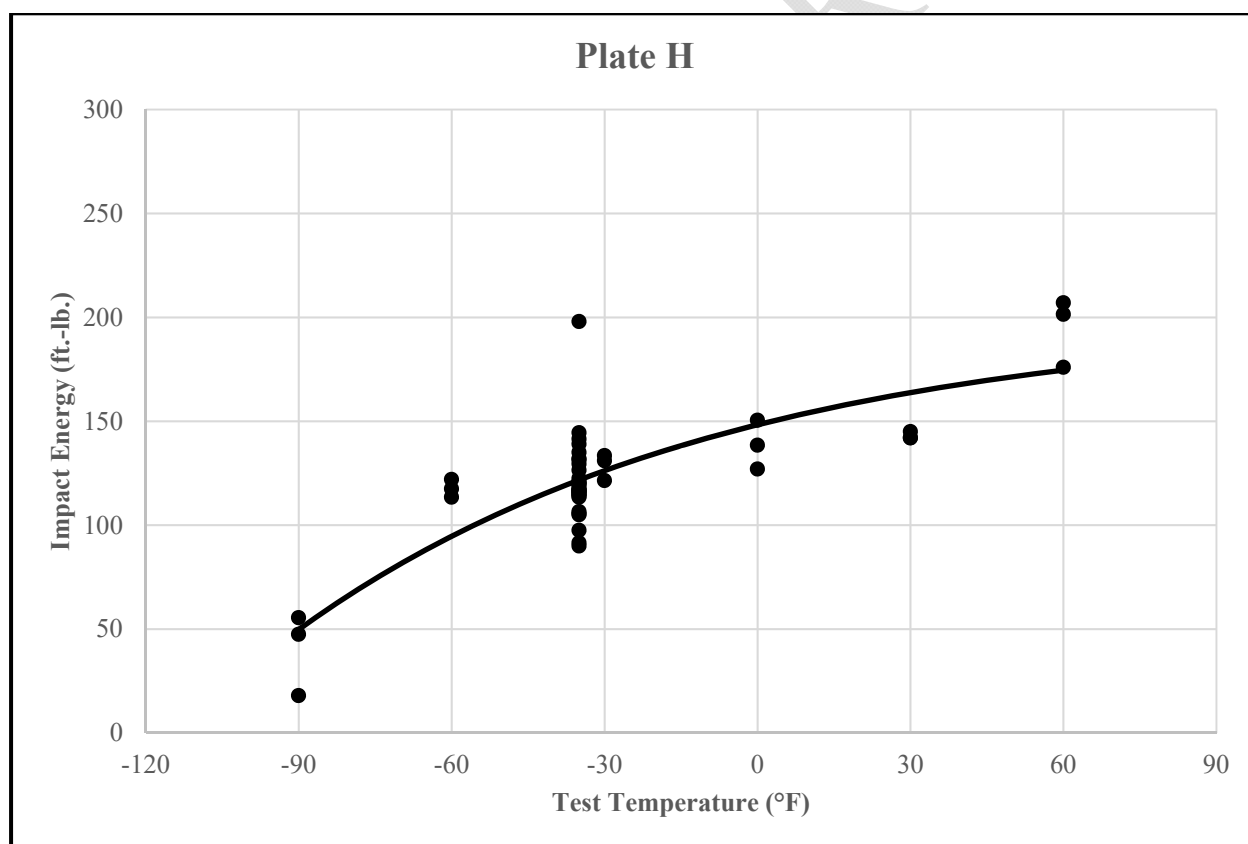


**Figure F.8: Plate H CVN impact data**

Table F.10: Plate I CVN impact data

Plate I			
Thickness: 2.0 in.	Heat: 500541		Grade: 50W
Specimen	Energy (ft.-lb.)	Temperature (°F)	% Shear
I1	6	-60	0
I2	5	-60	0
I3	4	-60	0
I4	13	-30	0
I5	12	-30	0
I6	17	-30	0
I7	30.5	0	10
I8	27	0	10
I9	17	0	5
I10	87	30	35
I11	21.5	30	10
I12	46.5	30	20
I13	74.5	60	30
I14	77.5	60	30
I15	55	60	25
I16	53.5	10	25
I17	40	10	20
I18	18.5	10	10
I19	89	10	30
I20	71.5	10	25
I21	93	10	30
I22	10	-60	5
I23	26	-60	10
I24	49	-60	15
I25	18	-60	5
I26	28.5	-60	10
I27	8	-60	0
I28	27	-60	10
I29	20.5	-60	10
I30	12	-60	0
I31	78.5	0	25
I32	48.5	0	15
I33	76.5	0	20

I34	55.5	-30	15
I35	40	-30	10
I36	16.5	-30	0

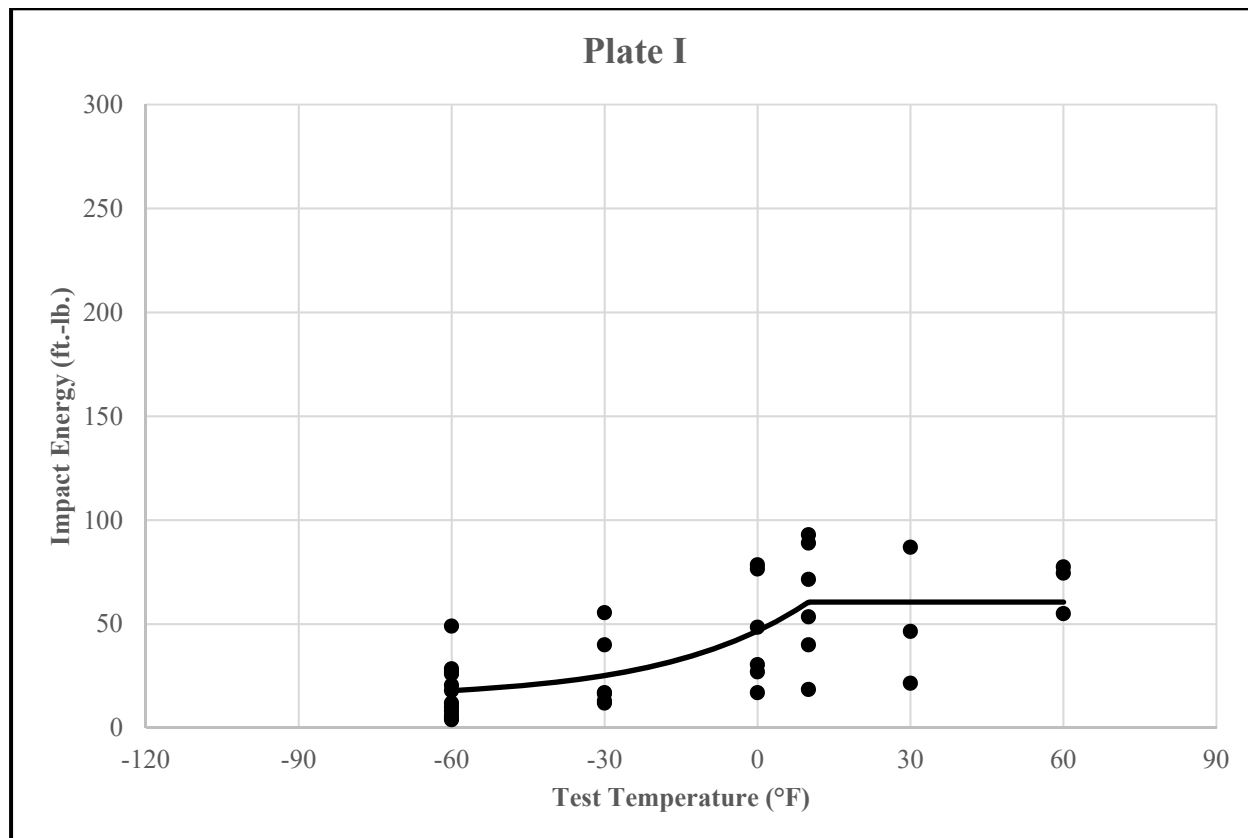


**Figure F.9: Plate I CVN impact data**

**Table F.11: Plate J CVN impact data**

<b>Plate J</b>			
<b>Thickness: 1.5 in.</b>	<b>Heat: 3507723</b>		<b>Grade: 50</b>
<b>Specimen</b>	<b>Energy (ft.-lb.)</b>	<b>Temperature (°F)</b>	<b>% Shear</b>
D1	46.5	-60	20
D2	48.5	-60	20
D3	27	-60	15
D4	67	-30	20
D5	68.5	-30	25
D6	85	-30	30
D7	87	0	35
D8	98	0	40
D9	97	0	40
D10	112.5	30	50
D11	101	30	35
D12	92.5	30	35
D13	143	60	85
D14	133.5	60	80
D15	128	60	70
D16	176	205	100
D17	158	205	100
D18	167.5	205	100
J19	122	60	60
J20	121	60	60
J21	129.5	60	60
J22	147	60	85
J23	91	60	40
J24	128	60	55
J25	122	60	55
J26	120	60	60
J27	121	60	60
J28	76	30	25
J29	50	30	20
J30	103	30	30
J31	120	60	50
J32	126	60	60
J33	125.5	60	65
J34	51	0	20

J35	66	0	20
J36	76	0	25
LTI-1	13	-90	N/A
LTI-2	13	-90	N/A
LTI-3	31	-90	N/A
LTI-4	6	-120	N/A
LTI-5	5	-120	N/A
LTI-6	4	-120	N/A

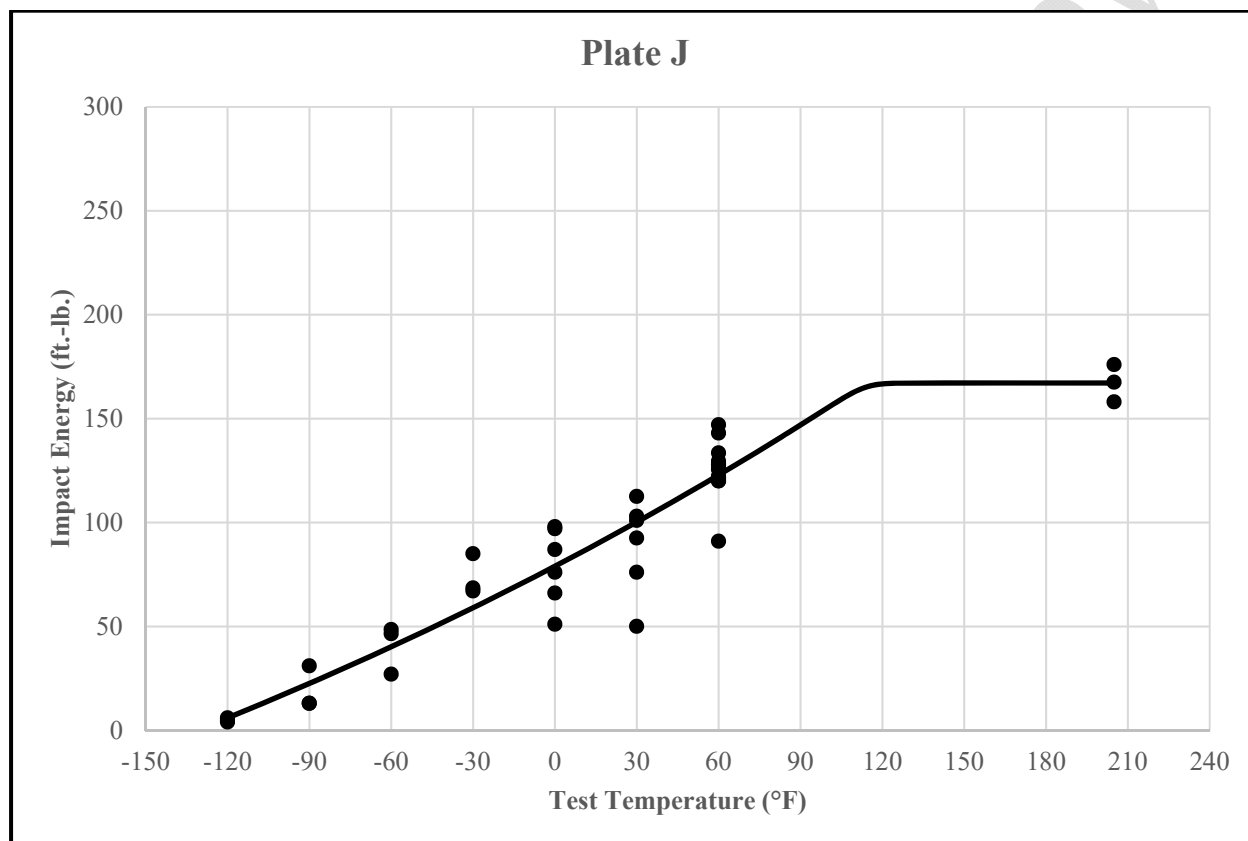


**Figure F.10: Plate J CVN impact data**

**Appendix G Master Curve Data**

DRAFT - For Review

**Table G.12: Plate E reference temperature specimen and test data**

Specimen	Test Temperature		Test Result $K_J$		B (xT)	Stable Tearing (in.)	$a_o$ (in.)	W (in.)
	(°C)	(°F)	(MPa√m)	(ksi√in.)				
E1	-175	-283	69.4	63.2	0.3930	-	0.2103	0.3940
E2	-160	-256	79.9	72.7	0.3930	-	0.2111	0.3940
E3	-160	-256	95.1	86.5	0.3930	-	0.2120	0.3940
E4	-160	-256	48.2	43.9	0.3925	-	0.2117	0.3935
E5	-145	-229	45.4	41.4	0.3930	-	0.2109	0.3935
E6	-145	-229	80.1	72.9	0.3930	-	0.2116	0.3935
E7	-145	-229	64.9	59.1	0.3930	-	0.2119	0.3940
E8	-130	-202	161.2	146.6	0.3930	0.0023	0.2118	0.3935
E9	-130	-202	80.2	72.9	0.3940	-	0.2103	0.3925
E10	-145	-229	62.7	57.1	0.3930	-	0.2119	0.3935
E11	-145	-229	155.3	141.4	0.3930	0.0020	0.2114	0.3935
E14	-160	-256	52.9	48.1	0.3930	-	0.2105	0.3935

**Table G.13: Plate E reference temperature validity data**

Specimen	$K_J$ Limit $K_{Jc(limit)}$	Tearing Limit	1T Equivalent $K_{Jc(1T)}$	Limit Censored Data	Final Master Curve Data $K_{Jc(1T)}$		T-T <sub>0</sub>	Weight Factor
	(MPa√m)	(in.)	(MPa√m)	(MPa√m)	(MPa√m)	(ksi√in.)	(°C)	(n)
E1	162.6	0.0092	59.1	-	59.1	53.8	-46.1	0.125
E2	154.2	0.0091	67.4	-	67.4	61.4	-31.1	0.143
E3	153.8	0.0091	79.4	-	79.4	72.3	-31.1	0.143
E4	153.7	0.0091	42.4	-	42.4	38.5	-31.1	0.143
E5	147.6	0.0091	40.2	-	40.2	36.5	-16.1	0.143
E6	147.3	0.0091	67.6	-	67.6	61.5	-16.1	0.143
E7	147.4	0.0091	55.6	-	55.6	50.6	-16.1	0.143
E8	141.9	0.0091	131.8	116.5	116.5	106.0	-1.1	-
E9	142.1	0.0091	67.7	-	67.7	61.6	-1.1	0.167
E10	147.2	0.0091	53.8	-	53.8	49.0	-16.1	0.143
E11	147.4	0.0091	127.2	120.8	120.8	110.0	-16.1	-
E14	154.2	0.0091	46.0	-	46.0	41.9	-31.1	0.143
<b>TOTAL WEIGHT FACTOR</b>								<b>1.435</b>

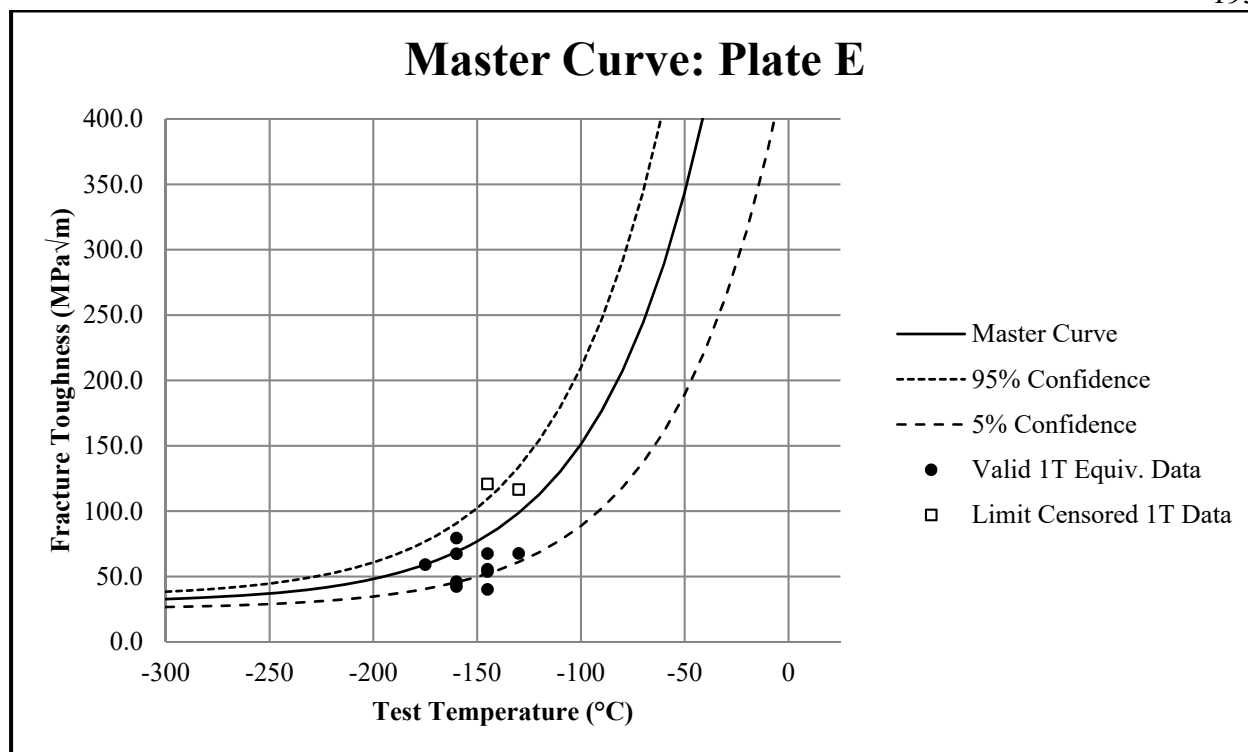


Figure G.11: Plate E master curve

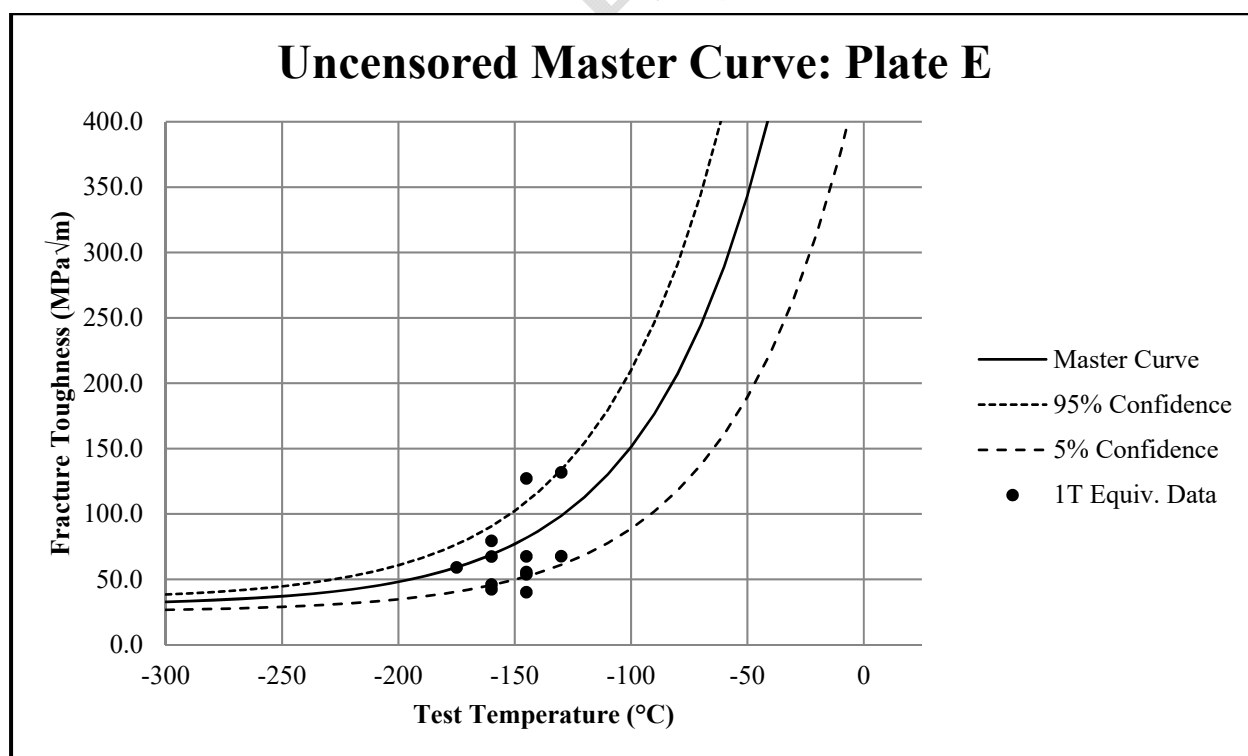


Figure G.12: Plate E uncensored master curve

**Table G.14: Plate H reference temperature specimen and test data**

Specimen	Test Temperature		Test Result $K_J$		B (xT)	Stable Tearing (in.)	$a_0$ (in.)	W (°C)
	(°C)	(°F)	(MPa√m)	(ksi√in.)				
H1	-156	-249	204.83	186.4	0.3935	0.0023	0.2094	0.3935
H2	-180	-292	99.18	90.3	0.3935	-	0.2088	0.3940
H3	-180	-292	90.67	82.5	0.3940	-	0.2113	0.3935
H4	-174	-281	70.93	64.5	0.3940	-	0.2097	0.3940
H5	-168	-270	113.13	102.9	0.3935	-	0.2102	0.3935
H6	-168	-270	67.58	61.5	0.3940	-	0.2097	0.3940
H7	-168	-270	150.15	136.6	0.3935	0.0017	0.2092	0.3940
H8	-168	-270	112.13	102.0	0.3940	0.0011	0.2086	0.3940
H11	-168	-270	183.82	167.3	0.3940	0.0020	0.2102	0.3930
H12	-174	-281	70.87	64.5	0.3940	-	0.2094	0.3935

**Table G.15: Plate H reference temperature validity data**

Specimen	$K_J$ Limit $K_{Jc(limit)}$	Tearing Limit	1T Equivalent $K_{Jc(1T)}$	Limit Censored Data	Final Master Curve Data $K_{Jc(1T)}$		T-T <sub>0</sub>	Weight Factor
	(MPa√m)	(in.)	(MPa√m)	(MPa√m)	(MPa√m)	(ksi√in.)	(°C)	(n)
H1	166.7	0.0092	166.4	136.2	136.2	123.9	13.4	-
H2	179.3	0.0093	82.7	-	82.7	75.3	-10.6	0.167
H3	177.9	0.0091	76.0	-	76.0	69.2	-10.6	0.167
H4	175.4	0.0092	60.4	-	60.4	54.9	-4.6	0.167
H5	171.8	0.0092	93.8	-	93.8	85.3	1.4	0.167
H6	172.2	0.0092	57.7	-	57.7	52.5	1.4	0.167
H7	172.5	0.0092	123.1	-	123.1	112.0	1.4	0.167
H8	172.8	0.0093	93.0	-	93.0	84.6	1.4	0.167
H11	171.5	0.0091	149.8	140.1	140.1	127.5	1.4	-
H12	175.3	0.0092	60.3	-	60.3	54.9	-4.6	0.167
<b>TOTAL WEIGHT FACTOR</b>								<b>1.333</b>

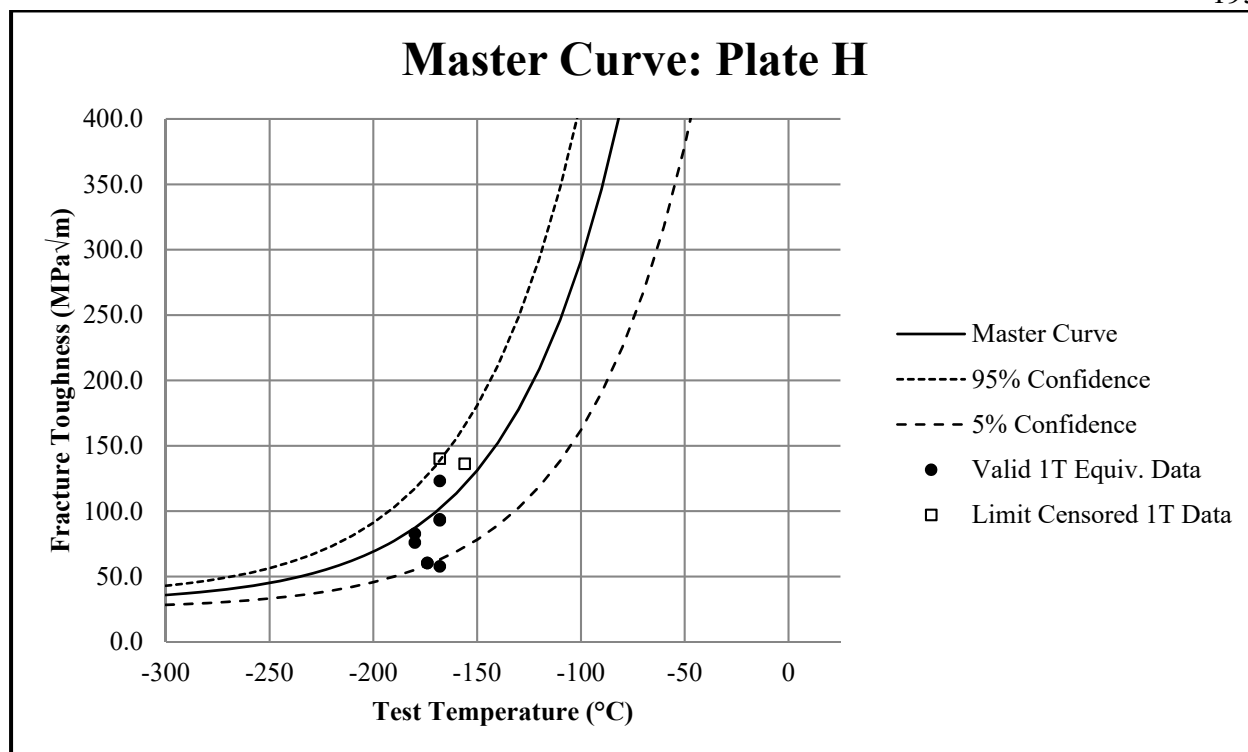


Figure G.13: Plate H master curve

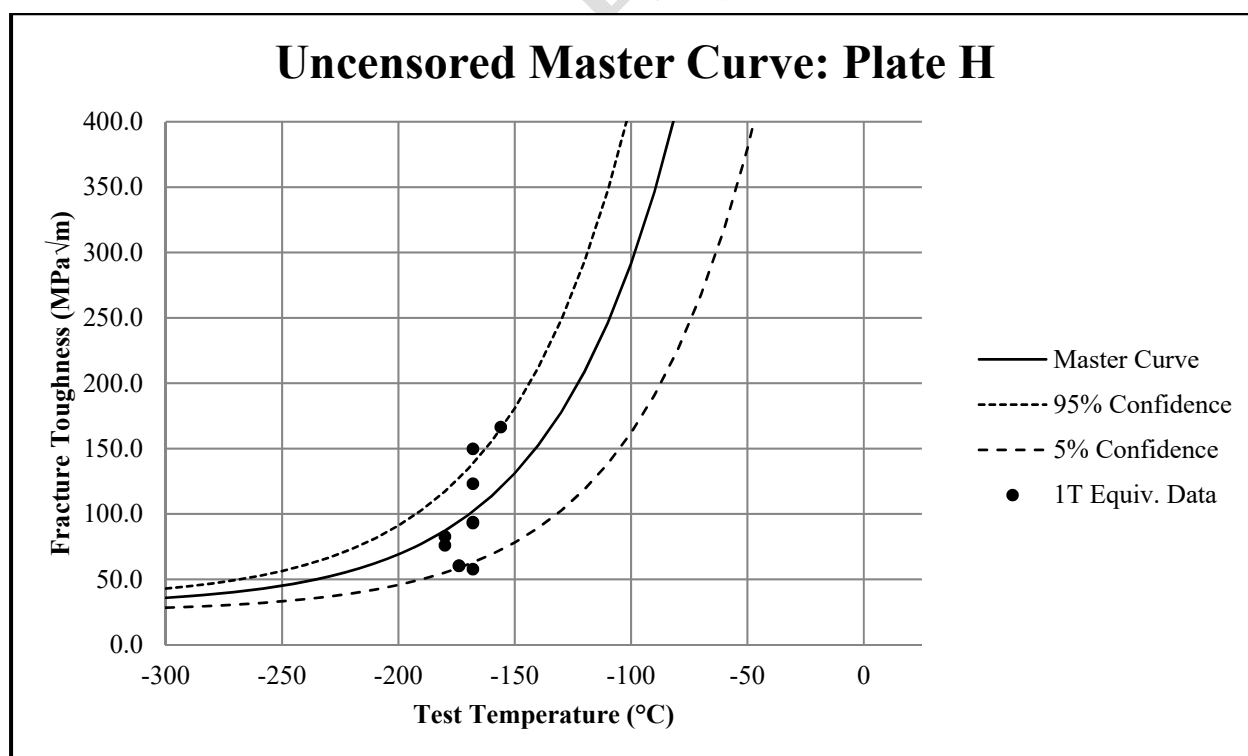


Figure G.14: Plate H uncensored master curve

**Table G.16: Plate I reference temperature specimen and test data**

Specimen	Test Temperature		Test Result $K_J$		B (xT)	Stable Tearing (in.)	$a_o$ (in.)	W (in.)
	(°C)	(°F)	(MPa√m)	(ksi√in.)				
I1	-75	-103	206.02	187.5	0.3925	0.0027	0.2103	0.3950
I3	-125	-193	110.73	100.8	0.3930	-	0.2105	0.3950
I4	-140	-220	121.08	110.2	0.3930	-	0.2099	0.3950
I5	-160	-256	120.37	109.5	0.3925	-	0.2110	0.3950
I6	-175	-283	137.31	125.0	0.3930	0.0018	0.2116	0.3950
I7	-160	-256	84.60	77.0	0.3930	-	0.2097	0.3950
I8	-160	-256	90.48	82.3	0.3925	-	0.2083	0.3950
I9	-160	-256	99.92	90.9	0.3925	-	0.2091	0.3950
I10	-160	-256	128.70	117.1	0.3925	-	0.2099	0.3950

**Table G.17: Plate I reference temperature validity data**

Specimen	$K_J$ Limit $K_{Jc(limit)}$	Tearing Limit	1T Equivalent $K_{Jc(1T)}$	Limit Censored Data	Final Master Curve Data $K_{Jc(1T)}$		T-T <sub>o</sub>	Weight Factor
	(MPa√m)	(in.)	(MPa√m)	(MPa√m)	(MPa√m)	(ksi√in.)	(°C)	(n)
I1	125.4	0.0092	167.2	103.5	103.5	94.1	79.1	-
I3	137.7	0.0092	91.8	-	91.8	83.6	29.1	0.167
I4	143.1	0.0093	100.0	-	100.0	91.0	14.1	0.167
I5	151.3	0.0092	99.4	-	99.4	90.5	-5.9	0.167
I6	159.3	0.0092	112.9	-	112.9	102.7	-20.9	0.143
I7	151.8	0.0093	71.1	-	71.1	64.7	-5.9	0.167
I8	152.4	0.0093	75.8	-	75.8	69.0	-5.9	0.167
I9	152.0	0.0093	83.3	-	83.3	75.8	-5.9	0.167
I10	151.7	0.0093	106.0	-	106.0	96.5	-5.9	0.167
<b>TOTAL WEIGHT FACTOR</b>								<b>1.310</b>

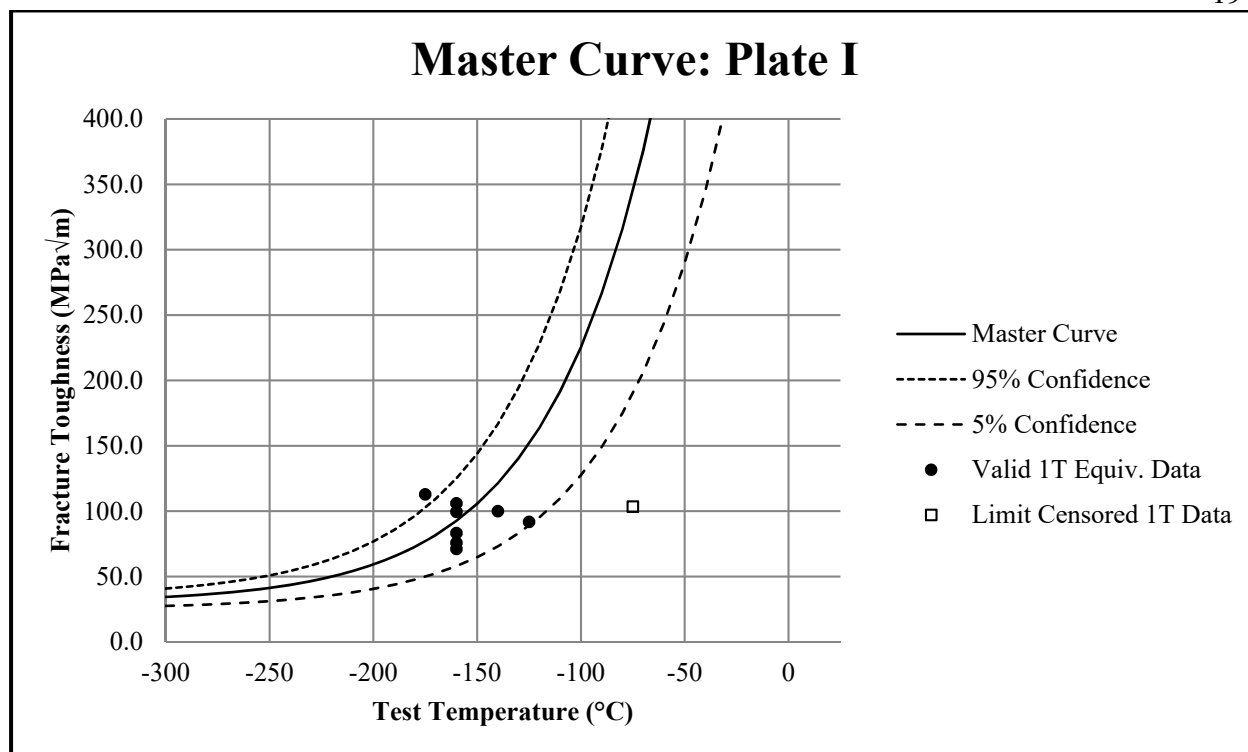


Figure G.15: Plate I master curve

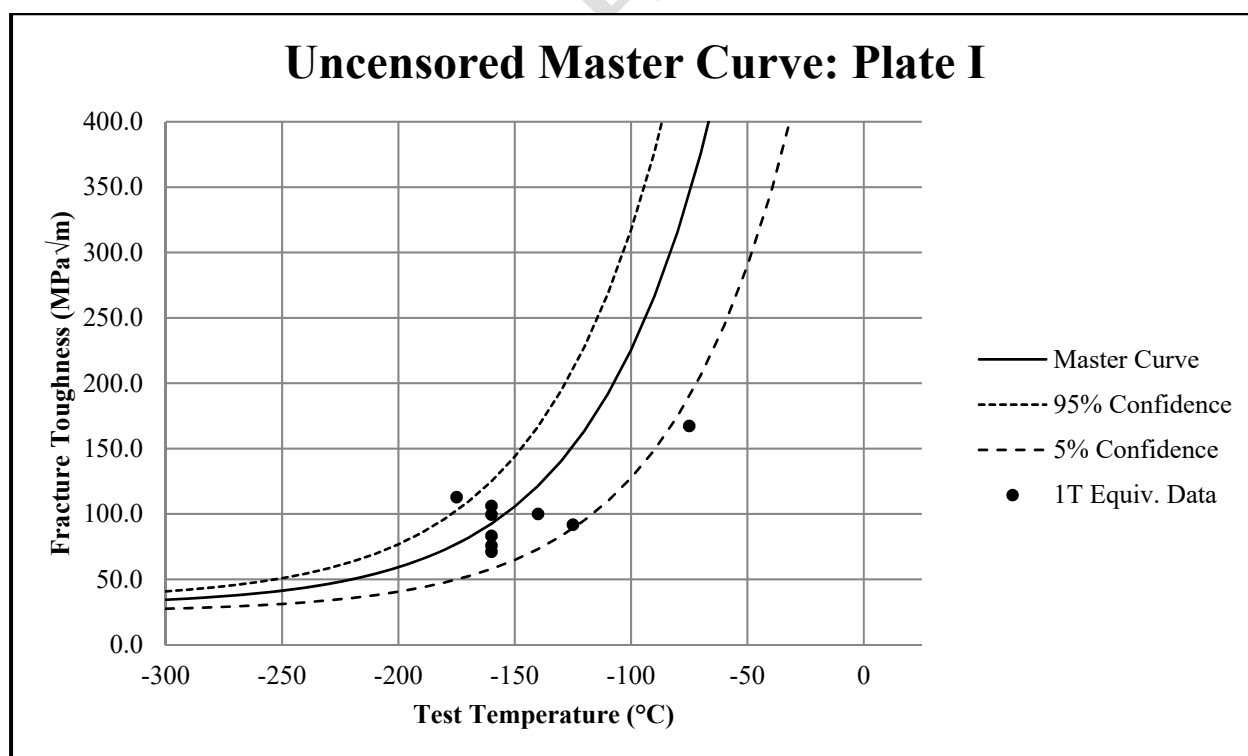


Figure G.16: Plate I uncensored master curve

**Table G.18: Plate J reference temperature specimen and test data**

Specimen	Test Temperature		Test Result $K_J$		B (xT)	Stable Tearing (in.)	$a_o$ (in.)	W (in.)
	(°C)	(°F)	(MPa√m)	(ksi√in.)				
J1	-140	-220	243.48	221.6	0.3935	0.0042	0.2107	0.3930
J2	-180	-292	137.34	125.0	0.3935	0.0019	0.2101	0.3930
J4	-180	-292	138.63	126.2	0.3935	0.0020	0.2092	0.3930
J5	-180	-292	67.90	61.8	0.3935	-	0.2104	0.3925
J6	-170	-274	108.47	98.7	0.3935	-	0.2101	0.3925
J7	-170	-274	67.02	61.0	0.3935	-	0.2093	0.3930
J8	-170	-274	119.12	108.4	0.3930	-	0.2098	0.3935
J9	-170	-274	110.03	100.1	0.3930	-	0.2113	0.3925

**Table G.19: Plate J reference temperature validity data**

Specimen	$K_J$ Limit $K_{Jc(limit)}$	Tearing Limit	1T Equivalent $K_{Jc(1T)}$	Limit Censored Data	Final Master Curve Data $K_{Jc(1T)}$		T-T <sub>0</sub>	Weight Factor
	(MPa√m)	(in.)	(MPa√m)	(MPa√m)	(MPa√m)	(ksi√in.)	(°C)	(n)
J1	139.9	0.0091	197.0	114.9	114.9	104.6	29.1	-
J2	160.4	0.0091	112.9	-	112.9	102.8	-10.9	0.167
J4	160.8	0.0092	114.0	-	114.0	103.7	-10.9	0.167
J5	160.0	0.0091	57.9	-	57.9	52.7	-10.9	0.167
J6	153.9	0.0091	90.1	-	90.1	82.0	-0.9	0.167
J7	154.5	0.0092	57.2	-	57.2	52.1	-0.9	0.167
J8	154.5	0.0092	98.5	-	98.5	89.6	-0.9	0.167
J9	153.4	0.0091	91.3	-	91.3	83.1	-0.9	0.167
<b>TOTAL WEIGHT FACTOR</b>								<b>1.435</b>

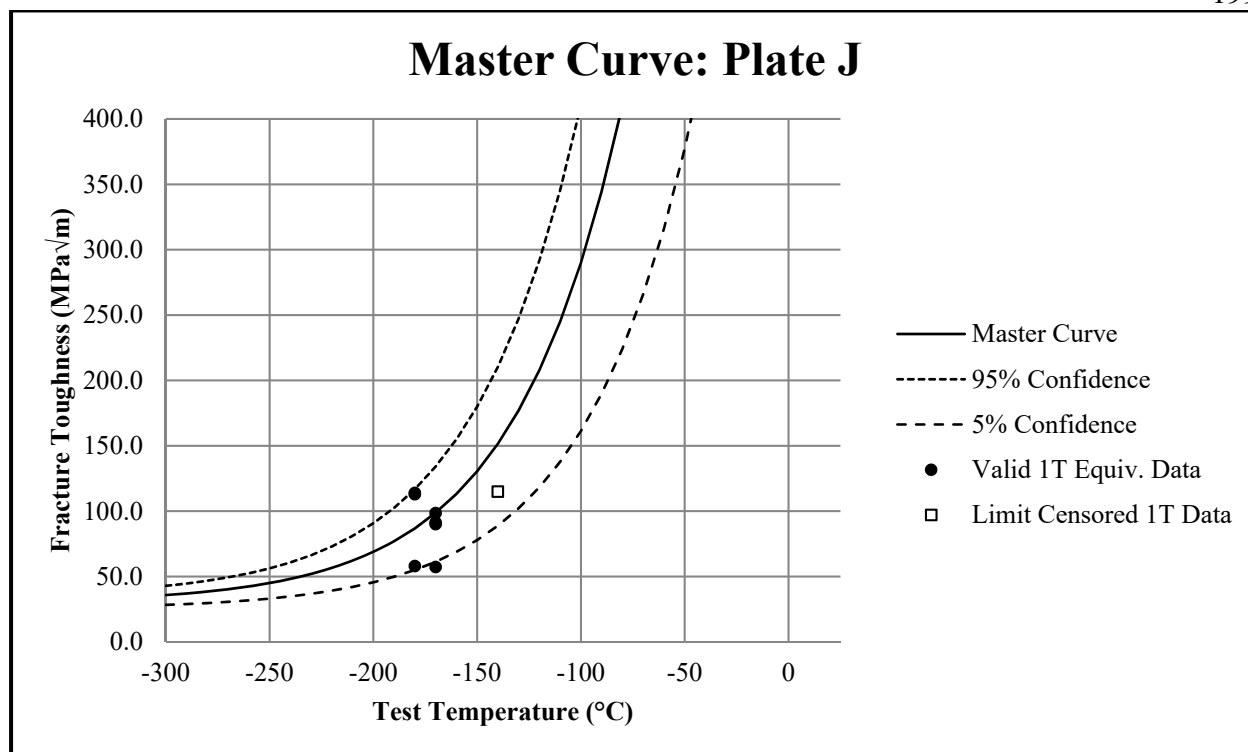


Figure G.17: Plate J master curve

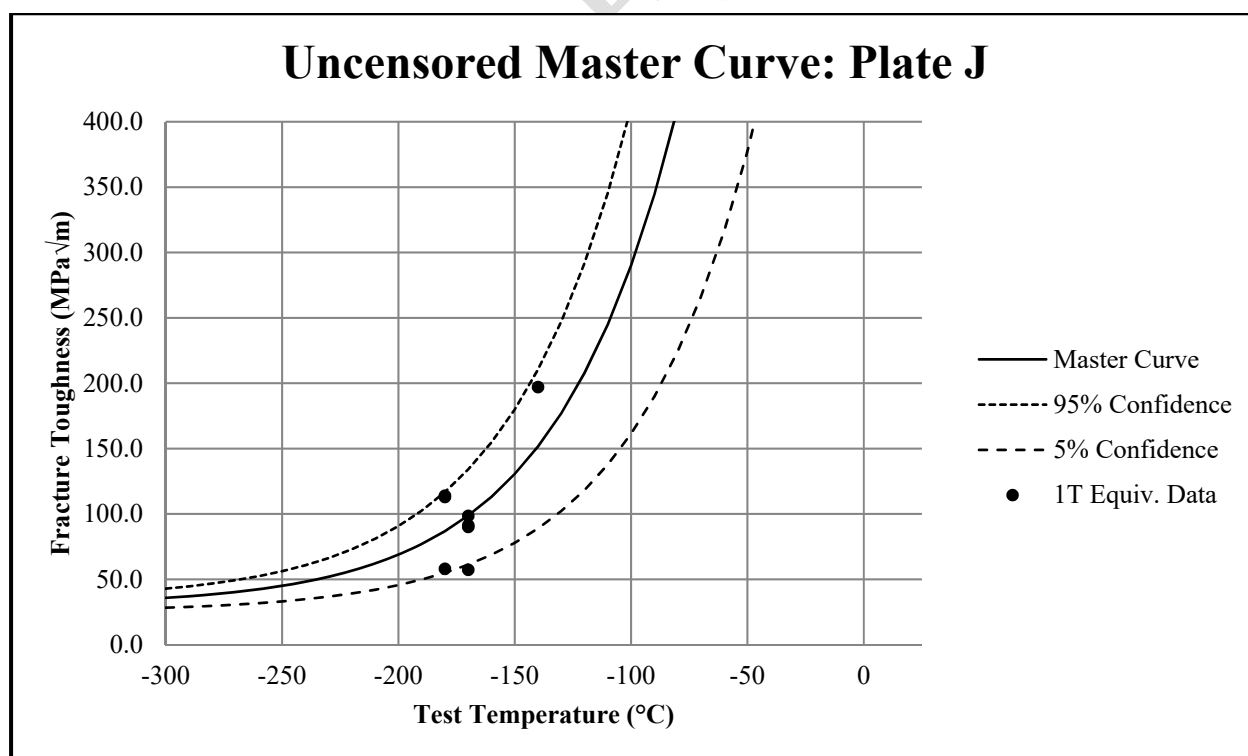


Figure G.18: Plate J uncensored master curve

**Appendix H Fatigue Life Estimates**

DRAFT - For Review

**Table H.20: Fatigue life edge crack current specification**

Thickness	Toughness	Width	Yield	Ultimate	Primary Stress	Initial Flaw	Critical Flaw	Cycles to Failure	Life	
(in.)	(ksi√in.)	(in.)	(ksi)	(ksi)	(ksi)	(in.)	(in.)	(N)	(yr.)	
1.0	38.6	18.0	50	65	37.5	0.0625	0.18	Infinite	Infinite	
						0.125	0.18	12,940,283	35.5	
						0.25	0.18	Fail	0.0	
	43.4		75	85	52.5	0.0625	0.12	Infinite	Infinite	
						0.125	0.12	Fail	0.0	
						0.25	0.12	Fail	0.0	
	51.1		100	115	75	0.0625	0.09	Infinite	Infinite	
						0.125	0.09	Fail	0.0	
						0.25	0.09	Fail	0.0	
2.0	35.3	18.0	50	65	37.5	0.0625	0.15	Infinite	Infinite	
						0.125	0.15	7,145,870	19.6	
						0.25	0.15	Fail	0.0	
	39.4		75	85	52.5	0.0625	0.10	Infinite	Infinite	
						0.125	0.10	Fail	0.0	
						0.25	0.10	Fail	0.0	
	45.9		100	115	75	0.0625	0.07	Infinite	Infinite	
						0.125	0.07	Fail	0.0	
						0.25	0.07	Fail	0.0	
	35.3	24.0	50	65	37.5	0.0625	0.15	Infinite	Infinite	
						0.125	0.15	7,620,114	20.9	
						0.25	0.15	Fail	0.0	
			39.4	75	85	52.5	0.0625	0.10	Infinite	Infinite
							0.125	0.10	Fail	0.0
							0.25	0.10	Fail	0.0
			45.9	100	115	75	0.0625	0.07	Infinite	Infinite
							0.125	0.07	Fail	0.0
							0.25	0.07	Fail	0.0
3.0	33.7	18.0	50	65	37.5	0.0625	0.14	Infinite	Infinite	
						0.125	0.14	4,118,590	11.3	
						0.25	0.14	Fail	0.0	
	37.4		75	85	52.5	0.0625	0.09	Infinite	Infinite	
						0.125	0.09	Fail	0.0	
						0.25	0.09	Fail	0.0	
	43.2		100	115	75	0.0625	0.06	Fail	0.0	
						0.125	0.06	Fail	0.0	
						0.25	0.06	Fail	0.0	

Table H.21: Fatigue life edge crack 100 ft.-lbs.

Thickness	Toughness	Width	Yield	Ultimate	Primary Stress	Initial Flaw	Critical Flaw	Cycles to Failure	Life	
(in.)	(ksi√in.)	(in.)	(ksi)	(ksi)	(ksi)	(in.)	(in.)	(N)	(yr.)	
1.0	127.2	18.0	50	65	37.5	0.0625	1.36	Infinite	Infinite	
						0.125	1.36	30,787,772	84.4	
						0.25	1.36	11,068,911	30.3	
			75	85	52.5	0.0625	0.89	Infinite	Infinite	
						0.125	0.89	29,193,192	80.0	
						0.25	0.89	9,474,319	26.0	
			100	115	75	0.0625	0.50	Infinite	Infinite	
						0.125	0.50	26,393,638	72.3	
						0.25	0.50	6,674,763	18.3	
2.0	109.8	18.0	50	65	37.5	0.0625	1.12	Infinite	Infinite	
						0.125	1.12	30,114,750	82.5	
						0.25	1.12	10,379,413	28.4	
			75	85	52.5	0.0625	0.69	Infinite	Infinite	
						0.125	0.69	28,089,082	77.0	
						0.25	0.69	8,404,149	23.0	
			100	115	75	0.0625	0.38	Infinite	Infinite	
						0.125	0.38	24,502,062	67.1	
						0.25	0.38	4,848,400	13.3	
		24.0	50	65	37.5	0.0625	1.20	Infinite	Infinite	
						0.125	1.20	30,491,516	83.5	
						0.25	1.20	10,758,276	29.5	
				75	85	52.5	0.0625	0.72	Infinite	Infinite
							0.125	0.72	28,371,608	77.7
							0.25	0.72	8,590,577	23.5
				100	115	75	0.0625	0.38	Infinite	Infinite
							0.125	0.38	24,725,108	67.7
							0.25	0.38	4,913,223	13.5
3.0	101.0	18.0	50	65	37.5	0.0625	0.99	Infinite	Infinite	
						0.125	0.99	29,631,646	81.2	
						0.25	0.99	9,947,388	27.3	
			75	85	52.5	0.0625	0.60	Infinite	Infinite	
						0.125	0.60	27,376,010	75.0	
						0.25	0.60	7,730,475	21.2	
			100	115	75	0.0625	0.32	Infinite	Infinite	
						0.125	0.32	23,027,206	63.1	
						0.25	0.32	3,397,849	9.3	

Table H.22: Fatigue life edge crack 125 ft.-lbs.

Thickness	Toughness	Width	Yield	Ultimate	Primary Stress	Initial Flaw	Critical Flaw	Cycles to Failure	Life	
(in.)	(ksi√in.)	(in.)	(ksi)	(ksi)	(ksi)	(in.)	(in.)	(N)	(yr.)	
1.0	142.2	18.0	50	65	37.5	0.0625	1.56	Infinite	Infinite	
						0.125	1.56	31,207,544	85.5	
						0.25	1.56	11,488,682	31.5	
			75	85	52.5	0.0625	1.06	Infinite	Infinite	
						0.125	1.06	29,891,800	81.9	
						0.25	1.06	10,172,931	27.9	
			100	115	75	0.0625	0.61	Infinite	Infinite	
						0.125	0.61	27,449,348	75.2	
						0.25	0.61	7,730,473	21.2	
2.0	122.4	18.0	50	65	37.5	0.0625	1.30	Infinite	Infinite	
						0.125	1.30	30,638,280	83.9	
						0.25	1.30	10,906,402	29.9	
			75	85	52.5	0.0625	0.83	Infinite	Infinite	
						0.125	0.83	28,921,654	79.2	
						0.25	0.83	9,228,543	25.3	
			100	115	75	0.0625	0.46	Infinite	Infinite	
						0.125	0.46	25,980,540	71.2	
						0.25	0.46	6,324,592	17.3	
		24.0	50	65	37.5	0.0625	1.42	Infinite	Infinite	
						0.125	1.42	31,054,688	85.1	
						0.25	1.42	11,318,133	31.0	
				75	85	52.5	0.0625	0.87	Infinite	Infinite
							0.125	0.87	29,218,856	80.1
							0.25	0.87	9,445,787	25.9
				100	115	75	0.0625	0.47	Infinite	Infinite
							0.125	0.47	26,168,930	71.7
							0.25	0.47	6,358,671	17.4
3.0	112.4	18.0	50	65	37.5	0.0625	1.15	Infinite	Infinite	
						0.125	1.15	30,214,860	82.8	
						0.25	1.15	10,523,223	28.8	
			75	85	52.5	0.0625	0.72	Infinite	Infinite	
						0.125	0.72	28,358,992	77.7	
						0.25	0.72	8,600,659	23.6	
			100	115	75	0.0625	0.39	Infinite	Infinite	
						0.125	0.39	24,859,860	68.1	
						0.25	0.39	5,251,433	14.4	

Table H.23: Fatigue life edge crack 150 ft.-lbs.

Thickness	Toughness	Width	Yield	Ultimate	Primary Stress	Initial Flaw	Critical Flaw	Cycles to Failure	Life	
(in.)	(ksi√in.)	(in.)	(ksi)	(ksi)	(ksi)	(in.)	(in.)	(N)	(yr.)	
1.0	155.7	18.0	50	65	37.5	0.0625	1.72	Infinite	Infinite	
						0.125	1.72	31,491,482	86.3	
						0.25	1.72	11,772,623	32.3	
			75	85	52.5	0.0625	1.21	Infinite	Infinite	
						0.125	1.21	30,391,906	83.3	
						0.25	1.21	10,673,043	29.2	
			100	115	75	0.0625	0.71	Infinite	Infinite	
						0.125	0.71	28,222,822	77.3	
						0.25	0.71	8,503,949	23.3	
2.0	133.8	18.0	50	65	37.5	0.0625	1.45	Infinite	Infinite	
						0.125	1.45	30,993,094	84.9	
						0.25	1.45	11,263,328	30.9	
			75	85	52.5	0.0625	0.96	Infinite	Infinite	
						0.125	0.96	29,524,798	80.9	
						0.25	0.96	9,826,579	26.9	
			100	115	75	0.0625	0.54	Infinite	Infinite	
						0.125	0.54	26,863,466	73.6	
						0.25	0.54	7,193,227	19.7	
		24.0	50	65	37.5	0.0625	1.61	Infinite	Infinite	
						0.125	1.61	31,462,438	86.2	
						0.25	1.61	11,723,764	32.1	
				75	85	52.5	0.0625	1.01	Infinite	Infinite
							0.125	1.01	29,834,764	81.7
							0.25	1.01	10,106,010	27.7
				100	115	75	0.0625	0.56	Infinite	Infinite
							0.125	0.56	27,125,354	74.3
							0.25	0.56	7,329,831	20.1
3.0	122.7	18.0	50	65	37.5	0.0625	1.30	Infinite	Infinite	
						0.125	1.30	30,641,508	83.9	
						0.25	1.30	10,906,410	29.9	
			75	85	52.5	0.0625	0.84	Infinite	Infinite	
						0.125	0.84	28,953,872	79.3	
						0.25	0.84	9,279,457	25.4	
			100	115	75	0.0625	0.46	Infinite	Infinite	
						0.125	0.46	25,996,442	71.2	
						0.25	0.46	6,274,364	17.2	

Table H.24: Fatigue life edge crack 175 ft.-lbs.

Thickness	Toughness	Width	Yield	Ultimate	Primary Stress	Initial Flaw	Critical Flaw	Cycles to Failure	Life	
(in.)	(ksi√in.)	(in.)	(ksi)	(ksi)	(ksi)	(in.)	(in.)	(N)	(yr.)	
1.0	168.2	18.0	50	65	37.5	0.0625	1.86	Infinite	Infinite	
						0.125	1.86	31,705,094	86.9	
						0.25	1.86	11,986,242	32.8	
			75	85	52.5	0.0625	1.35	Infinite	Infinite	
						0.125	1.35	30,751,398	84.3	
						0.25	1.35	11,032,538	30.2	
			100	115	75	0.0625	0.82	Infinite	Infinite	
						0.125	0.82	28,842,790	79.0	
						0.25	0.82	9,123,917	25.0	
2.0	144.3	18.0	50	65	37.5	0.0625	1.58	Infinite	Infinite	
						0.125	1.58	31,255,146	85.6	
						0.25	1.58	11,545,592	31.6	
			75	85	52.5	0.0625	1.08	Infinite	Infinite	
						0.125	1.08	29,980,046	82.1	
						0.25	1.08	10,278,393	28.2	
			100	115	75	0.0625	0.62	Infinite	Infinite	
						0.125	0.62	27,571,608	75.5	
						0.25	0.62	7,892,474	21.6	
		24.0	144.3	50	65	37.5	0.0625	1.77	Infinite	Infinite
							0.125	1.77	31,767,248	87.0
							0.25	1.77	12,027,132	33.0
				75	85	52.5	0.0625	1.15	Infinite	Infinite
							0.125	1.15	30,334,698	83.1
							0.25	1.15	10,570,070	29.0
				100	115	75	0.0625	0.64	Infinite	Infinite
							0.125	0.64	27,805,282	76.2
							0.25	0.64	8,018,099	22.0
3.0	132.2	18.0	50	65	37.5	0.0625	1.43	Infinite	Infinite	
						0.125	1.43	30,963,100	84.8	
						0.25	1.43	11,230,400	30.8	
			75	85	52.5	0.0625	0.94	Infinite	Infinite	
						0.125	0.94	29,445,700	80.7	
						0.25	0.94	9,764,001	26.8	
			100	115	75	0.0625	0.53	Infinite	Infinite	
						0.125	0.53	26,826,528	73.5	
						0.25	0.53	7,045,209	19.3	

Table H.25: Fatigue life edge crack 200 ft.-lbs.

Thickness	Toughness	Width	Yield	Ultimate	Primary Stress	Initial Flaw	Critical Flaw	Cycles to Failure	Life	
(in.)	(ksi√in.)	(in.)	(ksi)	(ksi)	(ksi)	(in.)	(in.)	(N)	(yr.)	
1.0	179.8	18.0	50	65	37.5	0.0625	1.98	Infinite	Infinite	
						0.125	1.98	31,866,874	87.3	
						0.25	1.98	12,148,023	33.3	
			75	85	52.5	0.0625	1.47	Infinite	Infinite	
						0.125	1.47	31,035,856	85.0	
						0.25	1.47	11,316,990	31.0	
			100	115	75	0.0625	0.91	Infinite	Infinite	
						0.125	0.91	29,308,332	80.3	
						0.25	0.91	9,589,460	26.3	
2.0	154.1	18.0	50	65	37.5	0.0625	1.70	Infinite	Infinite	
						0.125	1.70	31,466,850	86.2	
						0.25	1.70	11,756,205	32.2	
			75	85	52.5	0.0625	1.19	Infinite	Infinite	
						0.125	1.19	30,333,218	83.1	
						0.25	1.19	10,629,133	29.1	
			100	115	75	0.0625	0.70	Infinite	Infinite	
						0.125	0.70	28,156,680	77.1	
						0.25	0.70	8,471,031	23.2	
		24.0	50	50	65	37.5	0.0625	1.93	Infinite	Infinite
							0.125	1.93	32,013,882	87.7
							0.25	1.93	12,258,315	33.6
				75	85	52.5	0.0625	1.28	Infinite	Infinite
							0.125	1.28	30,722,754	84.2
							0.25	1.28	10,960,577	30.0
				100	115	75	0.0625	0.72	Infinite	Infinite
							0.125	0.72	28,371,608	77.7
							0.25	0.72	8,655,562	23.7
3.0	141.0	18.0	50	65	37.5	0.0625	1.54	Infinite	Infinite	
						0.125	1.54	31,180,890	85.4	
						0.25	1.54	11,479,018	31.4	
			75	85	52.5	0.0625	1.04	Infinite	Infinite	
						0.125	1.04	29,860,200	81.8	
						0.25	1.04	10,118,438	27.7	
			100	115	75	0.0625	0.60	Infinite	Infinite	
						0.125	0.60	27,376,010	75.0	
						0.25	0.60	7,730,475	21.2	

Table H.26: Fatigue life center crack current specification

Thickness	Toughness	Width	Yield	Ultimate	Primary Stress	Initial Flaw	Critical Flaw	Cycles to Failure	Life	
(in.)	(ksi√in.)	(in.)	(ksi)	(ksi)	(ksi)	(in.)	(in.)	(N)	(yr.)	
1.0	38.6	18.0	50	65	37.5	0.0625	0.44	Infinite	Infinite	
						0.125	0.44	32,241,980	88.3	
						0.25	0.44	Fail	0.0	
	43.4		75	85	52.5	0.0625	0.30	Infinite	Infinite	
						0.125	0.30	13,696,078	37.5	
						0.25	0.30	Fail	0.0	
	51.1		100	115	75	0.0625	0.21	Infinite	Infinite	
						0.125	0.21	Fail	0.0	
						0.25	0.21	Fail	0.0	
2.0	35.3	18.0	50	65	37.5	0.0625	0.37	Infinite	Infinite	
						0.125	0.37	25,045,806	68.6	
						0.25	0.37	Fail	0.0	
	39.4		75	85	52.5	0.0625	0.25	Infinite	Infinite	
						0.125	0.25	Fail	0.0	
						0.25	0.25	Fail	0.0	
	45.9		100	115	75	0.0625	0.17	Infinite	Infinite	
						0.125	0.17	Fail	0.0	
						0.25	0.17	Fail	0.0	
	35.3	24.0	50	65	37.5	0.0625	0.37	Infinite	Infinite	
						0.125	0.37	25,055,610	68.6	
						0.25	0.37	Fail	0.0	
			39.4	75	85	52.5	0.0625	0.25	Infinite	Infinite
							0.125	0.25	Fail	0.0
							0.25	0.25	Fail	0.0
			45.9	100	115	75	0.0625	0.17	Infinite	Infinite
							0.125	0.17	Fail	0.0
							0.25	0.17	Fail	0.0
3.0	33.7	18.0	50	65	37.5	0.0625	0.34	Infinite	Infinite	
						0.125	0.34	21,123,772	57.9	
						0.25	0.34	Fail	0.0	
	37.4		75	85	52.5	0.0625	0.23	Infinite	Infinite	
						0.125	0.23	Fail	0.0	
						0.25	0.23	Fail	0.0	
	43.2		100	115	75	0.0625	0.15	Infinite	Infinite	
						0.125	0.15	Fail	0.0	
						0.25	0.15	Fail	0.0	

Table H.27: Fatigue life center crack 100 ft.-lbs.

Thickness	Toughness	Width	Yield	Ultimate	Primary Stress	Initial Flaw	Critical Flaw	Cycles to Failure	Life	
(in.)	(ksi√in.)	(in.)	(ksi)	(ksi)	(ksi)	(in.)	(in.)	(N)	(yr.)	
1.0	127.2	18.0	50	65	37.5	0.0625	3.20	Infinite	Infinite	
						0.125	3.20	54,769,872	150.1	
						0.25	3.20	19,264,594	52.8	
			75	85	52.5	0.0625	2.17	Infinite	Infinite	
						0.125	2.17	52,849,568	144.8	
						0.25	2.17	17,344,292	47.5	
			100	115	75	0.0625	1.23	Infinite	Infinite	
						0.125	1.23	49,354,980	135.2	
						0.25	1.23	13,849,682	37.9	
2.0	109.8	18.0	50	65	37.5	0.0625	2.67	Infinite	Infinite	
						0.125	2.67	53,922,760	147.7	
						0.25	2.67	18,435,746	50.5	
			75	85	52.5	0.0625	1.71	Infinite	Infinite	
						0.125	1.71	51,473,684	141.0	
						0.25	1.71	16,003,928	43.8	
			100	115	75	0.0625	0.94	Infinite	Infinite	
						0.125	0.94	47,072,336	129.0	
						0.25	0.94	11,455,243	31.4	
		24.0	50	65	37.5	37.5	0.0625	2.90	Infinite	Infinite
							0.125	2.90	54,433,788	149.1
							0.25	2.90	18,926,786	51.9
				75	85	52.5	0.0625	1.77	Infinite	Infinite
							0.125	1.77	51,814,568	142.0
							0.25	1.77	16,257,366	44.5
				100	115	75	0.0625	0.95	Infinite	Infinite
							0.125	0.95	47,328,444	129.7
							0.25	0.95	11,698,723	32.1
3.0	101.0	18.0	50	65	37.5	0.0625	2.38	Infinite	Infinite	
						0.125	2.38	53,390,420	146.3	
						0.25	2.38	17,858,040	48.9	
			75	85	52.5	0.0625	1.48	Infinite	Infinite	
						0.125	1.48	50,658,676	138.8	
						0.25	1.48	15,098,994	41.4	
			100	115	75	0.0625	0.80	Infinite	Infinite	
						0.125	0.80	45,216,944	123.9	
						0.25	0.80	9,603,482	26.3	

Table H.28: Fatigue life center crack 125 ft.-lbs.

Thickness	Toughness	Width	Yield	Ultimate	Primary Stress	Initial Flaw	Critical Flaw	Cycles to Failure	Life	
(in.)	(ksi√in.)	(in.)	(ksi)	(ksi)	(ksi)	(in.)	(in.)	(N)	(yr.)	
1.0	142.2	18.0	50	65	37.5	0.0625	3.60	Infinite	Infinite	
						0.125	3.60	55,288,780	151.5	
						0.25	3.60	19,783,522	54.2	
			75	85	52.5	0.0625	2.56	Infinite	Infinite	
						0.125	2.56	53,733,532	147.2	
						0.25	2.56	18,228,248	49.9	
			100	115	75	0.0625	1.51	Infinite	Infinite	
						0.125	1.51	50,690,916	138.9	
						0.25	1.51	15,185,627	41.6	
2.0	122.4	18.0	50	65	37.5	0.0625	3.06	Infinite	Infinite	
						0.125	3.06	54,583,128	149.5	
						0.25	3.06	19,062,918	52.2	
			75	85	52.5	0.0625	2.04	Infinite	Infinite	
						0.125	2.04	52,535,308	143.9	
						0.25	2.04	17,002,546	46.6	
			100	115	75	0.0625	1.15	Infinite	Infinite	
						0.125	1.15	48,801,184	133.7	
						0.25	1.15	13,362,563	36.6	
		24.0	50	65	37.5	0.0625	3.39	Infinite	Infinite	
						0.125	3.39	55,137,540	151.1	
						0.25	3.39	19,627,178	53.8	
				75	85	52.5	0.0625	2.14	Infinite	Infinite
							0.125	2.14	52,873,384	144.9
							0.25	2.14	17,375,638	47.6
				100	115	75	0.0625	1.17	Infinite	Infinite
							0.125	1.17	49,109,524	134.5
							0.25	1.17	13,523,312	37.1
3.0	112.4	18.0	50	65	37.5	0.0625	2.75	Infinite	Infinite	
						0.125	2.75	54,088,392	148.2	
						0.25	2.75	18,561,178	50.9	
			75	85	52.5	0.0625	1.77	Infinite	Infinite	
						0.125	1.77	51,791,624	141.9	
						0.25	1.77	16,244,749	44.5	
			100	115	75	0.0625	0.98	Infinite	Infinite	
						0.125	0.98	47,515,356	130.2	
						0.25	0.98	11,945,434	32.7	

Table H.29: Fatigue life center crack 150 ft.-lbs.

Thickness	Toughness	Width	Yield	Ultimate	Primary Stress	Initial Flaw	Critical Flaw	Cycles to Failure	Life	
(in.)	(ksi√in.)	(in.)	(ksi)	(ksi)	(ksi)	(in.)	(in.)	(N)	(yr.)	
1.0	155.7	18.0	50	65	37.5	0.0625	3.93	Infinite	Infinite	
						0.125	3.93	55,643,044	152.4	
						0.25	3.93	20,137,776	55.2	
			75	85	52.5	0.0625	2.91	Infinite	Infinite	
						0.125	2.91	54,335,672	148.9	
						0.25	2.91	18,830,386	51.6	
			100	115	75	0.0625	1.77	Infinite	Infinite	
						0.125	1.77	51,682,668	141.6	
						0.25	1.77	16,177,378	44.3	
2.0	133.8	18.0	50	65	37.5	0.0625	3.38	Infinite	Infinite	
						0.125	3.38	55,022,652	150.7	
						0.25	3.38	19,530,012	53.5	
			75	85	52.5	0.0625	2.34	Infinite	Infinite	
						0.125	2.34	53,275,352	146.0	
						0.25	2.34	17,792,232	48.7	
			100	115	75	0.0625	1.35	Infinite	Infinite	
						0.125	1.35	50,046,272	137.1	
						0.25	1.35	14,491,217	39.7	
		24.0	50	65	37.5	0.0625	3.81	Infinite	Infinite	
						0.125	3.81	55,640,068	152.4	
						0.25	3.81	20,127,584	55.1	
				75	85	52.5	0.0625	2.49	Infinite	Infinite
							0.125	2.49	53,658,508	147.0
							0.25	2.49	18,155,782	49.7
				100	115	75	0.0625	1.38	Infinite	Infinite
							0.125	1.38	50,198,924	137.5
							0.25	1.38	14,723,922	40.3
3.0	122.7	18.0	50	65	37.5	0.0625	3.06	Infinite	Infinite	
						0.125	3.06	54,616,324	149.6	
						0.25	3.06	19,092,598	52.3	
			75	85	52.5	0.0625	2.05	Infinite	Infinite	
						0.125	2.05	52,596,296	144.1	
						0.25	2.05	17,057,206	46.7	
			100	115	75	0.0625	1.15	Infinite	Infinite	
						0.125	1.15	48,949,236	134.1	
						0.25	1.15	13,362,569	36.6	

Table H.30: Fatigue life center crack 175 ft.-lbs.

Thickness	Toughness	Width	Yield	Ultimate	Primary Stress	Initial Flaw	Critical Flaw	Cycles to Failure	Life	
(in.)	(ksi√in.)	(in.)	(ksi)	(ksi)	(ksi)	(in.)	(in.)	(N)	(yr.)	
1.0	168.2	18.0	50	65	37.5	0.0625	4.20	Infinite	Infinite	
						0.125	4.20	55,899,084	153.1	
						0.25	4.20	20,393,808	55.9	
			75	85	52.5	0.0625	3.21	Infinite	Infinite	
						0.125	3.21	54,783,752	150.1	
						0.25	3.21	19,278,476	52.8	
			100	115	75	0.0625	2.01	Infinite	Infinite	
						0.125	2.01	52,452,372	143.7	
						0.25	2.01	16,947,088	46.4	
2.0	144.3	18.0	50	65	37.5	0.0625	3.66	Infinite	Infinite	
						0.125	3.66	55,357,040	151.7	
						0.25	3.66	19,840,466	54.4	
			75	85	52.5	0.0625	2.62	Infinite	Infinite	
						0.125	2.62	53,848,400	147.5	
						0.25	2.62	18,324,204	50.2	
			100	115	75	0.0625	1.55	Infinite	Infinite	
						0.125	1.55	50,859,288	139.3	
						0.25	1.55	15,395,043	42.2	
		24.0	50	65	37.5	0.0625	4.17	Infinite	Infinite	
						0.125	4.17	56,026,744	153.5	
						0.25	4.17	20,493,854	56.1	
				75	85	52.5	0.0625	2.81	Infinite	Infinite
							0.125	2.81	54,264,936	148.7
							0.25	2.81	18,758,816	51.4
				100	115	75	0.0625	1.59	Infinite	Infinite
							0.125	1.59	51,160,124	140.2
							0.25	1.59	15,597,260	42.7
3.0	132.2	18.0	50	65	37.5	0.0625	3.34	Infinite	Infinite	
						0.125	3.34	54,987,456	150.7	
						0.25	3.34	19,465,986	53.3	
			75	85	52.5	0.0625	2.30	Infinite	Infinite	
						0.125	2.30	53,190,760	145.7	
						0.25	2.30	17,656,784	48.4	
			100	115	75	0.0625	1.32	Infinite	Infinite	
						0.125	1.32	49,805,232	136.5	
						0.25	1.32	14,390,154	39.4	

Table H.31: Fatigue life center crack 200 ft.-lbs.

Thickness	Toughness	Width	Yield	Ultimate	Primary Stress	Initial Flaw	Critical Flaw	Cycles to Failure	Life	
(in.)	(ksi√in.)	(in.)	(ksi)	(ksi)	(ksi)	(in.)	(in.)	(N)	(yr.)	
1.0	179.8	18.0	50	65	37.5	0.0625	4.43	Infinite	Infinite	
						0.125	4.43	56,088,584	153.7	
						0.25	4.43	20,583,300	56.4	
			75	85	52.5	0.0625	3.48	Infinite	Infinite	
						0.125	3.48	55,134,692	151.1	
						0.25	3.48	19,629,430	53.8	
			100	115	75	0.0625	2.24	Infinite	Infinite	
						0.125	2.24	53,045,072	145.3	
						0.25	2.24	17,539,794	48.1	
2.0	154.1	18.0	50	65	37.5	0.0625	3.89	Infinite	Infinite	
						0.125	3.89	55,612,904	152.4	
						0.25	3.89	20,097,414	55.1	
			75	85	52.5	0.0625	2.87	Infinite	Infinite	
						0.125	2.87	54,270,580	148.7	
						0.25	2.87	18,781,658	51.5	
			100	115	75	0.0625	1.73	Infinite	Infinite	
						0.125	1.73	51,614,208	141.4	
						0.25	1.73	16,074,187	44.0	
		24.0	154.1	50	65	37.5	0.0625	4.50	Infinite	Infinite
							0.125	4.50	56,312,500	154.3
							0.25	4.50	20,780,642	56.9
				75	85	52.5	0.0625	3.11	Infinite	Infinite
							0.125	3.11	54,746,808	150.0
							0.25	3.11	19,238,252	52.7
				100	115	75	0.0625	1.79	Infinite	Infinite
							0.125	1.79	51,881,356	142.1
							0.25	1.79	16,324,699	44.7
3.0	141.0	18.0	50	65	37.5	0.0625	3.57	Infinite	Infinite	
						0.125	3.57	55,245,312	151.4	
						0.25	3.57	19,760,392	54.1	
			75	85	52.5	0.0625	2.53	Infinite	Infinite	
						0.125	2.53	53,699,324	147.1	
						0.25	2.53	18,169,312	49.8	
			100	115	75	0.0625	1.48	Infinite	Infinite	
						0.125	1.48	50,658,676	138.8	
						0.25	1.48	15,098,994	41.4	